# Numerical analysis of light absorbing semiconducting devices beyond the conventional 3dB bandwidth

Yi, Qian

*Award date:*
2012

*Awarding institution:*
University of Bath

# Numerical Analysis of Light Absorbing Semiconducting Devices Beyond the Conventional 3dB Bandwidth

Qian Yi

A thesis submitted for the degree of Doctor of Philosophy

University of Bath
Department of Electronic and Electrical Engineering

January 2012

# Abstract

This thesis describes an investigation by computer simulation of the performance of two semiconductor device types at the heart of optical high speed data communications, namely the PIN photodiode and the electroabsorption modulator. Both device types operate by light absorption and are therefore likely to have similar factors that limit their performance at high speed.

In order to have high speed detection, the PIN photodiode has been investigated through varying the materials, and used a photodiode structure to improve its bandwidth. If output signals beyond the 3dB frequency limit can be well detected by the photodiode, then significant improvements in the detection speed can be achieved. This possibility is a motivation of this thesis. In this study the InP/InGaAs/InP PIN photodiode is chosen because the light at 1.55μm wavelength can be absorbed by InGaAs. At 1.55μm, the fibre is on low dispersion and low loss.

A numerical model of a PIN photodiode has been written in C. Comprehensive modelling of the PIN photodiode requires a self-consistent solution of the Poisson's equation for calculating the electrostatic potential and the continuity equations for the electron and hole currents. The PIN photodiode model has included the thermionic current over the hetero-junction, drift current and diffusion current that other models often ignore.

After completing an extensive study of the large signal performance of PIN photodiodes at data rates much higher than the conventional 3dB bandwidth, the model was extended to investigate InP/InGaAsP/InGaAs MQW-EAM under high speed applied bias pulses. The numerical modelling of the MQW-EAM requires a self-consistent solution of the Poisson's equation, the Schrödinger's equation and the current continuity equation. The Schrödinger's equation is for the estimation of carrier concentration in the quantum wells. The MQW-EAM numerical model has applied a special technique for adding the carrier concentration in the quantum wells to the charge density.

Large performance has been successfully analysed on PIN photodiode to reveal that optical pulses at repetition frequencies are substantially higher than the conventional 3dB limit can detect (1ps FWHM and up to 240Gb/s repetition rate) to give photocurrent pulses with an open eye diagram even in the presence of simulated noise, however, these output current pulses tend to spread and merge together sometimes. This tendency can be counteracted to a reasonable extent by using a suitable repetition time, and a large input average power. Similar Gaussian shaped applied bias pulses have also applied to the MQW-EAM, in order to generate fast Gaussian shaped light power, however; the output light pulses spread out nearly 3 times compared with its applied bias pulses under 5ps FWHM and 48Gb/s repetition rate. Thinner I-layer and less quantum wells in the MQW-EAM might be the solution.

## Acknowledgements

I am deeply indebted to my supervisor, Dr. Duncan W. E. Allsopp for introducing me to the field of semiconductor device structure and guiding me through the whole PhD. This thesis would not have been possible without his help and support.

Special thanks to Dr. Jianzhong Zhang, Dr. Kuanmeng Wong, Dr. Qin Chen and Mr. Russell Taylor for helpful advice and discussion. I am grateful to Dr. Jianzhong Zhang and Dr. Kuanmeng Wong's valuable discussion on the mathematic solution and model simulation set up. I also would like to thank Dr. Qin Chen for providing me his Matlab program on calculating the confinement factor on the waveguide device and Mr. Russell Taylor for writing the semiconductor hetero-junction band offset calculation in C program.

Thanks are also due to all my friends who have given me great encouragement during the PhD years, their names in turn of alphabet order are Mr. Adam Adrian-Kirby, Dr. Emmanuel Le Boulbar, Dr. Hui Yi Heng, Dr. Bo Li, Mr. Fred N. Pollard, Dr. Girish Rai Pudaruth, Miss Wenwen Shen, Miss Shuang Yu, Miss Yan Zhang.

Especially, I would like to give my special thanks to my parents Prof. Lijun Yi and Mrs. Zhiling Tang for their thoughtfulness and encouragement. I also wish to extend my thanks to my uncle Mr. Jingchi Tang for his kindness and financial support. Last but not least, I want to say thank you to my beloved husband Mr. Johnpaul Woodhead whose patient love enabled me to complete this work.

# Declaration

I declare that this Thesis and the work presented in it are entirely the result of my own independent investigation, except where stated in the text. This work has not been and is not currently submitted for any other degree.

Qian Yi

# List of Abbreviation

APD – avalanche photodiode
BW – bandwidth
C-P-S – current continuity equation-Poisson's equation-Schrödinger's equation
FTTH – fibre-to-the-home
FTTK – fibre-to-the-kerb
I-layer – intrinsic layer
MQW-EAM – multiple quantum wells electro-absorption modulators
QCSE – quantum confined Stark effect
QE – quantum efficiency

# List of Symbols

$|\hat{e} \cdot p_{cv}|^2$ – the momentum matrix

$A_s$ and $B_s$ – coefficients of field intensity $E_{xs}$ or $H_{xs}$

$A_{WF}$ and $B_{WF}$ – coefficient of general solution to the effective mass Schrödinger's equation

$B_{bias}$ – external magnetic field

$C_{Aug}$ – Auger coefficient

$C_{IC}$ – integration constant for obtaining normalized wavefunction

$C_j$ – junction capacitance

$c$ – speed of light in the vacuum

$D_{c(v)}(E)$ – density of state, subscript *c*-conduction band or *v*-valance band

$D_{h(e)}$ – diffusion coefficients or diffusion constants, subscript *h*-hole or *e*-electron

$E_0$ – the eigen state for one particle system

$E_{A(D)}$ – impurity energy level, subscript *A*-acceptor or *D*-donor

$E_{c(v)}$ – electrostatic potential energy, subscript *c*-conduction band or *v*-valance band

$E_{c(v),0(bias)}$ –electrostatic potential energy, subscript *c*-conduction band or *v*-valance band, 0-no applied bias or *bias*-with applied bias

$E_{fp(fn)}$ – quasi-Fermi energy, subscript *fp*- hole or *fn*-electron

$E_{f\text{-}real}$ – actual value of Fermi level

$E_{f\text{-}error(p)}$ – total error in the quasi-Fermi level calculation for hole

$E_{f\text{-}error(n)}$ – total error in the quasi-Fermi level calculation for electron

$E_{hm(en)}$ – eigen-state in quantum well, subscript *h*-hole or *e*-electron, *m*-number of eigen-state for hole or *n*-number of eigen-state for electron

$E_{g(Pg)(Ig)}$ – bandgap energy, subscript *g*-bandgap, *P*-P-layer or *I*-I-layer

$E_{lh1(hh1)(e1)}$ – lowest eigen-state energy in the well, subscript 1-1$^{st}$ eigen-state energy leve, *lh*-light hole, *hh*-heavy hole or *e*-electron

$E_{ref}$ – reference energy level

$E_{xs}$ – electrical field intensity of the first transverse mode (TE) propagating in the active region

$E_{hm}^{en}$ – band-edge transition energy

$F_{0(bias)}$ – electric field, subscript 0-with no applied bias or *bias*-with applied bias

$F_{dipole}$ – dipole field

$f_{c(v)}$ – Fermi distributions, subscript *c*-conduction band or *v*-valance band

$f_{RC}$ – frequency of RC time constant

$f_t$ – frequency of transit time

$G$ – generation term

$G_{QW}^{k}$ – recombination rate in the *k-th* well

$g_{A(D)}$ – the ground-state degeneracy factor of the impurity level, subscript *A*-acceptor or *D*-donor

$H_{xs}$ – magnetic field intensity of the first transverse mode (TM) propagating in the active region

$H$ – Hamiltonian operator

$H\left(\hbar\omega - E_{hm}^{en}\right)$– Heaviside step function

$H_{MP}$ – Hamiltonians factor in a many particle system

$h$ – Planck constant

$\hbar$ – reduced Planck constant/Dirac constant

$\hbar\omega$ – photon energy
$I_{light}$ – power intensity profile
$I_{out}$ – output current of PIN photodiode
$I_{hm}^{en}$ – integration of the complex product of the hole and electron wavefunctions
$J_{h(e)}$ – carrier fluxes, subscript *h*-hole or *e*-electron
$J_{th}$ – thermionic emission current
$J_{h(e),QW}^{esc}$ – escape current, subscript *h*-hole or *e*-electron
$J_{h(e),QW}^{cap}$ – capture current, subscript *h*-hole or *e*-electron
$J_{h(e),QW}^{3D}$ – 3 dimensional exchange current between well and bulk states, subscript *h*-hole or *e*-electron
$J_{h(e),QW}^{k}$ – 2 dimensional exchange current between well and bulk states, subscript *h*-hole or *e*-electron
$K$ – kinetic energy
$k$ – wave vector
$k_B$ – Boltzmann constant
$L_{dev}$ – device length
$l_{MFP}$ – mean free path
$L_{QW}$ – the width of well
$M_i$ – Matrix coefficient for solving general solution to the effective mass Schrödinger's equation
$m_0$ – free electron mass
$m_{1(2)(3)}$–bound states in quantum wells in valance band, subscript 1,2,3-number of bound states
$m_{h(e)}^{*}$ – the effective mass of carrier, subscript *h*-hole or *e*-electron
$m_{lh(hh)(e),\|}$ – in-plane mass of carriers in the well, subscript *lh*-light hole, *hh*-heavy hole or *e*-electron
$N_{A(D)}$ – total impurity concentration, subscript *A*-acceptor or *D*-donor
$N_{A(D)}^{-}(x)$ – ionized impurity concentration, subscript *A*-acceptor or *D*-donor
$n$ – electron concentration under bias
$n_0$ – electron concentration under equilibrium state
$n_{1(2)(3)}$– bound states in quantum wells in conduction band, subscript 1,2,3-number of bound states
$n_{bulk}$ – the electron concentration in the bulk material
$n_{In}$ – intrinsic semiconductor carrier concentration
$n_r$ – refractive index
$n_{QW}^{3D}$ –3 dimensional electron concentration in the quantum well
$n_{QW}^{k}(x)$ – 2 dimensional electron concentration inside the *k-th* quantum well
$P_0$ – average optical power
$P_{in}$ – incident optical power
$P_{out}$ – output optical power
$p$ – hole concentration under bias
$p_0$ – hole concentration under equilibrium state
$p_{bulk}$ – the hole concentration in the bulk material
$p_{QW}^{3D}$ – 3 dimensional hole concentration in the quantum well
$p_{QW}^{k}(x)$ – 2 dimensional hole concentration inside the *k-th* quantum well
$q$ – charge of one electron
$R$ – recombination term

$R_{Aug}$ – Auger recombination
$R_J$ – diode resistance
$R_L$ – external load resistance
$R_S$ –series resistance (bulk and contact resistance)
$R_T$ – total resistance of the equivalent circuit
$R_{SRH}$ – Shockley-Read-Hall recombination
$R_{QW}^k$ – generation rate in the *k-th* well
$\Re$ – responsivity
$\Re_{eye\_A}$ – eye diagram area ratio
$\Re_{eye\_H}$ – eye diagram height ratio
$r$ –convergence ratio of self-consistent calculation
$S_{absorp}$ – cross-sectional area of the absorption layer
$S_{recep}$ – the reception surface of the PIN photodiode
$T$ – temperature
$t$ – time
$\Delta t$ – time step
$V_{bias}$ – applied voltage across the device
$V_{EP}$ – electrostatic potential
$V_{ext}$ – the same external potential for each electron
$V_{nR}$ – recombination velocity
$V_{per}$ – periodic lattice potential
$v_d$ – carrier drift velocity
$v_{fit}$ – electron velocity fitting parameter
$v_{h(e)hf}$ – carrier saturated velocity, subscript *h*-hole or *e*-electron
$v_{th}$ – thermal velocity
$W_{Dep}$ – width of the depletion region
$W_I$ – width of I-layer
$\alpha_0$ – absorption coefficient under thermal equilibrium
$\alpha_{eff\_QW}$ – effective absorption coefficient of MQW-EAM
$\alpha_{FD}$ – absorption coefficient taken in band filling effect
$\alpha_{FD\_bulk}$ – absorption coefficient of bulk material taken in band filling effect
$\alpha_{FD\_i}$ – the absorption coefficient of wells taken in band filling effect, subscript *i*-well number
$\beta$ – propagation constant
$\Gamma_i$ – optical confinement factor for wells, subscript *i*-well number
$\varepsilon_0$ – permittivity in vacuum
$\varepsilon_r$ – the relative permittivity of the semiconductor
$\eta$ – reduced potentials of energy
$\eta_{\#2}$ – coefficient includes different effects, such as effective masses between the semiconductors, the quantum mechanical transmission into the barrier, and the quantum mechanical reflection at the interface
$\eta_{c(v)}$ – reduced potentials, subscript *c*-conduction band or *v*-valance band
$\theta_M$ – ratio of effective masses of two materials
$\lambda$ – input light wavelength
$\mu$ – permeability
$\mu_{h(e)}$ – carrier mobility, subscript *h*-hole or *e*-electron
$\mu_{h(e)}^0$ – carrier low-field mobility, subscript *h*-hole or *e*-electron
$\rho$ – charge density

$\rho_r^{2D}$ – two dimensional reduced density of states
$\tau_{RC}$ – RC time constant
$\tau_t$ – carrier transit time
$\tau_c$ – collision time between two particles
$\tau_{c\_mean}$ – mean time between collisions among the particles
$\tau_{h(e)}$ – carrier life time, subscript *h*-hole or *e*-electron
$\tau_{lh(hh)(e),th}$ – escape time under thermal equilibrium, subscript *lh*-light hole, *hh*-heavy hole or *e*-electron
$\Phi$ – many particle time-dependent Schrödinger's equation
$\phi$ – many particle time-independent Schrödinger's equation
$\varphi$ – general solution of the effective mass Schrödinger's equation
$\Psi$ – time dependent Schrödinger's equation
$\psi_{hm(en)}$ – time independent wavefunction, subscript *e*-electron,*h*-hole and *m*, *n*-eign-state number
$\psi_0$ – the Schrödinger's equation for one electron
$\psi_{F0}$– the envelope function
$\omega$ – input light angular frequency
$\omega_m$ – modulation angular frequency

# Table of Contents

# Chapter 1

## Introduction

## 1.1 Background

Over the last decade, the information age has changed the way people live their lives. Third or fourth generation of mobile phone technology enable the phones to do many different things [1]. That includes instant messaging platforms such as MSN, to personal web space offered by Myspace and on to social networking sites such as Facebook and Bebo [1]. What is more, the broadband connection to each dwelling is becoming commonplace in most countries. All of these technologies mean there is a trend in optical fibre systems to deliver upgraded broad band services to the home via fibre-to-the-home (FTTH) or fibre-to-the-kerb (FTTK) systems. Speeds of hundreds of Mb/s to each subscriber can reasonably be achieved in the foreseeable future [1]. This brings a need to rethink how broadband services can be delivered by optical technology at reasonable cost. Previously, FTTH was also limited by high cost, but in recent years, the cost has fallen because of huge service demand, thus it becomes cost effective in more and more situations [2]. The on-going pressure to reduce the cost of integrated circuits or devices can also contribute to lower the cost of FTTH [2].

Fast speed and low cost semiconductor devices are required for the improvement of all these new applications. This thesis is mainly concerned with analysing the PIN photodiode and multiple quantum well electro-absorption modulators (MQW-EAM), core devices in optical fibre communications networks.

Much research has already been carried out to develop photodiodes to improve their speed of operation [3, 4, 5, 6]. The premise at the core of the research described in this thesis is that the greater resilience of digital signalling to distortion compared with analogue methods should enable device operation at frequencies higher than the conventional 3dB bandwidth limit. Then the speed of a photodiode or a MQW-EAM will be improved by using the output signal beyond the 3dB frequency limit. No numerical simulation has been done on the performance of such photonic devices beyond 3dB frequency limit before. The numerical simulation of InP/InGaAs/InP PIN photodiodes and MQW-EAMs under different conditions has been set up for this purpose. The InP/InGaAs/InP PIN photodiode is an important component for long-wavelength (1.3μm or 1.55 μm) wideband microwave optical

links . That is because the low-loss and low-dispersion or zero-dispersion of optical silicon fibre at 1.55 μm wavelength [7, 8]. The expected growth in these application areas and the need to control infrastructure costs by extending the performance of existing optical communications links provide the motivation for examining the scope for component operation beyond the 3dB bandwidth limit.

Past numerical models often ignored both the carrier diffusion and recombination terms when simulating transport in the I-layer and the thermionic emission effect across the hetero-junction interference [9, 10]. The PIN photodiode model described here includes all the above terms and the important effects of field-dependent-diffusion and field-dependent-drift velocity. The band filling effect and the electric field will both affect the absorption rate in a PIN photodiode. Analysis of frequency response for a PIN photodiode has been performed in the past [11, 12], however, a numerical model has never been set up to analyse different types of signal notably large amplitude signals in the time domain before. This is a very powerful analytical numerical tool, especially for signals beyond the 3dB frequency limit. The similar material InP/InGaAsP/InGaAs MQW-EAM is also modulated to analyse if this device is able to generate the very fast repetition rate for digital optical signals.

## 1.2 Importance of Simulations of Device Performance

Nowadays, numerical modelling plays an important role in the development of semiconductor devices and understanding their operation. Device modelling techniques can substantially reduce the time and costs required for developing a specific device [13]. Comprehensive modelling of the PIN photodiode requires a self-consistent solution of the two equations: the Poisson's equation for calculating the electrostatic potential and continuity equations for the electron and hole currents. Numerical modelling of the MQW-EAM requires the additional complication of a self-consistent solution of the Poisson's equation, the Schrödinger's equation and the current continuity equation. The Schrödinger's equation is for the estimation of the carrier concentration in the quantum wells. Further, the presence of hetero-junction barriers in the PIN photodiode and MQW-EAM means that the thermionic and tunnelling contributions to the current flow need to be taken into account [14, 15, 16]. Finally, a true estimation of the

effective absorption coefficient requires the inclusion of the band filling effect in order to satisfy the quantum mechanical condition of an occupied initial electron state in the valance band and an unoccupied final electron state in the conduction band.

## 1.3 Aims and Objectives

The aim of this project is to test if the individual Gaussian output current pulses beyond the 3dB point can be clearly detected by the InP/InGaAs PIN photodiode and what might improve the quality of Gaussian current pulses beyond 3dB frequency limit. In this work, a means of using the eye diagram is devised to judge the quality of output Gaussian current pulses from a PIN photodiode obtained from a detailed device simulation. The model and concept has been extended to simulations of InP/InGaAsP /InGaAs MQW-EAMs, which have also been tested under different Gaussian pulses applied bias, in order to test how high the data rate can be operated at, in partnership with the photodiode performance.

Two separate programs for InP/InGaAs PIN photodiode and InP/InGaAsP /InGaAs MQW-EAM are required; each in turn needing the material parameters and optical parameters of different InGaAs Alloys in order to investigate the properties for these two devices. Both of the numerical models should include the most important physical principles in order to accurately investigate the fast repetition Gaussian pulses. Much of this physics is time dependent, and therefore a time dependent model is necessary. Both of the models should be flexible enough to modify the input optical power pulses shape for a PIN photodiode or applied bias pulses shape for MQW-EAM, as well as their interval between pulses. The PIN photodiode model also needs to be numerically robust to handle large signal operation, i.e. high input optical power. That is because the high input optical power might improve the quality of output current beyond the 3dB frequency limit.

### 1.3.1 InP/InGaAs PIN Photodiode Simulation

The InP/InGaAs PIN photodiode has been analysed beyond the 3dB limit of its frequency response with different types of time dependent input light wave stimulation. In particular for digital optical communication, it needs to be proven that the PIN photodiode can still produce recognizable pulse current waveform

when it is operated at frequencies higher than the 3dB point. The PIN photodiode will be tested under different conditions (such as applied bias, I-layer width, doping density and input light method) to investigate their influences on the 3dB limit. For this purpose, a one dimensional numerical model for a PIN photodiode has been written in C. The potential energy profile and electric field are estimated by Poisson's equation, and the time and position dependent carrier concentrations are obtained by solving the current continuity equation. For Poisson's equation modelling, the variation in the occupancy of the donor or acceptor impurity levels and in the position of the quasi-Fermi energy with distance lead to the band bending in the potential energy profile is considered, however; the quasi-Fermi energy can only be solved by the current continuity equation. Beside the drift current, the current continuity equation model also includes diffusion current across the device, a significant factor when the densities of photo-generated carriers are large, recombination in the I-layer and thermionic emission current over hetero-junction. Previous one dimensional PIN photodiode numerical models tended to exclude one or more of these key aspects [9, 10, 12]. Thus, the model will give a more complete physics diagram when a PIN photodiode is applied with bias. Since carrier distributions are time dependent, these effects may influence device behaviour at very high frequencies considered in this work. What is more, the generation term includes the band filling effect, because the absorption coefficient appears in the generation term which depends on the electron and hole Quasi-Fermi levels. The solution of Poisson's equation and the current continuity equation then need to be converged.

### 1.3.2 MQW-EAM Simulation

The numerical model for the MQW-EAM is also written in C. Besides the band filling effect, the absorption coefficient for MQW-EAM is strongly bias dependent. That is because it depends on the Quantum Confined Stark Effect (QCSE) specifically overlap of electron wavefunction and hole wavefunction. The overlap becomes smaller when the applied bias increases. Both of the band filling effect and QCSE are included in the absorption coefficient estimation in the MQW-EAM model. The carrier generation is assumed to only occur in the quantum well and the model must include the effect of the quasi-Fermi level variation through a multiple quantum well (MQW) structure.

## 1.4 Outline of Methods

In this thesis, two different light absorbing devices (PIN photodiode and multiple quantum wells electro-absorption modulator (MQW-EAM)) numerical models are presented. Firstly, the PIN photodiode model requires a time dependent self-consistent solution of the Poisson's equation for calculating the electrostatic potential and continuity equations for the electron and hole currents. The full model of the PIN photodiode is shown in Fig.1-1.

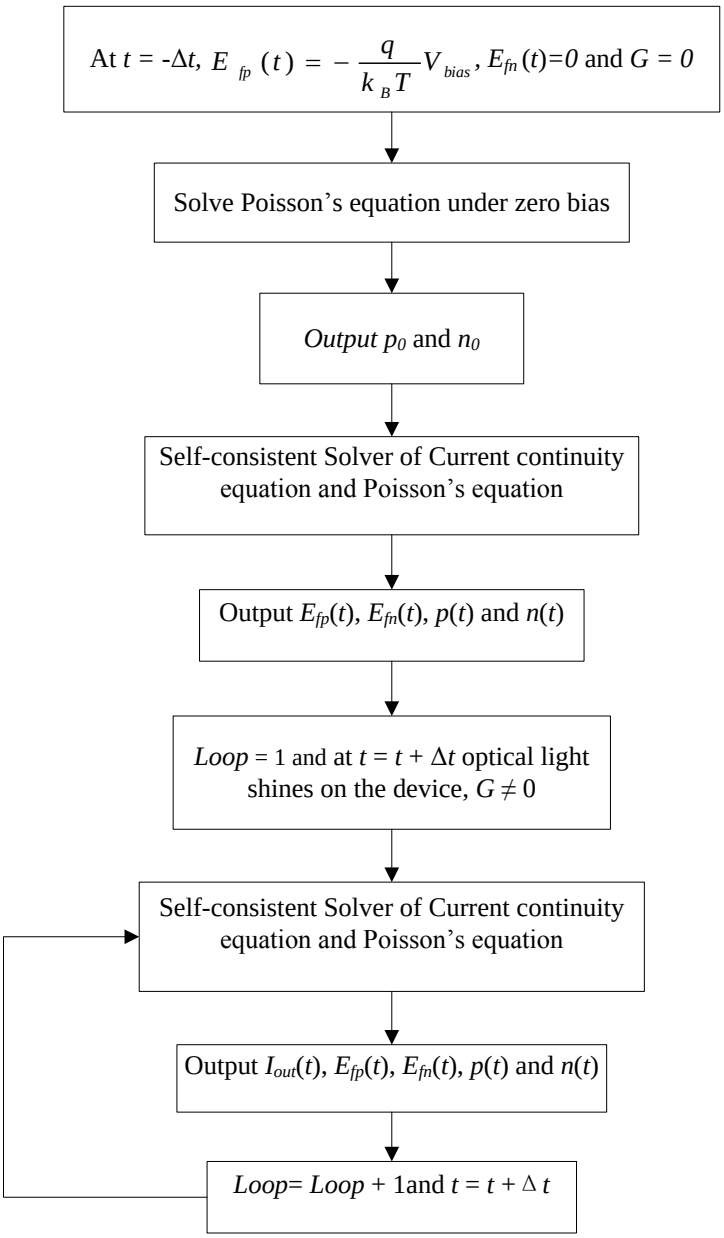


**Figure 1-1** Flow chart of modelling the PIN photodiode.

The solution of Poisson's equation is based on a shooting method which uses the Runge-Kutta method to solve the electric field and potential distribution across the

photodiode device [17]. Then the current continuity equation is solved using an inverse matrix method and finite different method to estimate the position and time dependent carrier concentration. Details of a self-consistent solution for Poisson's equation and the current continuity equation solved by C program developed will be discussed in Chapter 5. The developed software can be used to estimate the electric field, potential, quasi-Fermi level and output electric current.

The second model is set up for the MQW-EAM. Beside the Poisson's equation and current continuity equation, the Schrödinger's equation is added specially for solving the carrier concentration in quantum well structure. The flow chart of solving the three equations self-consistently for the MQW-EAM on a step wise time basis is shown in Fig. 1-2.

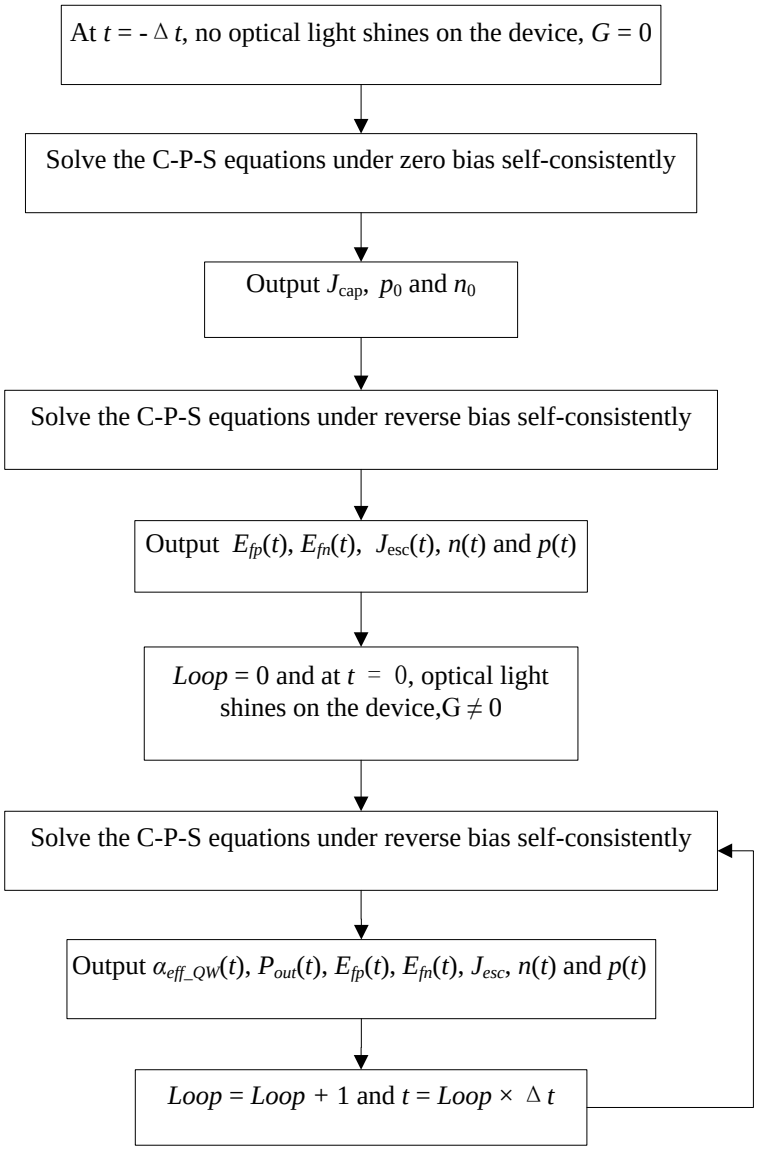


**Figure 1-2** Flow chart of solving MQW-EAM model.

The Poisson's equation and current continuity equation are based on the numerical methods used in the PIN photodiode device model. The Schrödinger's equation is solved by applying a transfer matrix method to obtain the eigen-state energies and the carrier concentration in the quantum well. The time dependent MQW-EAM Solver is also written in C, and the numerical methods details will be discussed in Chapter 6. The developed software can be used to estimate electric field, potential, quasi-Fermi level, time dependent absorption coefficient and output optical power.

## 1.5 Layout of Thesis

This thesis investigates the physical properties of InP/InGaAs/InP PIN photodiode and InGaAsP/InGaAs MQW-EAM. The research background and its objective were introduced in this chapter. Then a brief introduction on numerical methods for both the PIN photodiode and MQW-EAM modelling was presented.

The background and basic physics of a PIN photodiode will be introduced in Chapter 2. In bulk semiconductor material, the red shift is caused by the electric field, and this is defined as the Frank-Keldysh effect [18]. The excitonic effects can be neglected due to the thermal dissociation at room temperature, and the decreased overlap between electrons and holes caused by the applied electric field [18].III-V materials are used for PIN photodiodes which are used in $1.3\mu m$ and $1.55\mu m$ wavelength optical communications systems. In particular InGaAs(P) is used since its bandgap is able to absorb the light corresponding to zero material dispersion ($1.3\mu m$) or lowest loss ($1.55\mu m$) in silica optical fibres [19]. The performance of a photodiode can be characterized by its responsivity. This parameter is related to the quantum efficiency and bandwidth [20]. For analysing a sequence of Gaussian input light pulses, the eye diagram gives a more accurate analysis of digital system performance than responsivity. The reason will explained further in Chapter 2. The bandwidth of the PIN diode is limited by transit time and the RC time constant [21]. Both factors are dealt with in this thesis.

Chapter 3 discusses the multiple quantum wells electroabsorption modulator (MQWs-EAM). Unlike the bulk semiconductor material, the exciton effects remains strong in the quantum well under applied bias at room temperature, due to the carriers being confined in the well [18]. Therefore, the excitonic effects can

have a strong effect on the absorption for quantum wells structure. As well as the excitonic effects, the applied field decreases the effective bandgap, then a red shift in the absorption edge is realized [22]. This is referred to as quantum confined Stark effect (QCSE). In InGaAsP/InGaAs quantum wells, the exciton peaks are broadened under applied bias and the QCSE is more significant to the absorption changes. When a photon is applied to the quantum wells, an optical transition can occur. Optical transitions in quantum wells take two forms: inter-band transitions and inter-subband transitions. The inter-band optical transition is the dominant mechanism for the optical light in MQW-EAM [23]. The numerical model of quantum wells that has been set up in our MQW-EAM model is for InGaAs(P) alloys, which are very attractive for optical fibre communication systems.

Chapter 4 contains the method of estimating and determining the optical parameters for light absorbing semiconductors, such as the absorption coefficient, optical confinement factor, input light wavelength selection and the carrier generation term calculation. The simple estimations of effective absorption for bulk material and quantum wells are set up in the model. For a waveguide device, the absorption coefficient will be influenced by the confinement factor. Semiconductor devices can usually only perform normally within a range of optical light wavelength. The detailed selection of input light wavelength for both devices has been introduced in this chapter. The generation rate calculation for different input light methods, denoted here as top-entry mode and waveguide mode or edged-coupled is introduced in this chapter too.

In Chapter 5, a detailed definition of the modelling methods for a PIN photodiode is presented. Comprehensive PIN photodiode modelling requires a self-consistent solution of the Poisson's equation for calculating the electrostatic potential and of the continuity equations for the electron and hole currents. For a clearer understanding of both equations, the definitions of the equations have been introduced before applying the numerical method. A modified version of shooting method and Runge-Kutta method are applied to solve the Poisson's equation and the inverse matrix method and finite difference method are also used to solve the current continuity equation. Our model includes both the diffusion and recombination terms in the intrinsic region, and the thermionic emission effect

across the hetero-junction, factors that are often ignored [9, 10, 12]. The model also takes into account the effect of band filling on the effective absorption coefficient. A flow chart for obtaining the self-consistent solution of Poisson's equation and current continuity equation is listed in the last section of the chapter.

Chapter 6 contains a detailed definition of the modelling theory for the MQW-EAM. Comprehensive modelling of the MQW-EAM, requires self-consistent solutions of Poisson's equation, the current continuity equation and Schrödinger's equation [9]. The charge density term in Poisson's equation needs to include the carrier concentration in the quantum well [24], and the current continuity equation has separate forms for bulk material and quantum wells material. The solution to Schrödinger's equation leads to evaluating the single particle to give an approximate quantum mechanical description of the system [25]. The numerical methods for solving Poisson's equation and current continuity equations that are introduced in Chapter 5 can be still applied here. The transfer matrix method and single particle effective mass equation are presented to solve the Schrödinger's equation. Our model includes both the diffusion and recombination terms in the intrinsic region, the current transport in between quantum well and bulk material, and the thermionic emission effect across the hetero-junction. A special technique of adding the carrier concentration in the wells to the Poisson's equation to make a better rational approximation is used in the model. A flow chart for obtaining the self-consistent solution of Poisson's equation and Schrödinger's equation and a complete self-consistent solution of three equations are listed in the last section of the chapter.

Chapter 7 describes the results of PIN photodiode modelling. Specifically InP/InGaAs/InP PIN photodiodes under different external conditions have been simulated. Firstly, different shaped input optical signals have been tested. Furthermore, a more detail analysis of single and sequences of Gaussian shaped input optical waves have also been discussed in this chapter. Finally, the eye diagram ratio of a received signal current arising from Gaussian shaped light pulses has been estimated and compared under different conditions, such as I-layer width, applied bias, input average power, doping density and input light method (top entry or edge coupled). The signals beyond the 3dB frequency point have a detailed

analysis under the above mentioned conditions.

Chapter 8 shows the results of MQW-EAM modelling. The model has been tested under different types of applied bias. The calculated absorption coefficients are too noisy to analyse. Thus, a data smooth function is applied to the absorption coefficient data throughout the chapter. For square shaped pulses applied bias, different input average power and different on/off time has been tried on the device to investigate their influences on the absorption coefficient of the device. The estimated output power for the Gaussian shaped applied bias pulses has also been analysed under different FWHM.

Chapter 9 presents a conclusion for this thesis and future work for further research.

# Chapter 2

## PIN Photodiode Basics

## 2.1 Review of PIN Photodiodes

A photodiode is one of the significant components in the optical receiver, and its performance has a large influence on the receiver [26]. It is normally used to convert the modulated optical light signal that is transmitted by the optical fibre into an electronic signal (electrical current) [27]. There are many different types of photodiode, such as the PIN photodiode the avalanche photodiode (APD), the optically pre-amplified PIN detector and the uni-traveling-carrier photodiode [26, 28]. The PIN photodiode is perhaps the simplest detector as shown in Fig.2-1, the basic telecommunications PIN photodiode structure consists of a wide bandgap P-type semiconductor material followed by a low-doped narrow bandgap intrinsic layer (I-layer) and next a section of N-type semiconductor of either the same bandgap as the I-layer or wider bandgap to prevent absorption in this region.

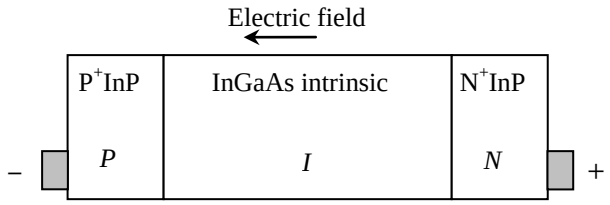


**Figure 2-1** A example of p-i-n InGaAs/InP photodiode.

The device has to be reverse biased in the photoconductive mode [29]. When the device is biased, the low-doped I-layer has relatively higher resistance. Therefore, the I-layer has most of the applied voltage and electric field across it [29]. If photons are incident on the I-layer, electron-hole pairs are created. Then the very strong field in the I-layer will sweep these carriers to the ends of device [26]. Some parameters of PIN photodiode must meet the requirements of optical fibre transmission; responsivity at the required wavelength, and a response time consistent with the electrical bandwidth of the signal [27].

Nonlinear processes are introduced by the Franz-Keldysh effect and band-filling effect in the PIN photodiode [30]. The Franz-Keldsh effect causes a red shift in the absorption spectrum of a semiconductor depending on the applied electric field [31], and it can also change the refractive index due to the applied electric field [22]. The change in refractive index is not developed in this work, however, the electric field dependent absorption coefficient is applied to the model and it will be introduced in

Chapter 4. The detail of Franz-Keldysh effect will be introduced later in section 2.2. The band-filling effect will be also taken account in the modelling and the details of the band-filling effect will also be described in Chapter 4.

Comprehensive PIN photodiode modelling requires a self-consistent solution of the Poisson's equation for calculating the electrostatic potential and continuity equations for the electron and hole currents. The PIN photodiode numerical model has been set up by many people before [9, 10, 12], however; the new model includes both the diffusion and recombination terms in the intrinsic region and the thermionic emission effect across the hetero-junction, factors that are often ignored. The model also takes into account the effect of band filling on the effective absorption coefficient. The optical parameters calculations and numerical methods of solving Poisson's equation and the current continuity equation for a PIN photodiode will be introduced in Chapter 4 and Chapter 5 respectively.

## 2.2 Franz-Keldysh Effect

The Franz-Keldysh effect occurs in bulk semiconductor materials. It is caused by an electric field which includes a change in the complex dielectric constant of a direct band gap semiconductor, occurring at photon energies close to the band edge [22]. It describes the primary shift and broadening of the band edge absorption when an electric field is applied [32, 33], and can be thought of as a photon assisted tunnelling effect [34]. Schematically, the Franz-Keldysh effect can be illustrated as the conduction band $E_c$ and valance band $E_v$ being tilted by the applied electric field as shown in Fig. 2-2 [35], then the wavefunctions of carriers in the bands tunnel into the tilted band gap so that photons need a lower energy $\hbar\omega$ to excite an electron into the conduction band [36].

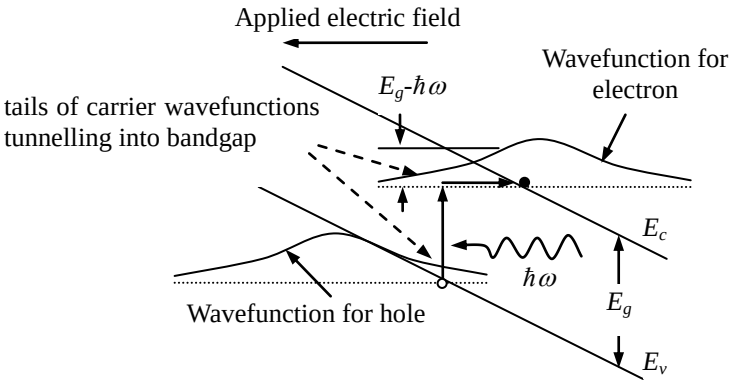


**Figure 2-2** Schematic diagram of Franz-Keldysh effect.

This effect induces an effective red shift in the bandgap energy, it changes both the absorption constant of the semiconductor and its refractive index [37] and has been used as basis for optical modulation [38, 39].

## 2.3 III-V Materials for PIN Photodiode

III-V semiconductor materials are commonly used in semiconductor devices due to their usually direct bandgap, which is favourable for optoelectronics [40] and excellent electron velocity characteristics that permit the operation of devices at very high frequencies [41]. InGaAsP, InAlAs and InGaAs alloys are very attractive for optical fibre communication systems, near infrared multichannel spectroscopy, radiant thermometry and non-destructive inspection system [42], because their bandgaps are such that these semiconductors emit or absorb light having wavelengths corresponding to those at which zero dispersion (1.3μm) or lowest loss (1.55μm) occurs in silica optical fibres [19]. For $In_{0.53}Ga_{0.47}As$, a direct bandgap semiconductor with high saturation drift velocity, the absorption coefficient at 1.3μm and 1.55μm is about $10^4 cm^{-1}$ and $0.7\times10^4 cm^{-1}$ respectively making it an excellent choice as the I-layer in a PIN photodiode [43]. $In_{0.53}Ga_{0.47}As$ lattice matched to InP is able to detect all the light emitted by InGaAs(P) and In(Al)GaAs materials matched to InP. Therefore, $In_{0.53}Ga_{0.47}As$ is most widely used as a light absorber in optical-fibre communications [44].

## 2.4 Quantum Efficiency and Responsivity

The effective absorption coefficient is related to the quantum efficiency (QE) which is the number of the electron-hole carrier pairs generated per incident photon of energy $\hbar\omega$ [45] or can be defined as,

$$QE = \frac{I_{out}}{q}\left(\frac{\hbar\omega}{P_{in}}\right) \tag{2-1}$$

where $I_{out}$ is the photocurrent, $\frac{P_{in}}{\hbar\omega}$ is photo flux and $P_{in}$ is the optical power that incident on the device.

The responsivity is the ratio of the generated photocurrent and the input optical power [21],

$$\Re = \frac{I_{out}}{P_{in}} \tag{2-2}$$

Therefore, QE can be related to the responsivity by,

$$QE = \frac{\Re\hbar\omega}{q} = \frac{2\pi\Re\hbar c}{\lambda q} \tag{2-3}$$

The larger the responsivity is, the better the photodiode performs. For the same amount of the input optical power, if the I-layer width increases, in other words, the light absorption volume increases, the output photocurrent will rise as well. Therefore, the wider the I-layer is, the larger the responsivity will be, however; the response time will be extended as the I-layer width increases. The response time is introduced in the section 2.6.

## 2.5 Eye Diagram Analysis

The responsivity only provides a measure of the average or the peak value of output photocurrent, however; it cannot measure the quality of the signal, especially for a sequence of Gaussian shaped pulses. For accurate analysis of a sequence of Gaussian pulses in the PIN photodiode, an eye diagram analysis is applied [46]. An eye diagram is formed by superimposing oscilloscope traces of the receiver filter output [47]. Each trace is triggered at the same phase within a symbol interval and lasts for a few symbols [47]. The eye diagram pattern of perfect sine wave as seen on the oscilloscope is shown in Fig. 2-3 [48].

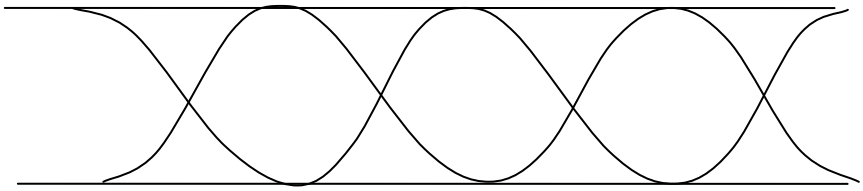

**Figure 2-3** Eye diagram as seen on the oscilloscope.

When a sequence of Gaussian shaped input light pulses is applied to the PIN photodiode device, a sequence of Gaussian shape current should be generated. When the repetition time gets faster (i.e. time interval between pulses get shorter), the current pulses tend to merge together. This effect will limit the ability of a system to distinguish pulses in the following way. First an eye diagram area ratio is defined. This is given by,

$$\Re_{eye\_A} = \frac{A_c}{A_p} \tag{2-4a}$$

where $A_p$ is the cross-hatched area in Fig.2-4(a), it is the area between forward half period power and actual input optical power. The same definition is applied to $A_c$ for output current, and it is the cross-hatched area in Fig.2-4(b). The eye diagram height ratio is defined by,

$$\Re_{eye\_H} = \frac{H_c}{H_p} \tag{2-4b}$$

$H_p$ is the height between the peak point of forward half period power and corresponding point of actual power as shown in Fig.2-4(a). The same definition applied to $H_c$ for output current and is shown in Fig.2-4(b)

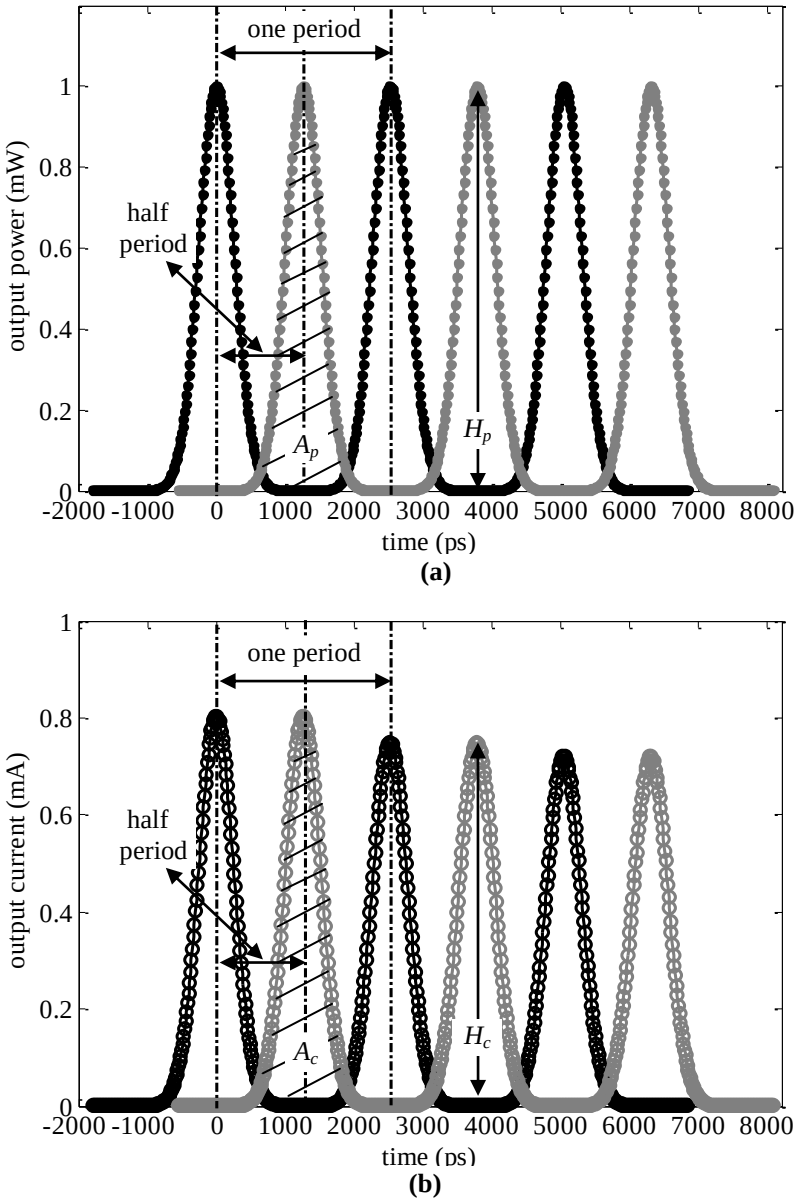


**Figure 2-4** The eye diagram of **(a)**input power and **(b)**output current.

## 2.6 Time Dependent Behaviours

The response time is the time required for the photodiode to respond to input optical input power and then produce an output current [49]. The response time of the photodiode is set by two different contributions mainly: the transit time and the RC time constant [27]. The response time of the diode is related to its usable small signal bandwidth [49]. The bandwidth of the PIN photodiode is conventionally defined as [46],

$$BW = \frac{1}{\sqrt{\left(\frac{1}{f_{RC}}\right)^2 + \left(\frac{1}{f_t}\right)^2}} \tag{2-5}$$

where $f_{RC} = \frac{1}{2\pi\tau_{RC}}$ , $f_t = \frac{1}{2\pi\tau_t}$, $\tau_{RC}$ is the RC time constant and $\tau_t$ is the carrier transit time.

### 2.6.1 Transit Time Effect

In small area photodiodes the response time primarily depends on the transit time [50]. The definition of the transit time for the photodiode is the time taken for photo-generated carriers to travel through the I-layer. One of two factors decides the response speed of the photodiode. Apparently, the shorter I-layer width results in a shorter transit time and faster response speed, however; the responsivity will fall as the I-layer width decreases [43]. To avoid the trade-off between responsivity and transit time, the light can be edge-coupled into the device which then acts like a waveguide [43]. Details of waveguide mode will be introduced in Chapter 4 section 4.4.2. The transit time is often approximated as [51],

$$\tau_t \approx \frac{W_i}{v_d} \tag{2-6}$$

where $W_i$ is the width of the intrinsic layer and $v_d$ is the carrier drift velocity. The transit time can be directly obtained by estimating the delay time between output current and input optical power, as shown in Fig. 2-5. In this example, the output current has 2ps time delay, so the transit time is 2ps.

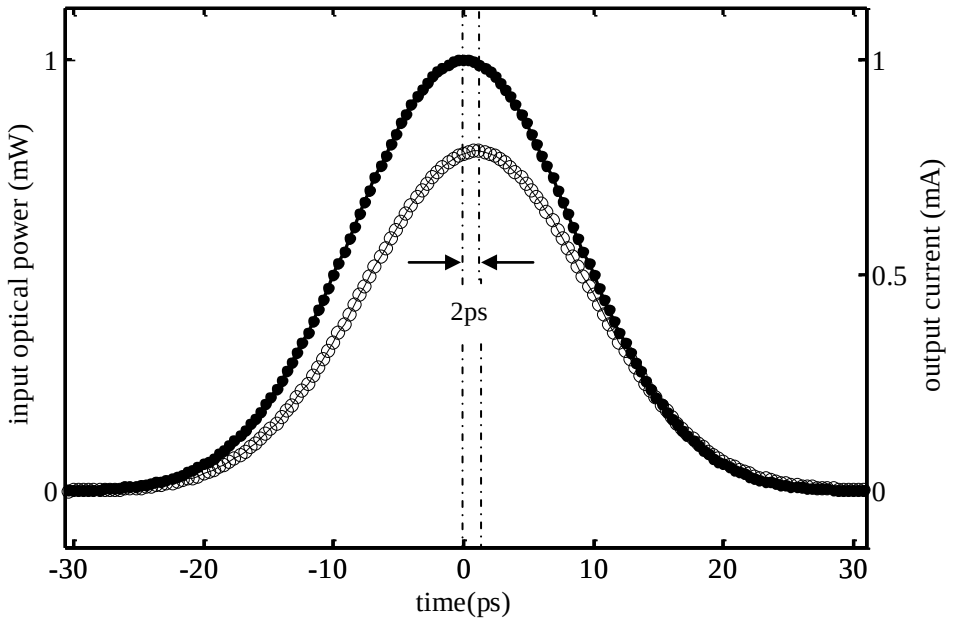


**Figure 2-5** The 20ps FWHM 1mW optical power input optical power (black dot) and output current (circle).

When a sequence of input optical pulses are applied to the device, an output current broadening effect can occur if the electrons that are generated by the first optical pulse are still in the I-layer when the second pulse has arrived at the same region. Then the electrons generated by the second pulse will merge with those that are generated by the first pulse [43].

### 2.6.2 RC Time Constant

The RC time constant is related with the circuit parameters that include junction capacitance ($C_J$), diode resistance ($R_J$), external load ($R_L$) and series resistance ($R_S$) [52]. The series resistance is bulk and contact resistance and is often neglected due to being usually only a few ohms [46, 52]. The equivalent circuit of PIN photodiode that includes all of circuit parameters is shown in Fig. 2-6.

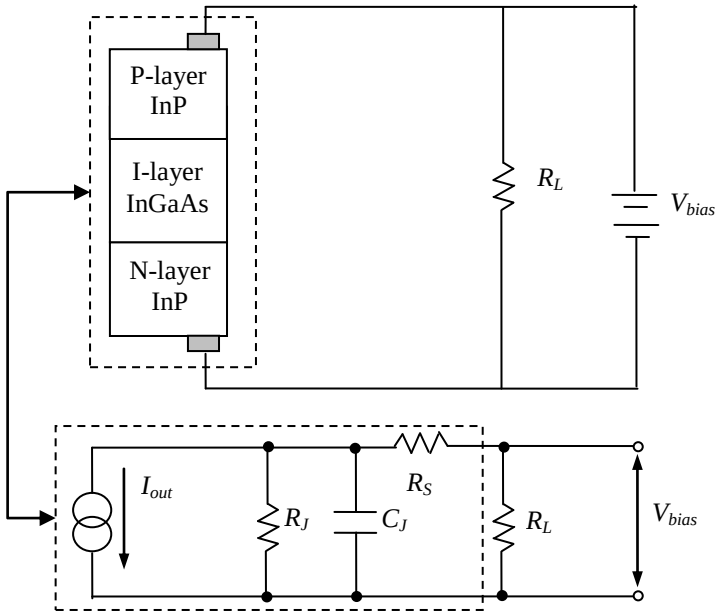


**Figure 2-6** Equivalent circuit of PIN model.

The equivalent junction capacitance is defined as,

$$C_J = \frac{\varepsilon_0 \varepsilon_r A}{W_{Dep}} \tag{2-7}$$

where $\varepsilon_o$ is the permittivity in vacuum, $\varepsilon_r$ is the relative permittivity of the semiconductor, $A$ is the area of the I-layer, and $W_{Dep}$ is the depletion width. The diode resistance $R_J$ can be found by Ohm's law,

$$R_J = \frac{V_{bias}}{I_{out}} \tag{2-8}$$

where $V_{bias}$ is the applied voltage across the device and $I_{out}$ is the current through I-layer. The external load resistance ($R_L$) represents the loading effects of any following circuit. The standard impedance $50\Omega$ is chosen to be the load resistance. Therefore, the total resistance of the equivalent circuit is given as,

$$R_T = \frac{R_J R_L}{R_J + R_L} \tag{2-9}$$

Then the photodiode capacitance also has significant influence on the overall response time via the RC time constant is defined as [46],

$$\tau_{RC} = R_T C_J \tag{2-10}$$

## 2.7 Summary

This chapter has introduced the basic physics of a PIN photodiode. The absorption coefficient is influenced by the band filling effect and the Franz-Keldysh effect.

The reason for choosing InGaAs as the I-layer for the PIN photodiode is because it can absorb the wavelengths corresponding to those at which zero dispersion (1.3μm), or lowest loss (1.55μm), occurs in silica optical fibres. The quality of the output current pulses in this thesis will be measured by eye diagram ratio rather than responsivity. Eye diagram ratio is a better measurement for a sequence of pulses because its value is reduced when the output pulses start merging, a condition that represents the true limiting conduction for unambiguous data interpretation in the case of large amplitude pulse operating conditions. That means the eye diagram ratio can detect if the output pulses start merging, however, the responsivity value does not fall since it only measures the peak value of output pulses. The eye diagram also can lead to an analysis of the pulse time spreading ratio that will be introduced in Chapter 7. The transit time effect and the RC time constant are the two major factors to the bandwidth of the photodiodes.

# Chapter 3

## Multiple Quantum Well Electroabsorption Modulators (MQW-EAM) Basics

## 3.1 Review of the MQW-EAM

Multiple Quantum Well Electroabsorption Modulators (MQW-EAM) are important components for long haul, large capacity optical fibre communications systems [53]. The MQW-EAM has been utilized in pulse generation, de-multiplexing, wavelength conversion and signal generation [54]. As data rates increase, they become more and more important in optical communications systems because of their large absorption change and hence large modulation depth and their broad modulation bandwidth.

Band filling and the Quantum Confined Stark Effect (QCSE) will both affect the absorption rate. The QCSE is the basis of the functionality of an MQW-EAM [54]. Typically, a MQW is embedded in the intrinsic layer of a hetero-junction PIN diode structure, see Fig. 3-1.

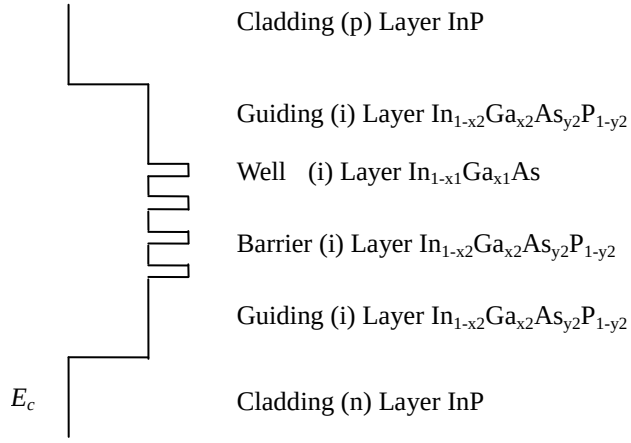


**Figure 3-1** Conduction band edge profile (neglecting band bending) in the basic structure of multiple quantum well electroabsorption modulators (MQW-EAM).

As a reverse bias is applied, the depletion field in the intrinsic layer increases, causing the effective absorption edge of the MQW to shift to lower energy, or in terms of light wavelength, red shift. If the incident light is only weakly absorbed when the MQW-EAM is in the unbiased state, the light becomes strongly absorbed when the reverse bias is applied, modulating the intensity of the light beam passing through the device. The QCSE is discussed more in section 2.2. When the wells are filled by the excited carriers the absorption becomes reduced, and this is called band filling [55].

Having a short photo-generated carrier escape time is very important for the

modulator, otherwise the device will perform poorly at high speed due to the building up of charge in the wells or in the intrinsic layer of the overall device structure. Short escape times can be obtained by reducing the wells depths or increasing the applied field [54].

For telecommunications applications, the basic structure of MQW-EAM takes the form of a dielectric waveguide which includes cladding layers, guiding layers with the multi-quantum well layers (wells and barriers) contained in the waveguide core. The chosen structure in the modelling described latter is assumed to be comprised of InP/InGaAsP/InGaAs. Its generic structure is shown in Fig 3-1.

The dynamic properties of MQW-EAM are to be investigated by setting up an appropriate numerical model. The dynamic properties to be modelled include changes in absorption under QCSE, field-dependent escape from and capture into the wells, optical generation and recombination of carriers and thermionic emission requires a detailed model [56]. For carrier transport in the MQW-EAM, the pertinent basic equations are Poisson's equation, the current continuity equation and Schrödinger's equation. Poisson's equation relates the potential to the charge distribution [9]. The continuity equations for holes and electrons control the conservation of carriers in any volume [9]. Schrödinger's equation gives the carrier density in terms of electron and hole eigen-state in hetero-junction devices [57]. An accurate carrier transport model requires the self-consistent solution of all three equations.

## 3.2 Quantum Confined Stark Effect (QCSE)

The Quantum Confined Stark Effect (QCSE) is related to the Franz-Keldysh effect [58]. The QCSE refers to the variations that occur in the electronic and optical spectra of a quantum well when the electric field is applied [33]. Based on this effect, optical modulators are able to have high modulation contrast and high speed at low bias voltage [59].

The QCSE effect occurs when an electric field is applied perpendicular to the quantum well layers [60]. This has two effects. First, the density of states edges undergoes a red shift, as shown in Fig. 3-2, the quantum confined equivalent of the

Franz-Keldysh effect. In addition, the effect of the applied field on exciton formation must be considered. The binding energy of an exciton decreases due to the applied field tending to ionize the exciton by pulling the electron – hole pair apart [61].

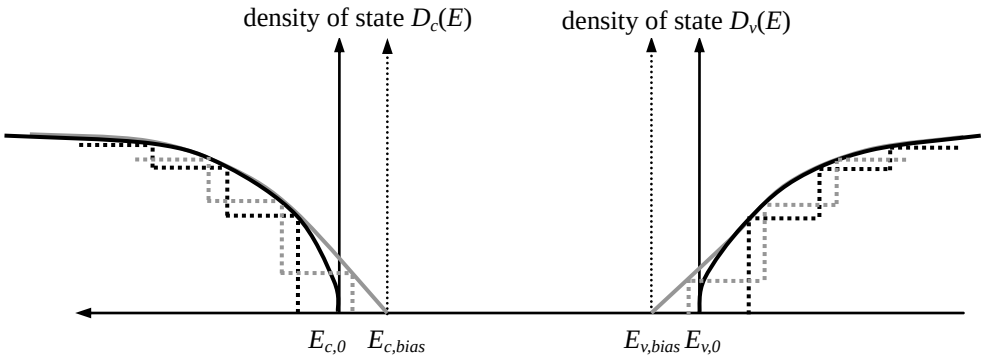


**Figure 3-2** Parabolic three dimensional density of state with (grey solid line) or without (black solid line) Franz-Keldysh effect and two dimensional density of states with (grey dash line) or without (black dash line) quantum confined Franz-Keldysh effect.

When the electric field is applied perpendicular to the layers, the ground state wavefunction of the electron and hole are pushed towards opposite sides of the quantum wells. Fig. 3-3 illustrates this effect.

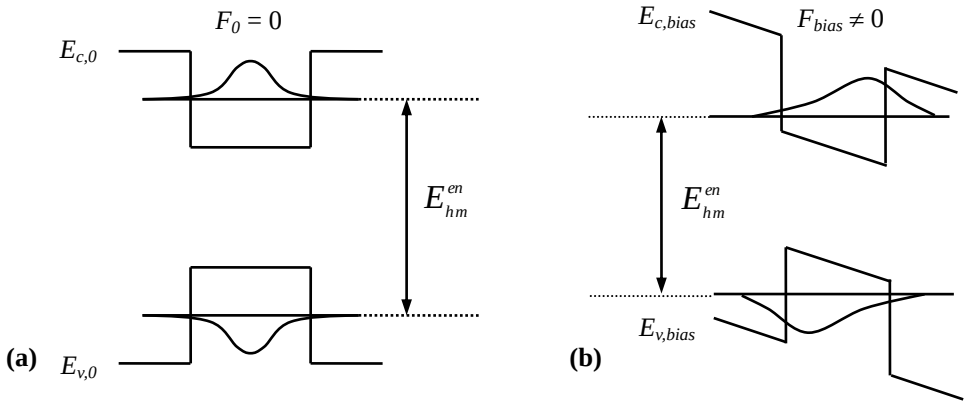


**Figure 3-3** Quantum well energy bands and wavefunction **(a)** with no field **(b)** with applied field.

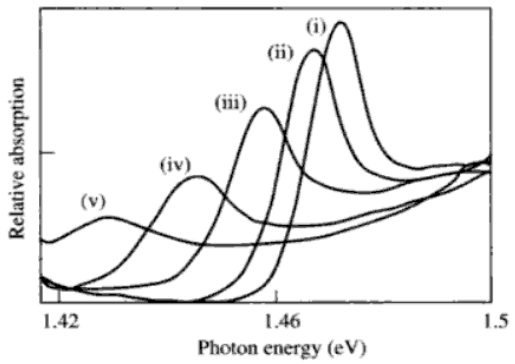


**Figure 3-4** Electroabsorption spectra for a 94Å AlGaAs/GaAs quantum well under electric field of (i) 0V/μm, (ii) 6V/μm, (iii) 11V/μm, (iv) 15V/μm, and (v) 20V/μm (Data from Schmitt-Rink et al.,1989).

The field induced absorption changes in typical quantum wells are shown in Fig.3-4 [62]. These changes are much larger than that of the Franz-Keldysh effect [63]. In Fig.3-4, it is obvious that the absorption coefficient has been reduced, broadened, and shifted, to lower energy after the electric field is applied [64]. Thus, the optical absorption is strongly electric field dependent.

The reasons for the causes of the changes in the absorption coefficients are listed below.

1. The effective bandgap energy $E_{hm}^{en}$ falls with the increasing electric field. Notice that the separation of the ground state conduction subband and valence subband has become smaller and the binding energy of excitons decreases, therefore the absorption coefficient has a red shift and the peak value has reduced after the field is applied [45]. The change in effective bandgap energy is mainly related to the exciton contribution to the absorption in InGaAs/AlGaAs quantum wells [65]. In InGaAsP/InGaAs quantum wells disorder introduced by random fluctuations in the composition of the layers causes the exciton peaks to broaden [66] and the relative contribution of the density of states shift to the absorption change becomes more significant [54, 67].
2. The exciton absorption line also broadens because of field induced carrier tunnelling [64]. In addition, the peak of absorption spectrum obviously gets smaller and smaller and even nearly disappears when the field increases to $20V\mu m^{-1}$. The disappearance of absorption peak coincides with the condition of complete exciton ionization [61]. Fig.3-5 shows a schematic diagram illustrating the effect of with and without applied field on the excitons and density of states contribution to the QCSE. In this work, on InGaAsP/InGaAs quantum wells only the density of states contribution to the absorption edge red shift is calculated.

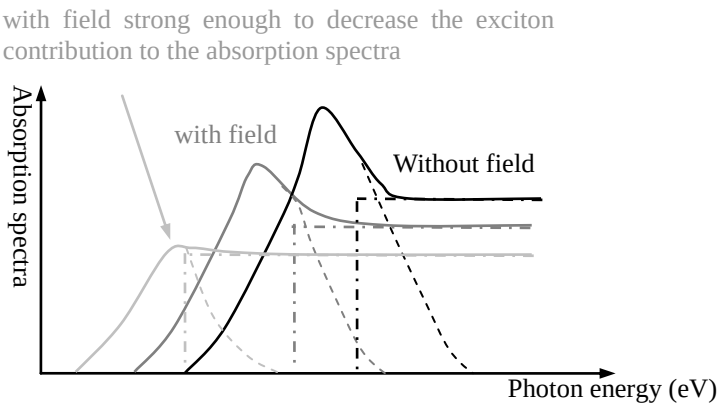


**Figure 3-5** Absorption spectra against photon energy:
area under dashed line – excitonic contribution to absorption spectrum
area under dashed point line – density of states contribution to absorption spectrum

## 3.3 Optical Transition in Quantum Wells

Optical transition can occur between states in quantum wells, since potential wells are formed in both conduction band and valance band, various transitions can be envisioned [68]. In the quantum wells, two different types of transition may take place, these are intersubband and interband transition depending on if the initial and final states belong to the same band or not [69].

### 3.3.1 Interband Transition

Interband transitions are observed in all solids [70]. The process that creates the electron and hole pairs in conduction band and valance band is defined as interband absorption [71]. The opposite process interband luminescence means an electron drops from a conduction band state to a valence band state by an emitting photon [70].

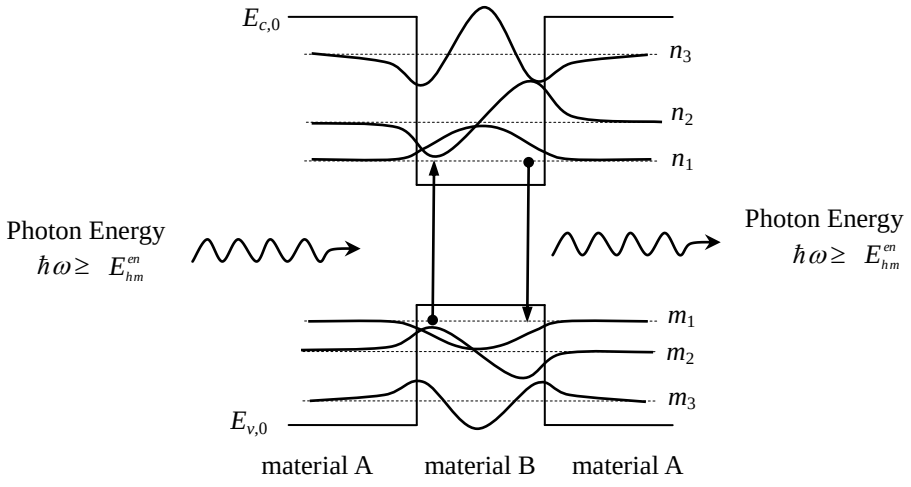


**Figure 3-6** The inter-band transition between valance band and conduction band.

In a quantum well, an interband transition is a vertical transition from the bound states in valance band to the bound states in conduction band, as shown in Fig. 3-6. When a photon comes in, an electron will be excited from a valance subband to a conduction subband. Using the labelling of the subbands shown in Fig. 3-6, the transition between the bound states, ($m_1$, $n_1$), ($m_2$, $n_2$) and ($m_3$, $n_3$) are the strongest transitions, whilst the transitions between the bound states, ($m_1$, $n_3$) and ($m_3$, $n_1$) are weaker because transitions between bound states of odd-even or even-odd index are not allowed in symmetric quantum wells [58]. The transition rule follows from the fact that the optical absorption strength is proportional to the overlap integral of the conduction and valence wavefunction [72]. The interband absorption calculation will be discussed in Chapter 4 section 4.2.2. A quantum well is known as a symmetric well when it has full inversion symmetry about its central axis. When the electric field is applied to a symmetric quantum well, the well changes to an asymmetric well [73], as shown in Fig.3-7.

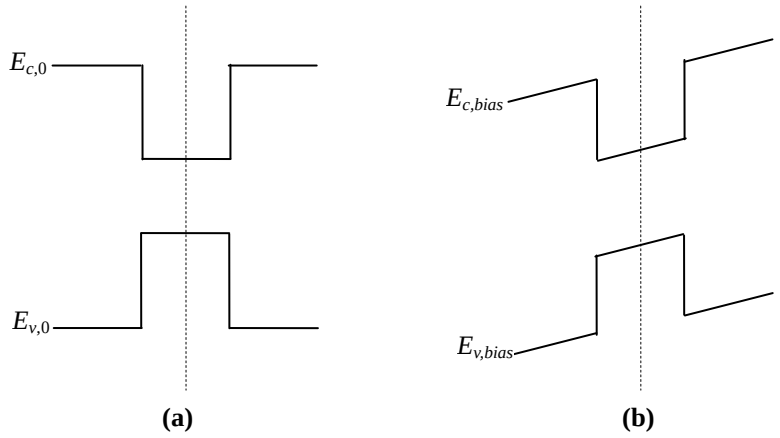


**Figure 3-7 (a)** Symmetric well changes to **(b)** asymmetric well when an electric field is applied.

### 3.3.2 Intersubband Transition

An intersubband transition occurs when electrons or holes are excited between levels (or subbands) within the same potential well. Intersubband absorption in the conduction band is shown in Fig.3-8 [70].

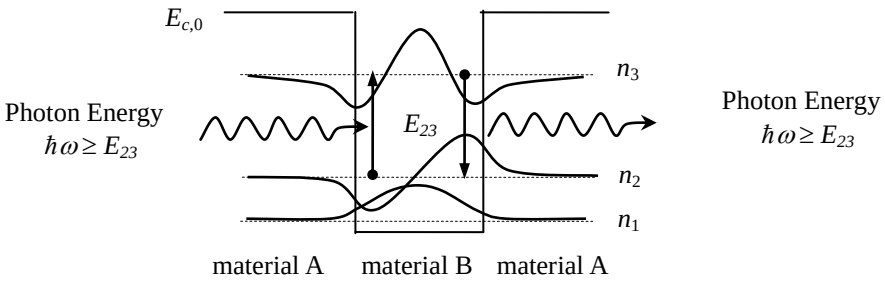


**Figure 3-8** An inter-subband transition between in conduction subbands.

The transition between ($n_2$, $n_3$) is the strongest transition, transition ($n_1$, $n_2$) has slightly weaker strength, and transition ($n_1$, $n_3$) is forbidden by the parity selection rule in a symmetric well [58]. The transition rule for intersubband still follows from the fact that the optical absorption strength is proportional to the overlap integral of the conduction and valence wave function [72].

Intersubband transitions have an extremely short absorption recovery time as the photo-excited carriers rapidly lose energy to phonons [74, 75]. What is more, intersubband transitions usually occur at much lower photon energy than interband transitions [76], so it potentially allows photon emission energies in the terahertz region of the spectrum by using band gap engineering [77]. Intersubband transitions are of growing interest in THz technology [78, 79] because of the advantages mentioned above.

## 3.4 InGaAs(P)/ InGaAsP Multiple Quantum Wells

As introduced in Chapter 2, the InGaAs(P) alloys are very attractive for optical fibre communication systems, because their bandgaps are such that these semiconductors emit or absorb light, having wavelengths corresponding to those at which zero dispersion ($1.3\mu m$) or lowest loss ($1.55\mu m$) occurs in silica optical fibres [19]. InGaAsP/InGaAsP quantum wells that operate in the long wavelength [55] region tend to confine electrons less strongly in the conduction band well because of the lower conduction band offset between the outer barriers and the quantum wells. As a result, the valance band offsets tend to be larger, and the valance band wells deeper [80], making it harder for holes to escape. This has the consequence that the barrier material must be carefully chosen to prevent photo-generated holes from piling up in the wells, especially at high input optical

intensities, for successful modulator performance [81]. On the other hand, the time dependence of this build-up of photo-generated charge may contribute to the ultra-fast response of the device.

## 3.5 Electroabsorption Effects of MQW-EAM

Electroabsorption effects for MQW-EAM have been an interesting research subject for many years, and the quantum wells have shown to have a more significant change of the absorption with the applied voltage than the bulk semiconductor due to quantum confined stark effect (QCSE) [82]. The one dimensional calculation model of electroabsorption coefficient was set up by Qin Chen (Chinese Academy of Science).

## 3.6 Time Dependent Behaviour

An MQW-EAM modulates the amplitude of an optical input signal with an electrical signal of much lower frequency. The Fig. 3-9 shows the modulation process.

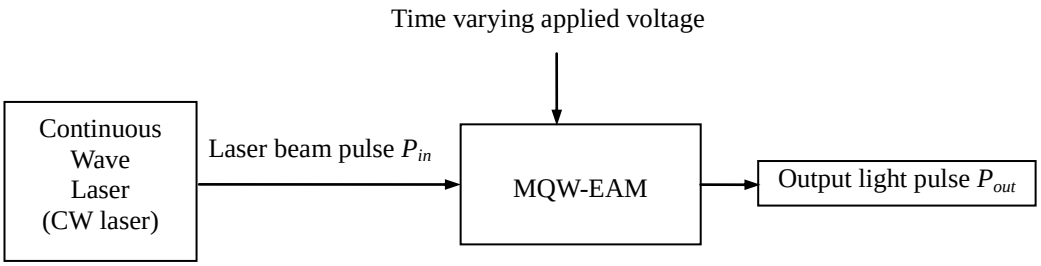


**Figure 3-9** MQW-EAM modulates the input signal from high frequency to lower frequency that can be responded by the device.

In Fig.3-9, an optical signal $P_{in}(t) = P_0\sin(\omega t)$ at really high frequency (i.e. the optical field frequency) is the optical input to the EAM, and the voltage applied to EAM is time varying, for example a square wave or sine wave pulse. In the case of the latter, the output signal will be $P_{out}(t) = P_{in}(t) + P_0\sin(\omega_m t)$. Further along the system, any detecting device generates a photocurrent with time dependence that detects at frequency $\omega_m$ not $\omega$, where $\omega_m < \omega$. This represents ideal optical intensity modulation.

Other factors can give rise to deviations from this ideal. Firstly, from a circuit

point-of-view an MQW-EAM behaves like a capacitor with a resistor in parallel (neglecting the resistance contributions from the electrodes, and neutral n-type and p-type cladding regions). Consequently, when driven by a voltage source of finite output impedance, the electrical bandwidth of a MQW-EAM will be RC time constant limited. At modulation frequencies close to or exceeding the 3dB cut-off frequency, the modulation depth of the slow periodic amplitude variation imposed on the light beam will be reduced.

## 3.7 Absorption Saturation

Absorption saturation arises from the finite escape time of photo-generated electrons and holes from the quantum well [83]. The requirements for interband optical absorption to take place in a quantum well that an electron must occupy a valance subband and that an unoccupied state exists in a conduction subband at the same value of electron k-vector and at an energy separation from the occupied valance subband state exactly equal to the photon energy. (These requirements exclude the effect of exciton formation.) In a MQW-EAM, the effective absorption edge derives from an electron transition from the h level (in the valance subband) to the e level (in the conduction subband), the very levels most likely to be occupied by photo-generated electrons and holes. If the top of the h1 subband is largely occupied by holes and/or the bottom of the e1 subband is occupied by electrons, the requirement for absorption is that the ground (h1) is occupied by an electron and excited (e1) is unoccupied, cannot be met. Under these circumstances the probability of absorption is negligible. This effect is known as absorption saturation of phase space (k-space) quenching. This effect is exploited in a device known as a saturable absorber [84].

Therefore, when the MQW-EAM absorbs a certain amount of light, the charge carriers generated in the quantum wells need to be swept out by the depletion field (i.e. bias field) of the PN or PIN junction. Charge carriers that are trapped in the QW also distort the external electric field by the local charge screening effect, causing the applied electric field across the quantum well to fall. This is illustrated schematically in Fig. 3-10.

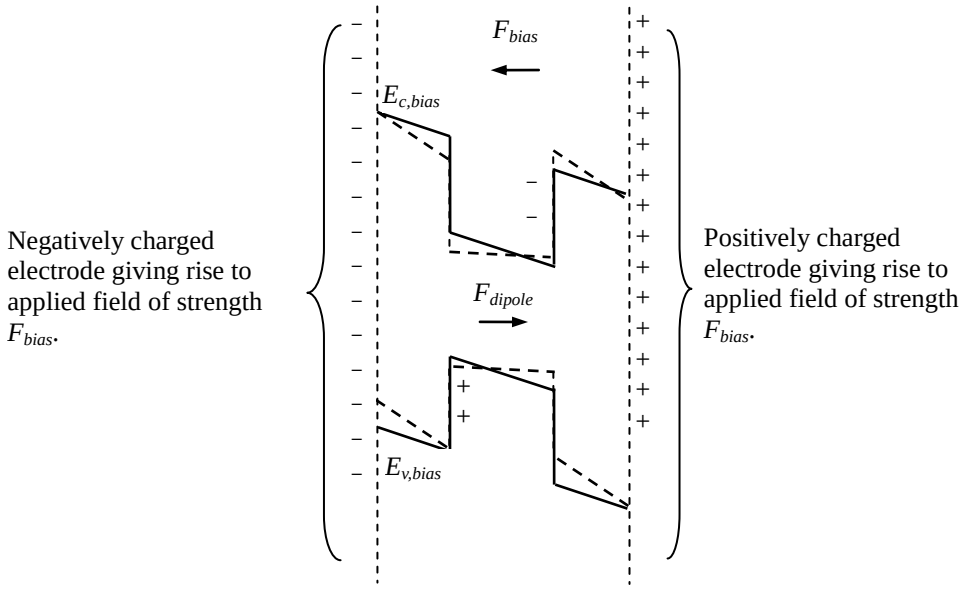


**Figure 3-10** Effect of dipole field inside the quantum well.
solid line – band edges with no photogenerated charge in quantum well
dashed line – band edges with photogenerated electrons and holes creating a dipole field $F_{dipole}$ across the quantum well in a direction that opposes applied field $F_{bias}$

The dipole field arising from trapped photo-generated carrier is in the opposite direction to the bias field used to shift the absorption edge by QCSE to a spectral position where the incident light is strongly absorbed. The net electric field across the well is reduced causing the absorption edge to shift to higher photon energy, hence the absorption decreases and the modulation depth of the optical signal decreases, as shown in Fig. 3-11.

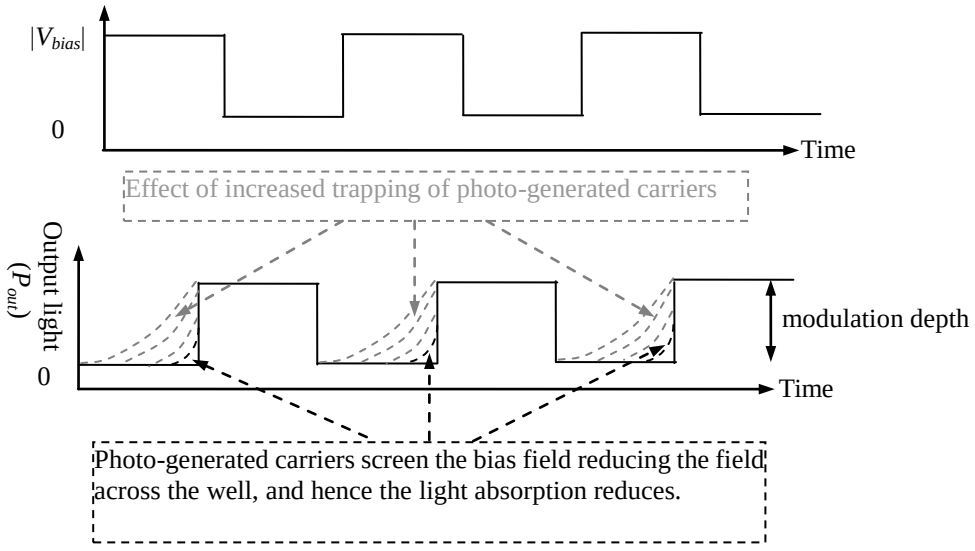


**Figure 3-11** Applied voltage and output light intensity against time.

As the densities of trapped photo-generated charge carriers build up in the wells, the output optical signal ceases to be an exact replica of the voltage pulses applied to

the MQW-EAM and the contrast ratio between binary "0" and binary "1" decreases. Two effects contribute to absorption saturation: (a) high input optical intensity and (b) the time interval between adjacent voltage pulses being shorter than the escape times of the photo-generated carriers from the wells. The first effect can be counteracted by operating the MQW-EAM with low incident optical intensity and the second by operating at a high bias field to help sweep out the photo-generated carriers. On the other hand, the escape times of electrons and holes from the wells determine the fastest data rate achievable using a MQW-EAM. One simple approach to increase operating speed of an MQW-EAM is to use shallow barriers to facilitate the carriers escaping from the well [85]. The saturation effect can be larger in the MQW-EAM than the bulk devices, due to the larger number of hetero-interfaces [86].

## 3.8 Summary

Chapter 3 presented a brief review of the physical properties involved in a MQW-EAM when it is operated. The basic functionality of MQW-EAM, the quantum confined Stark effect (QCSE) was introduced in section 3.2. The QCSE leads to a red shift in the absorption coefficient. Besides the QCSE, the absorption coefficient is also affected by band filling and excitonic effects. If the device absorbs a large amount of optical power, then absorption saturation might occur in the MQW-EAM. The trapped carriers in the well can screen the electric field. Therefore, a reduction in absorption coefficient and modulation depth can take place in the device. The estimation of absorption coefficient in the numerical model will include the QCSE and band filling, but no excitonic contribution will be involved in the absorption coefficient calculation.

# Chapter 4

## Theory of Modelling Light Absorbing Semiconductor Devices

## 4.1 Two Different Devices Models

In this chapter, the methods for estimating the optical parameters are introduced. Poisson's equation and the current continuity equation are both used in the PIN photodiode and MQW-EAM modelling, however; the optical parameters are defined differently because the PIN photodiode is a bulk material structure, and the MQW-EAM has the multiple quantum wells in the intrinsic layer. The optical parameters introduced in this chapter include the absorption coefficient, input light wavelength selection, and the photo-generation term.

## 4.2 Effective Absorption Coefficient

### 4.2.1 Bulk Material

Under thermal equilibrium, the absorption coefficient can be calculated by [82],

$$\alpha_0 = A\left(\hbar\omega - E_g\right)^{\frac{1}{2}} \tag{4-1}$$

where $A = \dfrac{q^2(2m_r)^{3/2}\left|\hat{e}\cdot p_{cv}\right|^2}{2\pi m_0^2 n_r \varepsilon_0 c\hbar^3\omega}$, $\left|\hat{e}\cdot p_{cv}\right|^2$ is the momentum matrix (listed in Appendix I) and $\dfrac{1}{m_r} = \dfrac{1}{m_e^*} + \dfrac{1}{m_h^*}$, $m_e^*$ is the effective mass of electron and $m_h^*$ is the effective mass of hole.

If $\hbar\omega < E_g$, then the light will only pass through the material; in other words, the semiconductor is transparent for this light. If $\hbar\omega > E_g$, and the light may still not be absorbed by the device owing to the requirements that the initial state must be occupied by an electron and the final state unoccupied, as shown in Fig.4-1 [87].

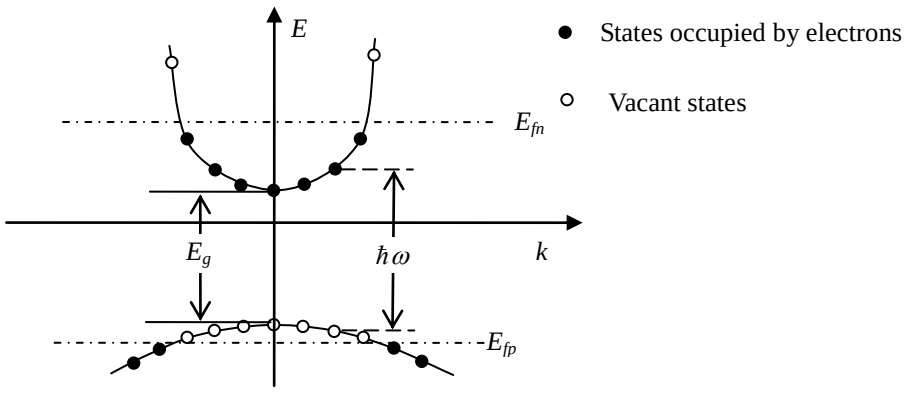


**Figure 4-1** A semiconductor with direct bandgap, the input light energy is smaller than the Fermi level difference.

That means states in the accessible conduction band states are full, and accessible states in the valence band are empty. Transition blocking occurs and the absorption coefficient decreases. This is called band filling [88]. By considering the band filling effect, the absorption coefficient should be defined as [89],

$$\alpha_{FD} = \alpha_0 [f_v - f_c] \tag{4-2}$$

where $f_c$ and $f_v$ are the Fermi distributions for electrons and holes respectively and are given by [90],

$$f_c = \frac{1}{1+\exp\left\{\frac{1}{k_B T}\left[\left(m_r / m_e^*\right)E - E_{fn} + E_g\right]\right\}} \tag{4-3}$$

$$f_v = \frac{1}{1+\exp\left\{\frac{1}{k_B T}\left[\left(m_r / m_h^*\right)E - E_{fp}\right]\right\}} \tag{4-4}$$

where $E = \hbar\omega - E_g$, $E_{fp}$ and $E_{fn}$ are the quasi-Fermi energy of holes and electrons respectively, $k_B$ is the Boltzmann constant and T is the temperature. If transition blocking occurs, when $\hbar\omega < (E_{fn} - E_{fp})$, photons cannot be absorbed by the material and recombination of the electron and hole causes a photon to be emitted (radiative recombination) and the radiation can be amplified by stimulated emission [87]. Therefore, the photon can only be absorbed by the semiconductor if the photon energy is larger than the band gap energy and there are available vacant states in the conduction band. That means $\hbar\omega > (E_{fn} - E_{fp})$ is the condition for a photon to be absorbed.

### 4.2.2 Quantum Well

Interband absorption in the quantum well is discussed in this section. For simple calculation, the exciton effect between holes and electrons due to Coulomb interaction is ignored. The absorption spectrum at thermal equilibrium is [82],

$$\alpha_0(\hbar\omega) = C_0 \sum_{n,m} \left|I_{hm}^{en}\right|^2 \left|\hat{e}\cdot p_{cv}\right|^2 \rho_r^{2D} H\left(\hbar\omega - E_{hm}^{en}\right) \tag{4-5}$$

where $C_0 = \frac{\pi q^2}{n_r c \varepsilon_0 m_0^2 \omega}$ is the coefficient, $I_{hm}^{en} = \int_{-\infty}^{\infty} dz\, \psi_{en}^*(x)\psi_{hm}(x)$ is the integration of the complex product of the hole and electron wavefunctions known as the overlap integral. The term $\left|\hat{e}\cdot p_{cv}\right|^2$ is the momentum matrix element (listed in

Appendix I), $\rho_r^{2D} = \frac{m_r}{\pi\hbar^2 L_w}$ is the two dimensional reduced density of states and $H(\hbar\omega - E_{hm}^{en})$ is the Heaviside step function. The term $E_{hm}^{en}$ is the transition energy and is defined as

$$E_{hm}^{en} = E_{en} - E_{hm}, \quad E_{hm} < 0.$$

Where $E_{en}$ is eigen-energy for electrons and $E_{hm}$ is the eigen-energy for holes. In a quasi-equilibrium state, the absorption depends on the quasi-Fermi level, so the absorption coefficient is given by,

$$\alpha_{FD}(\hbar\omega) = \alpha_0(\hbar\omega)\left[f_v^m(\hbar\omega - E_{hm}^{en}) - f_c^n(\hbar\omega - E_{hm}^{en})\right] \tag{4-6}$$

where $f_c^n$ and $f_v^m$ are the Fermi-Dirac population inversion factor, they are defined as,

$$f_c^n(E_t) = \frac{1}{1+\exp\left\{\frac{1}{k_B T}\left[E_g + E_{en} + (m_r / m_e^*)E_t - E_{fn}\right]\right\}} \tag{4-7}$$

$$f_v^m(E_t) = \frac{1}{1+\exp\left\{\frac{1}{k_B T}\left[E_{hm} - (m_r / m_h^*)E_t - E_{fp}\right]\right\}} \tag{4-8}$$

where $E_t = \hbar\omega - E_{hm}^{en}$.

### 4.2.3 Waveguide devices

The effective absorption coefficient for a MQW-EAM in a waveguide device is,

$$\alpha_{eff\_QW} = \sum_{i=1,2,..k} \alpha_{FD\_i}\Gamma_i \tag{4-9}$$

where $\Gamma_i$ is the optical confinement factor and $\alpha_{FD\_i}$ is the absorption coefficient of the *i-th* well. The confinement factor $\Gamma_i$ is defined as the optical power contained in the *i-th* quantum well to the total power carried by a given waveguide mode [91]. There are two common propagation modes: the transverse electric mode (TE mode) and the transverse magnetic mode (TM mode), as shown in Fig.4-2.

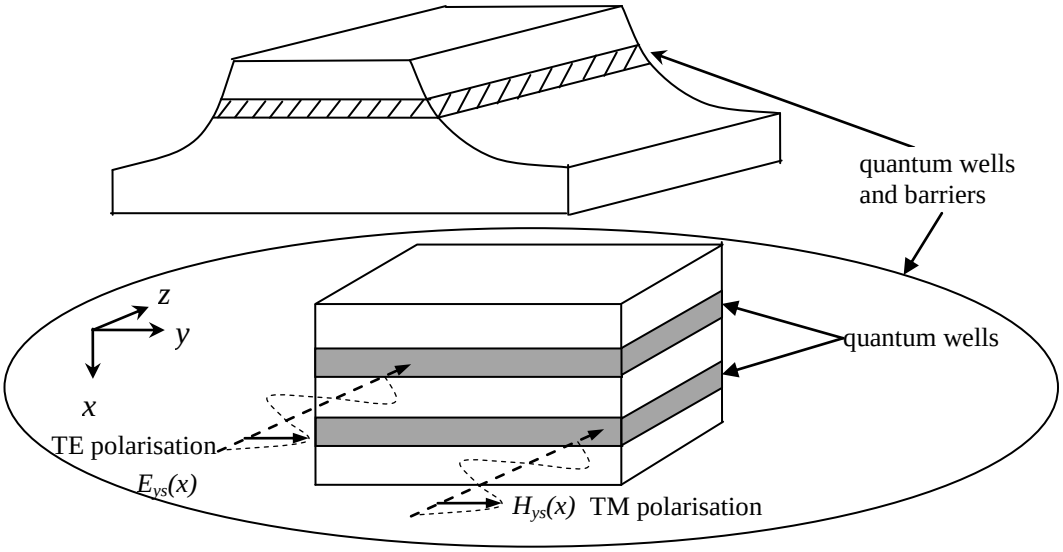


**Figure 4-2** TE and TM polarisation light propagation in the MQW-EAM.

Therefore, for a TM mode, the optical confinement factor for a single quantum well lying between an interface at $x$ and an interface at $x + L_{QW}$ is defined as,

$$\Gamma_i = \frac{\int_{x_i}^{x_i+L_{QW}} E_{xs}^2(x)dx}{\int_{-\infty}^{\infty} E_{xs}^2(x)dx} \tag{4-10}$$

where for a slab waveguide mode

$$E_{xs} = \frac{\beta}{\omega\varepsilon}[A_s \exp(jk_s x) + B_s \exp(-jk_s x)] \tag{4-11}$$

For a TM mode, the $H_s$ field has only a transverse component and does not have a component in the propagation direction [92]. It can be represented by [93]

$$E_{ys} = H_{xs} = H_{zs} = 0 \tag{4-12a}$$

$$E_{xs} = (\beta / \omega\varepsilon)H_{ys} \tag{4-12b}$$

$$E_{zs} = -(j / \omega\varepsilon)\partial H_{ys} / \partial x \tag{4-12c}$$

Where $\varepsilon$ is the permittivity.

From similar consideration, the confinement factor for slabs TE mode is given by

$$\Gamma_i = \frac{\int_{x_i}^{x_i+L_{QW}} H_{xs}^2(x)dx}{\int_{-\infty}^{\infty} H_{xs}^2(x)dx} \tag{4-13}$$

where for a slab waveguide mode

$$H_{xs} = \frac{\beta}{\omega\mu}[A_s \exp(jk_s x) + B_s \exp(-jk_s x)] \tag{4-14}$$

TE mode means the $E_s$ field does not contain any component in the direction of propagation [92]. Thereby for a TE mode [93],

$$H_{ys} = E_{xs} = E_{zs} = 0 \tag{4-15a}$$

$$H_{xs} = -(\beta / \omega\mu)E_{ys} \tag{4-15b}$$

$$H_{zs} = (j / \omega\mu)\partial E_{ys} / \partial x \tag{4-15c}$$

where $\beta$ is the propagation constant, $\mu$ is the permeability and $\omega$ is angular frequency.

Similarly, the effective absorption coefficient for PIN photodiode in a waveguide device is,

$$\alpha_{eff} = \alpha_{FD\_bulk}\Gamma_I \tag{4-16}$$

where $\Gamma_I$ is the optical confinement factor of I-layer and $\alpha_{FD\_bulk}$ is the absorption coefficient of the I-layer taken in the band filling effect. The confinement factor $\Gamma_I$ can be calculated by using similar equations as Eq.(4-10) or Eq.(4-13). There are also different equations for confinement factor under TE mode and TM mode, as shown in Fig.4-3.

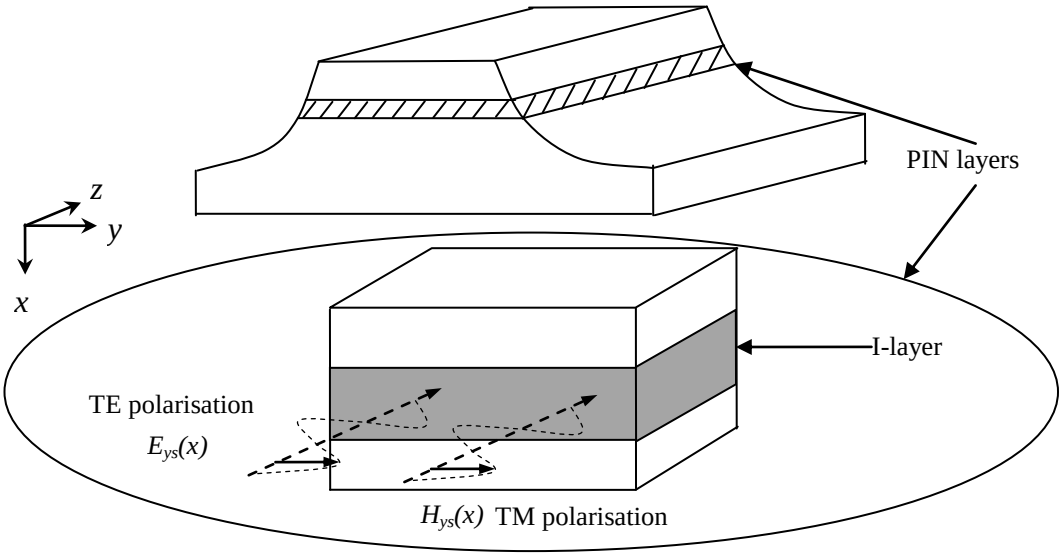


**Figure 4-3** TE and TM polarisation light propagation in the PIN photodiode.

For a TM mode, the optical confinement factor for PIN photodiode lying between an interface at $x$ and an interface at $x + W_I$ is defined as,

$$\Gamma_I = \frac{\int_{x}^{x+W_I} E_{xs}^2(x)dx}{\int_{-\infty}^{\infty} E_{xs}^2(x)dx} \tag{4-17}$$

where $E_{xs}$ is defined by Eq.(4-11). The confinement factor for slabs TE mode is given by

$$\Gamma_I = \frac{\int_{x}^{x+W_I} H_{xs}^2(x)dx}{\int_{-\infty}^{\infty} H_{xs}^2(x)dx} \tag{4-18}$$

where $H_{xs}$ is defined by Eq.(4-14).

## 4.3 Input Light Wavelength Selection

### 4.3.1 PIN Photodiode

The energy of an input photon needs to be bigger than the bandgap energy, in order for absorption to take place. For better efficiency of an InP/InGaAs/InP PIN photodiode, the absorption region should be only in the I-layer, whilst the P-layer and N-layer (wide bandgap layer) serve as transparent layers for the specific input light [94]. It is because the electron-hole pairs generated in the wide bandgap layers will first diffuse into the I-layer before they can be swept by the field, this carrier action will result in increased transit time [29]. Therefore, the energy of input light should be in the range of $E_{Ig} < \hbar\omega < E_{Pg}$, where the $E_{Pg}$ is the energy bandgap of the InP (P-layer) and the $E_{Ig}$ is the energy bandgap of the InGaAs (I-layer), as shown in Fig.4-4.

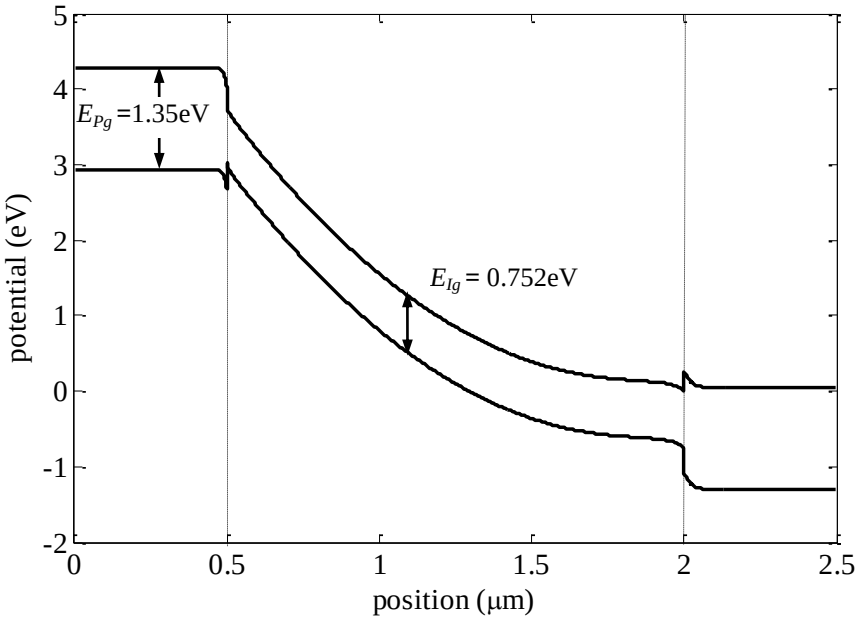


**Figure 4-4** Potential profile under -3V bias.

In Fig.4-4, the input light energy range is $0.752eV < \hbar\omega < 1.35eV$, therefore the wavelength of the input light should be in the range of $0.92647\mu m < \lambda < 1.6487\mu m$. For zero dispersion ($1.3\mu m$) or lowest loss ($1.55\mu m$) occurs in silica optical fibres [19], so both of these wavelength are chosen for use in the numerical model.

### 4.3.2 MQW-EAM

Light absorption is assumed to only occur in the quantum well in our model. Light absorption control is essential in MQW-EAM. The absorption process only can take place if the device is under reversed bias, and it ceases when the applied bias stops and is removed from the device. By example, Fig.4-5 shows that the InGaAs well band-edge transition energy is 0.784166eV under 0V bias, and decreases to 0.775622eV if -1V is applied. The band-edge transition energy is given by [82],

$$E_{hm}^{en} = E_{en} - E_{hm}, \quad E_{hm} < 0.$$

where $E_{en}$ is the eigen-state in the conduction band well and $E_{hm}$ is the eigen-state in the valence band well. Therefore the quantum wells will absorb light if optical photon energy is equal to or larger than $E_{hm}^{en}$.

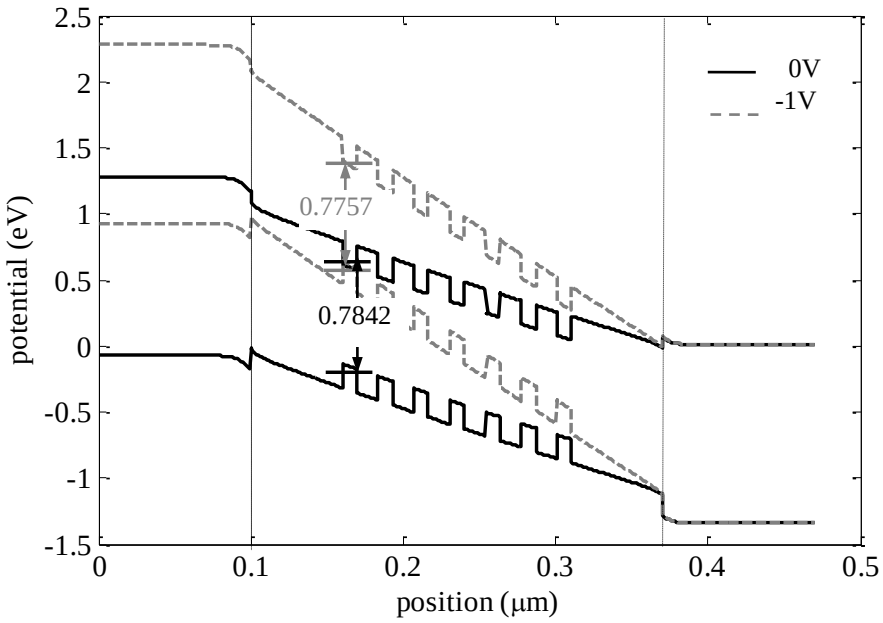


**Figure 4-5** Potential profile under 0V bias and -1V bias.

For realizing large light absorption under -1V bias and no absorption under 0V bias, the input light energy can be chosen to be a little bit smaller than the smallest band-edge transition energy of all wells under 0V applied bias, however; for a InGaAs quantum well MQW-EAM device is usually operated under 1.55μm wavelength input optical light [19]. That is because at this wavelength, the absorption coefficient drops to a very small value under 0V bias, however; the value of absorption coefficient increases as the reverse applied bias value increases. This is as shown as Fig. 4-6 [54].

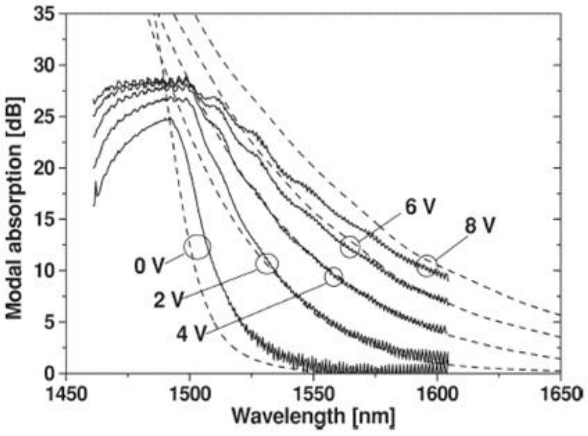


**Figure 4-6** Measured (solid line) and calculated (dashed line) TE spectra for modal Absorption. Data is taken from reference [54].

## 4.4 Effects of Carrier Generation on Effective Absorption

### 4.4.1 Vertical Entry Devices

Fig.4-7 illustrates the direction of light propagation relative to the layer structure of a PIN photodiode for a vertical entry device light generation should only take place in the intrinsic layer for a good efficient photodiode [95]. There are two types of vertical entry device. If light shines on the device from the P side, it is defined as top-illumination or top-entry, and if light illuminates from the N side, it is called sub-illumination or sub-entry [12].

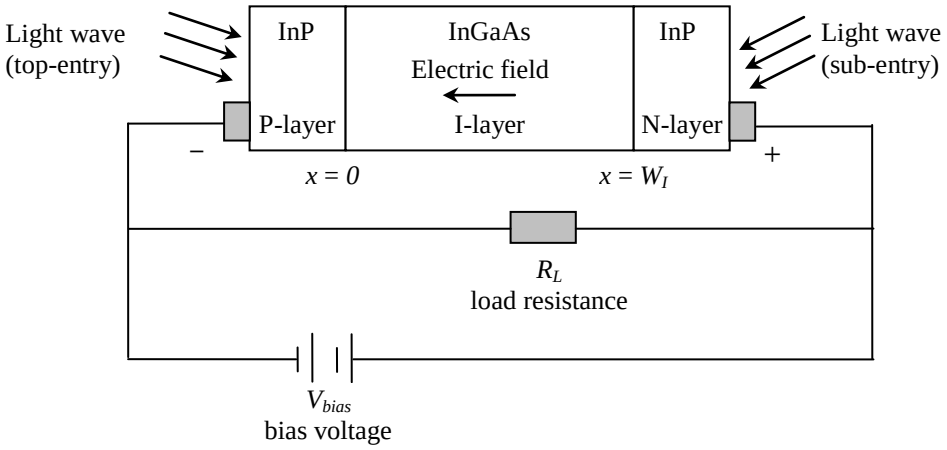


**Figure 4-7** Vertical entry PIN InGaAs/InP photodiode under two types of illumination and its external circuit.

The generation term in the intrinsic region under vertical entry is defined as [12],

$$G(x,t) = \frac{\alpha_{FD}\lambda}{hcS_{recep}} P(t) e^{-\alpha_{FD}x} \qquad \text{top-entry} \tag{4-19}$$

$$G(x,t) = \frac{\alpha_{FD}\lambda}{hcS_{recep}} P(t) e^{-\alpha_{FD}(W_I - x)} \quad \text{sub-entry} \tag{4-20}$$

where $P(t) = P_0 m I_{light}(t)$, $\alpha_{FD}$ is the optical absorption coefficient, $S_{recep}$ is the reception surface of the PIN photodiode, $\lambda$ is the optical wavelength, $W_I$ is the width of I-layer, $h$ is the Planck's constant, $c$ is the light speed, $m$ is the modulation depth, $P_0$ is the average optical power and $I_{light}(t)$ is the power intensity profile. The power intensity profile can be a normalized Gaussian function, normalized sine function or cosine function according to need.

### 4.4.2 Waveguide Mode or Edge-Coupled Structure

Another type of illumination is named as edge-coupled illumination or waveguide illumination. Edge-coupled illumination is gaining favour in high data rate systems because the device can have a greater chance to absorb light. The input light beam is perpendicular to the applied electric field [96]. The input light beam usually can be either TE polarisation or TM polarisation as shown in Fig.4-8.

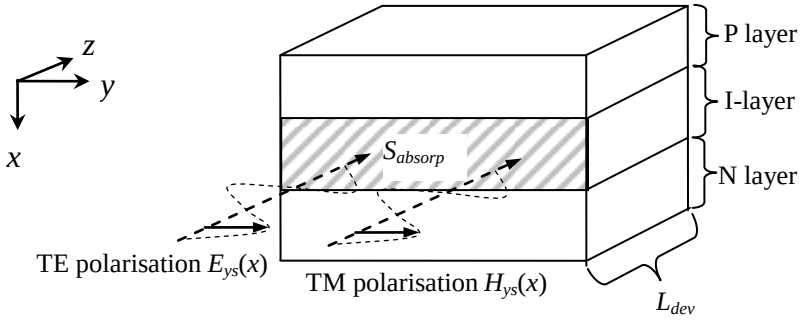


**Figure 4-8** TE and TM polarisation light propagation in the edge-coupled device.

Therefore, the generation term is defined as [97],

$$G(t) = \frac{\lambda P(t)\left[1 - e^{-\Gamma \alpha L_{dev}}\right]}{hcS_{absorp}L_{dev}} \tag{4-21}$$

where $S_{absorp}$ is the cross-sectional area of the absorption layer, $L_{dev}$ is the device length, $\alpha$ is the absorption coefficient and $\Gamma$ is the optical confinement factor that were both introduced in section 4.2 before.

For the quantum wells in the intrinsic layer, the Eq. (4-18) can still apply to generation term, but it only has value in the quantum well, with zero generation term in the other part of the material.

## 4.5 Summary

This chapter introduced estimation of the absorption coefficient calculation for bulk semiconductor structures and quantum wells structures. The band filling effect was defined in this chapter. This is a very important effect in the absorption coefficient for a photodiode and MQW-EAM. The confinement factors are included in the absorption coefficient estimation when the light input method is edge-coupled. A reasonable range of input light wavelength was chosen under the

consideration of the semiconductor device bandgap and red shift in the absorption coefficient. The method for the generation rate calculation is varied for different input light methods.

# Chapter 5

## Theory of Modelling PIN Photodiode

## 5.1 Poisson's Equation

The Poisson's equation is commonly used to determine the potential and electrostatic field distribution across the structure, caused by a charge density $\rho$ within the depletion layer [98].The Poisson's equation is introduced from the below Maxwell's equations,

$$\nabla \cdot D = \rho \tag{5-1}$$

$$\nabla \times F_{bias} = -\frac{\partial}{\partial t} B_{bias} \tag{5-2}$$

When there is no external magnetic field ($B_{bias}$ = 0) applied to the device, the solution of electric field is represented by the electrostatic potential $V_{EP}$ [45],

$$F_{bias} = -\nabla V_{EP} \tag{5-3}$$

Eq.(5-3) with $D = \varepsilon_0 F_{bias}$ can modify Eq. (5-3) into,

$$\nabla \cdot (\varepsilon_0 \nabla V_{EP}) = -\rho \tag{5-4}$$

$\rho$ is the charge density and it can be written as

$$\rho = q(p(x) - n(x) + N_D^+(x) - N_A^-(x)) \tag{5-5}$$

where $q$ is the magnitude of a unit charge, $p(x)$ is hole concentration, $n(x)$ is electron concentration, $N_D^+(x)$ and $N_A^-(x)$ are the ionized donor and ionized acceptor concentration respectively. The concentrations of the different carriers that are mentioned in the Eq.(5-5) will be introduced in more detail in the following sections.

The Poisson's equation can only be applied when the device is in an electrostatic state or quasi-static state [99].

### 5.1.1 Electron and Hole Concentration in Bulk Semiconductor

Each of the charge distributions on the right-hand side of Eq.(5-4) depends on the occupancy by electron of the energy states at the valence and conduction band edges ($p(x)$ and $n(x)$ respectively), and the acceptor and donor energy levels ($N_D^+(x)$ and $N_A^-(x)$ respectively). In the bulk semiconductor, the concentration of electrons is obtained by the integration of the density-of-state function $D(E)$ multiplying by the equilibrium probability distribution function $f_{p(n)}(E)$ over the full energy range of the conduction band [100],

$$n = \int_{E_{c\_bottom}}^{E_{c\_top}} D_n(E) f_n(E) dE \tag{5-6a}$$

where $D_n(E) = \frac{1}{2\pi^2}\left(\frac{2m_e^*}{\hbar^2}\right)^{3/2}(E - E_c)^{1/2}$ and $f_n(E) = \frac{1}{1+\exp\left[\left(E - E_{fn}\right)/k_B T\right]}$. The integration is bound in between of the top and the bottom of the conduction band[100].

For the hole concentration, the probability distribution is $f_p(E) = 1 - f_n(E)$ [101], and it integrates in between of the top and the bottom of the valance band,

$$p = \int_{E_{v\_bottom}}^{E_{v\_top}} D_p(E) f_p(E) dE \tag{5-6b}$$

where $D_p(E) = \frac{1}{2\pi^2}\left(\frac{2m_h^*}{\hbar^2}\right)^{3/2}(E_v - E)^{1/2}$ and $f_p(E) = \frac{1}{1+\exp\left[\left(E_{fp} - E\right)/k_B T\right]}$.

The Fermi-Dirac distribution function $f_n(E)$ and $f_p(E)$ is used to describe their probability of occupying a given set of energy levels at thermal equilibrium [102] and the value always varies in the range between zero and one [103]. Fermi-Dirac integral of order ½ is defined as the following [104]

$$F_{1/2}(\eta) = \frac{2}{\sqrt{\pi}} \int_0^\infty \frac{\xi^{1/2} d\xi}{1 + e^{\xi - \eta}} \tag{5-7}$$

Let $N_c = 2\left(\frac{2\pi m_e^* k_B T}{h^2}\right)^{3/2}$ and $N_v = 2\left(\frac{2\pi m_h^* k_B T}{h^2}\right)^{3/2}$. Thus, Eq.(5-6a) and Eq.(5-6b) can be modified into,

$$n = N_C F_{1/2}(\eta_c) \tag{5-8a}$$

$$p = N_V F_{1/2}(\eta_v) \tag{5-8b}$$

where $\eta_c, \eta_v$ are the reduced potentials,

$$\eta_c = \left(E_{fn} - E_c\right)/k_B T \tag{5-9a}$$

$$\eta_v = \left(E_v - E_{fp}\right)/k_B T \tag{5-9b}$$

Fermi-Dirac integrals $F_{1/2}(\eta)$ must be integrated numerically, with the consequence for device modelling that either computationally inconvenient look-up tables must be used or computationally efficient approximate functions used instead. Several researchers have developed approximations for Fermi-Dirac integral of order ½

[105]. The approximation used in this work is that developed by Roberts F. Pierret in 1988, due to its maximum error being within a reasonable range ($\pm 0.5\%$) for different reduced potentials [101]. Pierret's approximation is,

$$F_{1/2}(\eta) \approx \left[e^{-\eta} + \xi(\eta)\right]^{-1} \tag{5-10}$$

where $\xi(\eta) = 3\sqrt{\pi}/2\left[(\eta + 2.13) + \left(|\eta - 2.13|^{2.4} + 9.6\right)^{5/12}\right]^{-3/2}$ and $\eta$ can be obtained from its reverse function,

$$InvFDI = \eta \approx \frac{\ln u}{1-u^2} + \frac{\left(3\sqrt{\pi}u/4\right)^{2/3}}{1+\left[0.24+1.08\times\left(3\sqrt{\pi}u/4\right)^{2/3}\right]^{-2}} \tag{5-11}$$

### 5.1.2 Doping Carrier Concentration Calculation

In extrinsic semiconductors, impurities are deliberately introduced to produce materials and devices with desired properties [106]. The dopants are depending on the impurity energy level and the lattice temperature, not necessarily all ionized [98]. The ionized concentration for donors $N_D^+$ related to the total donor concentration $N_D$ is given by [98, 106],

$$N_D^+ = \frac{N_D}{1 + g_D \exp\left[\left(E_{fn} - E_D\right)/k_B T\right]} \tag{5-12}$$

where $g_D$ is the ground-state degeneracy factor of the donor impurity level. In compound semiconductor, the donors can accept electrons with either spin, thus $g_D$ is equal to 2 [107]. The ionized acceptors concentration $N_A^-$ can also be written in form of the total acceptor concentration $N_A$ [98, 106],

$$N_A^- = \frac{N_A}{1 + g_A \exp\left[\left(E_A - E_{fp}\right)/k_B T\right]} \tag{5-13}$$

where $g_A$ is the ground-state degeneracy factor of the acceptor impurity level. $g_A$ is equal to 4, because each acceptor accept one hole with either spin, and the impurity level doubly degenerate [107].

### 5.1.3 Boundary Condition

The Poisson's equation needs boundary conditions to obtain a unique solution. What is more, it is also required for first value calculation of the quasi static electric

field and reduced potential in Poisson's equation.

A requirement that the net charge is required to be zero at the extreme end of the device (i.e. as $x \to \infty$) then the current flow is zero is one boundary condition. If the calculation starts from the p junction, the carrier density should satisfy the following condition

$$p(\eta) - n(\eta) - N_A(\eta) = 0 \tag{5-14}$$

These charge distributions all depend on the reduced potential. A series trial values of $\eta$ can be used to make the net charge density achieve the neutrality condition at the end of the device. This $\eta$ value, determined by the neutrality condition, provides a reference value, however; it cannot become the starting value, since it makes the field constant across the structure. Therefore, adding-in a really small number to this value is necessary. This small number is determined by the shooting method that is introduced in the next section.

Another boundary condition is the field is zero at the two extreme ends, that means $\frac{d\eta}{dx} = 0$.

## 5.2 Numerical Methods for Solving the Poisson's Equation

### 5.2.1 Shooting Method

The shooting method is an established tool for solving two boundary values problems [108]. The two boundary values problem means the values need to be satisfied at two points, usually starting and ending values of the integration [108]. A shooting method narrows the number of solutions that satisfies one boundary condition at one point to one solution that satisfies both of them.

The general shooting method is illustrated schematically in Fig. 5-1. If the boundary conditions, *y(a)* and *y(b)* are known for the function, the calculation proceeds with $y = y(a) + y_{trial}$ and gradient $\frac{dy}{dx} = 0$. When the calculation reaches the $x = b$ point, the calculated value $y_c(b)$ is then compared with the boundary value $y(b)$. If the tolerance $\sigma = y_c(b) - y(b)$ does not meet the pre-defined accuracy, the

value of $\frac{dy}{dx}_{trial}$ at point $a$ is adjusted iteratively until $\sigma$ equals or is less than the required tolerance.

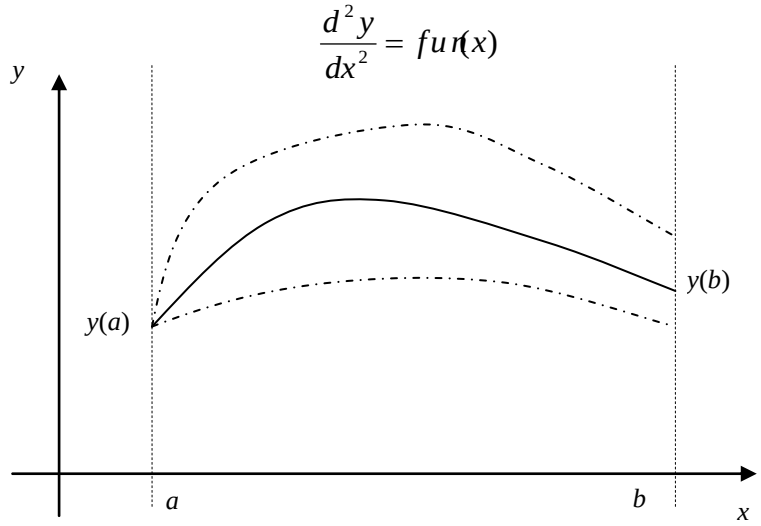


**Figure 5-1** An example of using shooting method in the second derivative equation.

Only a few people have solved Poisson's equation based on the shooting methods in recent years, such as Sambell et al [109] and Malagu et al [110]. This is because they are occasionally unstable in finding computed values of the trial function that match the target value [111]. In our model, the shooting method encounters problems when the width of the intrinsic layer is over 0.6μm or the P layer and N layer is over 1μm, however; the modification for the shooting method devised in this thesis can solve the instability in finding the end value.

In Fig. 5-2, if the boundary condition, $y(a)$ and $y(b)$ are known for the function, start the calculation with $y = y(a) + y_{trial}$ and gradient $\frac{dy(a)}{dx} = 0$. When the calculation reaches the $x = mid$ point, the value of $y_a(mid)$ is memorized. Then calculating the function with $y = y(b) + y_{trial}$ and gradient $\frac{dy(b)}{dx} = 0$, and when it reaches to $x = mid$ point, $y_b(mid)$ is then compared with the boundary value $y_a(b)$. If the tolerance $\sigma = y_b(b) - y_a(b)$ does not meet the pre-defined accuracy, the value of $y_{trial}$ at point $a$ is adjusted iteratively until $\sigma$ equals or is less than the required tolerance. The mid-point can be altered under different conditions, however, it must be converged before starting the calculation.

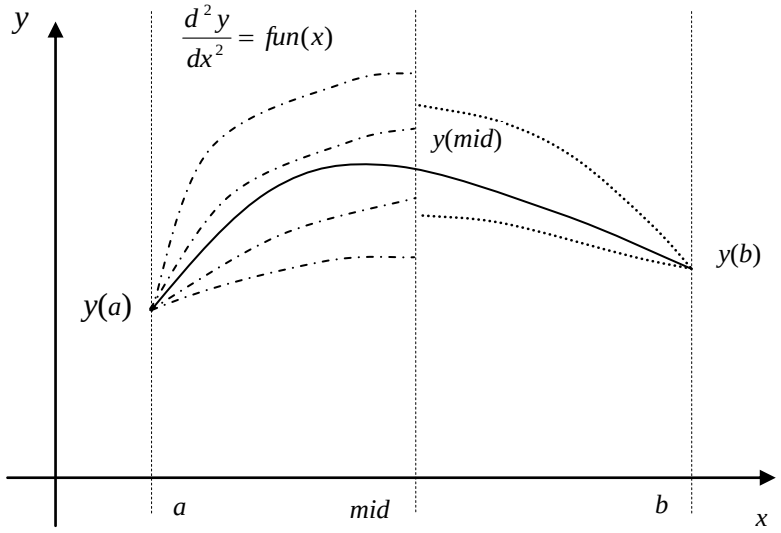


**Figure 5-2** An example of using shooting method in the second derivative equation.

This double shooting numerical method of Poisson's equation extends the width of layer, however, there will be a little step in the m point of $y(m)$. Single shooting method will be a better choice if the width of the I-layer is not too great.

One approach is applying the shooting method along with the Runge-Kutta method to solve Poisson's equation from both sides from p junction and n junction, for a given boundary condition $\eta(x_0)$, given by Eq. (5-14) and by applying the bisection method to root-finding is introduced in the next section.

### 5.2.2 Runge-Kutta Method

The Runge-Kutta method can be used for solving second order differential equations and it obtains the solution by combining the information over the interval from Euler style steps [108]. Once the initial value $\eta(x_0)$ and its first derivative $\eta'(x_0)$ are settled from the shooting method, $\eta(x)$ and $\eta'(x)$ can be calculated from the Runge-Kutta method.

Applying the Runge-Kutta formula to calculate reduced potential $\eta(x)$ and its differential $\eta'(x)$, the following formulas are used,

$$fun(\eta(x)) = \frac{d^2\eta(x)}{dx^2} = -\frac{e}{\varepsilon k_B T}(p - n - N_A + N_D) \tag{5-15}$$

$$\eta(x_1) = \eta(x_0) + h\eta'(x_0) + \frac{1}{3}(K_1 + K_2 + K_3) \tag{5-16}$$

$$\eta'(x_1) = \eta'(x_0) + \frac{1}{3h}(K_1 + 2K_2 + 2K_3 + K_4) \tag{5-17}$$

where $K_1 = \frac{h^2}{2} f(\eta(x_0))$ , $K_2 = \frac{h^2}{2} f\left(\eta(x_0) + \frac{h}{2}\eta'(x_0) + \frac{K_1}{4}\right)$ , $K_2 = K_3$ and $K_4 = \frac{h^2}{2} f(\eta(x_0) + h\eta'(x_0) + K_3)$.

From Eq.(5-16) and Eq.(5-17), if the reduced potential $\eta(x_0)$ and its derivative $\eta'(x_0)$ are known, the next step value $\eta(x_1)$ and $\eta'(x_1)$ can be calculated by applying Runge-Kutta method.

## 5.3 Current Continuity Equation for PIN Photodiode

When a bias voltage is applied, the semiconductor device is under a non-equilibrium condition. The processes of generation and recombination exist in order to restore the system to equilibrium [98]. The current continuity equation is position and time dependent. In the structure, it describes the carrier concentration at one point with the adjacent one at a given time [101]. It contains all the main carrier actions within the semiconductor, such as drifting, diffusion, generation, and recombination under bias [112], as shown in Fig.5-3.When a hetero-junction is present, the model also includes the thermionic emission current estimation. The thermionic emission current will be discussed in this section.

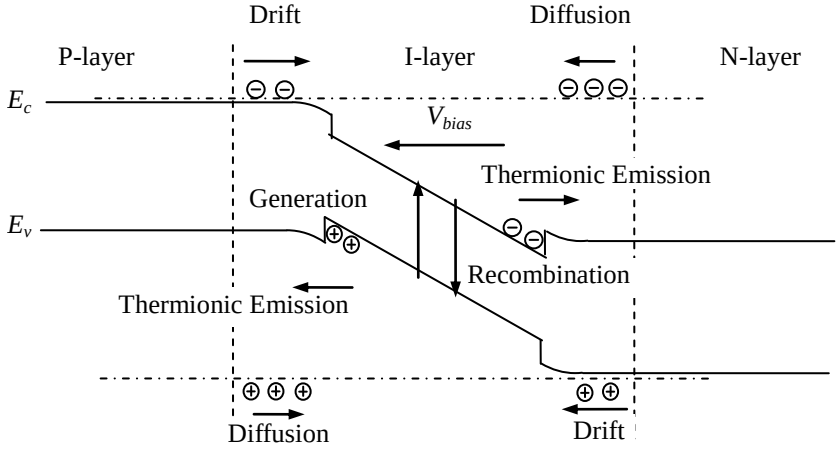


**Figure 5-3** Carrier actions in the PIN Photodiode under reverse bias.

The carrier flux continuity equations are [82]

$$\frac{\partial n}{\partial t} = \frac{1}{q}\frac{\partial J_e}{\partial x} + G - R \tag{5-18a}$$

$$\frac{\partial p}{\partial t} = -\frac{1}{q}\frac{dJ_h}{dx} + G - R \tag{5-18b}$$

where $G$ is the generation rate that has been defined in Chapter 4 section 4.4, $R$ is the recombination rate, $J_e$ and $J_h$ are the electron and hole fluxes respectively given by [82],

$$J_e = q\mu_e n F_{bias} + qD_e \frac{dn}{dx} \tag{5-19a}$$

$$J_h = q\mu_h p F_{bias} - qD_h \frac{dp}{dx} \tag{5-19b}$$

The first term on the right-hand side of Eq.(5-19a) and Eq.(5-19b) describes carrier drift, and the second term is the carrier diffusion. $F_{bias}$ denotes the electric field and it can be represented by the derivative of the reduced potential $\eta$,

$$F_{bias} = \frac{k_B T}{q}\frac{d\eta}{dx} \tag{5-20}$$

### 5.3.1 Drift Current

Drift is charged-particle motion in response to an applied electric field. When the electric field $F$ is applied across the semiconductor device, the positive charged holes tend to accelerate in the same direction of the electric field and the negative charged electrons tend to accelerate in the opposite direction [113]. The drift current is represented mathematically by the following equations [114]

$$J_e\big|_{drift} = q\mu_e n F_{bias} \tag{5-21a}$$

$$J_h\big|_{drift} = q\mu_h p F_{bias} \tag{5-21b}$$

where $\mu_{h(e)}$ is the mobility and under steady state, the mobility can be defined as

$$\mu_{h(e)} = \frac{q\tau_c}{m^*_{h(e)}} \tag{5-22}$$

where $\tau_c$ is collision time between two particles. If under non-steady state, the mobility is field-dependent and it is given by [9],

$$\mu_e(F_{bias}) = \frac{\mu_e^0 + v_{ehf} v_{fit} |F_{bias}|}{1 + v_{fit} F_{bias}^2} \tag{5-23a}$$

$$\mu_h(F_{bias}) = \frac{\mu_h^0 v_{hhf}}{v_{hhf} + \mu_h^0 F_{bias}} \tag{5-23b}$$

where $\mu_{h(e)}^0$ is the carrier low-field mobility, $v_{h(e)hf}$ is the carrier saturated velocity and $v_{fit}$ is the electron velocity fitting parameter. The field dependent carriers velocity for InGaAs is shown in Fig.5-4 [9].

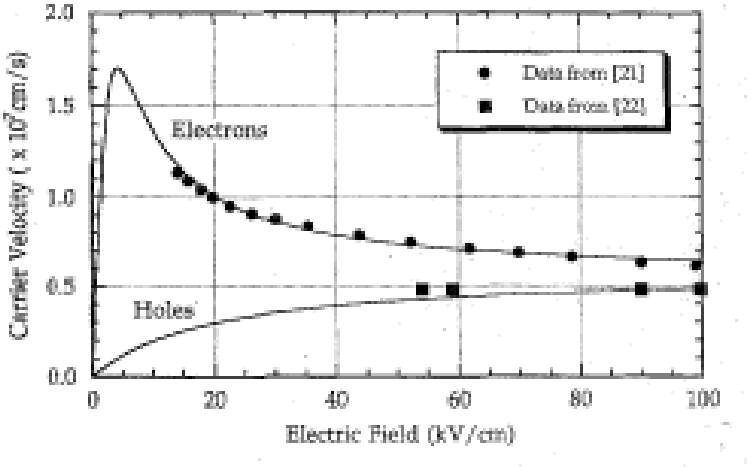


**Figure 5-4** Field dependent hole and electron velocities for InGaAs based on Eq.(5-23a) and Eq.(5-23b).

### 5.3.2 Diffusion Current

Carrier diffusion is due to thermal energy $k_BT$. It causes the carriers to migrate from a region of higher concentration to a region of low concentration even when no field is applied [115]. The electron and hole diffusion currents are given by [114]

$$J_e\big|_{diff} = qD_e \frac{dn}{dx} \tag{5-24a}$$

$$J_h\big|_{diff} = qD_h \frac{dp}{dx} \tag{5-24b}$$

where $D_e$ and $D_h$ are respectively the diffusion coefficients or diffusion constants for electrons and holes.

The diffusion constant is defined as the product of the thermal velocity and the mean free path [115]

$$D_{h(e)} = l_{MFP} v_{th} \tag{5-25}$$

where $v_{th} = \frac{l_{MFP}}{\tau_{c\_mean}}$ and $\tau_{c\_mean}$ is the mean time between collisions among the particles. From thermodynamics, electrons (holes) carry a thermal energy equal to

$\frac{k_B T}{2}$ for each degree of freedom [115],

$$\frac{k_B T}{2} = \frac{m^*_{h(e)} v_{th}{}^2}{2} \tag{5-26}$$

Combining these equations with Eq. (5-22) yield,

$$l_{MFP} v_{th} = \frac{m^*_{h(e)} v_{th}^2}{q} \frac{q \tau_{c\_mean}}{m^*_{h(e)}} = \frac{k_B T}{q} \mu_{h(e)} \tag{5-27}$$

Therefore,

$$D_{h(e)} = \frac{k_B T}{q} \mu_{h(e)} \tag{5-28}$$

This is defined as Einstein relation and strictly speaking it is only valid under steady state [115].

### 5.3.3 Recombination

When the physical mechanisms are considered, recombination includes primarily phonon transitions (Shockley-Read-Hall process), photon transitions, Auger or three particle transitions and impact ionization [116]. The SHR recombination and Auger recombination are considered in the model.

The SRH process involves four processes: electron capture, hole capture, electron emission and hole emission. These four processes are shown in Fig.5-5.

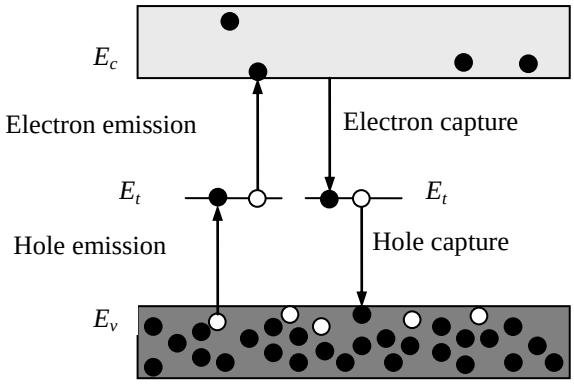


**Figure 5-5** SRH recombination and generation in semiconductor device.

The rate of Shockley-Read-Hall recombination is given by [117]

$$R_{SRH} = \frac{pn - n_{In}^2}{\tau_e (p + p_t) + \tau_h (n + n_t)} \tag{5-29}$$

where $n_t$ and $p_t$ are dependent on the position and occupancy of the traps, and the most effective trap centre occurs in the middle of the gap [118]. $\tau_{h(e)}$ is the carrier life time and $n_{In}$ is the intrinsic carrier concentration.

The Auger recombination means when the electron recombines with the holes in the valence band, the resulting energy is given off to another electron or hole [115]. The model is defined as [89]

$$R_{Aug} = C_{Aug} n(np - n_{In}^2) \tag{5-30}$$

where $C_{Aug}$ is the Auger coefficient.

The recombination terms can be simplified to the following form [115],

$$R_n = \frac{n_p - n_{po}}{\tau_n} \tag{5-31a}$$

$$R_p = \frac{p_n - p_{no}}{\tau_p} \tag{5-31b}$$

where the subscript "*n*" and "*p*" indicate the type of semiconductor and subscript "*o*" refers to the thermal equilibrium condition. The above equations are only valid for minority carriers in quasi-neutral semiconductors. Recombination in the depletion region cannot be described by these simple equations and the more elaborate expressions for the individual recombination mechanisms must be used [115].

### 5.3.4 Thermionic Emission Current across Hetero-junction

Thermionic emission is the process that the electrons are emitted across a barrier[119], as shown in Fig.5-6.

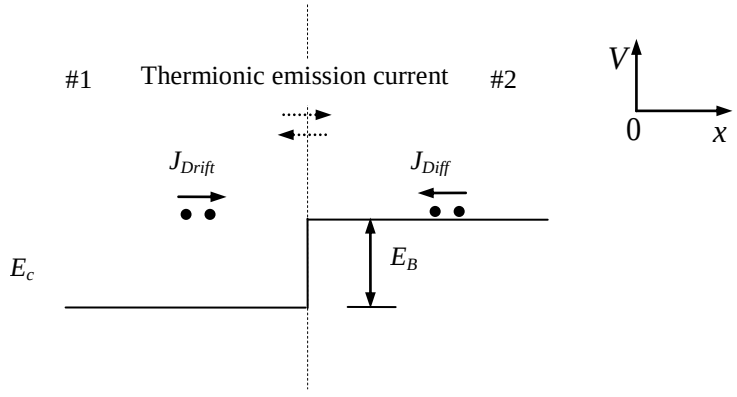


**Figure 5-6** Electron flux comes across the hetero-junction.

It means that the drift and diffusion model cannot describe the carrier motion accurately anymore. The current density across the hetero-junction must now be defined by thermionic emission current. The thermionic emission current can be modelled as the boundary condition [15] and it is defined by,

$$J_{th} = q\eta_{\#2}\left\{ n_{\#2,i+1}V_{eR\#2} - \theta_M n_{\#1,i-1}V_{eR\#1} \exp\left( -\frac{E_B}{k_B T} \right) \right\} \tag{5-32}$$

where $V_{eR} = \dfrac{4\pi m_e^* (k_B T)^2}{N_c h^3}$ is corresponding to the recombination velocity [15], $\theta_M = \dfrac{m_{\#2}^*}{m_{\#1}^*}$ and [120],

$$\eta_{\#2} = \theta_M - (\theta_M - 1)\exp\left( -\frac{E_B}{(\theta_M - 1)k_B T} \right) \qquad \theta_M > 1 \tag{5-33}$$

$$\eta_{\#2} = \theta_M^{-1} - (\theta_M^{-1} - 1)\exp\left( -\frac{E_B}{(\theta_M^{-1} - 1)k_B T} \right) \qquad \theta_M < 1 \tag{5-34}$$

## 5.4 Numerical Methods for Solving the Current Continuity Equation

### 5.4.1 Matrix Transform Method Steady State Solution

The steady state condition means the status quo is maintained by a trade-off between the electrons and holes shown in Fig.5-7 [101]. It also means that the average values of all macroscopic observables within the system are time independent [101]. In other words, in the current continuity equations $\dfrac{dn}{dt}$ and $\dfrac{dp}{dt}$ are both zero.

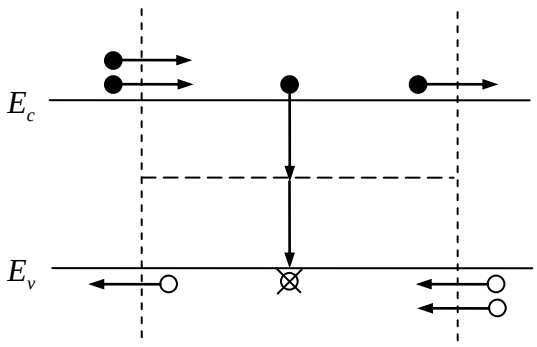


**Figure 5-7** Conceptualization of activity inside the semiconductor under steady-state conditions.

In this circumstance, Eq. (5-18a) becomes

$$q\big(R(x,0)-G(x,0)\big)=\frac{dJ_e(x,0)}{dx} \tag{5-35}$$

Eq. (5-35) with Eq. (5-19a) can be expanded to,

$$R-G=\frac{dn}{dx}\mu_e F_{bias}+n\frac{d}{dx}\left(\mu_e F_{bias}\right)+\frac{dD_e}{dx}\frac{dn}{dx}+D_e\frac{d^2n}{dx^2} \tag{5-36}$$

By Appling the finite difference method to first derivative and second derivative terms, Eq. (5-36) can be expressed as,

$$\begin{aligned}R-G=&\frac{n(x+\Delta x)-n(x-\Delta x)}{2\Delta x}\mu_e F_{bias}+n(x)\frac{d}{dx}\left(\mu_e F_{bias}\right)\\&+\frac{dD_e}{dx}\frac{n(x+\Delta x)-n(x-\Delta x)}{2\Delta x}+D_e\frac{n(x+\Delta x)-2n(x)+n(x-\Delta x)}{\Delta x^2}\end{aligned} \tag{5-37}$$

Rearranging Eq. (5-37) and defining a, b and c as,

$$a=\left(-\frac{1}{2h}\frac{dD_e}{dx}-\frac{1}{2\Delta x}\mu_e F_{bias}+\frac{1}{\Delta x^2}D_e\right) \tag{5-38}$$

$$b=\left(\frac{d\mu_e}{dx}F_{bias}+\mu_e\frac{dF_{bias}}{dx}-\frac{2}{\Delta x^2}D_e\right) \tag{5-39}$$

$$c=\left(\frac{1}{2\Delta x}\frac{dD_e}{dx}+\frac{1}{2\Delta x}\mu_e F_{bias}+\frac{1}{\Delta x^2}D_e\right) \tag{5-40}$$

and applying these definitions across the whole structure results in the following matrix equation,

$$\begin{bmatrix} b_0 & c_0 & \cdots & 0 & 0\\ a_1 & b_1 & c_1 & \ddots & 0\\ \vdots & \ddots & \ddots & \ddots & \vdots\\ \vdots & \ddots & a_{k-1} & b_{k-1} & c_{k-1}\\ 0 & \cdots & 0 & a_k & b_k \end{bmatrix}\begin{bmatrix} n_0\\ n_1\\ \vdots\\ \vdots\\ n_k \end{bmatrix}=\begin{bmatrix} R_0-G_0-a_0n_{-1}\\ R_1-G_1\\ \vdots\\ \vdots\\ R_k-G_k-c_kn_{k+1} \end{bmatrix} \tag{5-41}$$

$$\left[matrix_m\right]\cdot n_m=\sigma_m \tag{5-42}$$

$$n_m=\sigma_m\cdot\left[matrix_m\right]^{-1} \tag{5-43}$$

The electron density can be calculated from Eq. (5-43), the known inverse matrix multiple by the known number $\sigma_m$. The boundary conditions $n_{-1}=n_0$ and $n_{k+1}=n_k$ are estimated from Eq.(5-8a) under zero bias, and they both going to be equal to zero. The same method applies to holes.

### 5.4.2 Time Dependent Solution

The general time dependent equation $\frac{\partial y}{\partial t} = fun(y)$ can be solved by,

$$\frac{y\big|_{t+1} - y\big|_t}{\Delta t} = A \cdot fun(y)\big|_{t+1} + (1-A)\, fun(y)\big|_t \tag{5-44}$$

The best result can be obtained for a decoupled semiconductor equation when $A = 1$ [121]. Therefore, the Eq.(5-18a) changes to,

$$\frac{n(x)\big|_{t+\Delta t} - n(x)\big|_t}{\Delta t} == G(x, t+\Delta t) - R(x, t+\Delta t) + \frac{1}{q}\nabla J_e(x, t+\Delta t) \tag{5-45}$$

If we assume no light shines on the device at $t = 0$, then $n(x)\big|_{t=0}$ will be known by the steady-state calculation that has been analysed in section 5.4.1, therefore $n(x)\big|_{t=\Delta t}$ can be calculated by using the same numerical method as that applied for the steady-state, i.e.

$$\begin{bmatrix} b_0 & c_0 & \cdots & 0 & 0 \\ a_1 & b_1 & c_1 & \ddots & 0 \\ \vdots & \ddots & \ddots & \ddots & \vdots \\ \vdots & \ddots & a_{k-1} & b_{k-1} & c_{k-1} \\ 0 & \cdots & 0 & a_k & b_k \end{bmatrix} \begin{bmatrix} n_{0,\Delta t} \\ n_{1,\Delta t} \\ \vdots \\ \vdots \\ n_{k,\Delta t} \end{bmatrix} = \begin{bmatrix} R_{0,t+1} - G_{0,t+1} - \dfrac{n_{0,0}}{\Delta t} - a_0 n_{-1,0+\Delta t} \\ R_{1,t+1} - G_{1,t+1} - \dfrac{n_{1,0+\Delta t}}{\Delta t} \\ \vdots \\ \vdots \\ R_{k,t+1} - G_{k,t+1} - \dfrac{n_{k,0}}{\Delta t} - c_k n_{k+1,0+\Delta t} \end{bmatrix} \tag{5-46}$$

where

$$a = \left( -\frac{1}{2\Delta x}\frac{dD_{e,0+\Delta t}}{dx} - \frac{1}{2\Delta x}\mu_{e,0+\Delta t}F_{bias,0+\Delta t} + \frac{1}{\Delta x^2}D_{e,0+\Delta t} \right),$$

$$b = \left( -\frac{1}{\Delta t} + \frac{d\mu_{e,0+\Delta t}}{dx}F_{bias,0+\Delta t} + \mu_{e,0+\Delta t}\frac{dF_{bias,0+\Delta t}}{dx} - \frac{2}{\Delta x^2}D_{e,0+\Delta t} \right),$$

$$c = \left( \frac{1}{2\Delta x}\frac{dD_{e,0+\Delta t}}{dx} + \frac{1}{2\Delta x}\mu_{e,0+\Delta t}F_{bias,0+\Delta t} + \frac{1}{\Delta x^2}D_{e,0+\Delta t} \right).$$

a, b and c are the coefficients of the electron density. The electron density can then be calculated by inverse matrix method defined in Eq. (5-43). The boundary conditions $n_{-1,\Delta t} \approx n_0$ and $n_{k+1,\Delta t} = n_k$ are estimated from Eq.(5-8a) under zero bias and they both cannot be equal to zero. The same method can be applied to holes.

### 5.4.3 Thermionic Emission Current across Hetero-junction

The current near the hetero-junction and across the junction is shown in Fig.5-8,

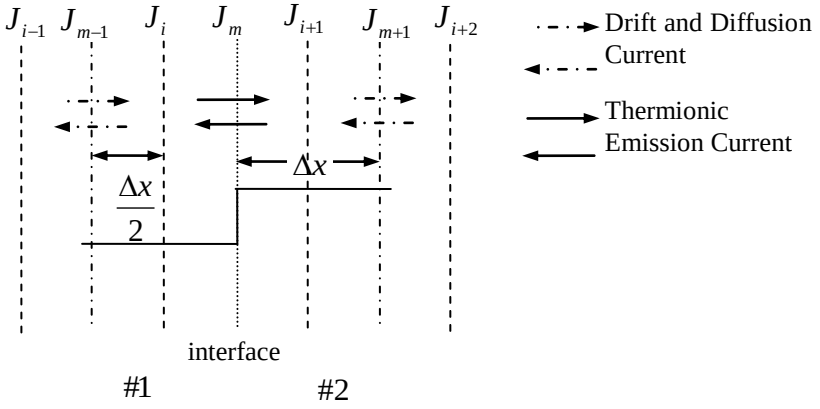


**Figure 5-8** Current near the hetero-junction and across the hetero-junction.

The continuity equations on the material #1 side of the hetero-junction can be written as,

$$R_i - G_i = \frac{1}{q}\frac{J_{e,m} - J_{e,m-1}}{\Delta x} \tag{5-47}$$

where $J_{e,m}$ is the thermionic emission current and $J_{e,m-1}$ is the drift and diffusion current. Replace them by using Eq. (5-32) and Eq.(5-19a),

$$\begin{aligned} R_i - G_i = {} & \frac{1}{\Delta x}\eta_{\#2}\left\{ n_{i+1}V_{eR\#2} - \theta_M n_i V_{eR\#1} \exp\left(-\frac{E_B}{k_B T}\right)\right\} \\ & - \frac{1}{\Delta x} n_{m-1}\mu_e F_{bias} - \frac{1}{\Delta x}\frac{k_B T}{q}\mu_e \frac{dn_{m-1}}{dx} \end{aligned} \tag{5-48}$$

where the terms $n_{m-1} = \frac{n_i + n_{i-1}}{2}$ and $\frac{dn_{m-1}}{dx} = \frac{n_i - n_{i-1}}{\Delta x}$. Then the Eq.(5-48) can be modified as,

$$\begin{aligned} R_i - G_i = {} & \frac{1}{\Delta x}\eta_{\#2}\left\{ n_{i+1}V_{eR\#2} - \theta_M n_i V_{eR\#1} \exp\left(-\frac{E_B}{k_B T}\right)\right\} \\ & - \frac{1}{\Delta x}\frac{n_i + n_{i-1}}{2}\mu_e F_{bias} - \frac{1}{\Delta x}\frac{k_B T}{q}\mu_e \frac{n_i - n_{i-1}}{\Delta x} \end{aligned} \tag{5-49}$$

Then the coefficient of electron density is $a_i = -\frac{1}{2\Delta x}\mu_e F_{bias} + \frac{1}{\Delta x^2}\frac{k_B T}{q}\mu_e$,

$b_i = -\frac{1}{\Delta x}\theta V_{eR\#1}\eta_{\#2}\exp\left(-\frac{E_B}{k_B T}\right) - \frac{1}{2\Delta x}\mu_e F_{bias} - \frac{1}{\Delta x^2}\frac{k_B T}{q}\mu_e$, $c_i = \frac{1}{h}V_{eR\#2}\eta_{\#2}$.

The continuity equation on the material #2 side of the hetero-junction is,

$$R_{i+1} - G_{i+1} = \frac{1}{q}\frac{J_{e,m+1} - J_{e,m}}{\Delta x} \tag{5-50}$$

where $J_{e,m}$ is the thermionic emission current and $J_{e,m+1}$ is the drift and diffusion current. Replace them by using Eq.(5-32) and Eq.(5-19a),

$$\begin{aligned} R_{i+1} - G_{i+1} = &-\frac{1}{\Delta x}\eta_{\#2}\left\{ n_{i+1}V_{eR\#2} - \theta_M n_i V_{eR\#1}\exp\left(-\frac{E_B}{k_B T}\right)\right\} \\ &+ \frac{1}{\Delta x} n_{m+1}\mu_e F_{bias} + \frac{1}{\Delta x}\frac{k_B T}{q}\mu_e \frac{dn_{m+1}}{dx} \end{aligned} \tag{5-51}$$

where the terms $n_{m+1} = \frac{n_{i+2} + n_{i+1}}{2}$ and $\frac{dn_{m+1}}{dx} = \frac{n_{i+2} - n_{i+1}}{\Delta x}$ can be written as and, therefore, the Eq.(5-51) can be modified as,

$$\begin{aligned} R_{i+1} - G_{i+1} = &-\frac{1}{\Delta x}\eta_{\#2}\left\{ n_{i+1}V_{eR\#2} - \theta_M n_i V_{eR\#1}\exp\left(-\frac{E_B}{k_B T}\right)\right\} \\ &+ \frac{1}{\Delta x}\frac{n_{i+2} + n_{i+1}}{2}\mu_e F_{bias} + \frac{1}{\Delta x}\frac{k_B T}{q}\mu_e \frac{n_{i+2} - n_{i+1}}{\Delta x} \end{aligned} \tag{5-52}$$

The coefficient of electron density is $a_{i+1} = \frac{1}{\Delta x}\theta_M V_{eR\#1}\eta_{\#2}\exp\left(-\frac{E_B}{k_B T}\right)$ ,

$b_{i+1} = -\frac{1}{\Delta x}V_{eR\#2}\eta_{\#2} + \frac{1}{2\Delta x}\mu_e F_{bias} - \frac{1}{\Delta x^2}\frac{k_B T}{q}\mu_e$, $c_{i+1} = \frac{1}{2\Delta x}\mu_e F_{bias} + \frac{1}{\Delta x^2}\frac{k_B T}{q}\mu_e$.

### 5.4.4 Estimation of Error Term in the Quasi Fermi Level

The Quasi-Fermi levels are found by using the inverse Dirac Fermi integral Eq. (5-11). The carrier concentration are calculated by using Eq. (5-9a) and Eq. (5-9b),

$$n = N_c F_{1/2}\left(\frac{E_{f-real(n)} - E_c}{k_B T}\right) \tag{5-53a}$$

$$p = N_v F_{1/2}\left(\frac{E_v - E_{fp-real(p)}}{k_B T}\right) \tag{5-53b}$$

where $E_{f-real}$ represents the actual Fermi level. The approximation to the Fermi Dirac integral used in Eq.(5-10) has an accuracy of $\pm 0.5\%$ [101]. The inverse Fermi Dirac integral gives another $\pm 0.5\%$ error.

$$E_{f-error(n)}(x) = E_{f-real(n)}(x) - \left[E_c + k_B T \times InvFDI\left(\frac{n}{N_c}\right)\right] \tag{5-54a}$$

$$E_{f-error(p)}(x) = E_{f-real(n)}(x) - \left[ E_v - k_B T \times InvFDI\left( \frac{p}{N_v} \right) \right] \quad (5\text{-}54b)$$

Therefore, the total error in the quasi-Fermi level calculation is $\pm 1\%$. Fig.5-8 shows an example of the difference between the real quasi-Fermi level and the approximated quasi-Fermi level. In Fig.5-9, the real Fermi level is equal to zero, the method of calculating Fermi levels both gives approximately 0.015Joules (J) error from the actual value and it is about $\pm 1\%$ from the actual value. It is thought to originate from the accumulation of the errors in the approximation used for the Fermi-Dirac integral and its inverse function.

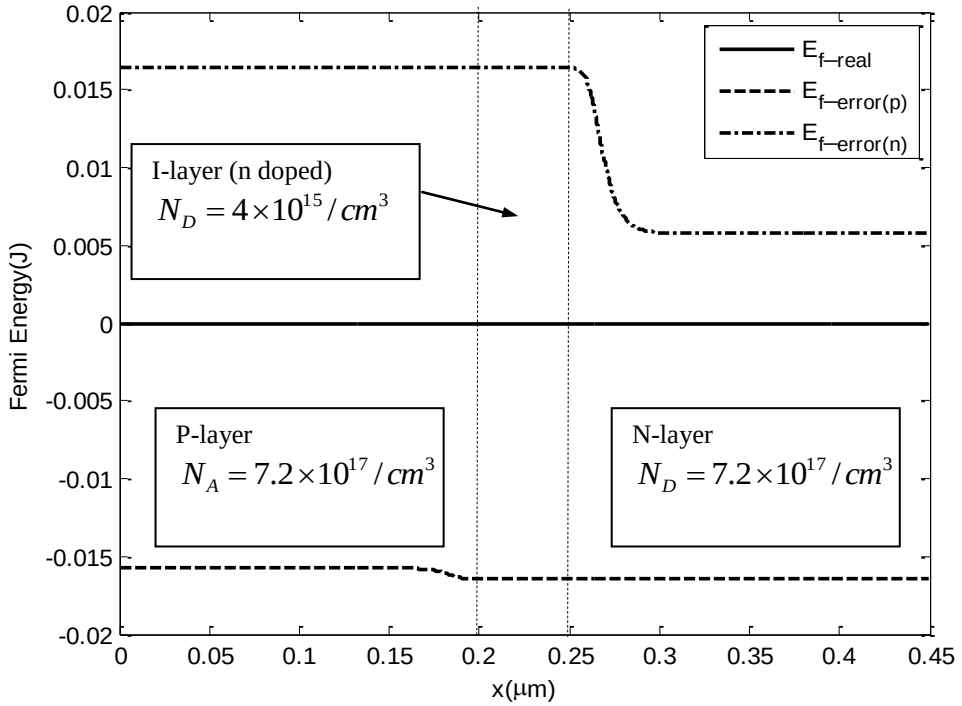


**Figure 5-9** Approximation Fermi level by using inverse Fermi Dirac integral and the actual Fermi level.

Since this offset potential appears to be systematic, the error in calculation of the Fermi energy leads to an offset value from the true value. Therefore, $E_{f-error}$ is added to the estimated quasi-Fermi levels, when calculating the positions of the quasi-Fermi levels.

## 5.5 Self-Consistent Calculations for Current-Poisson's Equations

The flow chart of self-consistent calculations of the current continuity equation and Poisson's equation is shown in Fig.5-10. For starting the calculation, the

quasi-Fermi levels $E_{fp}$ and $E_{fn}$ are assumed to take two constant values at $-\frac{q}{k_B T}V_{bias}$ and *0*. The potential profile and field are obtained by calculating the Poisson's equation under bias, and storing the potential profile in the value $\eta_{old}$. Using these known values, the carrier densities can be found by solving the continuity equations. Updated values of the quasi-Fermi levels $E_{fp}$ and $E_{fn}$ can now be obtained to solve the Poisson's equation again, this time storing the potential profile in the value $\eta_{new}$. Calculate the ratio $r = \frac{\eta_{new}}{\eta_{old}}$, if it is smaller than the required value, then the calculation is self-consistent. If not, the value of $\eta_{new}$ will replace the value of $\eta_{old}$. Then calculation of two equations will not stop until the ratio *r* is smaller than the required value and the calculation must be self-consistent.

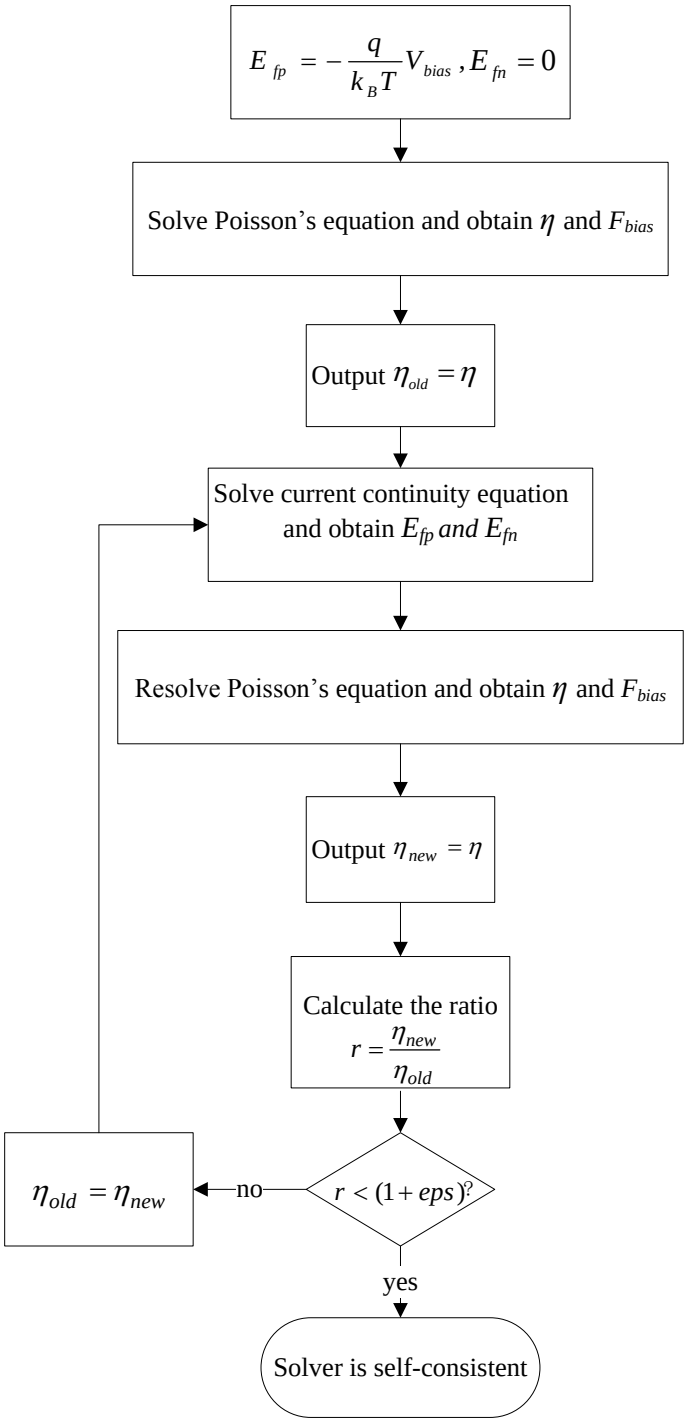


**Figure 5-10** Flow chart of self-consistent simulation of current-Poisson's equations.

The solver of PIN photodiode is shown in Fig. 5-11.

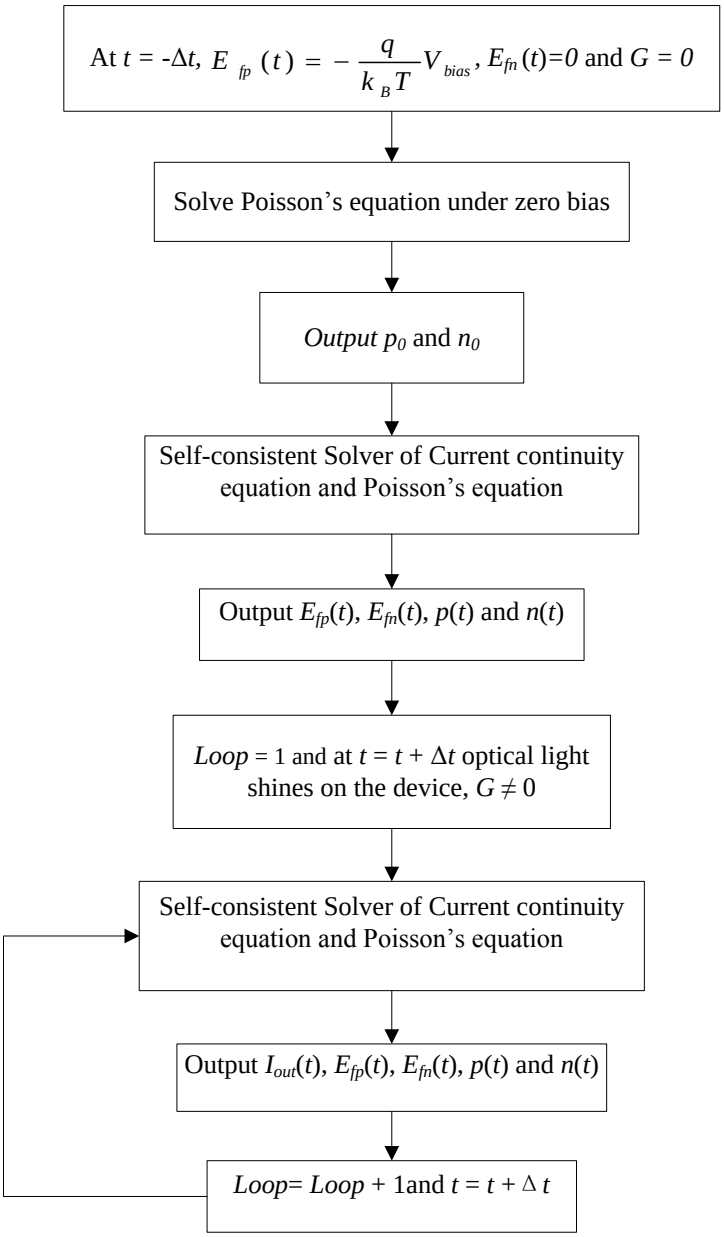


**Figure 5-11** Flow chart of modelling the PIN photodiode.

The Poisson's equation and current continuity equations have to be solved under zero bias first, to obtain the carrier concentration for the use in recombination term calculation in current continuity equation. The steady-state needs to be settled before solving the time dependent continuity equations. Again at the start of the calculation, the quasi-Fermi levels $E_{fp}$ and $E_{fn}$ are assumed to take two constant values at $-\frac{q}{k_B T} V_{bias}$ and *0*, and the generation term is zero. The self-consistent solver of Current-Poisson's equations gives the value of electric field, quasi-Fermi level and the carrier concentration. These values will be used in the time dependent

solver at $t = t + \Delta t$. In the time dependent state, the current continuity equation is solved with carrier densities in the previous time and non-zero generation term that depends on the input optical power and absorption coefficient.

## 5.6 Summary

The Poisson's equation and current continuity equation for bulk semiconductor material are defined in this chapter. The boundary conditions at both ends of PIN photodiode device are applied to settle a single group solution of both equations. Furthermore, the thermionic emission is also used as a boundary condition in the hetero-junction in the device. The flow chart for obtaining the self-consistent calculation of Poisson's equation and the current continuity equation and the flow chart for numerical modelling of PIN photodiode were presented and were explained in detail in this chapter.

# Chapter 6

## Theory of Modelling MQW-EAM

## 6.1 Poisson's Equation

Although the Poisson's equation is the same one as used in Chapter 5,

$$\nabla \cdot (\varepsilon \varepsilon_0 \nabla \Phi) = -\rho \tag{6-1}$$

the charge density $\rho$ is not as the same definition in Eq.(5-5), due to the additional quantum wells in the intrinsic layer. Therefore, the charge density is given by [24],

$$\rho = q(p_{bulk}(x) + p_{QW}^{3D}(x) - n_{bulk}(x) - n_{QW}^{3D}(x) + N_D^+(x) - N_A^-(x)) \tag{6-2}$$

where $p_{bulk}(x)$ and $n_{bulk}(x)$ are the carrier concentration in the bulk state, and $p_{QW}^{3D}(x) = \frac{p_{QW}^k(x)}{L_{QW}^k}$ and $n_{QW}^{3D}(x) = \frac{n_{QW}^k(x)}{L_{QW}}$. $L_{QW}$ is the width of the *k-th* quantum well layer, $p_{QW}^k(x)$ and $n_{QW}^k(x)$ are the carrier concentration inside the *k-th* quantum well. The definition of $p_{QW}^k(x)$ and $n_{QW}^k(x)$ are defined in the section 6.1.1.

### 6.1.1 Electron and Hole Concentration in the Quantum Wells

The electron concentration in quantum well is given by [122],

$$n_{QW}^k(x) = \frac{m_e^* k_B T}{\pi \hbar^2} \sum_n |\psi_{en}|^2 \ln\left[1 + \exp\left(-\frac{E_{en} - E_{fn}}{k_B T}\right)\right] \tag{6-3}$$

Where $m_e^*$ is the effective mass of the electron in the quantum well, $E_{en}$ is the eigen energy confined state in the quantum well and $\psi_{en}$ is the wavefunction. A similar formula is applied to find the hole density,

$$p_{QW}^k(x) = \frac{m_h^* k_B T}{\pi \hbar^2} \sum_m |\psi_{hm}|^2 \ln\left[1 + \exp\left(\frac{-E_g - E_{hm} - E_{fp}}{k_B T}\right)\right] \tag{6-4}$$

The properties and the calculation methodology of wavefunction will be introduced in section 6.4.

### 6.1.2 The Total Carrier Concentration in the Well Layers

When the carrier concentrations $p_{QW}^{3D}(x)$ and $n_{QW}^{3D}(x)$ are added to their three dimensional counterparts, it is important to notice that all of those densities contribute to the total electron density and total hole density. When adding these two terms to obtain the total density, care must be taken in order to avoid including a three dimensional concentration in the well region contributes twice [123]. As

shown in Fig.6-1 [124], inside the quantum well, particles with energy that is smaller than $E(B)$ are confined by the quantum well and $p_{QW}^{3D}(x)$ and $n_{QW}^{3D}(x)$ are used. For energy higher than the quantum well edge in the conduction band or lower than the well edge in the valance band, the energy above *E(B)* is still continuous and the carriers are no longer confined in the quantum well [125], $p_{bulk}(x)$ and $n_{bulk}(x)$ are used.

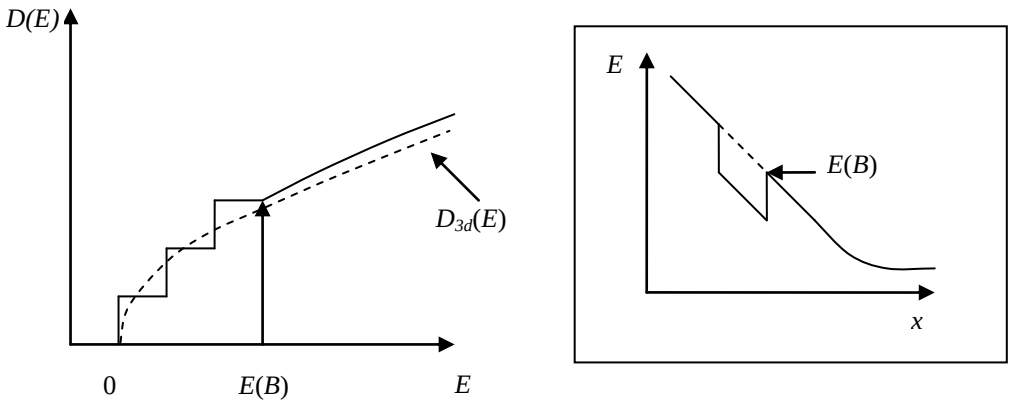


**Figure 6-1** Energy behaviour in and above the quantum well.

## 6.2 Current Continuity Equation for MQW-EAM

For a modulator under reverse bias, the carrier action in the bulk material semiconductor includes drift, diffusion, recombination, thermionic emission and the carrier action in the quantum wells contains generation, recombination, capture and escape. The carrier action under reverse bias in the MQW-EAM is shown in Fig.6-2.

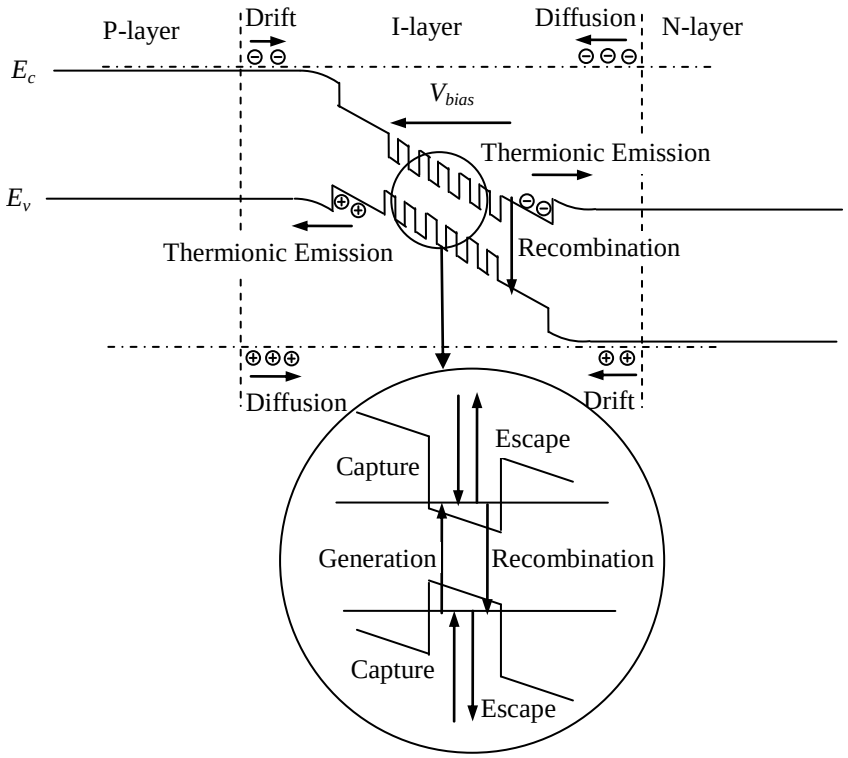


**Figure 6-2** Carrier actions in the MQW-EAM under reverse bias.

### 6.2.1 Current Continuity Equation for Bulk Material

The continuity equations for the electrons and holes in bulk states are defined as[54],

$$\frac{\partial n}{\partial t}=\frac{1}{q}\left(\frac{\partial J_e}{\partial x}+J_{e,QW}^{3D}\right)-R \tag{6-5}$$

$$-\frac{\partial p}{\partial t}=\frac{1}{q}\left(\frac{\partial J_h}{\partial x}+J_{h,QW}^{3D}\right)+R \tag{6-6}$$

where $J_e$ and $J_h$ are the electron and hole current densities, $R$ is the recombination rate in the bulk material, they have already been defined above. $J_{e,QW}^{3D}$ and $J_{h,QW}^{3D}$ are given by [54],

$$J_{h(e),QW}^{3D}=\begin{cases}\dfrac{J_{h(e),QW}^{k}}{L_{QW}^{k}}, & inside\ \ the\ \ well\\ 0, & otherwise\end{cases} \tag{6-7}$$

where $J_{h(e),QW}^{3D}$ is the current between well and bulk material for each well individually.

### 6.2.2 Current Continuity Equation for Quantum Well

The continuity equation for the quantum wells includes the optical excitation, recombination and carriers exchange between well states and bulk states. The continuity equations are defined as [54],

$$\frac{\partial n_{QW}^{k}}{\partial t} = -\frac{1}{q} J_{e,QW}^{k} - R_{QW}^{k} + G_{QW}^{k} \tag{6-8a}$$

$$\frac{\partial p_{QW}^{k}}{\partial t} = \frac{1}{q} J_{h,QW}^{k} - R_{QW}^{k} + G_{QW}^{k} \tag{6-8b}$$

where $p_{QW}^{k}$ and $n_{QW}^{k}$ are the carriers densities in the well *k*, $G_{QW}^{k}$ and $R_{QW}^{k}$ are the generation rate and recombination rate in the well *k*. $J_{e,QW}^{k}$ and $J_{h,QW}^{k}$ are the exchange current between well states and bulk states. They are given by,

$$J_{e,QW}^{k} = J_{e,QW}^{esc} + J_{e,QW}^{cap} \tag{6-9a}$$

$$J_{h,QW}^{k} = J_{h,QW}^{esc} + J_{h,QW}^{cap} \tag{6-9b}$$

where $J_{h(e),QW}^{esc}$ the escape current and $J_{h(e),QW}^{cap}$ is the capture current

### 6.2.3 Escape Current

The escape current means that the carriers are on the well states jumping to the bulk states. The escape current for electrons and holes are defined below [54],

$$J_{e,QW}^{esc} = -qn_{QW}^{k}\left(\frac{k_B T}{2\pi m_{e,\|}}\right)^{1/2} \exp\left(\frac{-E_b^c + E_{e1}}{k_B T}\right) \tag{6-10a}$$

$$\begin{aligned} J_{h,QW}^{esc} &= qp_{hh,QW}^{k}\left(\frac{k_B T}{2\pi m_{hh,\|}}\right)^{1/2} \exp\left(\frac{-E_b^v - E_{hh1}}{k_B T}\right) \\ &\quad + qp_{lh,QW}^{k}\left(\frac{k_B T}{2\pi m_{lh,\|}}\right)^{1/2} \exp\left(\frac{-E_b^v - E_{lh1}}{k_B T}\right) \end{aligned} \tag{6-10b}$$

where $m_{e,\|}$ ,$m_{lh,\|}$ and $m_{hh,\|}$ are the in-plane mass of carriers in the well, $E_{1e}$, $E_{1lh}$ and $E_{1hh}$ are the lowest eigen-state energy in the well, $E_b^c$ and $E_b^v$ are the barrier energy. All these energy such as $E_c$, $E_v$, $E_{1e}$, $E_{1lh}$, $E_{1hh}$ are reference with a single reference level $E_{ref}$, as shown in Fig.6-3.

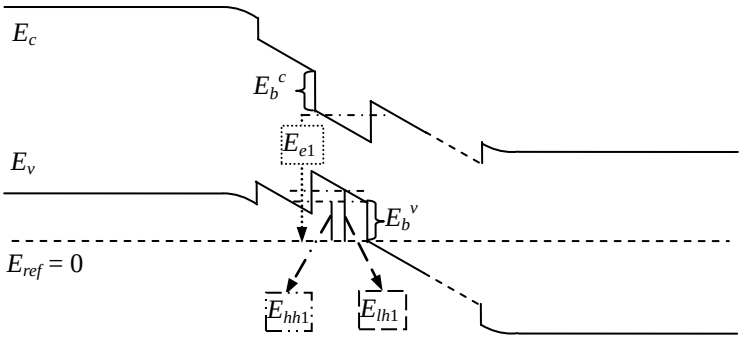


**Figure 6-3** Carrier actions in the MQW-EAM under reverse bias.

### 6.2.4 Capture Current

The capture current means that the carriers are on the bulk states jumping onto the well states. The capture current for electrons and holes are defined below [54],

$$J_{e,QW}^{cap} = \frac{qn_{QW}^{k}}{\tau_{e,th}} \tag{6-11a}$$

$$J_{h,QW}^{cap} = -q\frac{p_{QW}^{k}}{\tau_{hh,th}} - q\frac{p_{QW}^{k}}{\tau_{lh,th}} \tag{6-11b}$$

where $\tau_{e,th}$ $\tau_{hh,th}$ and $\tau_{lh,th}$ are the escape time under thermal equilibrium, the capture time is equal to the escape time under thermal equilibrium, and the capture of carriers is a slow processes in EAM, therefore the capture time is reasonable to be assumed the same under steady-state. The escape time is given by,

$$\tau_{e,th} = \left(\frac{k_B T}{2\pi m_{e,\|}}\right)^{-1/2} \exp\left(\frac{E_b^c - E_{e1}}{k_B T}\right) \tag{6-12a}$$

$$\tau_{lh,th} = \left(\frac{k_B T}{2\pi m_{lh,\|}}\right)^{-1/2} \exp\left(\frac{E_b^v + E_{lh1}}{k_B T}\right) \tag{6-12b}$$

$$\tau_{hh,th} = \left(\frac{k_B T}{2\pi m_{hh,\|}}\right)^{-1/2} \exp\left(\frac{E_b^v + E_{hh1}}{k_B T}\right) \tag{6-12c}$$

## 6.3 Numerical Methods for Solving the Current Continuity Equation for MQW-EAM

### 6.3.1 Bulk Material

Under steady-state, the inverse matrix method that was introduced in Chapter 5

section 5.4 can still be applied to Eq.(6-8a). The coefficients of the electron density a, b and c are still the same as Eq.(5-43), however; the $\sigma_m$ value in Eq.(5-43) is modified to,

$$\sigma_m = \begin{bmatrix} R_0 - \frac{1}{q} J_{e,QW}^{3D}(0) - a_0 n_{-1} \\ R_1 - \frac{1}{q} J_{e,QW}^{3D}(1) \\ \vdots \\ \vdots \\ R_k - \frac{1}{q} J_{e,QW}^{3D}(k) - c_k n_{k+1} \end{bmatrix} \tag{6-13}$$

The electron density $n_m$ can be calculated from Eq.(5-43), the known inverse matrix multiple by the known number $\sigma_m$ . The boundary conditions $n_{-1} \approx n_0$ and $n_{k+1} = n_k$ are still estimated from Eq.(5-8a), and they both cannot be equal to zero.

In the time dependent state, the coefficients of the electron density a, b and c are still the same as Eq.(5-46), but the $\sigma_m$ value is modified to

$$\sigma_m = \begin{bmatrix} R_{0,\Delta t} - \frac{n_{0,0}}{\Delta t} - \frac{1}{q} J_{e,QW}^{3D}(0,\Delta t) - a_0 n_{-1,\Delta t} \\ R_{1,\Delta t} - \frac{n_{1,0}}{\Delta t} - \frac{1}{q} J_{e,QW}^{3D}(1,\Delta t) \\ \vdots \\ \vdots \\ R_{1,\Delta t} - \frac{n_{k,0}}{\Delta t} - \frac{1}{q} J_{e,QW}^{3D}(k,\Delta t) - c_k n_{k+1,\Delta t} \end{bmatrix} \tag{6-14}$$

The boundary conditions $n_{-1} \approx n_0$ and $n_{k+1} = n_k$ are still estimated from Eq.(5-8a), and they both cannot be equal to zero. The same method applies to holes.

### 6.3.2 Inside Quantum Well

Under steady state, the term $\frac{\partial n_{QW}^k}{\partial t} = 0$, therefore the Eq.(6-8a) is modified to,

$$0 = -\frac{1}{q} J_{e,QW}^k - R_{QW}^k + G_{QW}^k \tag{6-15}$$

where $J_{e,QW}^k$ can be replaced by Eq.(6-10a) and Eq.(6-11a)

$$0 = n_{QW}^{k}\left(\frac{k_B T}{2\pi m_{e,\|}}\right)^{1/2} \exp\left(-\frac{E_b^c - E_{e1}}{k_B T}\right) - \frac{n_{QW}^{k}}{\tau_{e,th}} - R_{QW}^{k} + G_{QW}^{k} \tag{6-16}$$

Then the carrier concentration in the quantum well under steady state is

$$n_{QW}^{k} = \frac{R_{QW}^{k} - G_{QW}^{k}}{\left[\left(\frac{k_B T}{2\pi m_{e,\|}}\right)^{1/2} \exp\left(-\frac{E_b^c - E_{e1}}{k_B T}\right) - \frac{1}{\tau_{e,th}}\right]} \tag{6-17}$$

Under time dependence, the term $\frac{\partial n_{QW}^{k}}{\partial t} \neq 0$, use Eq.(6-10a) and Eq.(6-11a) to replace $J_{QW}^{k}$ in Eq.(6-8a) ,

$$\frac{\partial n_{QW}^{k}(t)}{\partial t} = n_{QW}^{k}\left(\frac{k_B T}{2\pi m_{e,\|}}\right)^{1/2} \exp\left(-\frac{E_b^c - E_{e1}}{k_B T}\right) - \frac{n_{QW}^{k}(t)}{\tau_{e,th}} - R_{QW}^{k} + G_{QW}^{k} \tag{6-18}$$

Solve $\frac{\partial n_{QW}^{k}}{\partial t}$ by using Eq.(5-44), then the Eq.(6-18) becomes,

$$\frac{n_{QW}^{k}(t) - n_{QW}^{k}(t-\Delta t)}{\Delta t} = n_{QW}^{k}(t)\left(\frac{k_B T}{2\pi m_{e,\|}}\right)^{1/2} \exp\left(-\frac{E_b^c - E_{e1}}{k_B T}\right) - \frac{n_{QW}^{k}(t)}{\tau_{e,th}} - R_{QW}^{k} + G_{QW}^{k} \tag{6-19}$$

Then the carrier concentration in the quantum well under time dependence is

$$n_{QW}^{k}(t_k) = \frac{R - G - \frac{n_{QW}^{k}(t_k - \Delta t)}{\Delta t}}{\left[-\frac{1}{\Delta t} + \left(\frac{k_B T}{2\pi m_{e,\|}}\right)^{1/2} \exp\left(-\frac{E_b^c - E_{e1}}{k_B T}\right) - \frac{1}{\tau_{e,th}}\right]} \tag{6-20}$$

The same methods are applied to the holes.

## 6.4 Schrödinger's Equation for Multiple Quantum Wells

The state of a quantum particle is described by a wavefunction[126], that is normally represented by a symbol $\Psi(r,t)$. Every wavefunction in the quantum well corresponds to a definite energy state and it is called eigen energy $E_{hm(en)}$ or orbital. The eigen-state and the wavefunction for the quantum well can be obtained by solving Schrödinger's equation. The Schrödinger's equation is the probability of the presence of electrons being maximal at the centre of the nucleus [127], and it is defined as [126] ,

$$j\hbar\frac{\partial}{\partial t}\Psi(r,t)=H\Psi(r,t) \tag{6-21}$$

where $\hbar=\frac{h}{2\pi}$ ($h$ is the Planck's constant), and $H$ is the Hamiltonian operator. Hamiltonian operator is the total energy in the system, the sum of kinetic and potential energy [126], and is given by,

$$H=-\frac{\hbar^2}{2m}\nabla^2+V_{EP}(r,t) \tag{6-22}$$

where $\nabla^2=\frac{\partial^2}{\partial x^2}+\frac{\partial^2}{\partial y^2}+\frac{\partial^2}{\partial z^2}$ is the Laplacian operator and $V_{EP}(r,t)$ is the electrostatic potential energy that can be calculated by the Poisson's equation Eq.(6-1).

The time dependent wavefunction $\Psi(r,t)$ can be written as[25],

$$\Psi(r,t)=\psi(r)fun(t)=\psi(r)e^{-jEt/\hbar} \tag{6-23}$$

where $\psi(r)$ is the time-independent wavefunction. Eq.(6-22) with Eq.(6-23) , the time independent Schrödinger's equation is modified to,

$$E\psi(r)=\left[-\frac{\hbar^2}{2m}\nabla^2+V_{EP}(r)\right]\psi(r) \tag{6-24}$$

The quantized energy levels for electron $E_{en}$ with corresponding wavefunction $\psi_{en}$ both can be found by solving Eq.(6-24). The subscript e represents electron and $n$ denotes the band index.

### 6.4.1 Many Particles Schrödinger's Equation

The Schrödinger's equation is the basic equation of quantum mechanics and can be generalized for the many particles case [128]. The solution of the many particle wavefunction includes the quantum probability amplitude for every possible configuration of electrons and nuclei,

$$\Phi=\Phi(r_1,r_2,...r_N,t) \tag{6-25}$$

where $r_i$ is the position vector of *i-th* electron comprising the subsystem. Substitute Eq.(6-23) into Eq.(6-25), the time-independent wavefunction can be obtained,

$$\Phi=e^{-jEt/\hbar}\phi(r_1,r_2,...r_N) \tag{6-26}$$

The many particle time-independent Schrödinger's equation is given by,

$$H_{MP}\phi(r_1, r_2, ..., r_N) = E\phi(r_1, r_2, ..., r_N) \tag{6-27}$$

Where $H_{MP}$ is the Hamiltonians factor in a many particle system and $\phi(r_1, r_2, ..., r_N)$ is the many particle wavefunction. For an N-electron system, the many particle wavefunction becomes as a determinant, this is known as the Slater determinant [58, 128],

$$\phi(r_1, r_2, ..., r_N) = \frac{1}{\sqrt{N!}} \begin{vmatrix} \psi_1(r_1) & \psi_2(r_1) & \cdots & \psi_N(r_1) \\ \psi_1(r_2) & \psi_2(r_2) & \cdots & \psi_N(r_2) \\ \vdots & \vdots & \ddots & \vdots \\ \psi_1(r_N) & \psi_2(r_N) & \cdots & \psi_N(r_N) \end{vmatrix} \tag{6-28}$$

where $\psi_i$ ($i$ = 1,2,…,$N$) is the normalized single electron wavefunction. The method of normalizing the wavefunction will be introduced in the section 6.4.4.

In the solid, every electron must feel the coulomb repelling from other electrons and Coulomb attraction from nuclei [129]. To test an electron wandering through the crystal, one of the methods is to calculate the forces from all the other electrons and nuclei one by one, then add them all up[129]. This is defined as the many-particle potential. Therefore, the Hamiltonians factor for electrons is given by [58],

$$H_{MP} = \sum_{i=1}^{N}\left[-\frac{\hbar}{2m_e}\frac{\partial^2}{\partial \vec{r}_i^{\,2}} + V_{ext}(\vec{r}_i)\right] + \frac{1}{2}\sum_{i,l\neq i}^{N}\frac{q^2}{|\vec{r}_i - \vec{r}_l|} + \frac{q^2}{\varepsilon}\sum_{l\neq i}^{N}\int d\vec{r}_l \frac{|\psi_i(\vec{r}_l)|^2}{|\vec{r}_i - \vec{r}_l|} \tag{6-29}$$

where $m_e$ is the mass of electron, $V_{ext}$ is the same external potential for each electron, the term $\frac{1}{2}\sum_{i,l\neq i}^{N}\frac{q^2}{|\vec{r}_i - \vec{r}_l|}$ is the Coulomb repulsion between each pair of electrons and the term $\frac{q^2}{\varepsilon}\sum_{l\neq i}^{N}\int d\vec{r}_l \frac{|\psi_i(\vec{r}_l)|^2}{|\vec{r}_i - \vec{r}_l|}$ is the Hartree potential energy [130]. The Hartree potential describes the potential energy of the *i-th* particle in the Coulomb potential produced by the charge distribution of the remaining particles [131]. The overall potential must also reflect the correlation between position of *i-th* electron and the positions of all the remaining electrons and the effect of swapping the subscript label of the wavefuctions [132]. Therefore, the many particle Schrödinger's equation is given by [58],

$$\left(\sum_{i=1}^{N}\left[-\frac{\hbar}{2m_e}\frac{\partial^2}{\partial\vec{r}_i^{\,2}}+V_{ext}(\vec{r}_i)\right]+\frac{1}{2}\sum_{i,l\neq i}^{N}\frac{q^2}{|\vec{r}_i-\vec{r}_l|}+\frac{q^2}{\varepsilon}\sum_{l\neq i}^{N}\int d\vec{r}_l\frac{|\psi_i(\vec{r}_l)|^2}{|\vec{r}_i-\vec{r}_l|}\right)\psi_i(\vec{r}) \\ -\frac{q^2}{\varepsilon}\sum_{l\neq i}\int d\vec{r}'\frac{|\psi_l^*(\vec{r}')\psi_i(\vec{r}')|}{|\vec{r}-\vec{r}'|}\psi_i(\vec{r})=E_i\psi_i(\vec{r}) \tag{6-30}$$

where $\frac{q^2}{\varepsilon}\sum_{l\neq i}\int d\vec{r}'\frac{|\psi_l^*(\vec{r}')\psi_i(\vec{r}')|}{|\vec{r}-\vec{r}'|}\psi_i(\vec{r})$ is the exchange-correlation potential. This exchange term is the manifestation of the Pauli Exclusion Principle. Thus the Hartree-Fock theory has shown the motion of an electron in an effective potential created by all other electrons of the system [132], however; Eq.(6-30) remains difficult to solve, because of the huge number of summations and is usually unknown [130]. In the MQW-EAM model, the Fermi energy variance because of applied bias and input optical light has more important effect on the electron than interaction caused by the other particles [133]. Therefore, the exchange-correlation effect and repulsion effect can be neglected and the Eq.(6-30) can be simplified to,

$$\left(\sum_{i=1}^{N}\left[-\frac{\hbar}{2m_e}\frac{\partial^2}{\partial\vec{r}_i^{\,2}}\right]+\frac{q^2}{\varepsilon}\sum_{l\neq i}^{N}\int d\vec{r}_l\frac{|\psi_i(\vec{r}_l)|^2}{|\vec{r}_i-\vec{r}_l|}\right)\psi_i(\vec{r})=E_i\psi_i(\vec{r}) \tag{6-31}$$

and the Hartree potential is the solution from the Poisson's equation. Solving Eq.(6-31) is still very complicated, since there are $\sim 10^{23}$ electrons/cm$^3$ in the material, and they are all interacting with each other and with the numerous phonons that constitute the lattice vibration [122]. Also because of the complicated numerical model for MQW-EAM, we need to use the other simpler optional way to solve the Schrödinger's equation. The method is to calculate the force from the screened periodic potential just like there were no other electrons around [129]. In another words, obtain the wavefunction and eigen energy by solving one particle Schrödinger's equation.

### 6.4.2 One Particle Schrödinger's Equation

The one particle wavefunction approximation is an approximation of independent electrons and static lattice. In other words, the electrons are not interacting with each other and lattice vibrations are considered to be frozen in time [129]. Therefore, the electron is under some average potential and the carrier concentration in the well is calculated by an appropriate statistical average over many electrons in the model. The one particle Schrödinger's equation is defined

as[122],

$$j\hbar\frac{\partial}{\partial t}\Psi_0(r,t)=\left[-\frac{\hbar^2}{2m_0}\nabla^2+V_{EP}(r,t)\right]\Psi_0(r,t) \tag{6-32}$$

where $m_0$ is free electron mass, $\Psi_0(r,t)$ is the wavefunction for one electron and its squared magnitude is proportional to the probability of finding the electron at a point in space (r) at time (t). Solving the one particle problem is much simpler than the many particles equation, however, it is still quite difficult in general due to the complex calculation of the space and time variable $V_{EP}(r,t)$ [122]. Further simplification is possible because only a one dimensional numerical model is required. Then Eq.(6-32) becomes,

$$j\hbar\frac{\partial}{\partial t}\Psi_0(x,t)=\left[-\frac{\partial^2}{\partial x^2}\frac{\hbar^2}{2m_0}+V_{EP}(x,t)\right]\Psi_0(x,t) \tag{6-33}$$

Substitute Eq.(6-23) into Eq.(6-33) ,

$$E_0\psi_0(x)=\left[-\frac{\partial^2}{\partial x^2}\frac{\hbar^2}{2m_0}+V_{EP}(x)\right]\psi_0(x) \tag{6-34}$$

### 6.4.3 Effective Mass Equation

The electron's energy-momentum relation is not the simple parabolic relation of free space when electrons are subject to any forces, however; near the edge of the conduction band and valance band, the electron can be described by an effective mass [134]. Effective mass theory is commonly used in condensed matter physics in which the effect of the periodic lattice potential $V_{per}$ is hidden in an effective mass tenser $m^*$ [135]. If the scattering is neglected, the time independent electron wave function can be found by solving [136],

$$E_0\psi_0(x)=\left[-\frac{d^2}{dx^2}\frac{\hbar^2}{2m_0}+V_{EP}(x)+V_{per}(x)\right]\psi_0(x) \tag{6-35}$$

where Eq.(6-35) can be further simplified to an equation similar to Eq.(6-34) if the carriers are near the bottom of a simple, spherical, parabolic band. This simplified equation can be written as [136],

$$E\psi_{F0}(x)=\left[-\frac{\partial^2}{\partial x^2}\frac{\hbar^2}{2m^*}+V_{EP}(x)\right]\psi_{F0}(x) \tag{6-36}$$

where $\psi_{F0}(x)$ is the envelope function. The envelope function is the actual wave function when the wave vector is zero [136],

$$\psi_0(x) = \psi_{F0}(x)\big|_{k=0} \tag{6-37}$$

as shown in Fig.6-4 [134].

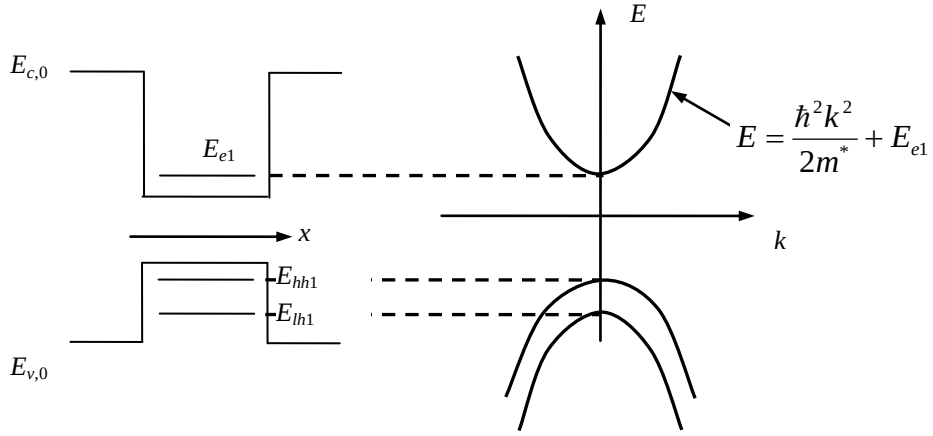


**Figure 6-4** Eigen-states in the Quantum well.

Eq.(6-36) is mathematically identical to the one particle Schrödinger's equation, apart from the free electron mass $m_0$ has been replaced by the electron effective mass $m^*$ [132].

Solving Eq. (6-36) is not straightforward for numerical estimation. Deriving a reasonable general solution to the Schrödinger equation for a finite length well can save lots of calculation time [137]. Inside the well, where $k$ = 0, Eq.(6-36) can be expressed as,

$$\frac{d^2\psi_0(x)}{dx^2} = \frac{2m^*(E - V_{EP}(x))}{\hbar^2}\psi_0(x) = -\alpha_{WF}^2\psi_0(x) \qquad E > V_{EP} \tag{6-38}$$

where $\alpha_{WF} = \frac{\sqrt{2m^*(E - V_{EP}(x))}}{\hbar^2}$. The second derivative of $\psi_0(x)$ is equal to the negative of the same function multiplied by a known constant $\alpha_{WF}^2$. Both of the sine and cosine functions satisfy the requirement [137]. Therefore, the most general solution to the equation is a linear combination of both solutions;

$$\varphi(x) = A_{WF}\sin(\alpha_{WF}x) + B_{WF}\cos(\alpha_{WF}x) \qquad E > V_{EP} \tag{6-39}$$

where $A_{WF}$ and $B_{WF}$ are constants. For the barrier, where $k$ = 0 and under equilibrium state, Eq.(6-36) can be modified into,

$$\frac{d^2\psi_0(x)}{dx^2} = \frac{2m^*(V_{EP}(x) - E)}{\hbar^2}\psi_0(x) = \beta_{WF}^2\psi_0(x) \qquad E < V_{EP} \tag{6-40}$$

where $\beta_{WF} = \frac{\sqrt{2m^*(V_{EP}(x) - E)}}{\hbar^2}$. The solution to the function $\psi_0(x)$ whose second

derivative is the same function multiplied by a known constant $\beta_{WF}^2$. The most general solution to Eq. (6-40) is represented in the form of exponential functions,

$$\varphi(x) = A_{WF}\exp(\beta_{WF}x) + B_{WF}\exp(-\beta_{WF}x) \qquad E < V_{EP} \tag{6-41}$$

where $A_{WF}$ and $B_{WF}$ are constants.

To ease computation further, a stepwise approximation to $V_{EP}(x)$ is made as shown in Fig. 6-5. This approximation requires a small step length $\Delta x$ and its validity can be tested by systematically halving the step length and examing the effect on the eigenvalues.

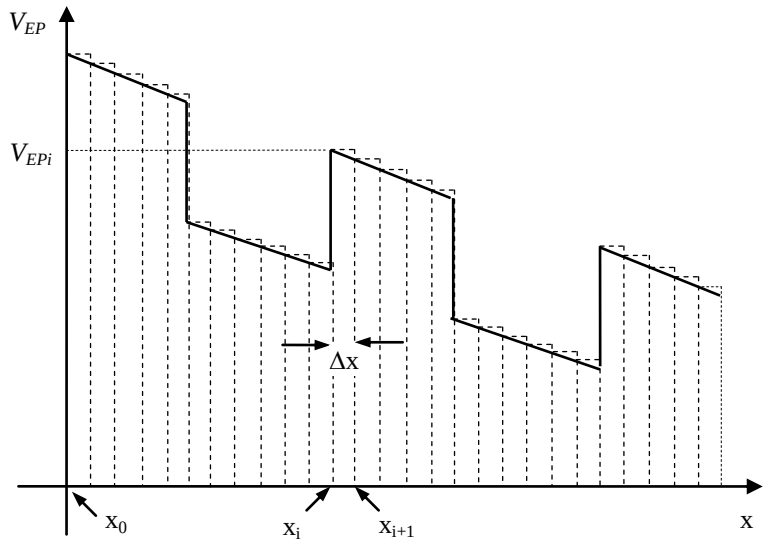


**Figure 6-5** Potential profile is discretised to perform matrix transfer method (refer to section 6.5).

With the stepwise approximation of the potential, the solution of the Schrödinger's equation separates into two cases. Inside the well, the total energy $E > V_{EPi}$, the solution is a simple combination of plane wave and it will oscillate [128]. This implies the kinetic energy $K > 0$. When $E < V_{EPi}$, the solution exponentially rises or decays, and that means $K < 0$ which is impossible in classical physics, however; in quantum physics, it can be explained by the phenomenon of tunneling [138]. The solution is [128]

$$\varphi_i(x) = \begin{cases} A_{WFi}\sin(\alpha_{WFi}x) + B_{WFi}\cos(\alpha_{WFi}x) & E > V_{EPi} \\ A_{WFi}\exp(\beta_{WFi}x) + B_{WFi}\exp(-\beta_{WFi}x) & E < V_{EPi} \end{cases} \tag{6-42}$$

Where $\alpha_{WFi}$ and $\beta_{WFi}$ are both real and are given by $\alpha_{WFi} = \sqrt{\frac{2m_i^*}{\hbar^2}(E - V_{EPi})}$,

$\beta_{WFi} = \sqrt{\frac{2m_i^*}{\hbar^2}(V_{EPi} - E)}$. Eq.(6-42) is the actual Schrödinger's equation solved in the MQW-EAM model.

The electron effective mass $m^*$ is a material property dependent parameter. In the model, the carrier effective mass of material $In_{1-x}Ga_xAs$ and $In_{1-x}Ga_xAs_yP_{1-y}$ can be estimated by mathematical description in Eq.(6-43) and Eq.(6-44) respectively[139],

$$m_{InGaAs} = xm_{GaAs} + (1-x)m_{InAs} \quad (6\text{-}43)$$

$$m_{InGaAsP} = xym_{GaAs} + x(1-y)m_{GaP} + (1-x)ym_{InAs} + (1-x)(1-y)m_{InP} \quad (6\text{-}44)$$

The effective mass values for the alloy GaAs, GaP, InAs, InP are listed in Table 6-1 [139].

| Effective mass | | | | |
|---|---|---|---|---|
| | GaAs | GaP | InAs | InP |
| $m_e^*$ | 0.067 | 0.17 | 0.023 | 0.08 |
| $m_{lh}^*$ | 0.074 | 0.14 | 0.027 | 0.089 |
| $m_{hh}^*$ | 0.62 | 0.79 | 0.6 | 0.85 |

**Table 6-1** Effective mass of electron, light hole and heavy holes

Generally speaking the effective mass equation gives a quite accurate approximation of the wavefunction in the quantum wells offering some justifications for switching the free electron mass to effective mass in the Schrödinger's equation.

### 6.4.4 Normalization of Wavefunction

A full solution of the Schrödinger's equation requires a calculation of the amplitude factors $A_{WFi}$ and $B_{WFi}$ in Eq.(6-42). The actual amplitude factors can be obtained by noting that $\psi_i(x)\psi_i^*(x)dx$ is the probability of finding a particle (e.g. an electron) between $x$ and $x + dx$. Therefore, for quantisation in one dimension the integral $\int_{-\infty}^{\infty} \psi_i(x)\psi_i^*(x)dx$ must equal unity. Fulfilling this requirement is known as normalisation. The normalized wavefunction for $\varphi_i(x)$ can be obtained by using the following formula

$$\psi_i(x) = \frac{\varphi_i(x)}{\sqrt{C_{IC}}} \tag{6-45}$$

where $C_{IC}$ is the integration constant and can be calculated from $\int \varphi_i(x)\varphi_i^*(x)dV = C_{IC}$. $C_{IC}$ has the unit metre (m).

Only the normalized wavefunction can be used to calculate the carrier concentration in the well by using Eq. (6-3) and Eq. (6-4).

### 6.4.5 Boundary Conditions

Under equilibrium conditions, the boundary conditions of the Schrödinger's equation for a quantum well inside MQW device are that the wavefunction and its first-order derivative are both zero at the extreme ends of the solution domain. Therefore, the barriers need to be wide enough in order to prevent the wavefunctions from adjacent potential wells from overlapping in the barriers.

The condition $\psi \to 0$ at both end of the solution domain cannot be met in a biased quantum well.

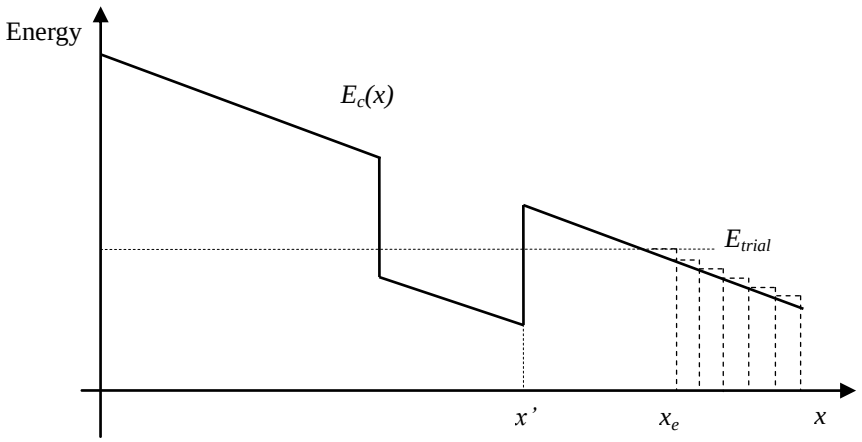


**Figure 6-5** Biased QW Potential profile with trial eigenenergy.

This is because there is always a point $x_e$ (shown in Fig. 6-5) where the trial value of the eigen energy $E_{trial} \geq E_c(x)$ . When this happens, $E > V_{EP}(x)$ and the form of the wavefunction becomes

$$\psi_i(x) = A_{WFi}\sin(\alpha_{WFi}x) + B_{WFi}\cos(\alpha_{WFi}x) \tag{6-46}$$

which is the oscillatory for all $x > x_e$. There $\psi_i(x)$ can never tend to zero as $x \to \infty$. The boundary condition $\psi_i \to 0$ at $x \to \infty$ needs to be replaced with

$\psi_i \to 0$ at $x = x_e$. This is quite a good approximation if $x_e - x'$ is large.

Next, at the interfaces between the barriers and the wells, the wavefunction and its first-order derivative must be continuous, requiring,

$$\psi_i(x)\big|_{x=x_i} = \psi_{i+1}(x)\big|_{x=x_{i+1}} \tag{6-47}$$

$$\frac{1}{m_i^*}\frac{d\psi_i}{dx}\bigg|_{x=x_i} = \frac{1}{m_{i+1}^*}\frac{d\psi_{i+1}}{dx}\bigg|_{x=x_{i+1}} \tag{6-48}$$

## 6.5 Numerical Methods for Solving One-Dimensional Schrödinger's Equation

### 6.5.1 Eigen-State Energy Searching and Bisection Method

The purpose of solving the Schrödinger's equation is to find approximate values of the sets of eigen energy $E_i$ and wavefunctions $\psi_i$ with sufficient accuracy to obtain reliable values of the two-dimensional electron and hole densities from Eq. (6-3) and Eq.(6-4). These can be obtained by noting that bounded wavefunction (i.e. $\psi_i(x) \to 0$ as $x_i \to \pm\infty$) can only occur when $E = E_i$. In other words, the total energy can be used as a search parameter.

Starting with the conduction band with no electric field applied, the barriers on both side of the well are of equal height. The first step is to obtain the number of the confined particle states in the well. This can be obtained by inputting into the numerical solving the maximum energy that can exist in the well. The maximum energy is a bit smaller than the top of the barriers. That is because the wavefunction should exponentially decay to zero in the extreme ends of the barrier. According to Eq. (6-42), the real eigen-state energy should be smaller than the barrier energy. The number of eigen-state energy is then determined by counting the number of the zero crossings that exist in the calculated wavefunction, as shown in Fig.6-6,

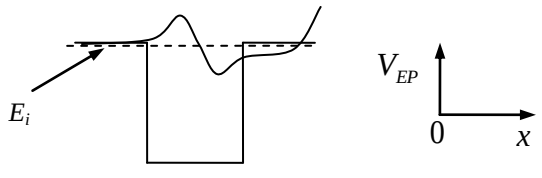


**Figure 6-6** An example of calculating number of eigen-state energy at the maximum energy.

There are two zero crossings in this example, indicating that in this well, there will be two eigen-state energies (two modes). The next step is to search for the approximate range for each eigen-state energy. If the energy is larger than the lowest energy eigen-state, the number of zero crossings is one (Fig.6-7(b)). If the energy is smaller than the eigen-state energy, there is no zero crossing (Fig.6-7(c)). In both cases, the wavefunction diverges from zero, however; as $x \to \infty$, the behaviour of the wavefunction differs and the two trial values of the eigen-energy bracket the exact value, one trial value being higher, the other lower.

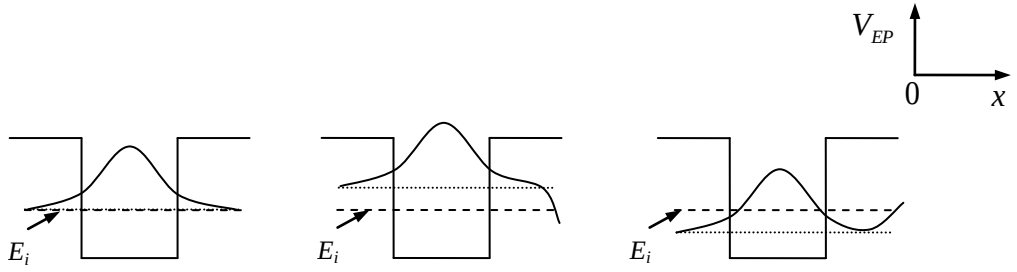


**Figure 6-7** Wavefunction for different energy (a) real eigen-state energy (b) trial energy > real eigen-state energy (c) trial energy < real eigen-state energy.

Successive improvements in the trial value of the eigen-energy can be made by using $E_{trial} = \frac{1}{2}\left(E_{upper} + E_{lower}\right)$ and updating $E_{upper}$ or $E_{lower}$ depending on the number of zero crossings in the trial wavefunction obtained by $E_{trial}$. Now, let $E_{lower}$ be equal to $E_{higher}$ for the next higher eigen-energy in the quantum well, and the new $E_{higher}$ produces a wavefunction with two nodes in order to bracket the next higher eigen-energy. This procedure is repeated until the last mode.

When an electric field is applied to the well, the same method can still be applied, but one detail needs to be changed. That is the calculation of zero crossing should not include the ones that is outside the quantum well as shown in the Fig.6-8.

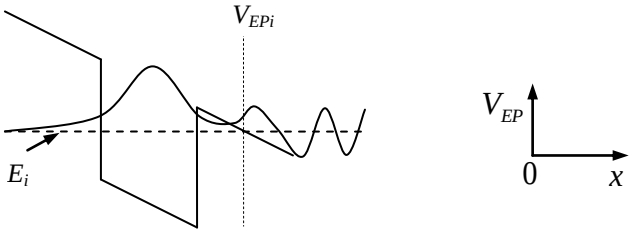


**Figure 6-8** Wavefunction becomes unbound when an electric field is applied to a potential well.

Now the wavefunction is unbound on the lower potential side of the barrier and an oscillatory solution is obtained to the Schrödinger's equation. The correct solutions are now obtained by neglecting the zero crossings when $V_{EPi} < E_i$. An EAM operates by optical absorption between the ground state eigen energies of the valance band and conduction band potential wells. These energy levels tend to be deeply confined in their respective potential wells.

For the valance band, the sign of potential profile is negative. In order to simplify the calculation, the same calculation method can be applied to the valance band, however; the potential profile needs to be modified by taking the absolute value of its original value and then flipping the value to the other side, as shown in Fig.6-9. Then the eigen-state $\psi_i$ that is obtained by this method needs to be flipped back when the calculation is over, in order to obtain the correct result. This calculation method is valid and correct, because the Schrödinger's equation represents the behaviour of a particle inside its respective well.

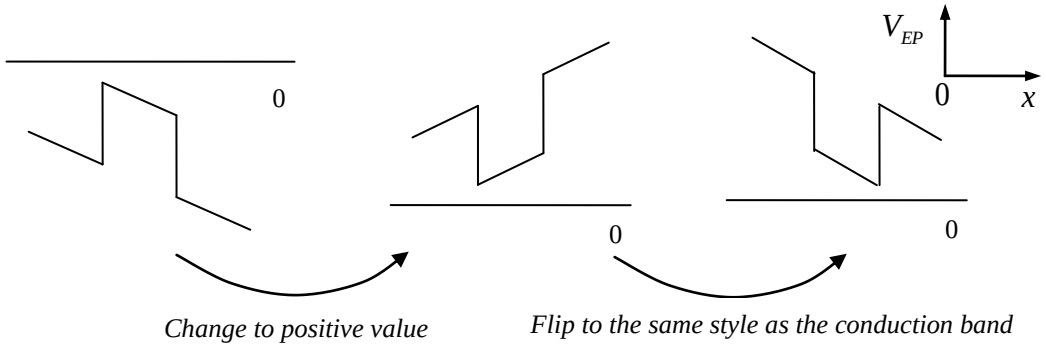


**Figure 6-9** Modification of valance band.

### 6.5.2 Coefficients Calculation and Transfer Matrix

The coefficients $A_{WFi}$ and $B_{WFi}$ in Eq. (6-42) can be obtained by using the boundary conditions and the transfer matrix. For example, at interface between layer $i$ and $i+1$in Fig. 6-10,

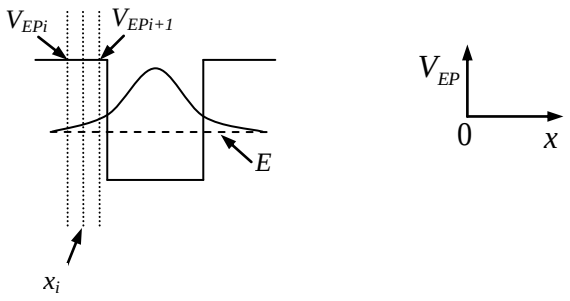

**Figure 6-10** An example to apply transfer matrix to Schrödinger's equation.

The Eq. (6-42) under the case of $E < V_{EPi}$ with boundary condition Eq.(6-47) and Eq.(6-48) have the relationship,

$$\begin{aligned} &A_{WFi}\exp(\beta_{WFi}x_i)+B_{WFi}\exp(-\beta_{WFi}x_i) \\ &=A_{WFi+1}\exp(\beta_{WFi+1}x_i)+B_{WFi}\exp(-\beta_{WFi+1}x_i) \end{aligned} \tag{6-49}$$

$$\begin{aligned} &\frac{A_{WFi}\beta_{WFi}\exp(\beta_{WFi}x_i)}{m_i^*}-\frac{B_{WFi}\beta_{WFi}\exp(-\beta_{WFi}x_i)}{m_i^*} \\ &=\frac{A_{WFi+1}\beta_{WFi+1}\exp(\beta_{WFi+1}x_i)}{m_{i+1}^*}-\frac{B_{WFi}\beta_{WFi+1}\exp(-\beta_{WFi+1}x_i)}{m_{i+1}^*} \end{aligned} \tag{6-50}$$

Rearranging Eq.(6-49) and Eq.(6-50) into the matrix format yields

$$\begin{aligned} &\begin{bmatrix} \exp(\beta_{WFi}x_i) & \exp(-\beta_{WFi}x_i) \\ \exp(\beta_{WFi}x_i) & -\exp(-\beta_{WFi}x_i) \end{bmatrix}\begin{bmatrix} A_{WFi} \\ B_{WFi} \end{bmatrix} \\ &=\begin{bmatrix} \exp(\beta_{WFi+1}x_i) & \exp(-\beta_{WFi+1}x_i) \\ \dfrac{\beta_{WFi+1}m_i^*}{\beta_{WFi}m_{i+1}^*}\exp(\beta_{WFi+1}x_i) & -\dfrac{\beta_{WFi+1}m_i^*}{\beta_{WFi}m_{i+1}^*}\exp(-\beta_{WFi+1}x_i) \end{bmatrix}\begin{bmatrix} A_{WFi+1} \\ B_{WFi+1} \end{bmatrix} \end{aligned}$$

Let

$$M_i=\begin{bmatrix} \exp(\beta_{WFi}x_i) & \exp(-\beta_{WFi}x_i) \\ \exp(\beta_{WFi}x_i) & -\exp(-\beta_{WFi}x_i) \end{bmatrix}\begin{bmatrix} \exp(\beta_{WFi+1}x_i) & \exp(-\beta_{WFi+1}x_i) \\ \dfrac{\beta_{WFi+1}m_i^*}{\beta_{WFi}m_{i+1}^*}\exp(\beta_{WFi+1}x_i) & -\dfrac{\beta_{WFi+1}m_i^*}{\beta_{WFi}m_{i+1}^*}\exp(-\beta_{WFi+1}x_i) \end{bmatrix}^{-1}$$

Then the $M_i$ can be recombined into,

$$M_i=\begin{bmatrix} \dfrac{1}{2}\left(1+\dfrac{\beta_{WFi}m_{i+1}^*}{\beta_{WFi+1}m_i^*}\right)\exp\left[(\beta_{WFi}-\beta_{WFi+1})x_i\right] & \dfrac{1}{2}\left(1-\dfrac{\beta_{WFi}m_{i+1}^*}{\beta_{WFi+1}m_i^*}\right)\exp\left[(-\beta_{WFi}-\beta_{WFi+1})x_i\right] \\ \dfrac{1}{2}\left(1-\dfrac{\beta_{WFi}m_{i+1}^*}{\beta_{WFi+1}m_i^*}\right)\exp\left[(\beta_{WFi}+\beta_{WFi+1})x_i\right] & \dfrac{1}{2}\left(1+\dfrac{\beta_{WFi}m_{i+1}^*}{\beta_{WFi+1}m_i^*}\right)\exp\left[(-\beta_{WFi}+\beta_{WFi+1})x_i\right] \end{bmatrix}$$

This method simplifies as,

$$\begin{pmatrix} A_{WFi+1} \\ B_{WFi+1} \end{pmatrix}=M_i\begin{pmatrix} A_{WFi} \\ B_{WFi} \end{pmatrix} \tag{6-51}$$

The equations for $M_i$ under different conditions are given in appendix II.

## 6.6 Self-Consistent Solution of the Coupled Poisson's – Schrödinger's Equations

The solution of the Poisson's-Schrödinger's equations needs to be self-consistent.

An estimate of the potential profile is obtained by the solving of Poisson's equation without considering the carrier density inside the quantum well in the first iteration. This potential profile is then used in Schrodinger's equation to calculate the carrier densities inside the quantum well. The resulting carrier densities inside the well are now added to the charge density that was calculated from the old potential profile and used to re-solve Poisson's equation. The Schrödinger's equation is solved again if the difference between the new potential at each point and the old value is large, or the procedure is halted if the difference is small. The resulting potential profile and charge distribution is then calculated self-consistently. The procedure is illustrated in Fig.6-11.

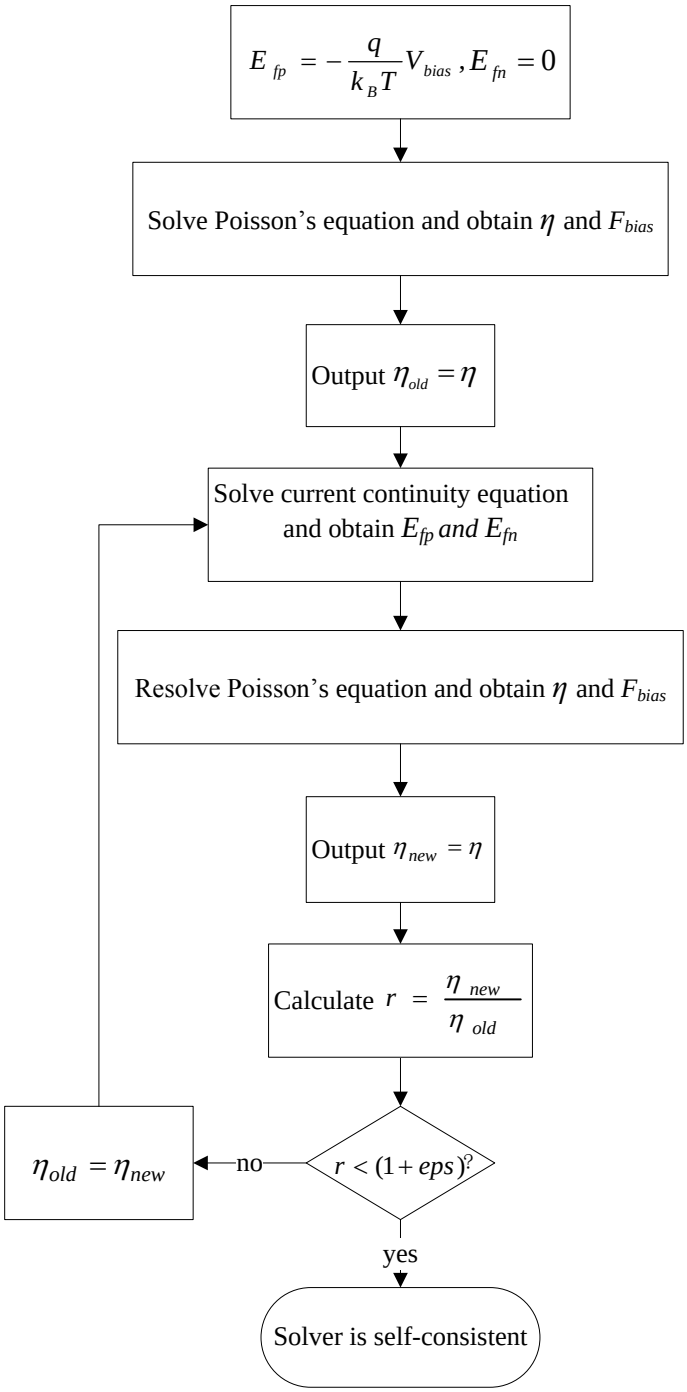


**Figure 6-11** Flow chart of self-consistent calculation for Poisson's-Schrödinger's equations.

## 6.7 Self-Consistent Solutions of the Current-Poisson's-Schrödinger's Equations

Beside both calculations of the current-Poisson's equations and the Poisson's-Schrödinger's equations having to be self-consistent, the calculation of current-Poisson's-Schrödinger's equations (C-P-S equations) must be self-consistent as well. The flow chart of Self-Consistent Solutions of the C-P-S Equations is shown in Fig.6-12.

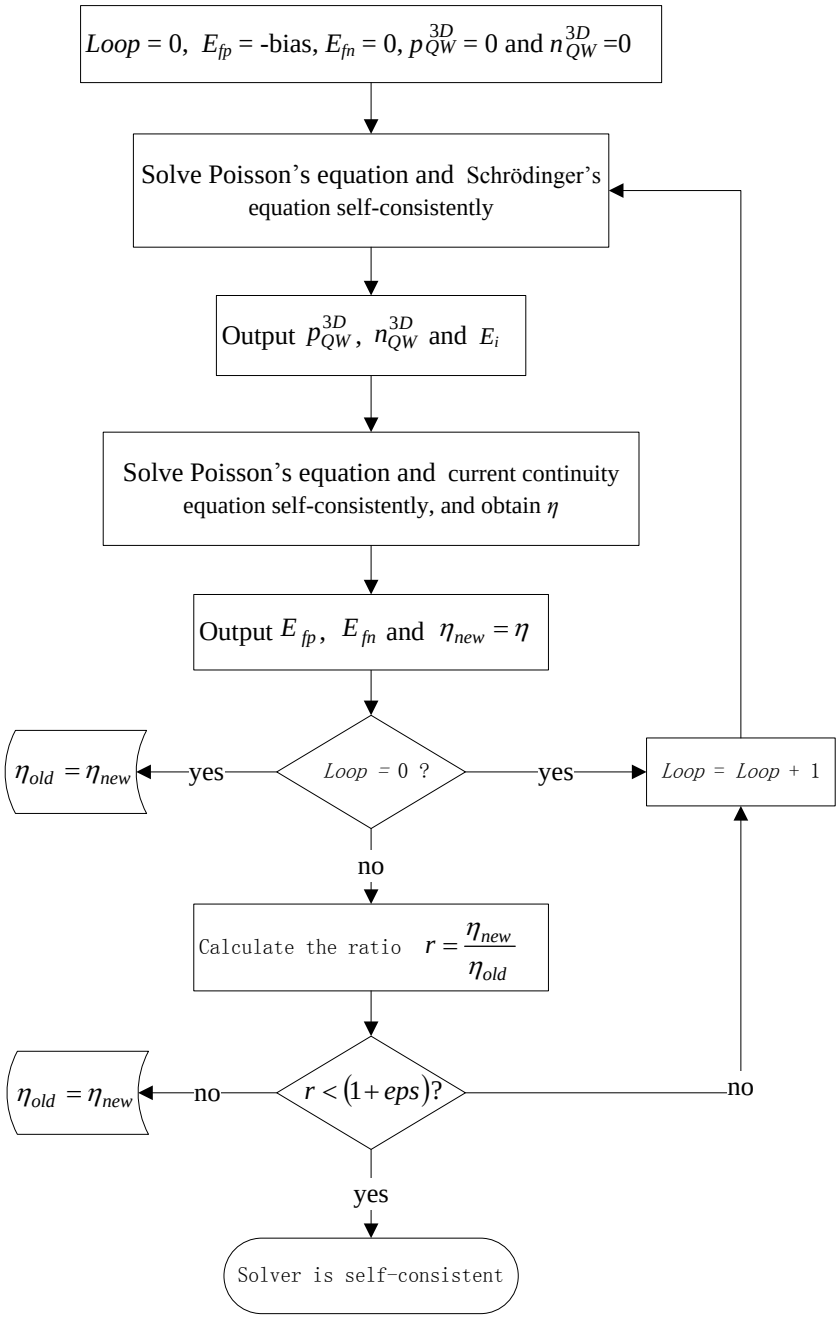


**Figure 6-12** Flow chart of self-consistent calculation for C-P-S equation.

Before starting the calculation of Poisson's equation, the quasi Fermi level $E_{fp} = -\frac{k_B T}{q} V_{bias}$, $E_{fn} = 0$ and the carrier concentrations in the quantum well $p_{QW}^{3D} = 0$, $n_{QW}^{3D} = 0$ are assumed. With the above assumptions, the self-consistent calculation of the Poisson's-Schrödinger's equations will update the values of carriers density in the well and Eigen-state energy. The eigen value $E_i$ is for the estimation of current exchange between quantum well and barrier. All of these values help to obtain the potential profile $\eta_{new}$ and the value of quasi-Fermi

level $E_{fp}$ and $E_{fn}$ from the self-consistent calculation of the current-Poisson's equations. If the loop only runs for the first time (*Loop* = 0), the value of potential profile $\eta_{new}$ will be saved into a value named as $\eta_{old}$. Then *Loop* is increased by 1, and the Poisson's-Schrödinger's equations and current-Poisson's equations are re-solved with the updated values. The calculation will come to the point that the reduced potential $\eta_{new}$ is obtained once more. This time the value of $\eta_{new}$ is compared with the value of $\eta_{old}$, if their ratio is very close to 1, then the self-consistent calculation of C-P-S equation is converged, otherwise the value of $\eta_{new}$ will be stored in $\eta_{old}$ again, and the calculation cycles once more.

In order to have a clear understanding on the modelling of MQW-EAM, a flow chart is needed again and it is shown in Fig.6-13.

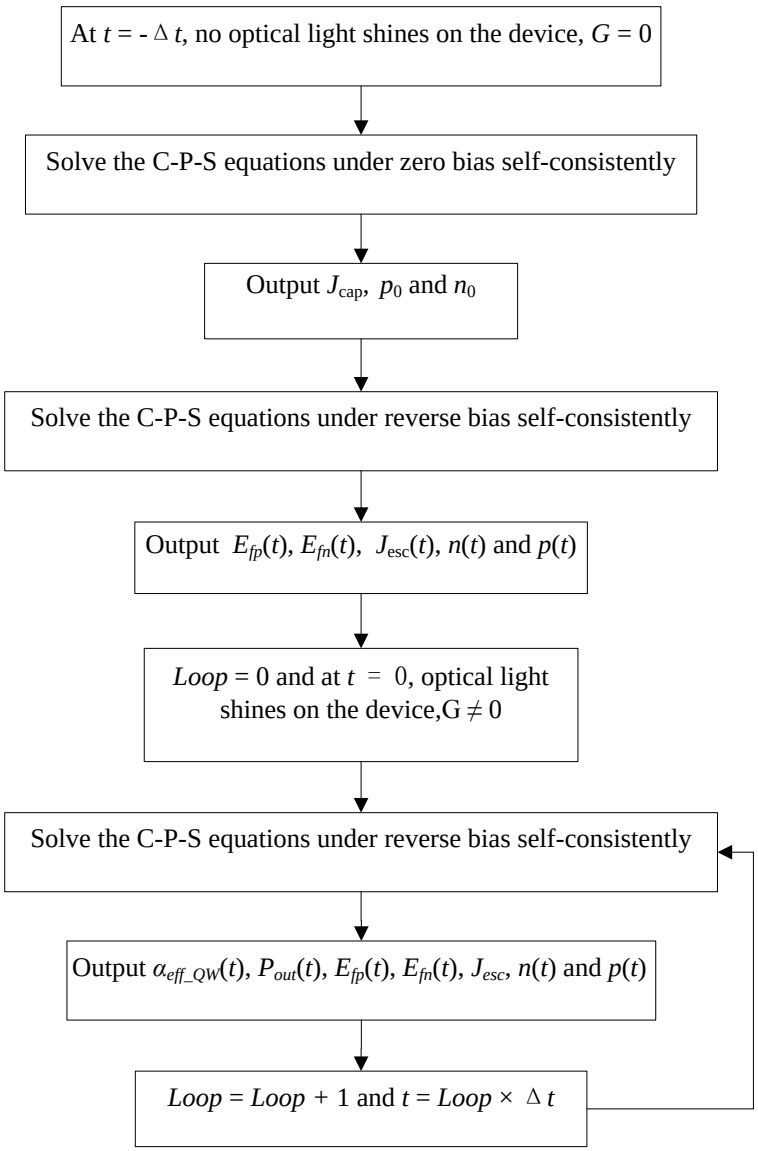


**Figure 6-13** Flow chart of solving MQW-EAM model.

At time $t$ = 0, assume no optical light shines on the device, which means the generation term is zero. Firstly, the C-P-S equations are calculated under zero bias. Then the carrier concentration $p_0$, $n_0$ under zero bias and the capture current $J^{cap}_{h(e),QW}$ are calculated first. The C-P-S equations are calculated under reverse bias. The quasi-Fermi level $E_{fp}$, $E_{fn}$, the escape current $J^{esc}_{h(e),QW}$ and the carrier concentration under reverse bias $p(t = 0)$, $n(t = 0)$ can be estimated. All of the above outputs can be input parameters to calculate C-P-S equations when generation term is not zero at time $t = \Delta t$. The output light power $P_{out}(t)$ can be estimated when the C-P-S equations calculation is converged.

## 6.8 Summary

The Poisson equation and current continuity equation for quantum wells material are defined in this chapter. Both of the equations for bulk material are the same as in Chapter 5. The carrier distribution in the quantum wells that are estimated by the one-particle effective mass Schrödinger's equation were also introduced in this chapter. The reason for not using many-particle Schrödinger's equation for solving the MQW-EAM numerical model is because of its complexity. Boundary conditions for both the Poisson's equation and current continuity equation for the MQW-EAM were still the same as the PIN photodiode. The boundary conditions for the Schrödinger's equation were applied to the individual well in the MQW-EAM device. A special technique for estimating the carrier density in the quantum wells region is used for better approximation. The flow chart of the three equations self-consistent calculation and the flow chart of numerical solver for MQW-EAM device were shown and introduced in detail in this chapter.

# Chapter 7

## Simulation Results for PIN Photodiodes

## 7.1 Introduction

This chapter presents the detailed analysis performed on InP/InGaAs/InP PIN photodiodes. The developed numerical model can be applied to the mesa-type or planar type PIN photodiodes. Firstly, four different large signal time dependences of input light intensity modulation are considered. Those are square wave, sine wave, constant intensity wave and Gaussian light pulses. A sequence of Gaussian pulses has been applied to the device to investigate in depth the response of different device geometries. Various conditions including different I-layer width, applied bias, average input optical power, doping density and light input orientation have been applied to the model. The eye opening ratio and pulse spreading ratio are the two important parameters to judge whether large signal output current pulses are distinguishable and recognized. Both of them have been estimated over different pulse FWHM (full width half maximum) and pulse repetition frequency to define the bandwidth of the PIN photodiode. The eye opening ratio at repetition frequencies greater than the usual 3dB frequency has been investigated. This is of significant interest in digital telecommunications systems as it is shown here that identifiable pulses are still detected beyond the 3dB frequency limit. Below the 3dB point, for the same FWHM Gaussian pulses, the repetition time is limited by the pulse itself and the device. This will be discussed in section 7.3. After discussion of the results, conclusions are drawn at the end of the chapter. Throughout this chapter it is mostly assumed that a large optical power level is available prior to detection. Therefore, the analysis is a true large signal approach. Such high optical power levels could be possible if optical amplifiers are used prior to photo detection.

## 7.2 Different Input Light Testing

The modelled mesa-type device structure is shown in Fig.7-1. In Fig7-1, $L$ and $T$ represent the length and the thickness of device respectively, $W_I$ is the width of I-layer, $S_{absorp}$ is the absorption area for waveguide input light method and $S_{recep}$ is the reception area of device and is the absorption area for top-entry or sub-entry light input method.

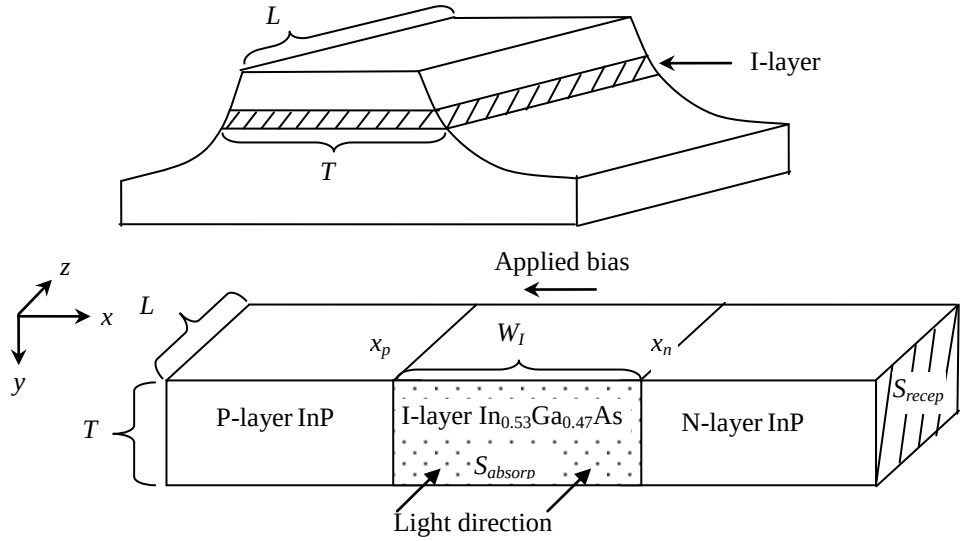


**Figure 7-1** The structure of PIN InP/InGaAs/InP photodiode.

For edge-coupled devices, the input light wave propagates along the *z*-axis. The generation term is defined as,

$$G(t) = \frac{\lambda P(t)\left[1 - e^{-\Gamma \alpha z}\right]}{hcS_{absorp}L_{dev}} \tag{7-1}$$

where $\alpha$ is the absorption coefficient and $\Gamma$ is the optical confinement factor. According to the generation equation, the generation term should exponentially decay along the *z*-axis. The numerical model for an edge-coupled PIN photodiode is a one dimensional model along the *x*-axis, i.e. orthogonal to the direction of light propagation. That means $z = L_{dev}$. Therefore the model over-estimates the effect of carrier photo-generation on the electrostatic potential and current flow in the *x*-axis direction. As such it represents a worst case in terms of effects of band-filling in the responsivity but neglects the effect of carrier diffusion along the *z*-axis direction which will influence, possibly slowing the photo response. For top-entry photo diode structures, the light path and the direction of current flow coincide and therefore any such problem is removed.

In order to test the accuracy of the model, the same type and same materials of PIN photodiode shown in Fig.7-1 and the material parameters list in the Table 7-1 are applied to our model with the 1mW input average power and 0.5 modulation depth under -3V applied bias. The comparison of output current under the continuous sine wave with Dentan's model is presented in Fig.7-2.

| | P-layer | I-layer | N-layer |
|---|---|---|---|
| Material | InP | $In_{0.53}Ga_{0.47}As$ | InP |
| Width(μm) | 0.5 | 1.5 | 0.5 |
| Doping($1/cm^3$) | $1\times10^{18}$ | $3\times10^{15}$ | $1\times10^{17}$ |
| Refractive index | 3.2026 | 3.7262 | 3.2026 |
| $D$ (μm) | | | 20 |
| $S_{recep}$ ($\mu m^2$) | | | 400 |

**Table 7-1** The simulation parameters for PIN photodiodes

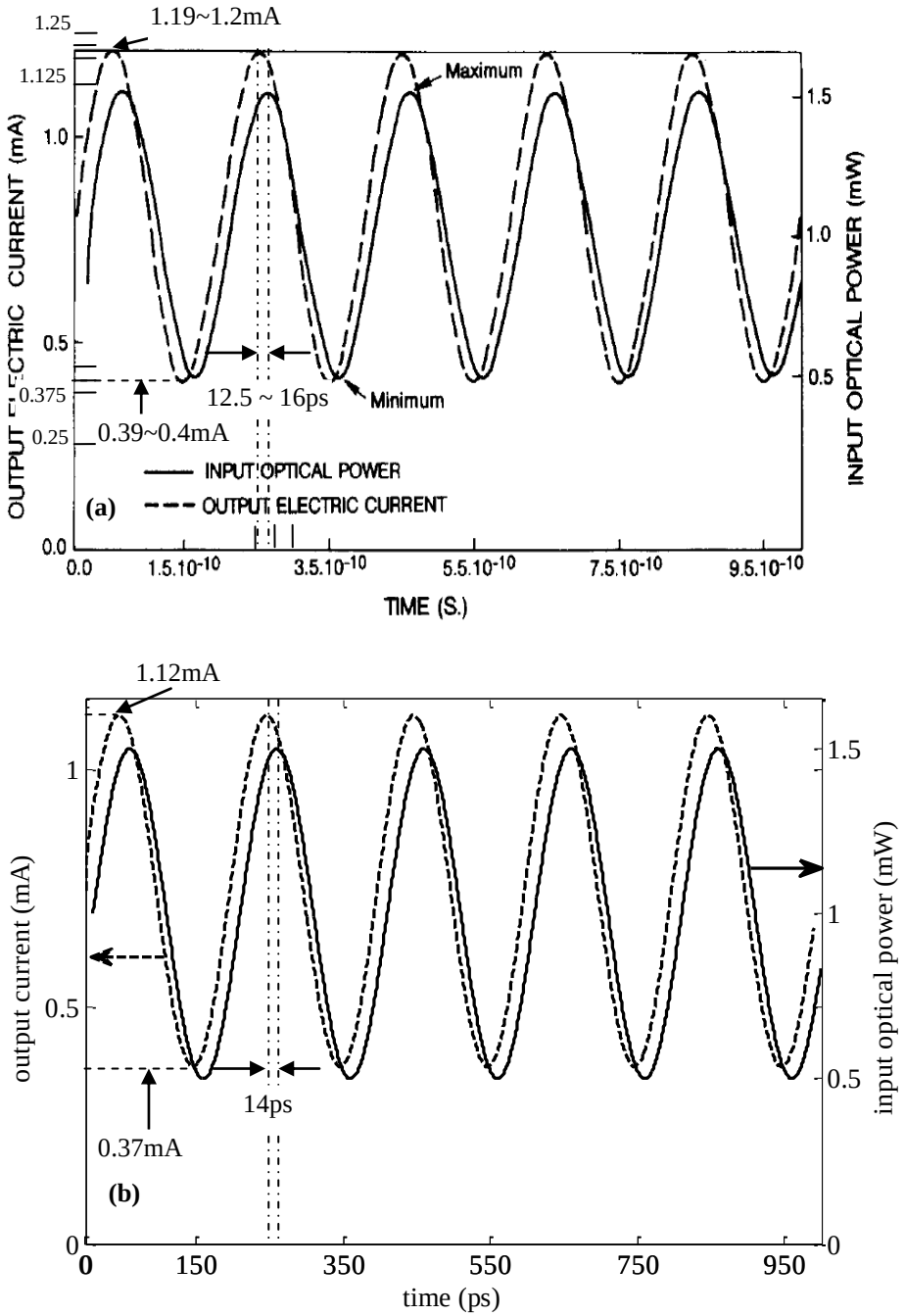


**Figure 7-2** Input continuous sine wave (solid line) with output current (dashed line) for top-entry $InP/In_{0.53}Ga_{0.47}As/InP$ PIN photodiode (specification in Table 7-1) with 1mW input average power and 0.5 modulation depth under -3V applied bias **(a)** result from Dentan's paper **(b)** result from the model.

The Fig.7-2(a) is quoted from Dentan's paper [10], and Fig.7-2(b) is the result from the model. Measuring the data in Fig.7-2(a), the phase shift in Dentan's result is around 12.5ps ~ 16ps and the depth of the current is about 0.79 ~ 0.81mA (the depth of the current is measure by the difference between peak and valley point of the current). For our model, as Fig. 7-2(b) shown, the current gives 14ps phase shift and 0.75mA depth of the current. The output current in Fig. 7-2 (a) and (b) has very close values in the depth of the current and the phase shift between the input optical signal and the resulting photocurrent. It proves the accuracy of the model. Dentan's model neglects the recombination term in the space and charge area and the thermionic current across the hetero-junction in the model. These are all included in our numerical model. That is probably the reason why the depth of current is slightly smaller than Dentan's model.

The model has been tested under different conditions. The reversed bias must be applied to the device, and the simulation parameters are listed in the Table 7-2.

| | P-layer | I-layer | N-layer |
|---|---|---|---|
| Material | InP | $In_{0.53}Ga_{0.47}As$ | InP |
| Width(μm) | 1 | 0.1~0.5 | 1 |
| Doping($1/cm^3$) | $1\times10^{18}$ | $3\times10^{15}$ | $1\times10^{18}$ |
| Refractive index | 3.2026 | 3.7262 | 3.2026 |
| $L$ (μm) | | | 25 |
| $T$ (μm) | | | 2 |
| $S_{recep}$ ($\mu m^2$) | | | 50 |

**Table 7-2** The simulation parameters for PIN photodiodes

For an edge-coupled photodiode, the waveguide confinement factor which appears in the generation term is calculated first for each structure. The Table 7-3 lists the calculated waveguide confinement factors for the different I-layer widths shown in Table 7-3. The program for calculating the one dimensional $E_s$ field in Eq.(4-11) and $H_s$ field in Eq.(4-14) were originally written by Qin Chen (Chinese Academy of Science).

| I-layer Width (μm) | 0.1 | 0.2 | 0.3 | 0.4 | 0.5 |
|---|---|---|---|---|---|
| Confinement factor | 0.1356 | 0.3467 | 0.5206 | 0.6411 | 0.7238 |

**Table 7-3** The simulation parameters for PIN photodiodes

### 7.2.1 Large Signal Square Wave, Sine Wave Intensity Modulation

The performance of the different photodiodes structures specified in the preceding section has been investigated under optical stimulation by optical pulses of various shapes. The considered pulse shapes are square wave, sine wave, Gaussian shaped pulses with different mark-space ratio. As a baseline for assessing the performance of the different photodiode structures, their response to a step change in the incident light level has also been modelled. With the listed parameters in Table 7-2 and Table 7-3, under -3V applied bias (reverse bias is always expressed as a negative voltage in this thesis), three different shapes of input light sequences have been tested in the model to obtain the output current. In each case, the photocurrent is compared to the incident light pulse. For the square wave the input light pulse sequence is defined as,

$$P(t) = \begin{cases} mP_0 & k\Delta t < t < (k+1)\Delta t \\ 0 & (k+1)\Delta t < t < (k+2)\Delta t \end{cases} \qquad k = 0,1,2...N \qquad (7\text{-}2)$$

where $m$ is the modulation index, $P_0$ is the input average optical power and $\Delta t$ is the time length shown in Fig.7-3. $m$ is assumed to be 1 in all following calculations. A sequence of three square waves and its output current is shown in Fig.7-3. When the pulse-on time and pulse-off time are equal and of 20ps duration, for the edge-coupled PIN photodiode with the specification given in Table 7-3 with an $In_{0.53}Ga_{0.47}As$ I-layer width of 0.5μm. The intensity of the light pulse was 1mW.

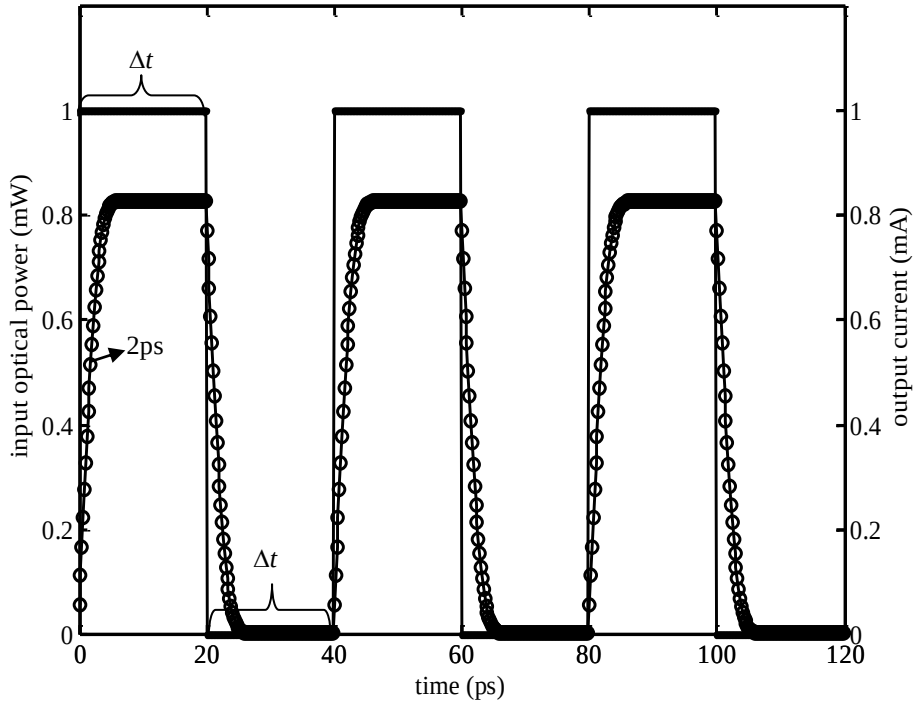


**Figure 7-3** Input square wave optical light (dot line) with output current (circle line): ($t_{on}$ = $t_{off}$ =Δ$t$= 20ps) for edge-coupled InP/$In_{0.53}Ga_{0.47}As$/InP PIN photodiode (specification in Table 7-2, 0.5μm I-layer width is chosen) with 1mW input average power and 1.0 modulation depth under -3V applied bias.

In Fig.7-3, the shape of output current pulse is not a perfect square wave. This is because the photon generated carriers will take some time to travel through the I-layer (the transit time effect). This leads to a time delay of the output current pulse with respect to the incident optical pulse sequence. When the current reaches its 3dB point, the corresponding time is the time delay of current pulse. The current time delay in this case is around 2ps.

Under the same parameters, when the input optical light changes to constant intensity light, the constant intensity light is defined as,

$$P(t) = mP_0 \tag{7-3}$$

The input light with output current is shown in Fig.7-4. For a constant light intensity of 1mW switched on at $t$ = 0ps.

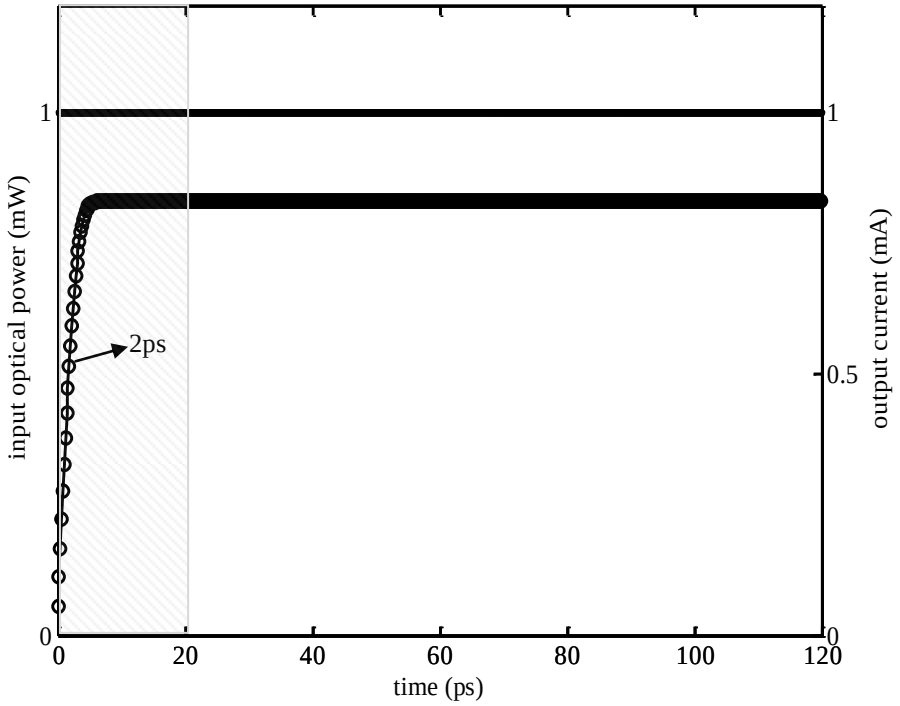


**Figure 7-4** Input constant intensity light (dot line) with output current (circle line): ($t_{tot}$ = 120ps) for edge-coupled InP/$In_{0.53}Ga_{0.47}As$/InP PIN photodiode (specification in Table 7-2, 0.5μm I-layer width is chosen) with 1mW input average power and 1.0 modulation depth under -3V applied bias.

The photo current pulse has a finite rise time for the same reason as mentioned above. The on-time delay is also defined by the time taken for the photocurrent to reach the 3dB current point. For this constant intensity light case, the time delay stays the same at ~2ps. For the optical intensity level considered the rise and fall times of the photocurrent are pretty much equal. A close examination of the first 20ps of the time interval (indicated as grey area in Fig.7-4), for different I-layer width in the range 0.1μm~0.5μm is shown in Fig.7-5.

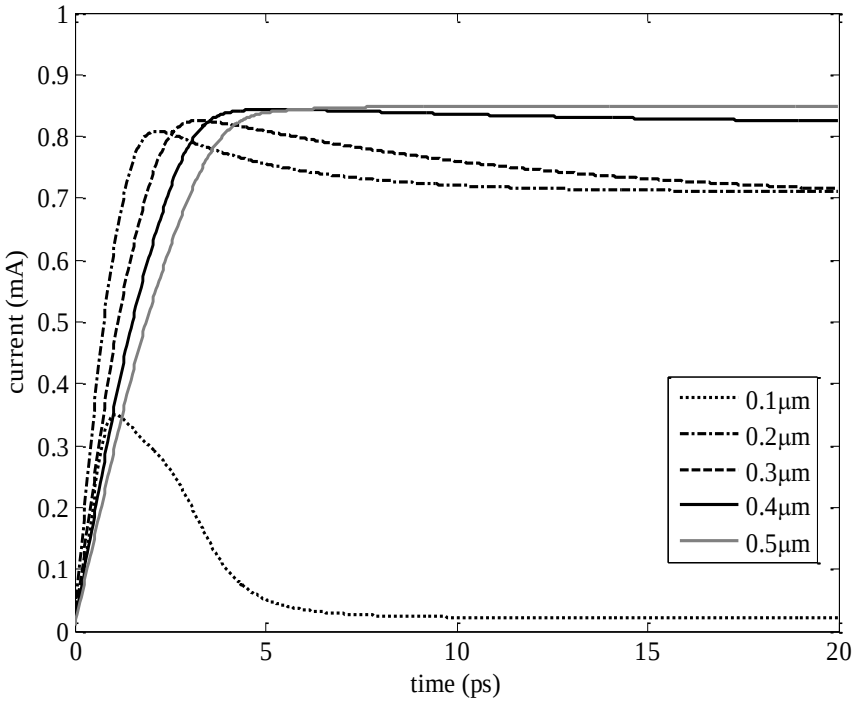


**Figure 7-5** The first 20ps of the time dependence of the photocurrent induced in an InP/$In_{0.53}Ga_{0.47}As$/InP PIN photodiode by a step change in the input optical power from 0 to 1mW with I-layer width as parameter. The rest of the PIN photodiode specification is given in Table 7-2, 0.5μm I-layer width and 1.0 modulation depth are chosen and the applied bias is -3V.

In Fig.7-5, the shorter the I-layer is, the faster the response is. This is because the carriers need a shorter time to travel through thinner I-layers. The output current starts falling once it reaches its peak value. This drop in the photocurrent becomes more and more obvious when the I-layer width reduced. When I-layer width is 0.1μm, the current reduces to nearly zero after 5ps. This is because of the absorption saturation effect in the device.

Again, under the same condition, another form of time dependent input optical light has been applied to the device, namely a sinusoid. This allows a direct and obvious relationship between the large signal photodiode response and signal frequency to be ascertained. A common sine wave usually contains positive and negative values, however; the input optical power should be greater than zero. Therefore, the sine wave power modulation has be defined as,

$$P(t) = mP_0 \sin(2\pi ft)^2 \tag{7-4}$$

The input sine wave optical signal and corresponding output current is shown in Fig.7-6.

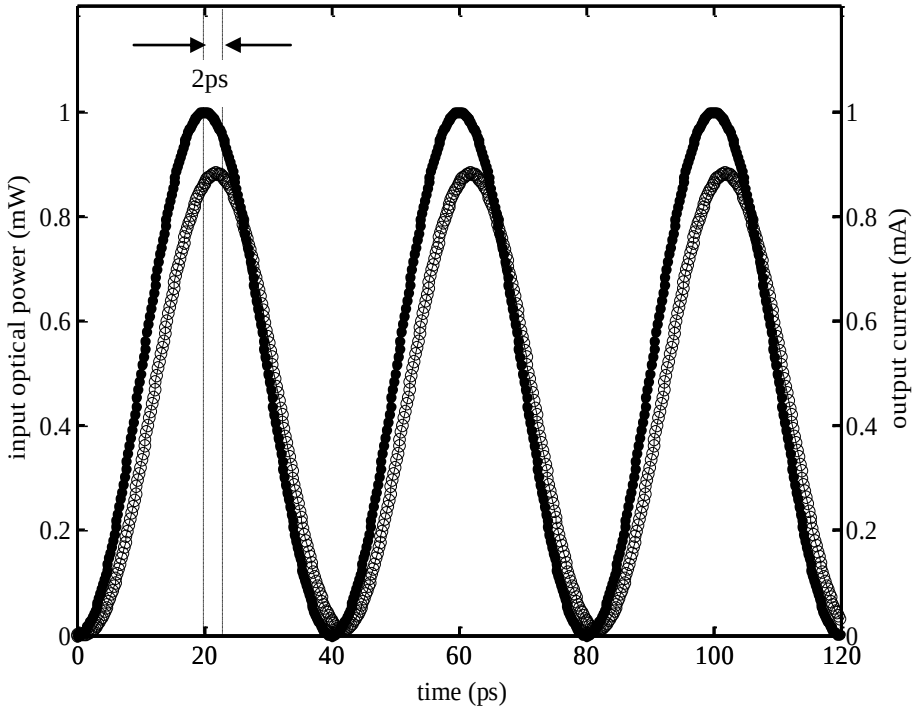


**Figure 7-6** Input Sine wave optical light (dot line) with output current (circle line): ($t_{on}$ = $t_{off}$ = 20ps) for edge-coupled InP/$In_{0.53}Ga_{0.47}As$/InP PIN photodiode (specification in Table 7-2, 0.5μm I-layer width is chosen) with 1mW input average power and 1.0 modulation depth under -3V applied bias.

The time delay for the output current is estimated by the difference between the corresponding time of peak values for input optical power and output current. The time delay under this definition is ~2ps.

In each case, the output current has around 2ps time delay with respect to the input optical power. The time delay is due to the time taken for photo-generated carriers to transit through the 0.5μm I-layer.

### 7.2.2 Gaussian Pulse

Gaussian shaped pulses are widely used to simulate the response of active devices and optical fibres in digital communications systems. There are also other reasons why Gaussian pulses are chosen as the input light pulses. The Gaussian pulse is a good model for output modes of many important lasers, and has less diffraction than others from laser [140]. A Gaussian pulse train can be varied by the full width at half maximum (FWHM) of the signal, the repetition rate of the sequence of Gaussian pulses and the number of pulses in the sequence. This enables the PIN photodiode properties to be investigated more fully by varying the input Gaussian

wave properties. The Gaussian wave can be described as,

$$P(t) = mP_0 e^{-\frac{t^2}{2\sigma^2}} \tag{7-5}$$

where $\sigma$ is the standard deviation and controls the width for Gaussian wave. It is related to FWHM via,

$$FHWM = 2\sqrt{2\ln 2}\sigma \tag{7-6}$$

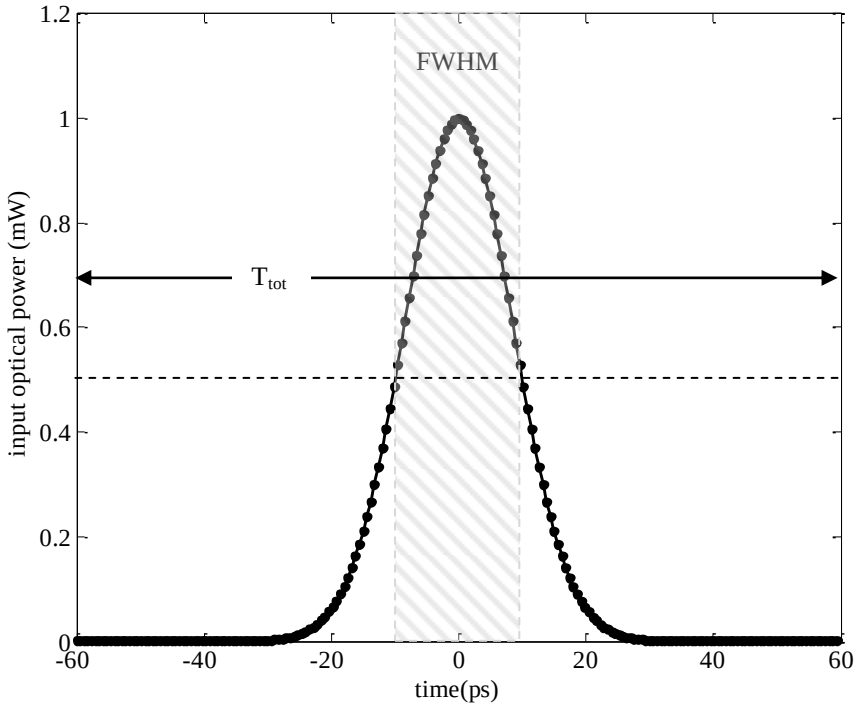


**Figure 7-7** The example of input Gaussian wave FWHM = 20ps.

The time length of a single Gaussian pulse is infinity by definition, and it is impossible to realize in the program. Therefore, to allow adequate simulation of the influence of FWHM and repetition rate on device response, a reasonable time range $T_{tot}$ (also named as total time) is defined as shown in Fig.7-7 and mathematically described by,

$$T_{tot} = 6 \times FWHM \tag{7-7}$$

Fig. 7-8(a) and Fig. 7-8(b) show calculated photocurrent response for the edge-coupled PIN photodiode structure defined in Table 7-2 with an $In_{0.53}Ga_{0.47}As$ I-layer width of 0.5μm. The intensity of the light pulse was 1mW and the device at a reverse bias of -3V for a FWHM of 20ps and 2ps.

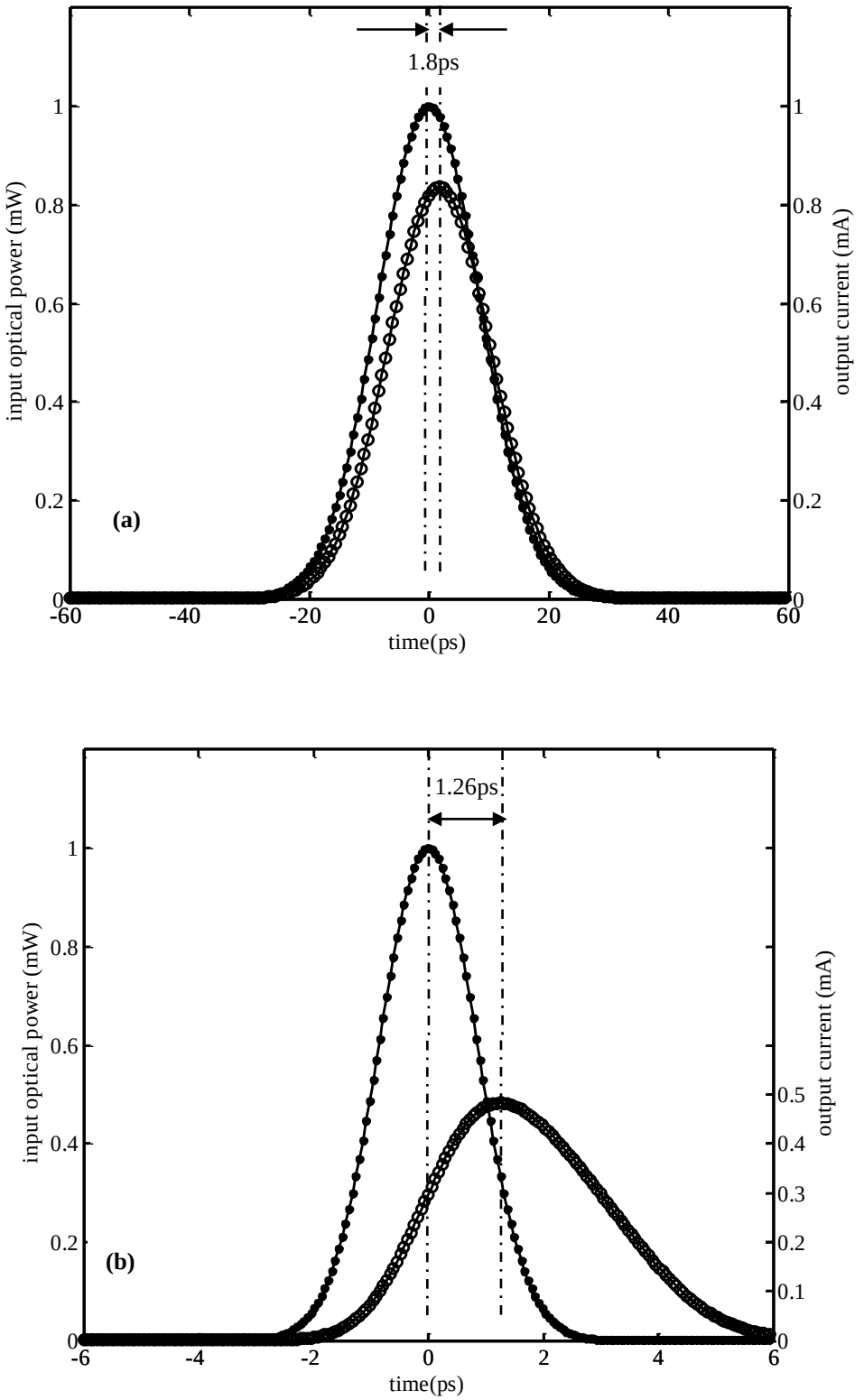


**Figure 7-8** Input Gaussian pulse (dot line) for (a) FWHM = 20ps (b) FWHM =2ps with output current (circle line) for edge-coupled InP/$In_{0.53}Ga_{0.47}As$/InP PIN photodiode (specification in Table 7-2, 0.5μm I-layer width is chosen) with 1mW input average power and 1.0 modulation depth under -3V applied bias.

The peak output current decreases as the FWHM of the Gaussian wave becomes

smaller. The smaller FWHM of Gaussian wave means the time of absorption for the material is shorter. This leads to the output current peak reducing quite simply because fewer photons are absorbed. It is easily noticed that the peak current time delay with respect to the peak in the optical pulse in Fig.7-8(b) is not the same as that in Fig.7-8(a). This does not mean the transit time has decreased as the FWHM becomes shorter. It occurs because the input optical pulse nearly reduces to zero at 2ps in Fig.7-8(b), and it forces the output current pulse to start rolling off before carriers have completed travelling through the device. Therefore, the time difference between the input power peak and output current peak can no longer be accurately described by the transit time in this case. In this regime the time variation of the stimulus is shorter than escape time from I-layer. This is the reason why the fall time of the current pulse relative to its rise-time is broadened when FWHM is reduced from 20ps to 2ps. This is referred to as the "tail problem" throughout the thesis.

If a sequence of Gaussian pulses illuminates the device, a repetition time $t_{rep}$ (as shown in Fig.7-9) must be defined where $t_{rep}$ is the time difference between the peak of power and the nearby peak of power.

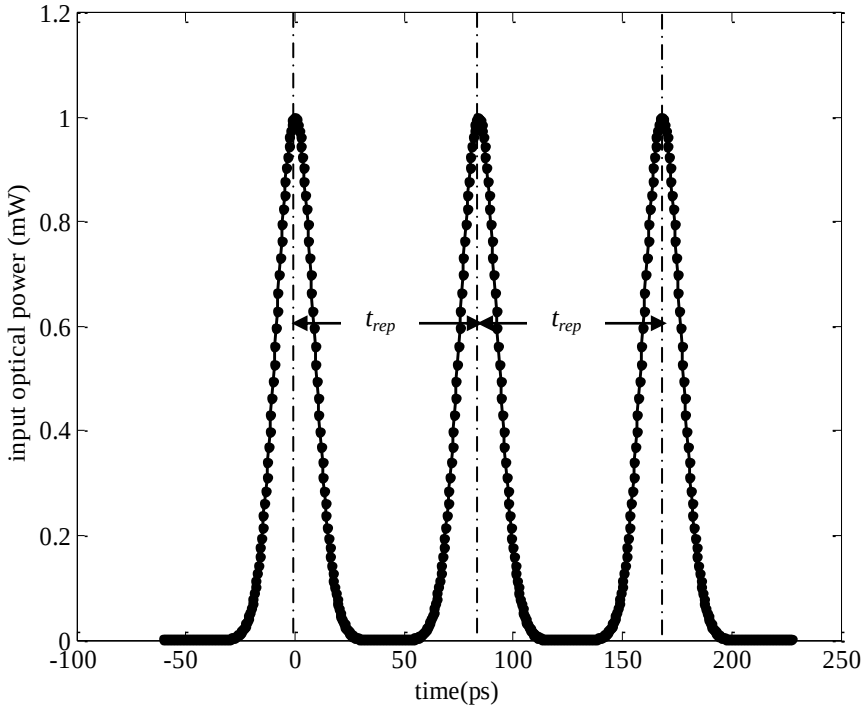


**Figure 7-9** The example of a sequence of Gaussian wave with 20ps FWHM and 84ps repetition time.

To relate $t_{rep}$ with $t_{tot}$ (the effective sum of the rise and fall times of the Gaussian pulses) a dimensionless number is defined such that,

$$t_{rep} = r_{rep} \times T_{tot} \tag{7-8}$$

where $r_{rep}$ is the repetition ratio and it is a dimensionless number. If $r_{rep}$ < 0.6, the sequential Gaussian pulses will overlap with non-zero illumination occurring in the interval between the pulses. To minimize the effect of pulse overlap a maximum repetition rate dependent on the FWHM must be used in the simulations. A value $r_{rep} = 0.7$ has been chosen, therefore with Eq. (7-6) the repetition time becomes,

$$t_{rep} = 4.2FWHM \tag{7-9}$$

The repetition frequency is now defined as,

$$f_{rep} = \frac{1}{t_{rep}} \tag{7-10}$$

An example of a train of three Gaussian light pulses with 20ps FWHM and 84ps repetition time (12GHz repetition frequency) and output current is shown in Fig. 7-10, with an $In_{0.53}Ga_{0.47}As$ I-layer width of 0.5μm. The intensity of the light pulse was 1mW and the device at a reverse bias of -3V.

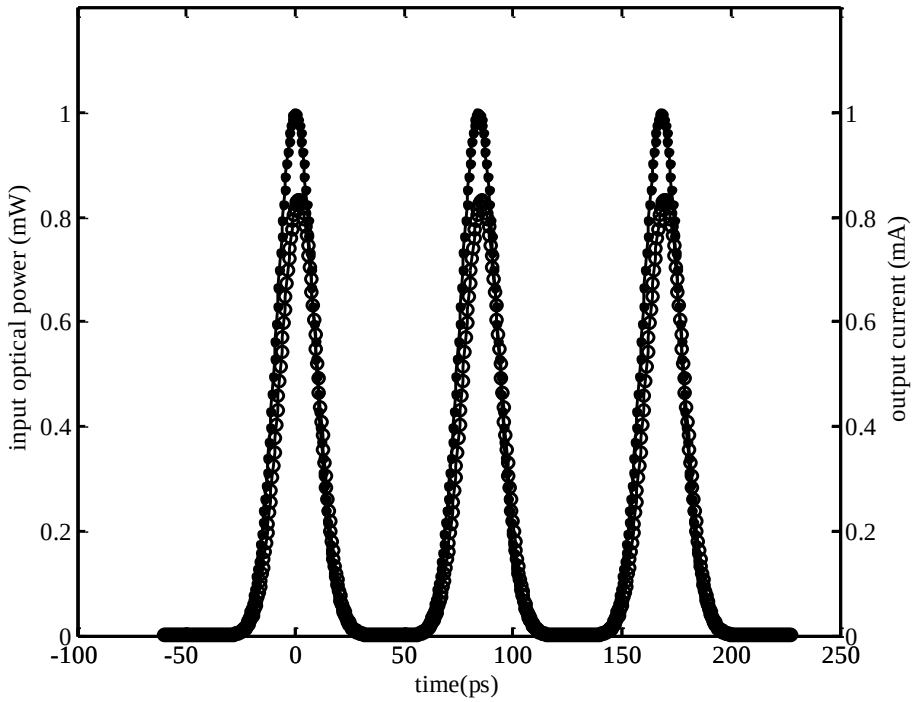


**Figure 7-10** Gaussian input optical wave (dot) with FWHM 20ps and 84ps repetition time and output current (circle) for edge-coupled InP/$In_{0.53}Ga_{0.47}As$/InP PIN photodiode (specification in Table 7-2, 0.5μm I-layer width is chosen) with 1mW input average power and 1.0 modulation depth under -3V applied bias.

The output current wave follows the trace of the incident Gaussian pulses very well, however; if the Gaussian optical pulses train has a FWHM of just 2ps and with 8.4ps (4.2FWHM) with the repetition time for the same parameters as before, the output current takes the form shown in Fig.7-11. The corresponding repetition frequency is 119Gb/s.

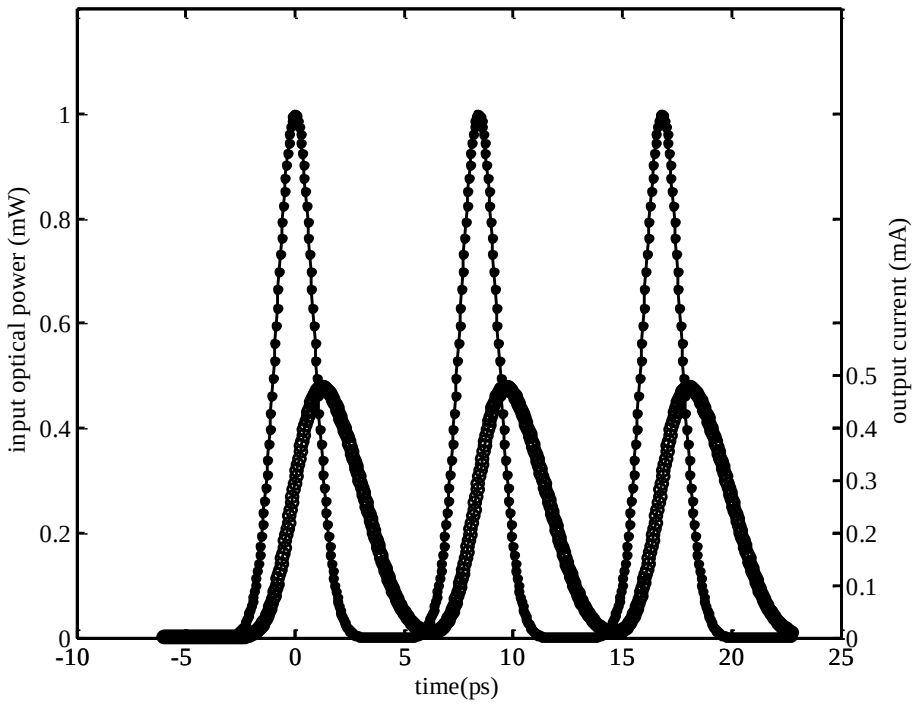


**Figure 7-11** Gaussian input optical wave (dot) with FWHM 2ps and 8.4ps repetition time and output current (circle) for edge-coupled InP/$In_{0.53}Ga_{0.47}As$/InP PIN photodiode (specification in Table 7-2, 0.5μm I-layer width is chosen) with 1mW input average power and 1.0 modulation depth under -3V applied bias.

As mentioned above, the individual output current pulse is now measurably broadened compared with the optical pulses when the FWHM of the Gaussian wave is 2ps. Because of the "tail problem" mentioned above, with the longer fall-time relative to the rise-time being the main cause in the degradation of the pulse shape. Even so with 6.4ps interval between the 3dB points of the falling and rising edges of adjacent pulses there is sufficient time for the photo-generated charge to escape the photodiode for distinguishable current pulses to be observed, this is for a pulse repetition frequency of nearly 120GHz. Further, the results show that the response of hetero-junction InP/InGaAs/InP photodiodes is fall-time limited and not rise-time limited.

The above results demonstrate there is scope to optimize mark-space ratio of a train

of optical pulses to achieve ultra-high bandwidth photo-detection in conventional photodiode structures. The optimization of repetition time on the fixed FWHM value is analysed in the following section. This will be considered in detail later on for both top entry and edge-coupled photodiode structure. Further, it should be noted that edge-coupled PIN photodiodes with I-layer width of 0.3 μm have been demonstrated in practice [141], however; this practical study considered only their small signal bandwidth performance.

## 7.3 Effect of Parameters Values on 3dB Bandwidth of InP/InGaAs/InP Photodiode

In this section, a more detailed analysis of the response of InP/InGaAs/InP double hetero-junction photodiodes to optical stimulation by a Gaussian pulse train is carried out under different conditions that include the effects of applied bias, input average power, input light method, I-layer width and doping density.

As a starting point the eye opening ratios that are defined in Eq.(2-4a) and Eq.(2-4b) in Chapter 2 are repeated here,

$$\Re_{eye\_A} = \frac{A_c}{A_p} \tag{7-11a}$$

$$\Re_{eye\_H} = \frac{H_c}{H_p} \tag{7-12b}$$

where $A_c$ and $A_p$ are indicated as the cross-hatched area in Fig.7-12, and $H_c$ and $H_p$ are the height also shown in Fig.7-12.

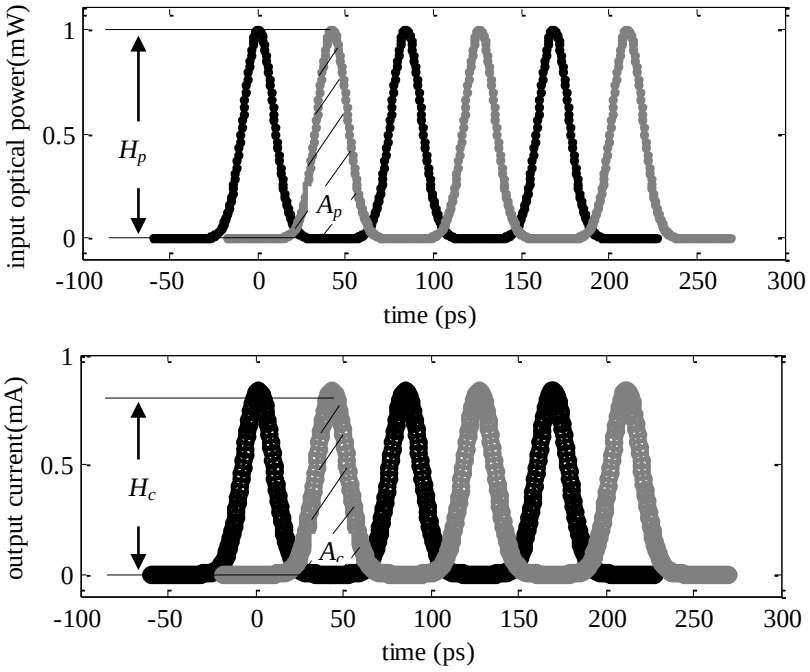


**Figure 7-12** The eye diagrams for input optical power (20ps FWHM and 84ps) and output power for edge-coupled InP/$In_{0.53}Ga_{0.47}As$/InP PIN photodiode (specification in Table 7-2, 0.5μm I-layer width is chosen) with 1mW input average power and 1.0 modulation depth under -3V applied bias.

If the parameters listed in table 7-2 with the FWHM of Gaussian wave varied from 600ps to 0.5ps and the repetition rate $t_{rep} = 4.2FWHM$ under -3V applied bias and an I-layer width of 0.5$\mu$m, the eye opening ratio for both area ($\Re_{eye\_A}$) and height ($\Re_{eye\_H}$)over repetition frequency is shown in Fig.7-13.

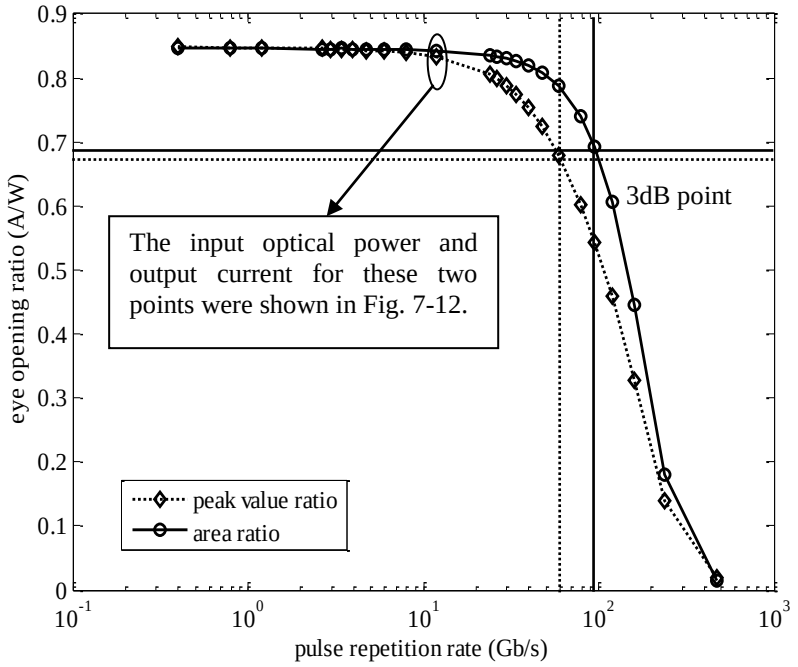


**Figure 7-13** Height and area eye opening ratio over repetition frequency for edge-coupled InP/$In_{0.53}Ga_{0.47}As$/InP PIN photodiode (specification in Table 7-2, 0.5μm I-layer width is chosen) with 1mW input average power and 1.0 modulation depth under -3V applied bias.

Fig. 7-13 shows that $\Re_{eye\_H}$ reduces faster than $\Re_{eye\_A}$, that means the bandwidth defined in term of the eye opening area ratio $\Re_{eye\_A}$ is higher. The reason is that the Gaussian input light wave with small FWHM will generate a relatively broader output pulse, as shown in Fig.7-11. The eye opening area ratio $\Re_{eye\_A}$ will include the effect of broadening. That is the reason that $\Re_{eye\_A}$ rolls off more slowly than $\Re_{eye\_H}$. The effect of broadening will be analysed separately by the spreading ratio, a factor that will be introduced later. Therefore, as the worst case $\Re_{eye\_H}$ is chosen for analysing the output current signal. Thus, the use of Eq.(2-4b) provides a robust analysis of the large signal photodiode performance at frequencies higher than 3dB bandwidth limit. Below the 3dB bandwidth limit of the $\Re_{eye\_H}$ parameter, the Gaussian input light is able to have distinguishable output current pulse when the repetition time increased. That is the reason why the analysis of fixed FWHM with different repetition time under 3dB point is important. More detail of this analysis will be presented in sections 7.2.1 to 7.2.5.

As the FWHM of the input light pulses gets shorter, the output current pulses are both reduced in height and broadened. The perfect input Gaussian wave should be

symmetric around $t = t_0$, however; as shown in Fig7.14, the output current pulses are not symmetric, and the roll off part of the signal is longer than the rise time of the signal.

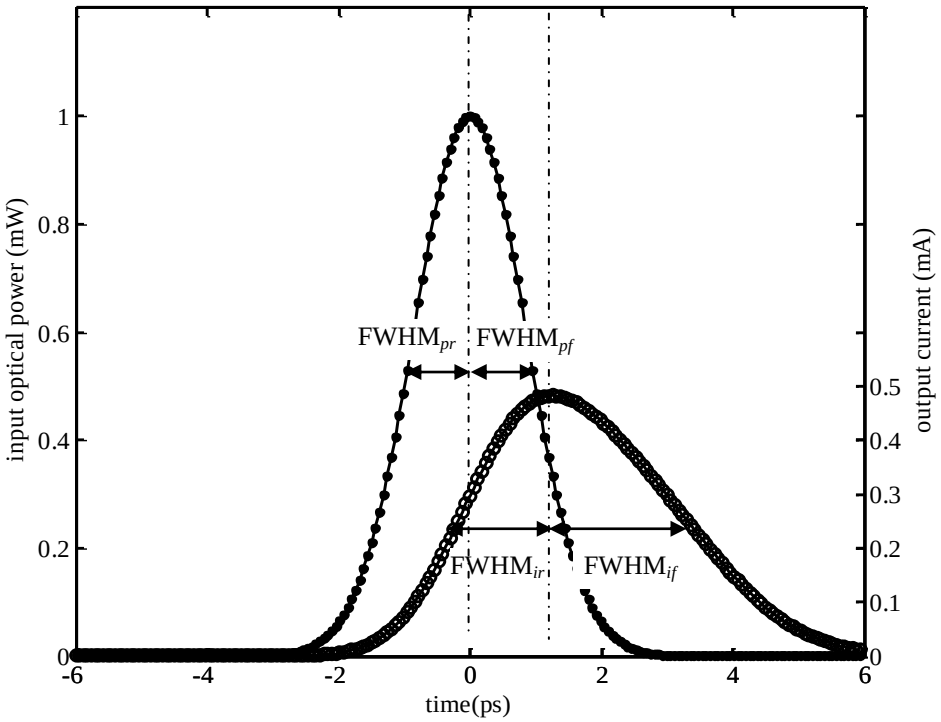


**Figure 7-14** Input Gaussian pulse (dot line) (FWHM = 2ps) with output current (circles) for edge-coupled InP/$In_{0.53}Ga_{0.47}As$/InP PIN photodiode (specification in Table 7-2, 0.5μm I-layer width is chosen) with 1mW input average power and 1.0 modulation depth under -3V applied bias.

Therefore, for good understanding of the current pulse broadening problem over the pulse repetition rate, a rise time spreading ratio $R_{sr}$ and fall time spreading ratio $R_{sf}$ are defined as,

$$R_{sr} = \frac{FWHM_{pr}}{FWHM_{ir}} \tag{7-13a}$$

$$R_{sf} = \frac{FWHM_{pf}}{FWHM_{if}} \tag{7-13b}$$

where $FWHM_{pr} = FWHM_{pf}$. Computed values $R_{sr}$ and $R_{sf}$ are shown in Fig7-14 for different light pulse FWHM and hence repetition frequencies as defined in Eq.(7-10). The FWHM of Gaussian light wave was varied from 600ps to 0.5ps and the PIN photodiode conformed to the parameters in Table 7-2, under -3V applied bias and a 0.5 μm I-layer was assumed.

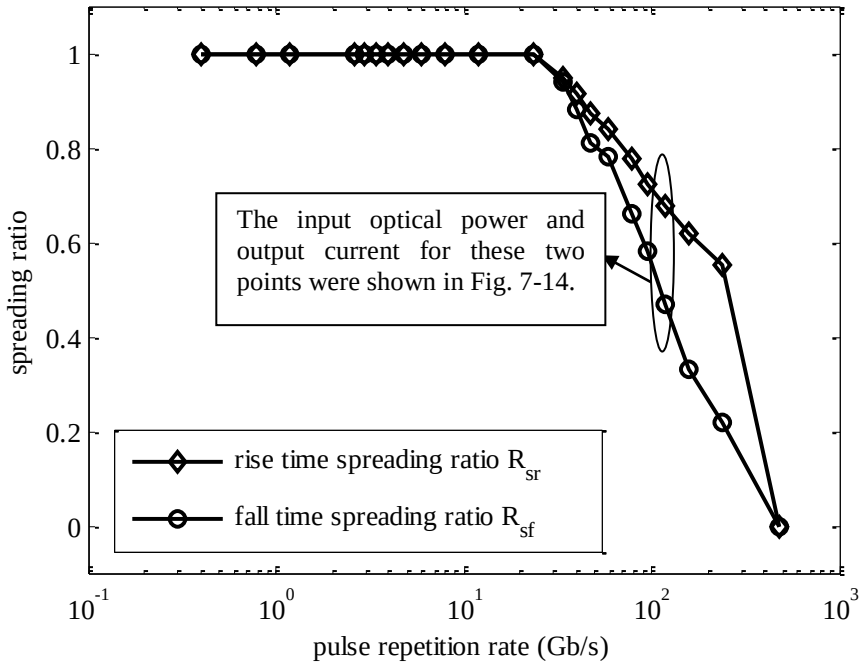


**Figure 7-15** Spreading ratios for rise time and fall time of output current over repetition frequency for edge-coupled InP/$In_{0.53}Ga_{0.47}As$/InP PIN photodiode (specification in Table 7-2, 0.5μm I-layer width is chosen) with 1mW input average power and 1.0 modulation depth under -3V applied bias.

In Fig. 7-15, $R_{sr}$ and $R_{sf}$ have very similar values at large FWHM, i.e. at lower repetition frequency. The spreading problem is more serious on the right hand side of output signal. That is due to the "tail problem" that has been mention in the section 7.2.2 in this Chapter. To unify the spreading ratio results under different condition, a total spreading ratio is defined as,

$$R_S = R_{sr} + R_{sf} \tag{7-14}$$

The value of $R_s$ should still be in the range of $0 < R_s \leq 1$.

### 7.3.1 Analysis of Eye Opening Ratio with Different I-Layer Width

This section describes the effect when the I-layer width is varied in a basic edge-coupled device structure from 0.1μm to 0.5μm, with other parameters as listed in Table 7-2. With the confinement factors listed in Table 7-3, if a FWHM 20ps of Gaussian input wave of peak intensity 1mW is applied to the device, then the output current for I-layer widths of 0.1, 0.2 ad 0.4μm are as shown in Fig.7-16.

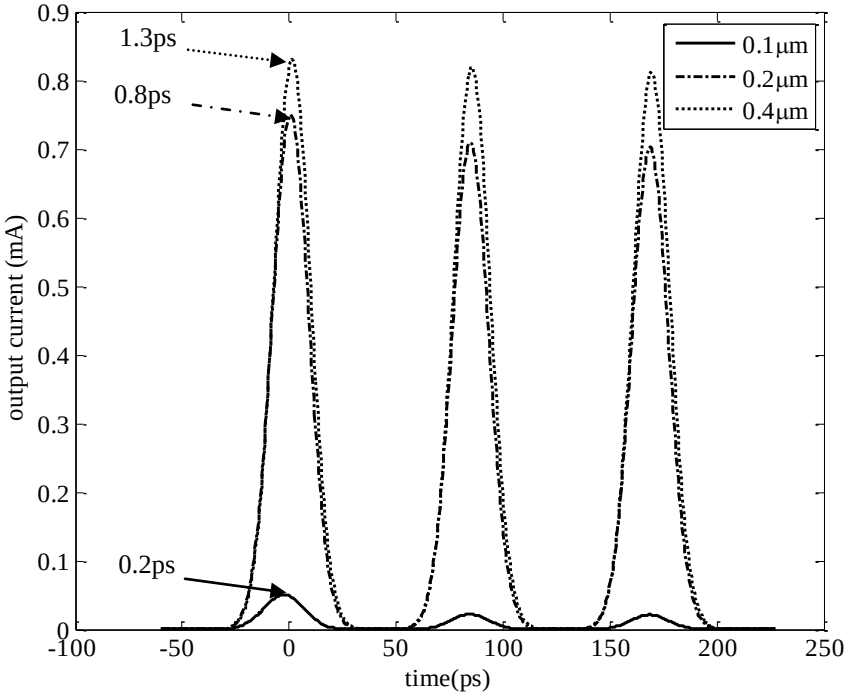


**Figure 7-16** Output current under different I-layer width 0.1μm, 0.2μm and 0.4 μm for edge-coupled InP/$In_{0.53}Ga_{0.47}As$/InP PIN photodiode (specification in Table 7-2) with 1mW input average power and 1.0 modulation depth under -3V applied bias.

As the I-layer width is increased, the time delays of peak current increase as well. This is due to the carriers taking a longer time to travel through the wider I-layer, however; if the I-layer width is too narrow, such as the 0.1μm shown in Fig.7-16, the volume of the absorption layer is too small to achieve an acceptable responsivity. This can only be compensated by higher light intensity. Specifically, the predicted output current is more than 20 times smaller compared with the 0.2μm I-layer width. The major cause of the 20-fold reduction in responsivity is the over two times reduction in optical confinement factor (refer to Table 7-3) as the I-layer width is reduced from 0.2μm to 0.1μm, noting that the optical power is lost from the propagating light wave as

$$P(x) = P_0 \exp\left(-\Gamma \alpha_{eff} z\right) \tag{7-15}$$

For $t_{rep} = 4.2FWHM$ , the eye opening ratio for FWHM values between 0.5ps to 600ps versus repetition frequency for different intrinsic layer width is shown in Fig.7-17. In the Fig.7-17, different styled lines indicate the 3dB point for corresponding I-layer width. It is easy to notice that the bandwidth reduces as the I-layer width increases from 0.2μm to 0.5μm. The 0.2μm I-layer width has the widest bandwidth but the peak eye opening ratio at the lower frequency is the

smallest. This is because the reduced optical confinement factor (refer to Table7-3) causes a decrement in the maximum responsivity.

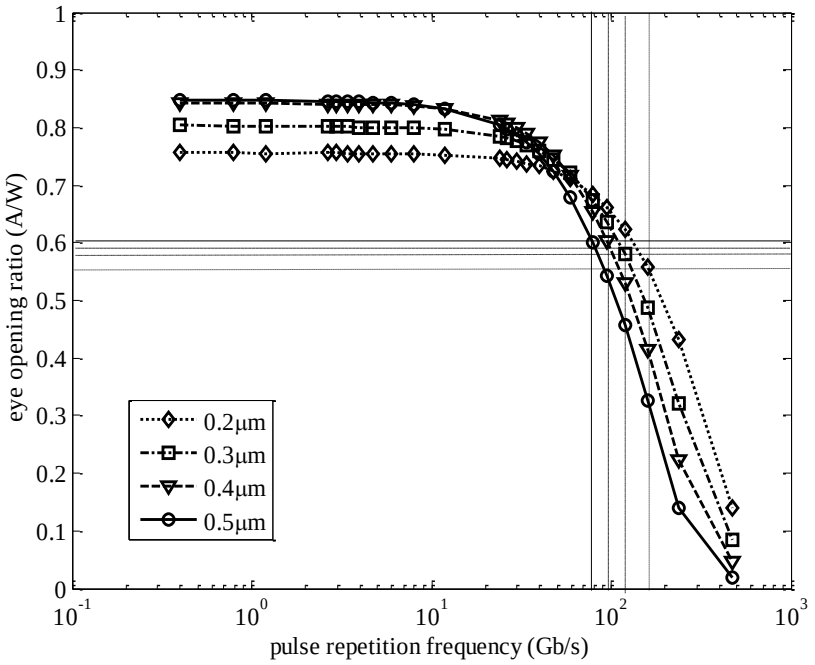


**Figure 7-17** Eye opening ratio over repetition frequency for different I-layer width for edge-coupled InP/$In_{0.53}Ga_{0.47}As$/InP PIN photodiodes (specification in Table 7-2) with 1mW input average power and 1.0 modulation depth under -3V applied bias.

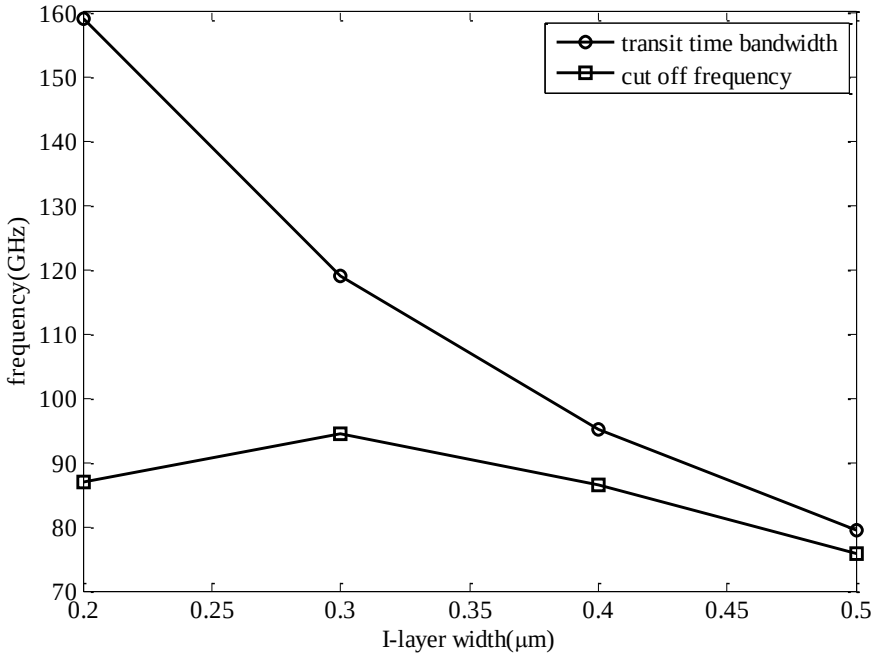


**Figure 7-18** The transit time bandwidth and cut-off frequency against different I-layer width for edge-coupled InP/$In_{0.53}Ga_{0.47}As$/InP PIN photodiode (specification in Table 7-2) with 1mW input average power and 1.0 modulation depth under -3V applied bias.

The cut-off frequency which includes the RC time constant effect in addition to the transit time effect as defined by Eq.(2-5), for different I- layer widths is shown in

Fig. 7-18. The cut-off frequency initially increases as the I-layer width is decreased to 0.3μm. This is because the carriers need less time to travel through the I-layer when the I-layer width is decreased. Therefore, the cut-off frequency is mainly affected by the transit time effect for I-layer width ≥0.3μm, however; when the I-layer width is reduced to 0.2μm, the cut-off frequency is reduced. The reason is that when the I-layer is too thin, the capacitance of the device is increased and the RC time constant starts to dominate the cut-off frequency. Then the cut-off frequency falls. Therefore, the I-layer width 0.3μm is the best choice for large cut-off frequency.

The pulse spreading ratio defined by Eq.(7-14) over the repetition frequency is shown in Fig. 7-19.

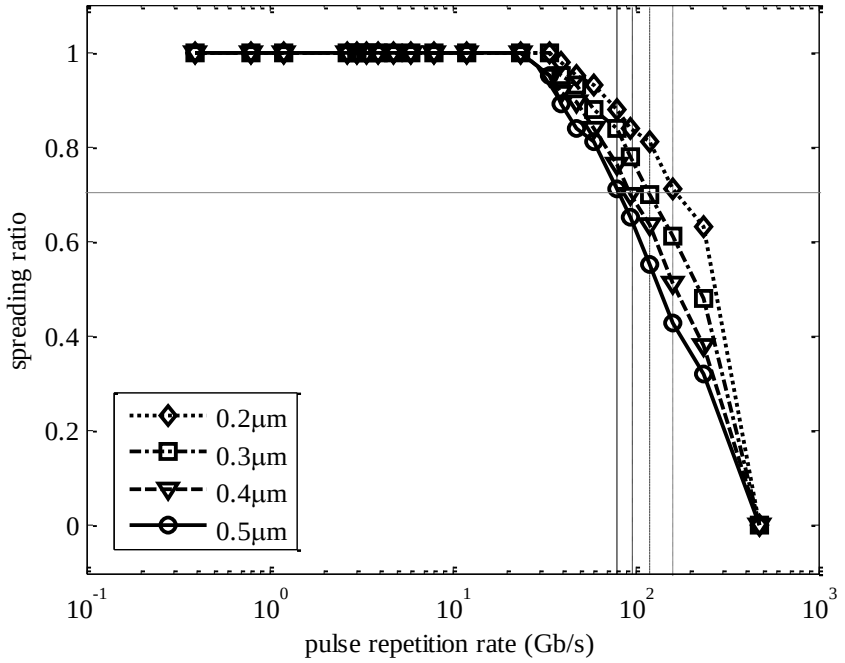


**Figure 7-19** Spreading ratios over repetition frequency under different I-layer width for edge-coupled InP/$In_{0.53}Ga_{0.47}As$/InP PIN photodiodes (specification in Table 7-2) with 1mW input average power and 1.0 modulation depth under -3V applied bias.

Fig.7-19 shows that pulse spreading gets progressively worse when the period of the pulse train becomes smaller. What is more, the rate of spreading becomes more rapid as if the I-layer width becomes wider. This is because the photo-generated carriers take longer time to transit the device if the I-layer is wider. What is more, the spreading gets more serious when the FWHM of Gaussian pulse is shorter, due to the "tail problem" the cause of which has been mentioned in section 7.2.2. The effect of pulse spreading will cause the output current pulse increasingly to merge

as the number of pulses in the train increases. For a smaller FWHM, such as 1ps, if the repetition rate is increased to a suitable value, there is still a chance to obtain well resolved output current pulses by increasing the off period between the pulses, as shown in Fig. 7-20. This corresponds to a pulse repetition rate of ~ 238Gb/s, i.e. well beyond the conventional 3dB bandwidth and where the roll-off in the spreading ratio is becoming severe (≤0.5).

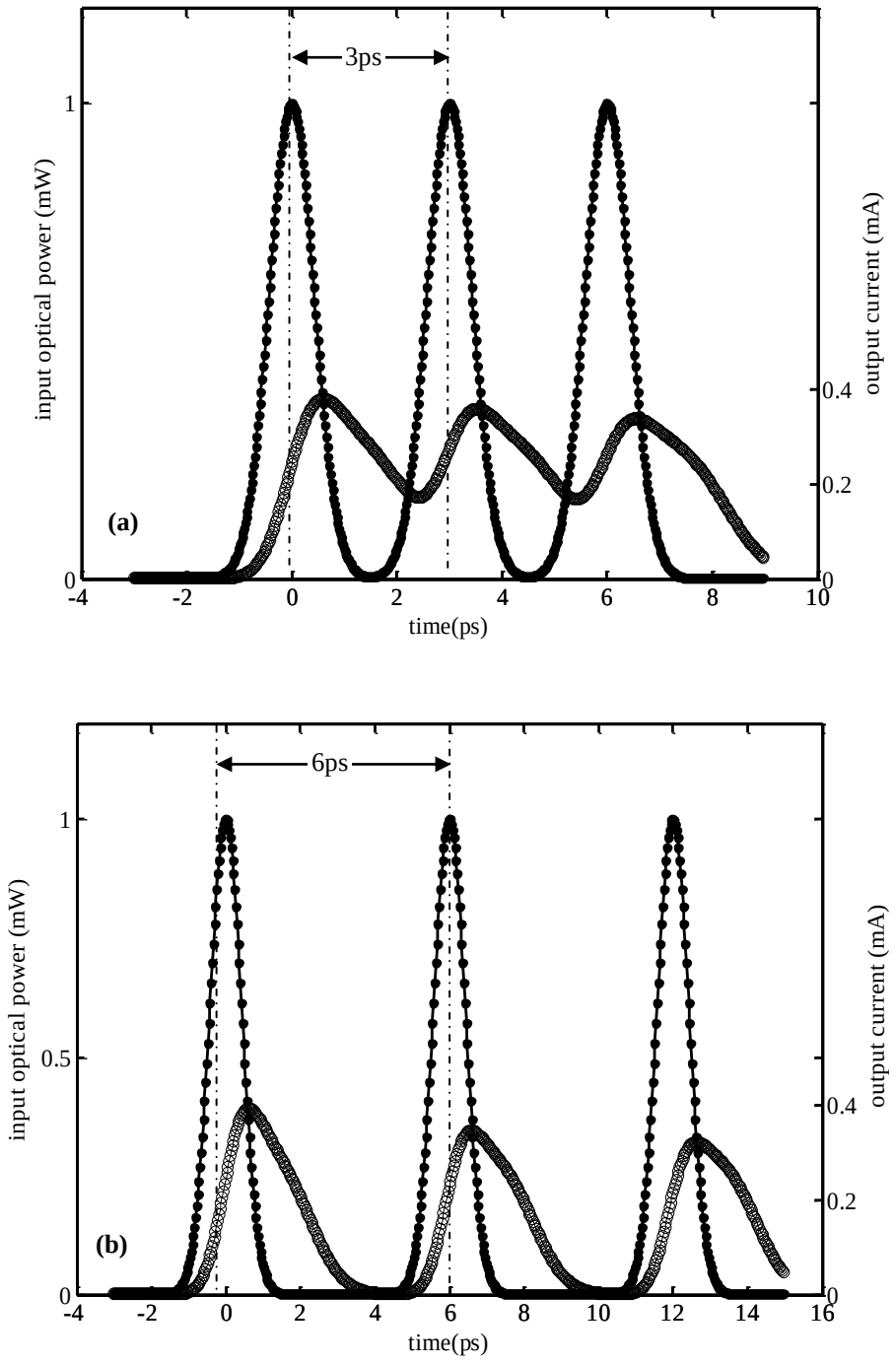


**Figure 7-20** Input Gaussian light pulse trains with FWHM=1ps with different repetition time **(a)** $r_{rep}$ = 0.5 **(b)** $r_{rep}$ = 1.0 showing the resulting output current for edge-coupled InP/$In_{0.53}Ga_{0.47}As$/InP PIN photodiode (specification in Table 7-2, 0.3μm I-layer width is chosen) with 1mW input average

power and 1.0 modulation depth under -3V applied bias.

In Fig. 7-20, a close inspection of Fig. 7-20(a) reveals that the peak amplitude of successive photocurrent pulses decreases. This is because the effective absorption coefficient decreases owing to the occupancy functions $f_c$ and $f_v$ increasing in Eq.(4-3) and Eq.(4-4) as the photo-generated charge builds up in the I-layer. For an I-layer width of 0.3μm and FWHM = 1ps, but the repetition rates are $r_{rep} = 0.5$ for Fig.7-19(a) and $r_{rep} = 1.0$ for Fig.7-20(b), corresponding to $t_{rep}$ = 3FWHM and $t_{rep}$ = 6FWHM respectively. Fig 7-20(b) shows the importance of off-time as determined by $r_{rep}$ in retaining distinguishable pulses at data rates close to and greater than the 3dB point. That means the output current wave at data rates beyond the 3dB point still comprises distinct pulses if a suitable off-time is applied. For pulse widths of under 1ps FWHM, although the peak of output current is greatly reduced and the output current pulse width significantly broadened relative to the incident light pulse compared with larger FWHM Gaussian pulses (such as 20ps or 50ps), the repetition frequency is faster than for pulse trains of such longer pulses. Fundamentally, the impulse, i.e. rise time response of the double hetero-junctions PIN photodiode with I-layer width ~0.3μm is not a system limiting factor and this fast response can be exploited.

The small magnitude problem can be overcome by varying other conditions and these will be introduced in the following sections, for example using larger average input optical power.

In this section the effect of varying the off-time, equivalently varying $r_{rep}$ over the range 0.3 to 1.8, on the eye opening ratio of a train of Gaussian input light wave of 1ps FWHM is shown in Fig. 7-21.

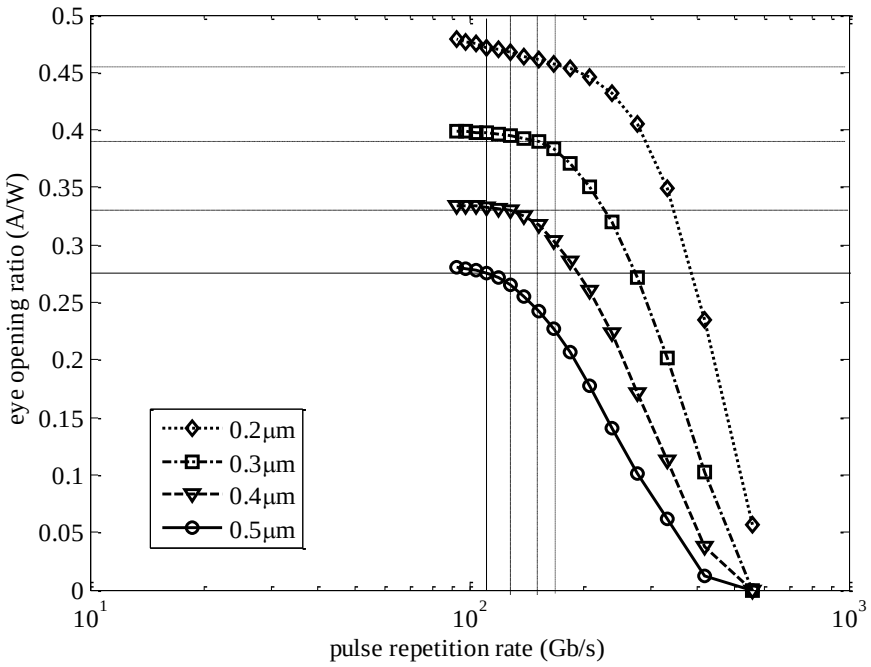


**Figure 7-21** Variation in the eye diagram ratio of the photocurrent pulses induced by pulse trains comprising 1ps FWHM Gaussian pulses versus the repetition frequency for edge-coupled InP/$In_{0.53}Ga_{0.47}As$/InP PIN photodiode (specification in Table 7-2) under different I-layer width with 1mW input average power and 1.0 modulation depth under -3V applied bias.

In Fig. 7-21, the vertical lines indicate the points where the output current pulses just start getting merged. Therefore, they are the fastest repetition frequency at which Gaussian light pulses of 1ps FWHM now be unambiguously detected using double hetero-junction PIN photodiodes with I-layer width from 0.2μm to 0.5μm. For 0.2μm I-layer width, the eye opening ratio is largest and the output current pulses are distinguishable and without any merging until the repetition frequency exceeds 167GHz. That means beyond the 3dB point, the shorter the I-layer width, the better the device works. Significantly, the eye diagram method for characterizing the high frequency performance of photodiodes reveals that thinner I-layers actually impose the ability to distinguish individual pulses at data rates beyond the usual in all signal 3dB bandwidth. This occurs because pulse spreading arising from the degraded fall-time is less when the I-layer width is reduced.

If the spreading ratio of a current pulse is equal or close to 1.0 (such as 20ps FWHM), then the individual pulse amount output current pulses will still be resolved even when the repetition rate of input Gaussian light pulses is smaller than 0.5, as shown in Fig. 7-22.

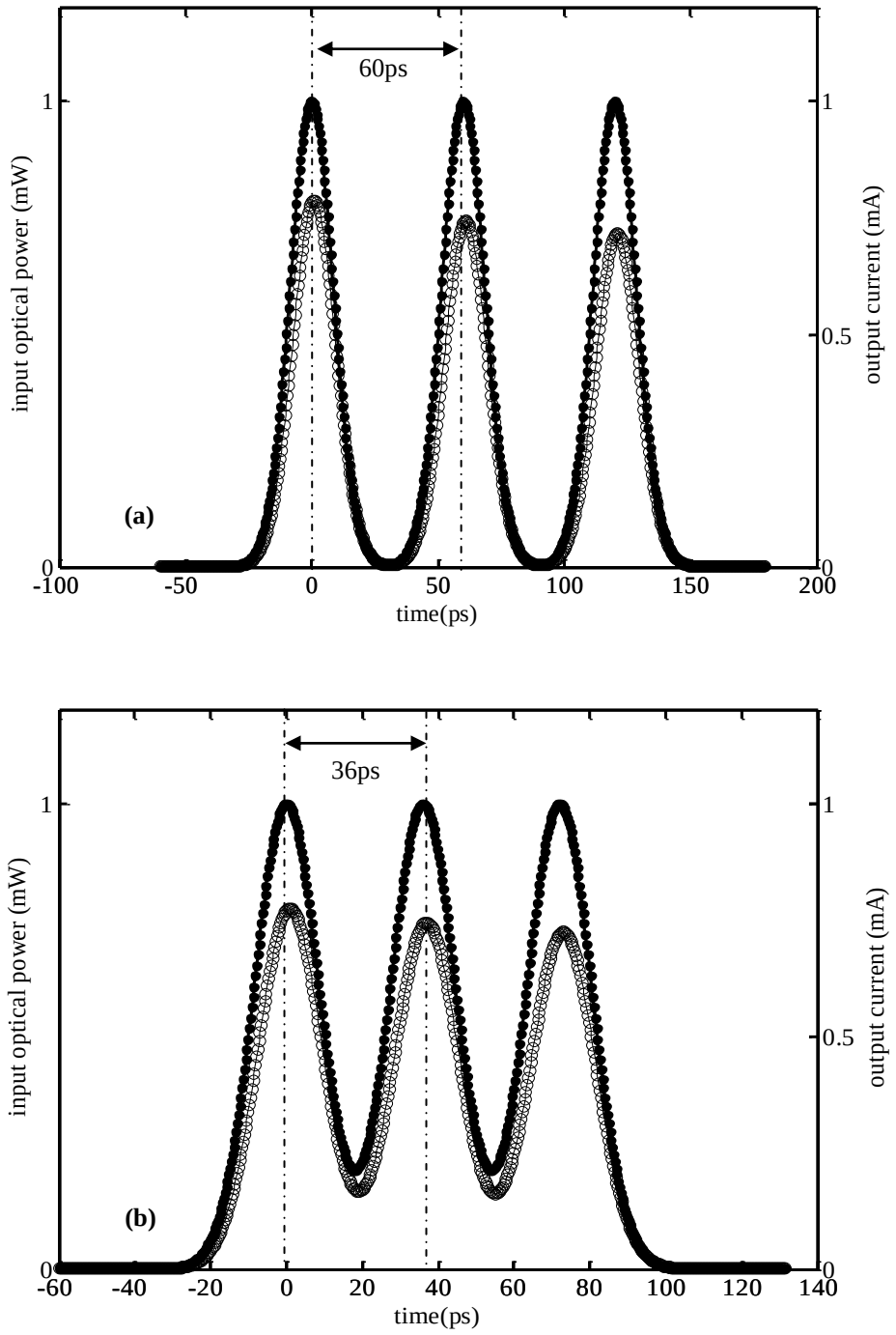


**Figure 7-22** Comparison of the input Gaussian pulse train (dot line) with FWHM=20ps under different repetition time **(a)** $r_{rep}$ = 0.5 and **(b)** $r_{rep}$ = 0.3 with output current (circles) for edge-coupled InP/$In_{0.53}Ga_{0.47}As$/InP PIN photodiode (specification in Table 7-22, 0.3μm I-layer width is chosen) with 1mW input average power and 1.0 modulation depth under -3V applied bias.

In Fig.7-22(a), the repetition rate is still $r_{rep}$ = 0.5, but the output current pulses have not spread much and still track the input optical amplitude modulation. Even when the input optical pulses start emerging together in Fig.7-22(b), the output current still tracks the input optical wave, however; even in Fig.7-22(b), the repetition frequency is only around 28GHz, i.e. around the more usually understood high

frequency limit of a double hetero-junction PIN photodiode [142]. This means that the repetition time is limited by the FWHM of input Gaussian light wave under these conditions.

### 7.3.2 Eye Opening Ratio under Different Applied Bias

The effect on eye opening ratio is also studied for the 0.3μm I-layer width device under different applied bias. The same parameters listed in Table 7-2 will be used but with different applied bias from -2V to -5V. If $t_{rep}$ = 4.2FWHM is chosen, then the eye opening ratio with different applied bias is shown in Fig.7-23.

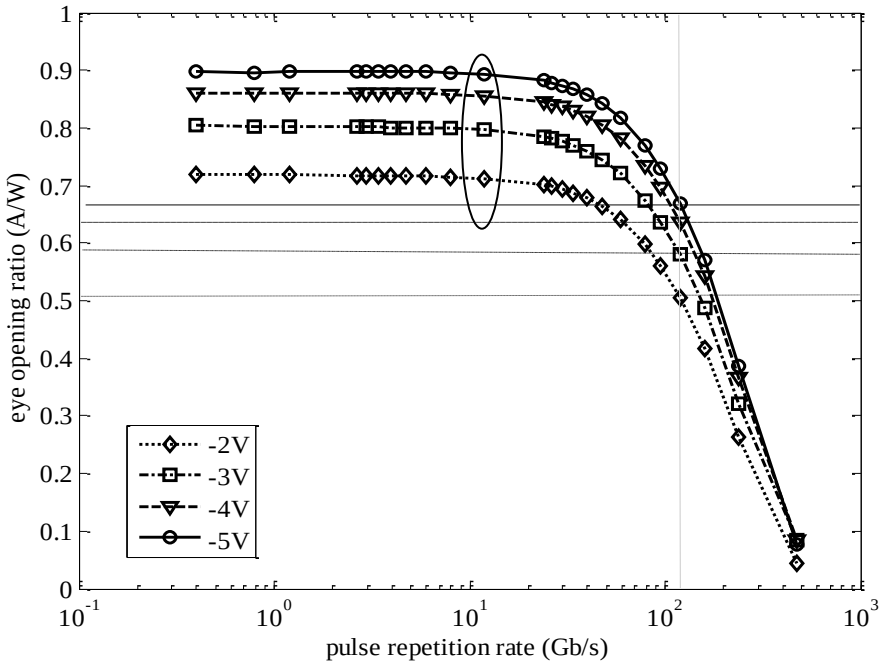


**Figure 7-23** Eye opening ratios versus pulse repetition frequency under different applied bias for edge-coupled InP/$In_{0.53}Ga_{0.47}As$/InP PIN photodiode (specification in Table 7-2, 0.3μm I-layer width is chosen) with 1mW input average power and 1.0 modulation depth.

Fig.7-23 shows that the bandwidth is independent of the applied bias as indicated by the grey vertical solid line. It is one of the methods to improve the output current pulse shape without sacrificing the repetition frequency. The responsivity as measured by the eye opening ratio is increased when the applied bias increased. It could be affected by the absorption coefficient. An example of 20ps FWHM with 84ps repetition time is tested as indicated in circle in Fig.7-23. The time dependence of the average effective absorption coefficient has also been calculated via,

$$ave\_\alpha(t) = \frac{\int_{x=x_n}^{x=x_p} \alpha(x,t)dx}{x_n - x_p} \tag{7-16}$$

Where $\alpha(x,t)$ is effective absorption coefficient for different $x$ point for each time point, $x_p$ is the interface point on the $x$-axis between P-layer and I-layer and $x_n$ is the interface point on the $x$-axis between I-layer and N-layer. $x_p$ and $x_n$ are indicated in the Fig.7-1. The variation in average absorption coefficient with time for the different applied bias conditions considered is shown in Fig.7-24.

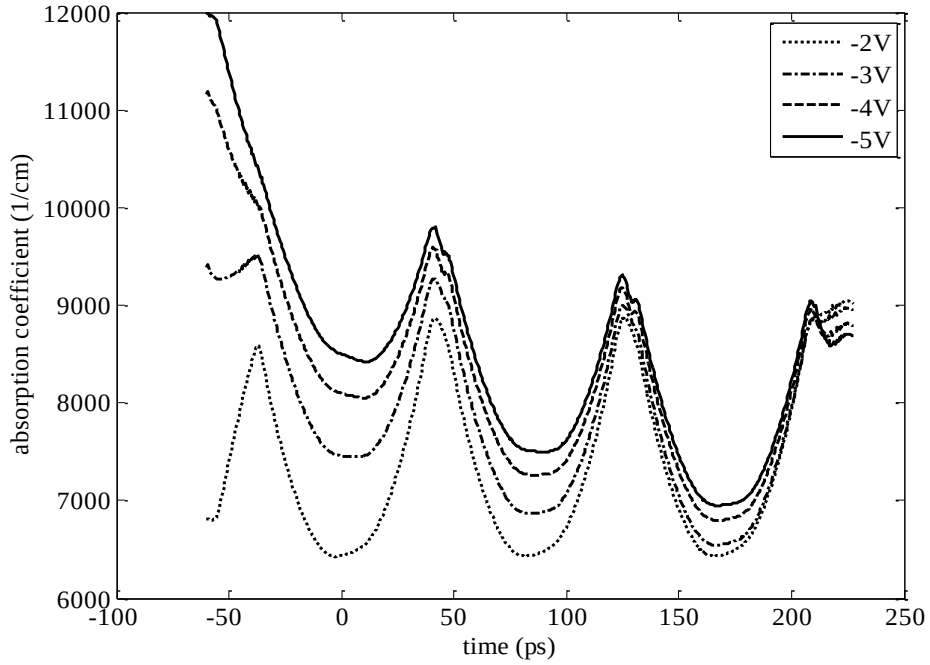


**Figure 7-24** Average absorption coefficient for 20ps FWHM Gaussian input optical power with 84ps repetition time under different applied bias for edge-coupled InP/$In_{0.53}Ga_{0.47}As$/InP PIN photodiode (specification in Table 7-2, 0.3μm I-layer width is chosen) with 1mW input average power and 1.0 modulation depth.

As shown in Fig.7-24, the average absorption coefficient $ave\_\alpha(t)$ increases with applied bias. According to the Eq.(4-2) for absorption coefficient, the occupancy factors $f_c$ and $f_v$ making $ave\_\alpha(t)$ bigger. The reason for lower $f_c$ and $f_v$ is probably less carrier storage at the hetero-interfaces: as the stronger depletion field caused by high applied bias helping to pull the photo-generated electrons and holes out of the I-layer. There is another factor that might also contribute to the larger eye ratio when the applied bias is increased. That is less recombination rate as the higher depletion field pulls the carriers apart in the I-layer. This can be tested by plotting average hole and electron concentrations. The average hole and electron concentration at every time step has been calculated using the formulae,

$$ave\_p(t) = \frac{\int_{x=x_n}^{x=x_p} p(x,t)dx}{x_n - x_p} \quad (7\text{-}17a)$$

$$ave\_n(t) = \frac{\int_{x=x_n}^{x=x_p} n(x,t)dx}{x_n - x_p} \quad (7\text{-}17b)$$

where $p(x,t)$ and $n(x,t)$ are the carrier concentrations on each $x$ point at the specific time step, $x_p$ is the interface point on the $x$-axis between P-layer and I-layer and $x_n$ is the interface point on the $x$-axis between I-layer and N-layer. $x_p$ and $x_n$ are indicated in the Fig.7-1. The average hole and electron concentration for 20ps FWHM with 84ps repetition time over the time in the I-layer are shown in Fig. 7-25.

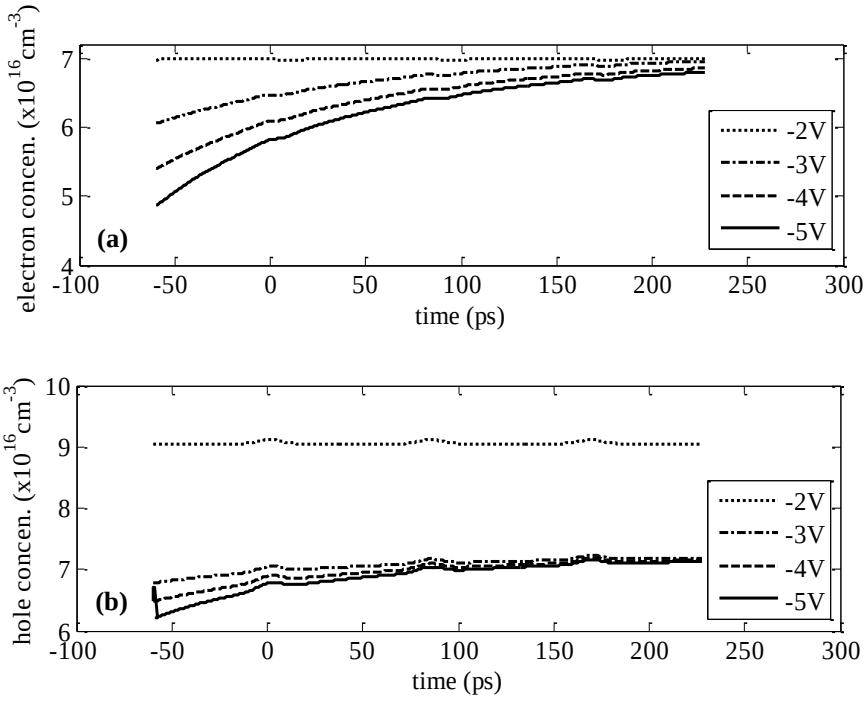


**Figure 7-25 (a)** Average electron concentration and **(b)** average hole concentration for 20ps FWHM Gaussian input optical power with 84ps repetition time under different applied bias for edge-coupled InP/$In_{0.53}Ga_{0.47}As$/InP PIN photodiode (specification in Table 7-2, 0.3μm I-layer width is chosen) with 1mW input average power and 1.0 modulation depth.

As shown in Fig.7-25, both average carrier concentrations fall as the applied bias increases. Therefore, there are fewer carriers to recombine as the higher depletion field pulls the electron and hole apart in the I-layer.

The spreading ratios of the Gaussian wave over the repetition frequency under different applied bias are shown in Fig. 7-26.

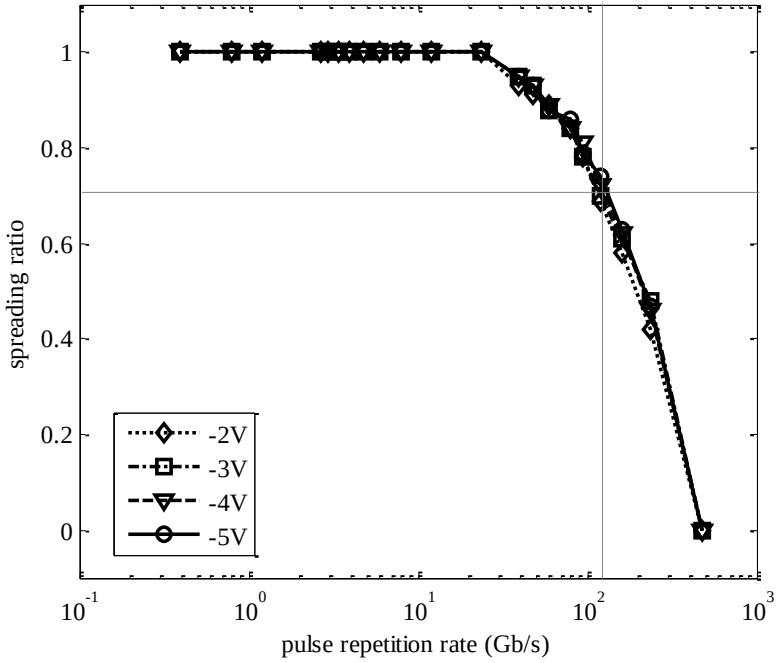


**Figure 7-26** Spreading ratios over the repetition frequency under different applied bias for edge-coupled InP/$In_{0.53}Ga_{0.47}As$/InP PIN photodiode (specification in Table 7-2, 0.3μm I-layer width is chosen) with 1mW input average power and 1.0 modulation depth.

The spreading ratios for different applied bias keep a very similar value to each other across the repetition frequency. Therefore, the applied bias has very small effect on the spreading ratio. An analysis for repetition frequencies that are greater than 3dB frequency is present under different applied bias.

If the repetition ratio is varied between 0.3 ~ 1.8 for 1ps FWHM Gaussian wave, then the eye diagram over the repetition frequency is shown in Fig. 7-27. In Fig.7-27, the larger the applied bias, the bigger the eye opening ratio is but the roll-off is unchanged. The fastest repetition frequency (at the point when the current pulses start merging) is nearly independent of P-layer and N-layer doping and is still around 152Gb/s.

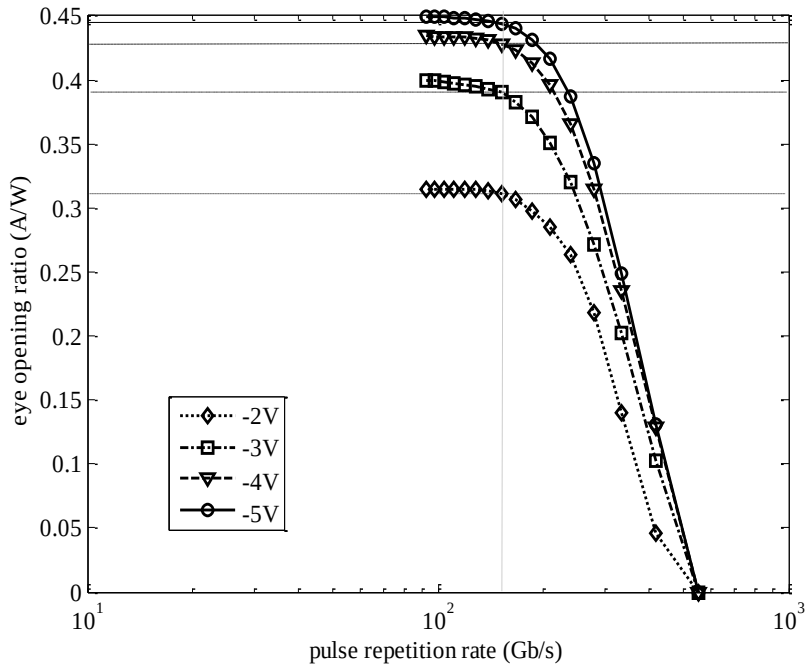


**Figure 7-27** Variation in the eye opening ratio of the photocurrent pulses induced by pulse trains comprising 1ps FWHM Gaussian pulses versus the repetition frequency under different applied bias for edge-coupled InP/$In_{0.53}Ga_{0.47}As$/InP PIN photodiode (specification in Table 7-2, 0.3μm I-layer width is chosen) with 1mW input average power and 1.0 modulation depth.

### 7.3.3 Eye Opening Ratio under Different Input Average Optical Power

The eye opening ratio is also calculated for a double hetero-junction PIN photodiode with a 0.3μm I-layer width under different input average optical power. The same parameters listed in Table 7-2 are used but with different input average optical power (10μW to 1mW). If $t_{rep} = 4.2FWHM$ is chosen with different FWHM ranges from 600ps to 0.5ps, then the eye opening ratio with different applied bias is shown in Fig.7-28.

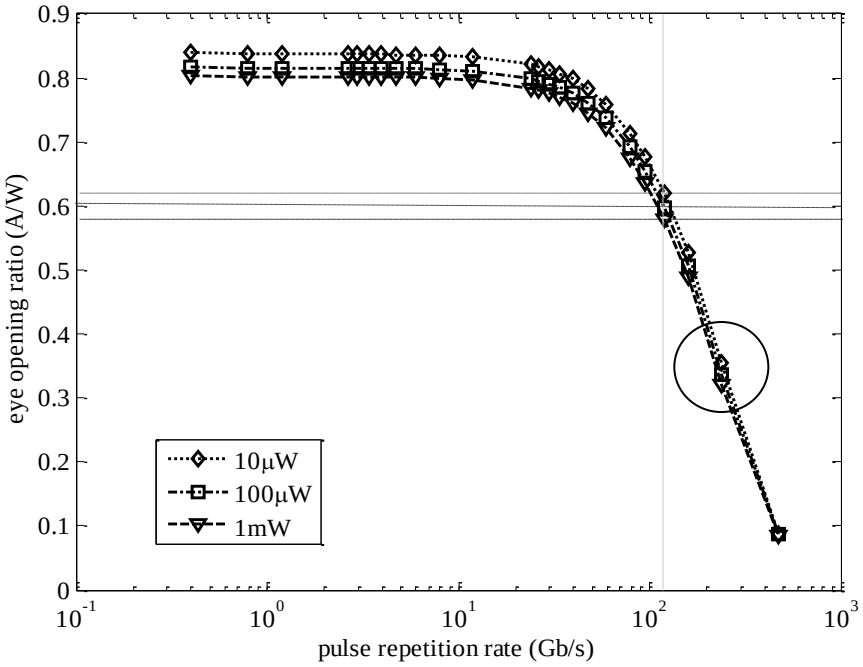


**Figure 7-28** Eye opening ratio over repetition frequency with different input average optical power and 1.0 modulation depth for edge-coupled InP/$In_{0.53}Ga_{0.47}As$/InP PIN photodiode (specification in Table 7-2, 0.3μm I-layer width is chosen) under -3V applied bias.

Different dashed lines indicate the 3dB point for different input optical power. The circle indicates the operational point for the for 1ps FWHM Gaussian wave with a repetition time of 4.2ps. The peak eye opening ratio slightly decreases as the average input power increases by two decades. This is because the larger the input average optical power is applied to the device, the more carriers in the I-layer are generated, however as the small decrease in eye opening ratio under 3dB bandwidth due to the band-filling effect indicates that the photo-generated carriers are readily extracted from the device for input optical power up to 1mW. Whilst the eye opening ratio is nearly independent of input optical power, the output current increases rapidly with larger input power. For example, the output current caused by 1ps FWHM Gaussian light pulses with 4.2ps repetition time and different input optical average power (1mW and 100μW) is shown in Fig.7-29. The equivalent pulse repetition rate (PRR) is around 240Gb/s which is well beyond the 3dB point of the eye opening ratio versus PRR curve (indicated in Fig.7-29).

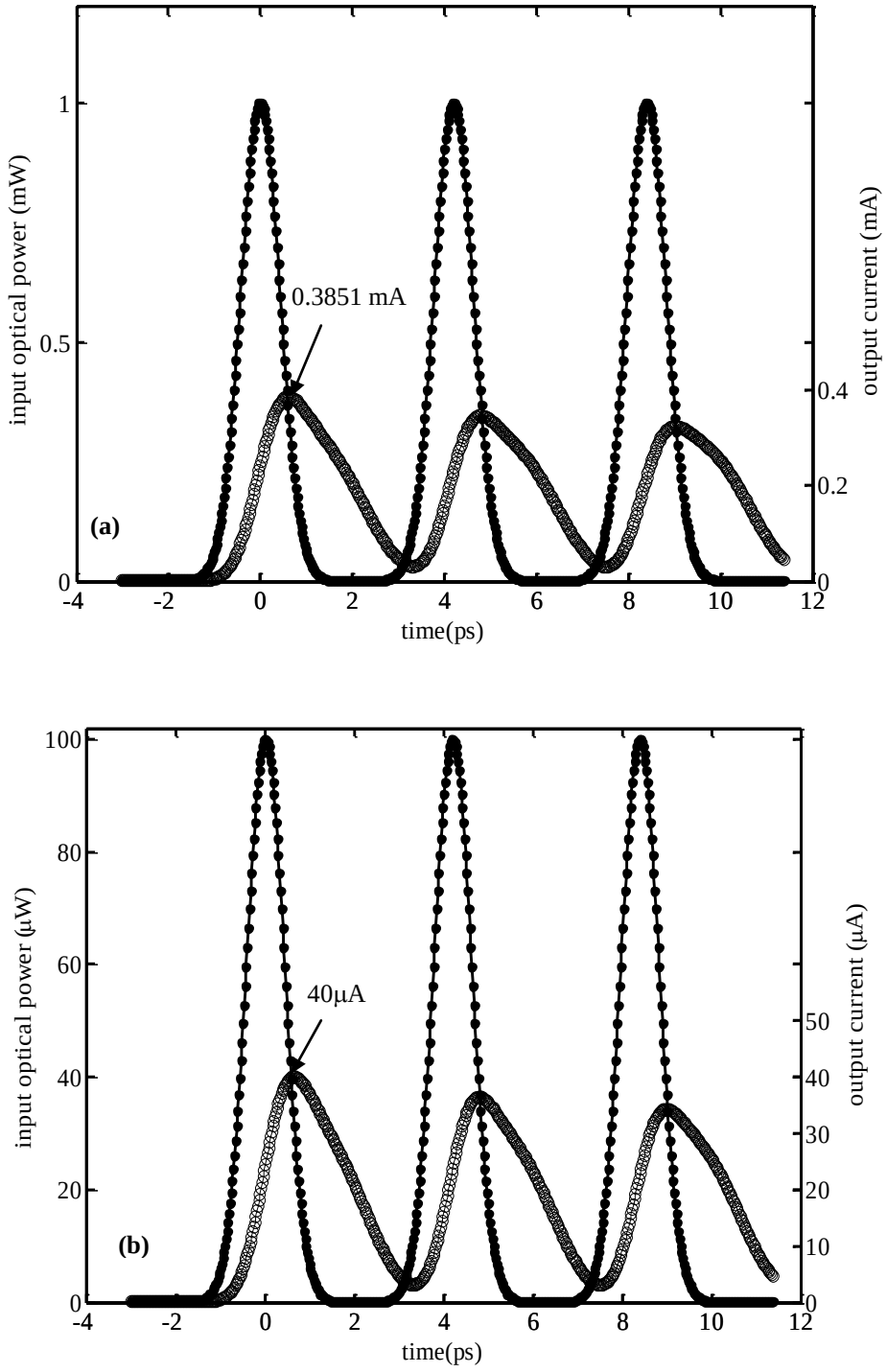


**Figure 7-29** Input Gaussian light pulses (1ps FWHM and 4.2ps repetition time) of **(a)** 1mW **(b)** 100μW power with 1.0 modulation depth and resulting output current for edge-coupled InP/$In_{0.53}Ga_{0.47}As$/InP PIN photodiode (specification in Table 7-2, 0.3μm I-layer width is chosen) under -3V applied bias.

The input Gaussian pulses of 1mW input average power generates the output current with a peak that is around 10 times bigger than the input Gaussian wave with 100μW input average power, offering further evidence the responsivity is not degraded by band filling at these power levels and data rates. Further, in systems

dominated by thermal noise (i.e. independent of input optical power). 1mW input average power Gaussian pulses will have a better eye diagram than 100μW. The 1mW input average power is shown in Fig.7-30 where random noise of between 25μA to -25μA (a) or between 5μA to -5μA (b) is added arbitrarily to the output current.

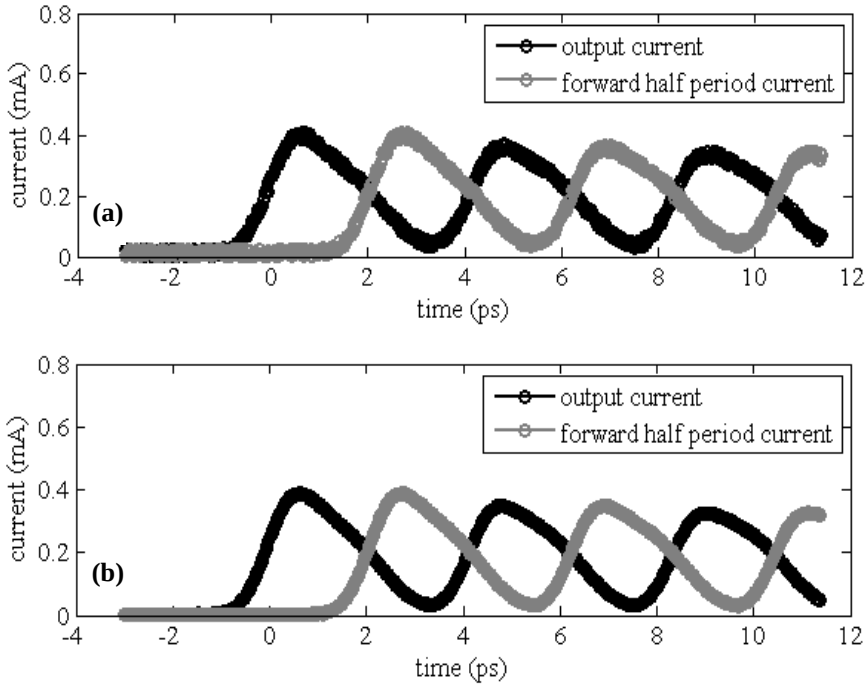


**Figure 7-30** Eye diagram by output current that generated by input Gaussian wave (1ps FWHM and 4.2ps repetition time) 1mW input average power and 1.0 modulation depth with a noise level between **(a)** 25μA and -25μA or **(b)** 5μA and -5μA for edge-coupled InP/$In_{0.53}Ga_{0.47}As$/InP PIN photodiode (specification in Table 7-2, 0.3μm I-layer width is chosen) under -3V applied bias.

In the case of 1mW average input power, both noise levels seem not large enough compared to the peak current to degrade the eye diagram. The 100μW input average power is also shown in Fig.7-31 where a random noise of between 25μA to -25μA (a) or between 5μA to -5μA (b) is added to the output current.

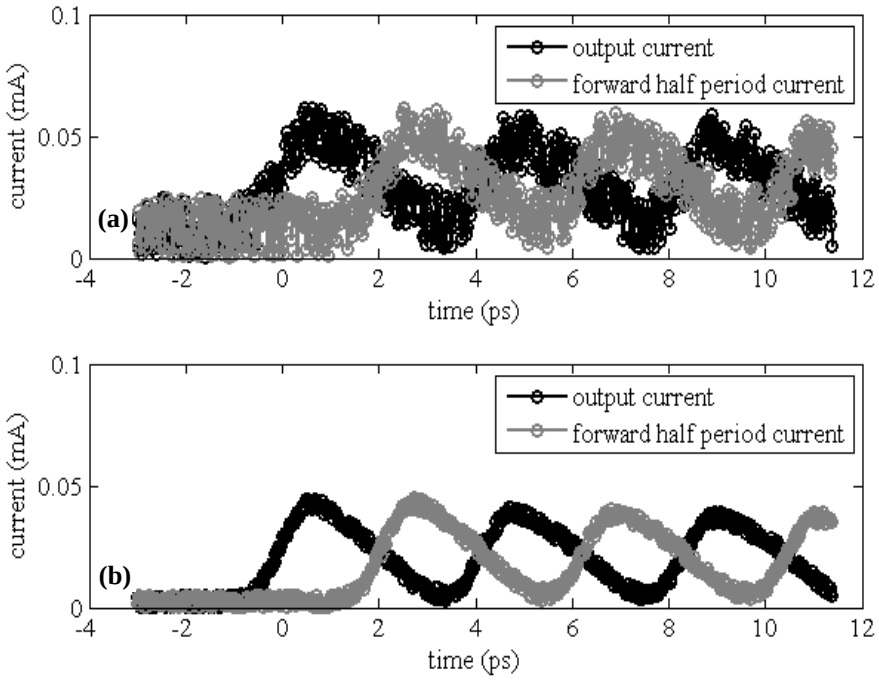


**Figure 7-31** Eye diagram by output current that generated by input Gaussian wave (1ps FWHM and 4.2ps repetition time) 100μW input average power and 1.0 modulation depth with a noise level between **(a)** 25μA and -25μA **(b)** 5μA and -5μA for edge-coupled InP/$In_{0.53}Ga_{0.47}As$/InP PIN photodiode (specification in Table 7-2, 0.3μm I-layer width is chosen) under -3V applied bias.

Now the random noise level of 25μA to -25μA has big influence on the output current pulses in the case of input average power 100μW. This is because the noise level value is quite close to the value of output current. If the random noise level changes to 5μA to -5μA, then the influence on the output current pulses will be small. Therefore, in a practical implementation, increasing the input optical power is one of the methods to improve the current eye diagram at the data rates beyond the 3dB point in the case when the random noise level is close to the value of output current.

When considering eye diagrams constructed from a single pulse, or trains of two or three pulses, band filling has a small effect on the eye opening ratio for data rates up to 240Gb/s, however inspection of Fig.7-30 reveals that the amplitude of each current pulse is monotonically lower than the preceding causing the eye to close. This implies that not all the photo-generated charge is escaping between successive pulses. Fig 7-32 illustrates the effect of a train of eight 1mW Gaussian light pulses of 1ps FWHM and 4.2ps repetition time (8 bits data) have applied to the model, the output current with its forward half period value are also shown.

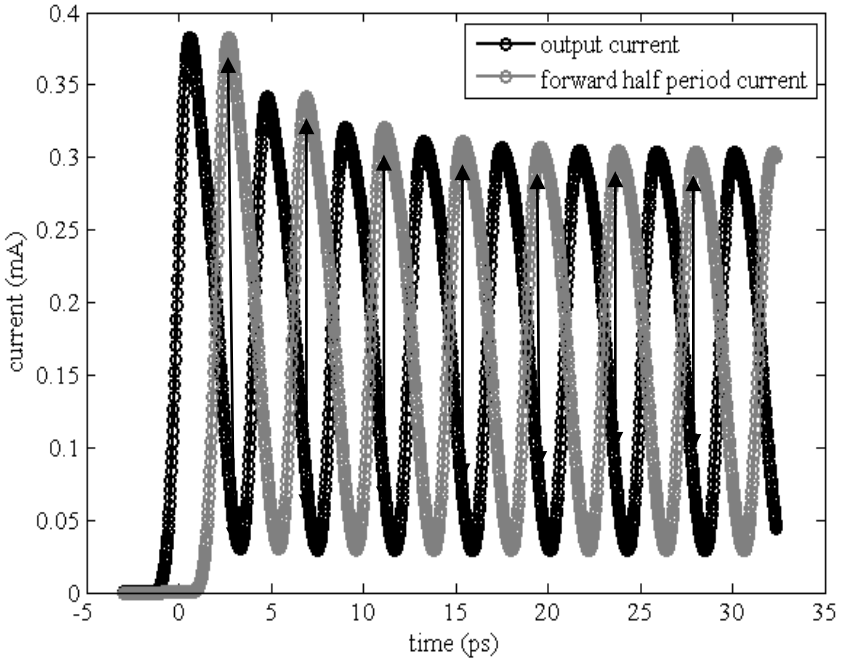


**Figure 7-32** Eye diagram by output current that generated by input Gaussian wave (1ps FWHM and 4.2ps repetition time) 1mW input average power and 1.0 modulation depth for edge-coupled InP/$In_{0.53}Ga_{0.47}As$/InP PIN photodiode (specification in Table 7-2, 0.3μm I-layer width is chosen) under -3V applied bias.

As more input light pulses are detected by the device, the output current eye diagram closes up. The eye opening ratios for the sequential output current pulses (indicated with black double arrows in Fig 7-32) are shown in Fig.7-33 for input optical powers of 1mW and 100μW.

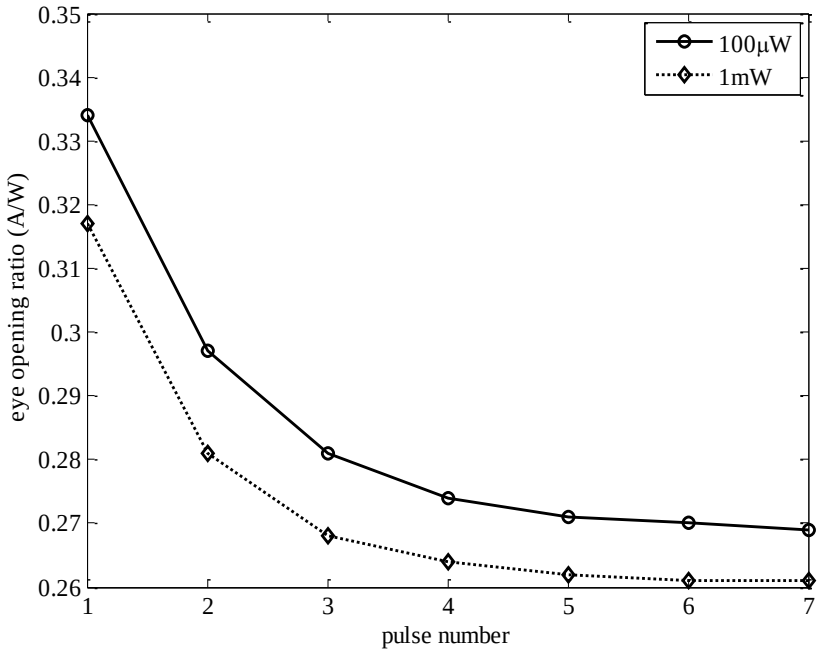


**Figure 7-33** Eye opening ratio for the pulses train with 100μW and 1mW input average power and 1.0 modulation depth for edge-coupled InP/$In_{0.53}Ga_{0.47}As$/InP PIN photodiode (specification in

Table 7-2, 0.3μm I-layer width is chosen) under -3V applied bias.

In Fig.7-33, the eye opening ratios of first four output current pulses decreases faster than the following output current pulses. The eye opening ratios for the current pulses have an exponential decay with time. Despite this decay eye diagram remains sufficiently open for all eight current pulses to prove that the device can receive 1byte data at a very high data rate in this case nearly 240Gb/s.

This is only an optimistic prediction, as the effect of noise has so far been neglected; also the influence of carrier transport by diffusion along the light pulse (*z*-axis direction) is neglected in this model. Therefore the current will probably be too small to detect in the real time device at these ultra-high data rates.

In order to give the reason why the eye diagram closes with successive fast light pulses an analysis of the average carriers concentration as calculated by Eq.(7-17a) and Eq.(7-17b) and the average effective absorption coefficient in Eq.(7-16) will be necessary. Fig.7-34 shows the time variation in the average hole and electron concentrations in the I-layer.

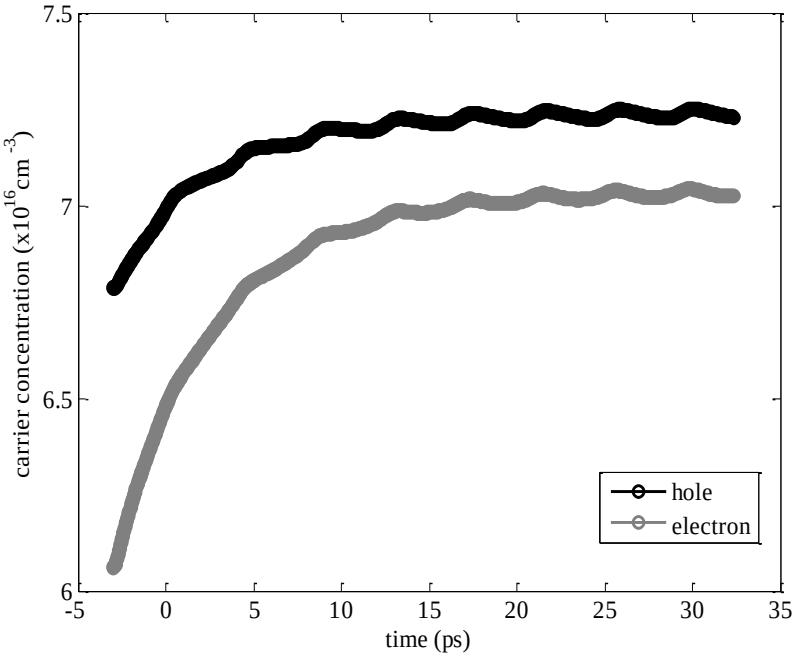


**Figure 7-34** Average hole and electron concentration in the I-layer against time for edge-coupled InP/$In_{0.53}Ga_{0.47}As$/InP PIN photodiode (specification in Table 7-2, 0.3μm I-layer width is chosen) with 1mW input average power and 1.0 modulation depth under -3V applied bias.

The average hole and electron concentration in the I-layer rapidly increases at the

beginning of the fast light pulse sequence and does not decay away. Instead the hole and electron concentrations saturate after about 4-5 pulses (~15ps) with only a small ripple occurring with each subsequent light pulse. The average hole concentration is bigger than electron concentration in the I-layer. This is because electrons are lighter and have a higher average velocity than holes, so escape the I-layer more rapidly than holes. Fig.7-35 shows the average effective absorption coefficient in the I-layer over the time period corresponding to the eight light pulses shown in Fig7-32. Again the light pulses were assumed to be Gaussian shaped with 1ps FWHM, repetition time of 4.2ps and 1mW peak power level.

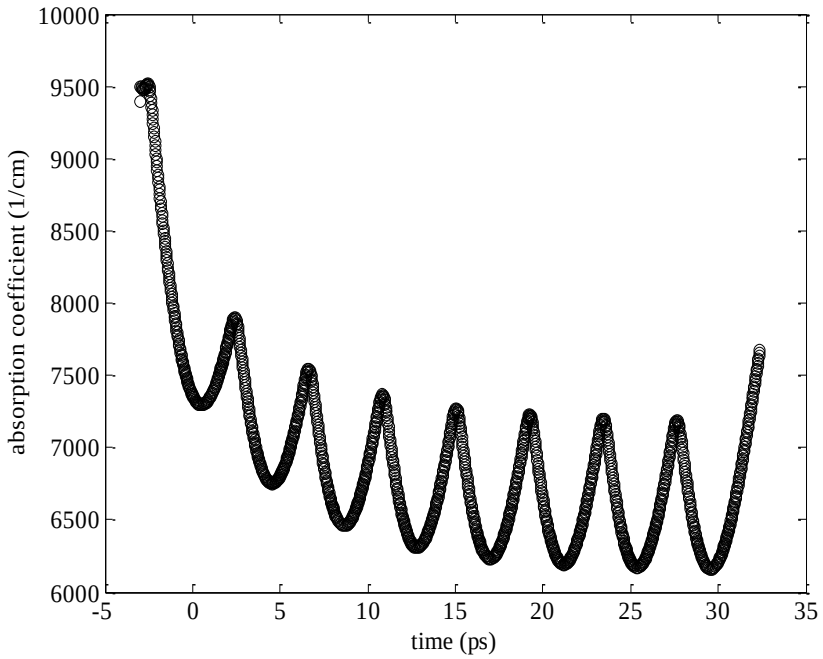


**Figure 7-35** Average effective absorption coefficient in the I-layer against time for edge-coupled InP/$In_{0.53}Ga_{0.47}As$/InP PIN photodiode (specification in Table 7-2, 0.3μm I-layer width is chosen) with 1mW input average power and 1.0 modulation depth under -3V applied bias.

The average absorption coefficient is largest at the time when the input light first shines on the device. Then it reduces due to the band filling effect, to which both electrons and holes contribute Fig.7-34 and reduces to only ~40% of its peak value. That is the main reason why the output current eye diagram ratio that has been shown in Fig.7-32 decrease with time. Whilst this is significant, it is insufficient to critically degrade the predicted eye opening, which is stabilized after ~8 pulses. Further, the 8 pulses correspond to the byte "1111 1111" which will occur infrequently in a digital system. On this basis data rates of up to 240Gb/s are possible unless noise has a major effect.

If the repetition rate is varied between 0.3 ~ 1.8 for 1ps FWHM Gaussian wave, then the eye diagram over the repetition frequency is as shown in Fig. 7-36.

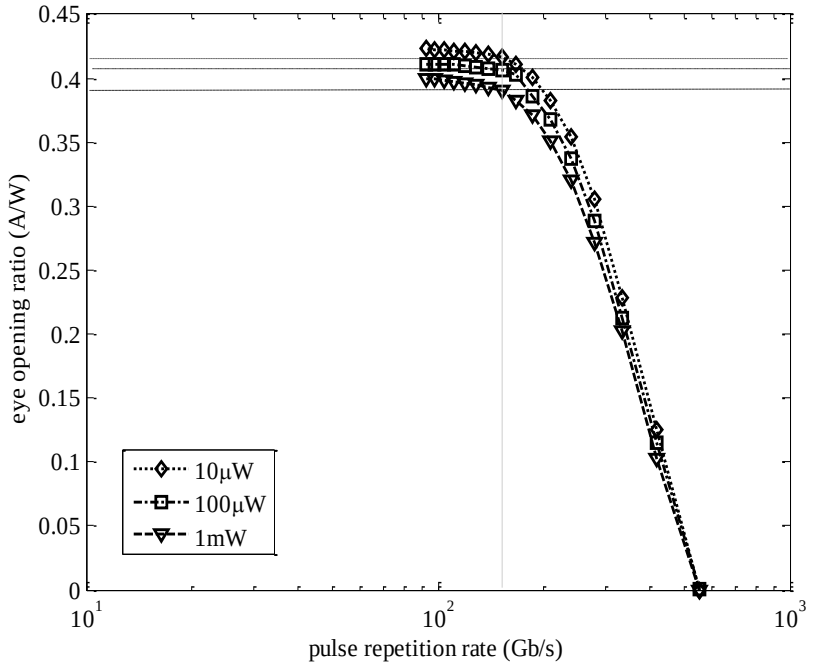


**Figure 7-36** Variation in the eye opening ratio of the photocurrent pulses induced by pulse trains comprising 1ps FWHM Gaussian pulses versus the repetition frequency with different input optical average power and 1.0 modulation depth for edge-coupled InP/$In_{0.53}Ga_{0.47}As$/InP PIN photodiode (specification in Table 7-2 , 0.3μm I-layer width is chosen) under -3V applied bias.

For 1ps FWHM, the eye diagram ratio is inversely proportional with value of the input average power. The fastest repetition frequency (at the point when the current pulses start merging) is nearly independent of P-layer and N-layer doping and is still around 152Gb/s.

The time spreading ratio has also been analysed under different input average power. The time spreading ratio for different FWHM with repetition time $t_{rep} = 4.2FWHM$ is shown in Fig.7-37.

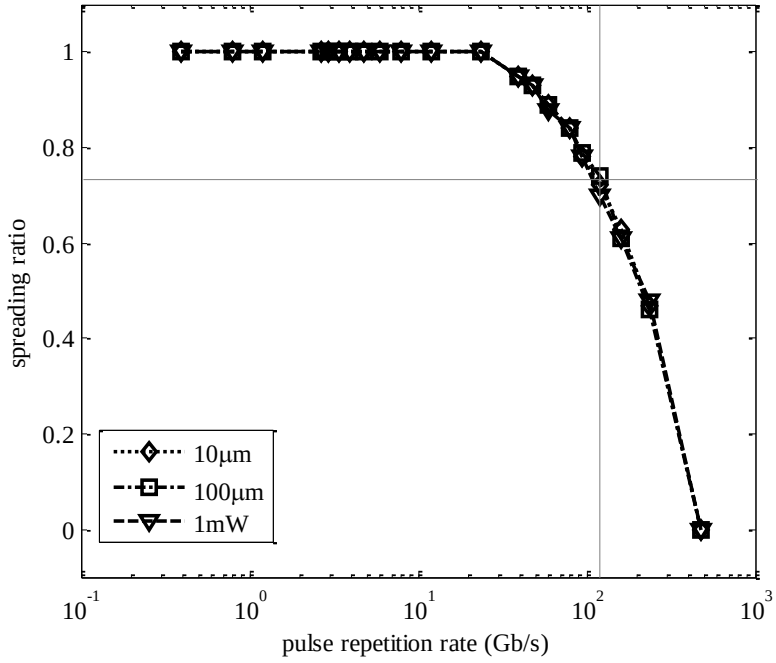


**Figure 7-37** Spreading ratios over repetition frequency under different input average optical power and 1.0 modulation depth for edge-coupled InP/$In_{0.53}Ga_{0.47}As$/InP PIN photodiode (specification in Table 7-2, 0.3μm I-layer width is chosen) under -3V applied bias.

The time spreading ratio stays the same as the input average optical power is varied. The 3dB frequency stays the same as before and is around 119GHz. This is because the concentrations of photo-generated charge (Fig.7-34) remain too low to screen out the depletion field. Thus, drift still dominates carrier transport through the I-layer despite the high optical power levels considered in much of this chapter.

### 7.3.4 Eye Opening Ratio under Different Doping Density in P-layer and N-layer

The effect of different doping density in the P and N layers has also been tested in the model. Fig.7-38 shows the effect of changing the doping density in P-layer to $5\times10^{7}cm^{-3}$ and doping density in N-layer to $5\times10^{7}cm^{-3}$ and $1.5\times10^{8}cm^{-3}$, whilst keeping other parameters in table 7-2 the same. In all cases the pulse repetition time was 4.2 times the FWHM of the Gaussian pulse train with a peak optical power of 1mW.

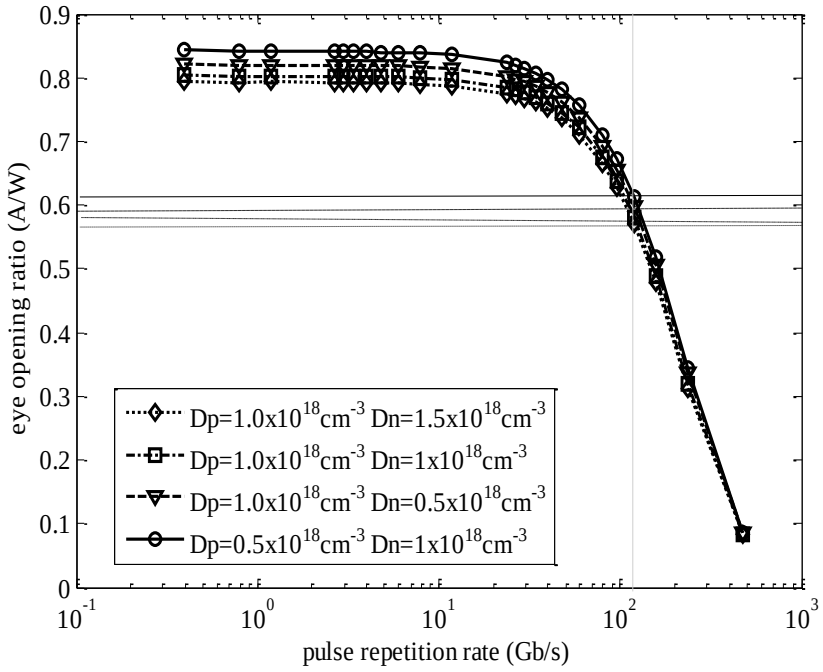


**Figure 7-38** The eye opening ratios of the different FWHM over the repetition frequency under different doping density for edge-coupled InP/$In_{0.53}Ga_{0.47}As$/InP PIN photodiode (specification in Table 7-2, 0.3μm I-layer width is chosen) with 1mW input optical power and 1.0 modulation depth under -3V applied bias.

The peak eye opening ratio slightly rises when the doping in P-layer or the doping in N-layer decreases. This is because a decrease in the doping density in the P-layer and N-layer will cause an increase in the width of the depletion region in which carrier transport by drift predominates. This leads to a small increase in the total current. The modification in doping of P-layer and N-layer hardly changes the bandwidth since the change in transit time is small.

The time spreading ratio is also estimated and shown in Fig 7-39. In Fig. 7-39, the time spreading ratio is again independent of the doping density and only depends on the FWHM of the input Gaussian wave.

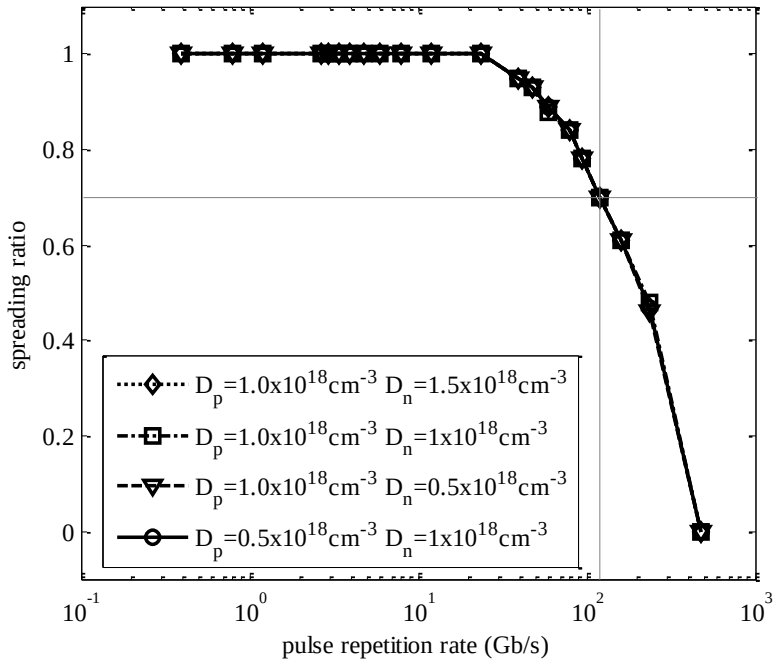


**Figure 7-39** The time spreading ratios of the different FWHM over the repetition frequency under different doping density for edge-coupled InP/$In_{0.53}Ga_{0.47}As$/InP PIN photodiode (specification in Table 7-2, 0.3μm I-layer width is chosen) with 1mW input optical power and 1.0 modulation depth under -3V applied bias.

The effect of varying the repetition ratio $r_{rep}$ as defined before, between $0.5 \leq r_{rep} \leq 1.8$ for a 1ps FWHM Gaussian pulse train on the eye opening ratio versus the repetition frequency relationship was shown in Fig. 7-40.

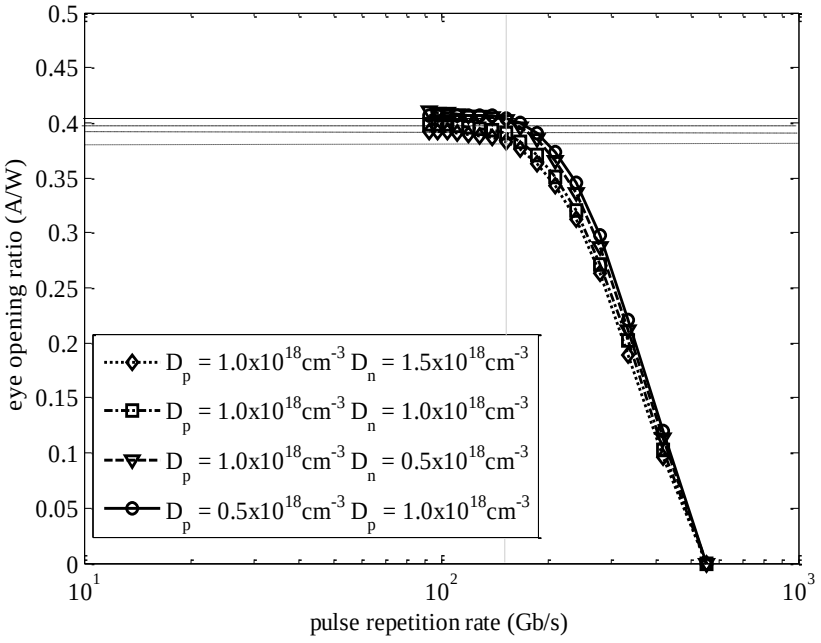


**Figure 7-40** Variation in the eye opening ratio of the photocurrent pulses induced by pulse trains comprising 1ps FWHM Gaussian pulses versus the repetition frequency under different doping density for edge-coupled InP/$In_{0.53}Ga_{0.47}As$/InP PIN photodiode (specification in Table 7-2 , 0.3μm I-layer width is chosen) with 1mW input optical power and 1.0 modulation depth under -3V applied

bias.

The variation on the peak of the eye diagram ratio of 1ps FWHM Gaussian light pulses depends on the doping density too; the smaller the doping density is, the bigger the peak point is. The fastest repetition frequency (at the point when the current pulses start merging) is nearly independent of P-layer and N-layer doping and is still around 152Gb/s.

### 7.3.5 Eye Opening Ratio for Different Input Light Method

As introduced in Chapter 4, beside the edge-coupled waveguide mode of operation, photodiodes can operate as top-entry or sub-entry vertical mode. By using Eq.(4-16) and Eq.(4-17), the top-entry and sub-entry variants of vertical mode are defined. This is the most widely used mode of photodiode operation. The generation terms for different input light method have been defined in Eq.(4-16), Eq.(4-17) and Eq.(4-18) in Chapter 4 are redefined here to help explanation:

$$G(x,t) = \frac{\alpha\lambda}{hcS_{recep}} P(t)e^{-\alpha x} \qquad \text{top-entry (vertical)} \qquad (7\text{-}18a)$$

$$G(x,t) = \frac{\alpha\lambda}{hcS_{recep}} P(t)e^{-\alpha(W_i - x)} \qquad \text{sub-entry (vertical)} \qquad (7\text{-}18b)$$

$$G(x,t) = \frac{\lambda P(t)\left[1 - e^{-\Gamma\alpha L}\right]}{hcS_{absorp}L} \qquad \text{edge-coupled} \qquad (7\text{-}18c)$$

where $P(t) = P_0 mI(t)$ , $\alpha$ is the optical absorption constant, $\lambda$ is the optical wavelength, $h$ is the Planck's constant, $c$ is the light speed, $m$ is the modulation depth, $P_0$ is the average optical power and $I(t)$ is the power intensity profile, $W_i$, $L$, $S_{absorp}$ and $S_{recep}$ are all shown in Fig. 7-1. These three input light methods have been modelled using the same parameters listed in Table 7-2, then for 0.3 μm I-layer width, the input optical light with output current has shown in Fig. 7-41.

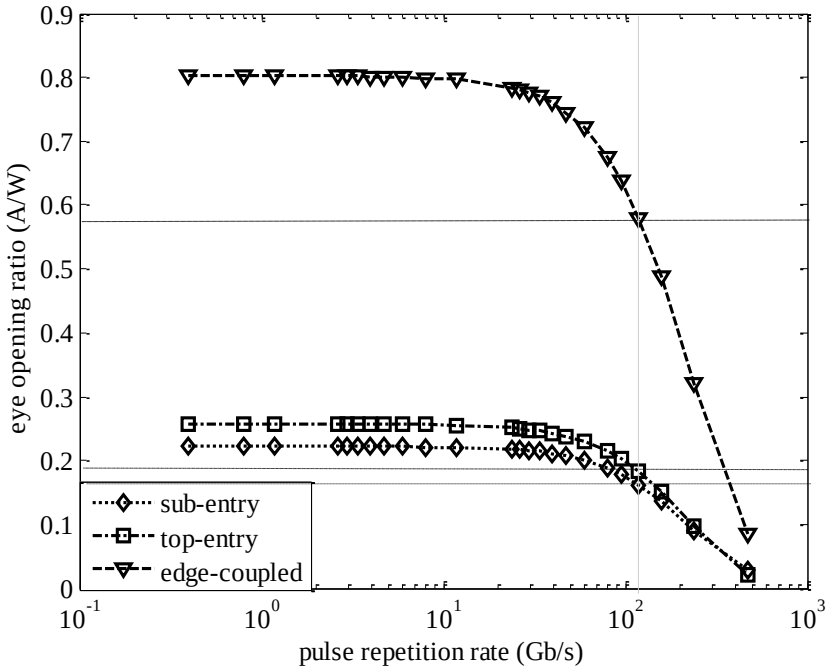


**Figure 7-41** The eye opening ratios of the different FWHM over the repetition frequency under different input light methods for InP/$In_{0.53}Ga_{0.47}As$/InP PIN photodiode (specification in Table 7-2, 0.3μm I-layer width is chosen) with 1mW input optical power and 1.0 modulation depth under -3V applied bias.

The change of light input method does not change the transit time 3dB bandwidth, however the vertical light input methods (sub-entry and top-entry) have lower peak eye opening ratios. This is because the generation term varies inversely with the light absorption area $S_{recep}$ whilst with the vertical input light methods, it decays exponentially with $W_I$. The larger eye diagram ratio for edge-coupled photodiode comparing with others makes it a better choice especially for output current beyond 3dB frequency limit. Further, when the edge-coupled light input method is applied to the device, the absorption area decreases as $S_{absorp}$ (4.6μm$^2$) < $S_{recep}$ (50μm$^2$) and the input light is equally distributed across $W_I$. The top-illumination has slightly larger peak eye diagram ratio compared with the sub-illumination, due to the input light method intensity exponentially decaying with $W_I$ from the side where the input light shines on, and the output current is estimated on interface between P-layer and I-layer.

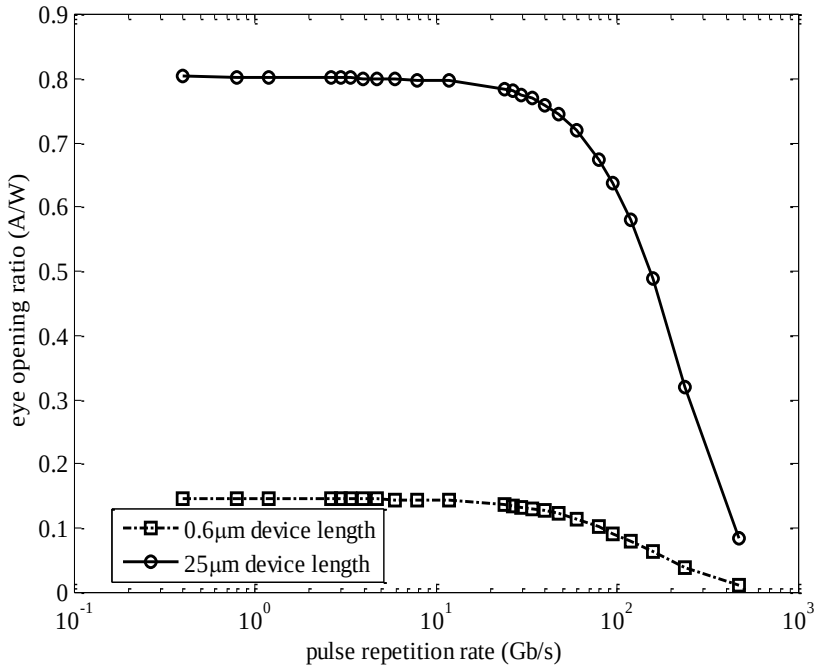


**Figure 7-42** The eye opening ratios of the different FWHM over the repetition frequency under different device length for edge-coupled InP/$In_{0.53}Ga_{0.47}As$/InP PIN photodiode (specification in Table 7-2, 0.3μm I-layer width is chosen) with 1mW input optical power and 1.0 modulation depth under -3V applied bias.

Fig.7-42 shows the effect of reducing the device length over which absorption occurs in an edge-coupled structure. Once the device length is reduced from 25μm to 0.6μm, the eye opening ratio reduces more than 4 times. This also proves that the model that has been set up for edge-coupled device over estimates the performance enhancement relative to a vertical entry structure. This can be improved by updating to 3-Dimensional modelling.

The time spreading ratio is shown in Fig. 7-43. The time spreading ratio does not depend of the input light method and only depends on the FWHM of the input Gaussian wave.

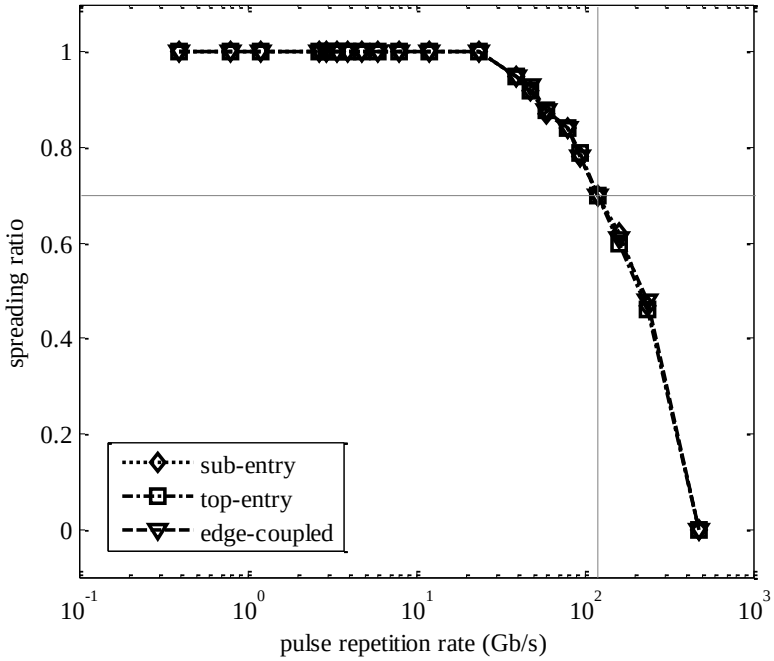


**Figure 7-43** The time spreading ratios of the different FWHM over the repetition frequency under different input light method for InP/$In_{0.53}Ga_{0.47}As$/InP PIN photodiode (specification in Table 7-2, 0.3μm I-layer width is chosen) with 1mW input optical power and 1.0 modulation depth under -3V applied bias.

The effect of varying the repetition ratio $r_{rep}$ as defined before, between $0.5 \leq r_{rep} \leq 1.8$ for a 1ps FWHM Gaussian pulse train on the eye opening ratio versus the repetition frequency relationship is shown in Fig. 7-44.

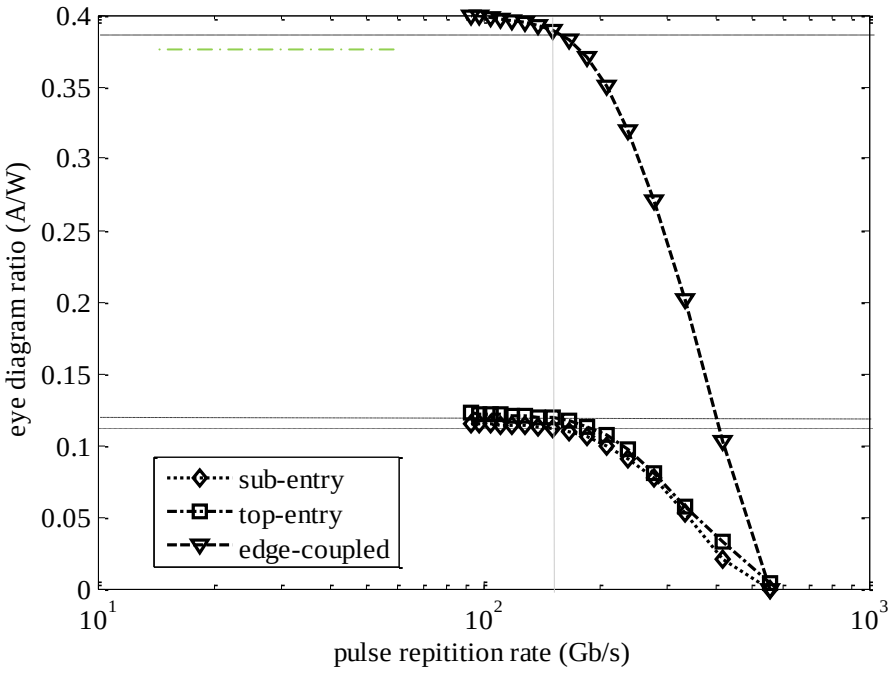


**Figure 7-44** Variation in the eye diagram ratio of the photocurrent pulses induced by pulse trains comprising 1ps FWHM Gaussian pulses versus the repetition frequency under different input light method for InP/$In_{0.53}Ga_{0.47}As$/InP PIN photodiode (specification in Table 7-2 , 0.3μm I-layer width

is chosen) with 1mW input optical power and 1.0 modulation depth under -3V applied bias.

The variation on peak the eye diagram ratio of 1ps FWHM also depends on the input light method. The waveguide input light method has the largest peak eye diagram ratio amount those input light methods. The reasons have been mentioned above. The fastest repetition frequency (at the point when the current pulses start merging) is independent of input light methods and is around 152GHz. The edge-coupled device provides the best way to gain a good output eye diagram without sacrificing the bandwidth.

## 7.4 Discussion

The effect of illuminating an InP/InGaAs/InP double hetero-junction PIN photodiode with Gaussian shaped light pulses of different FWHM values but fixed repetition rate has been analysed in detail in this chapter. For pulse repetition rates greater than the 3dB point, the output current wave can still have recognizable individual near Gaussian shaped pulses, however; the pulse is asymmetrically broadened with the fall-time becoming longer than the rise-time (tail problem). The edge-coupled input light method can give a significantly better eye opening ratio due to two effects. First, the input light absorption area can be smaller than for the vertical input light method to decrease the RC time constant. Second, the effective absorbing length is much greater and counteracts the effect of incomplete optical confinement to the I-layer. The modification in I-layer width can change both the peak of the eye diagram ratio and the bandwidth in InP/InGaAs/InP photodiode. Although the smaller the I-layer width is the wider the transient bandwidth is, the RC time constant bandwidth is reduced when the I-layer is smaller as the capacitance of the device increases. Therefore, when the I-layer is too small, the RC time constant dominates the total bandwidth. The larger the input average optical power is the smaller the eye opening ratio is. That is because the large input average optical power will generate more carriers, and this will lead to the band-filling effect, however larger average input power still produces larger output current with only small degradation of the eye opening ratio by band filling for very fast pulses (1ps FWHM, 4.2ps repetition time). That means the noise will only have a small effect on the large output current. This will definitely benefit the output current for device operation beyond its conventional 3dB point. Modification of doping density in the P-layer and N-layer and applied bias will only make a small change to

the peak value of output current and has little effect of the maximum data rate achievable.

## 7.5 Conclusion

This chapter presented the results of PIN photodiode numerical model. The accuracy of the model was tested by comparing the output current with result from the paper of Dentan [10]. When applying a sequence of Gaussian light pulses to InP/InGaAs/InP photodiode, at data rates significantly greater than the 3dB point, the output current pulse can still be distinct, however the pulses will have a lower peak amplitude and will be asymmetrically broadened compared with output current pulses at lower frequency. For improving the eye diagram of output current, the method of increasing the input average optical power or having comparable smaller I-layer width can be used. Thus optical amplification up to peak power levels $\geq$ 0.1mW immediately prior to detection will bring major benefits to ultra-high data rate digital optical system.

# Chapter 8

## Simulation Results for MQW-EAM

## 8.1 Introduction

In the previous chapter, the performance of InP/InGaAs/InP photodiode structures beyond the 3dB frequency limit has been analysed by detailed device modelling. In this chapter, the one dimensional model of multiple quantum well electro-absorption modulators (MQW-EAM) is applied to study the effect of fast time varying applied bias, in particular for rectangular and Gaussian pulse trains. An example of a rectangular voltage pulse train comprising 40ps/40ps on/off time steps between -1V and 0V is shown in Fig.8-1.

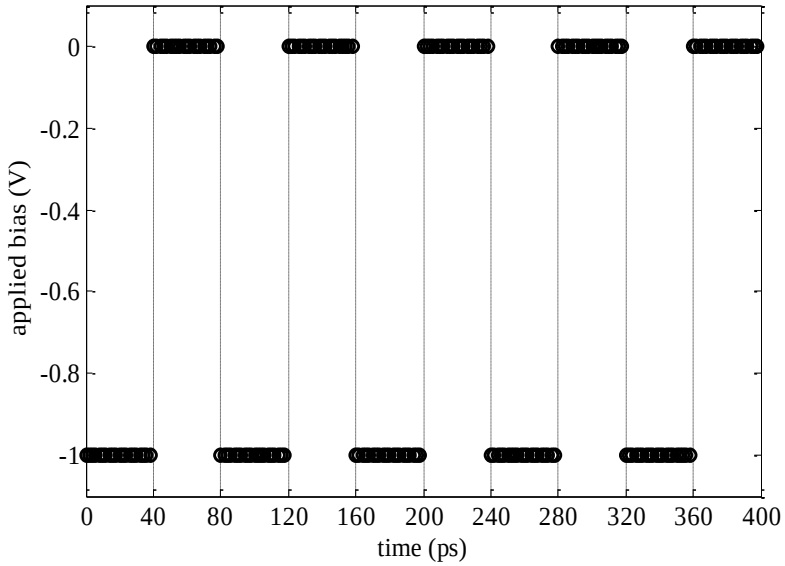


**Figure 8-1** Applied bias -1V/0V with 40ps/40ps on/off time step base for MQW-EAM.

In Fig. 8-1, the black thin dashed line indicates the time when the applied bias changes between -1V and 0V and back again. The black thin dashed line will appear in the rest of the graphs to indicate when the bias is changed. Between 0ps ~ 39ps, 80ps ~ 119ps, 160ps ~ 199ps, 240ps ~ 279ps and 320ps ~ 359ps the bias is equal to -1V. That is the period that the MQW-EAM is able to absorb most of the light under 1.55μm wavelength is indicated as “on time” for the MQW-EAM device. For the other time period, the bias is 0V. This is the time that the MQW-EAM absorb very little amount of light under 1.55μm wavelength is indicated as “off time” for the MQW-EAM device. In real life, the time delay between on and off time need to be taken into consideration and cannot be neglected. In order to analyse the output optical power time delay purely on the effect of carriers, the zero time delay is assumed for applied voltage. The model is a one dimensional modelling meaning that it does not take into account changes in the optical power as light waves

propagate along the waveguide, nor carrier fluxes in the same direction. Two errors introduced by such one-dimensional modelling are that diffusion currents along the waveguide are neglected and the effect of decreasing optical power with distance propagated on photo generation is neglected.

## 8.2 MQW-EAM Model Structure

The basic mesa-type MQW-EAM device structure and its numerical model structure are shown in Fig.8-2.

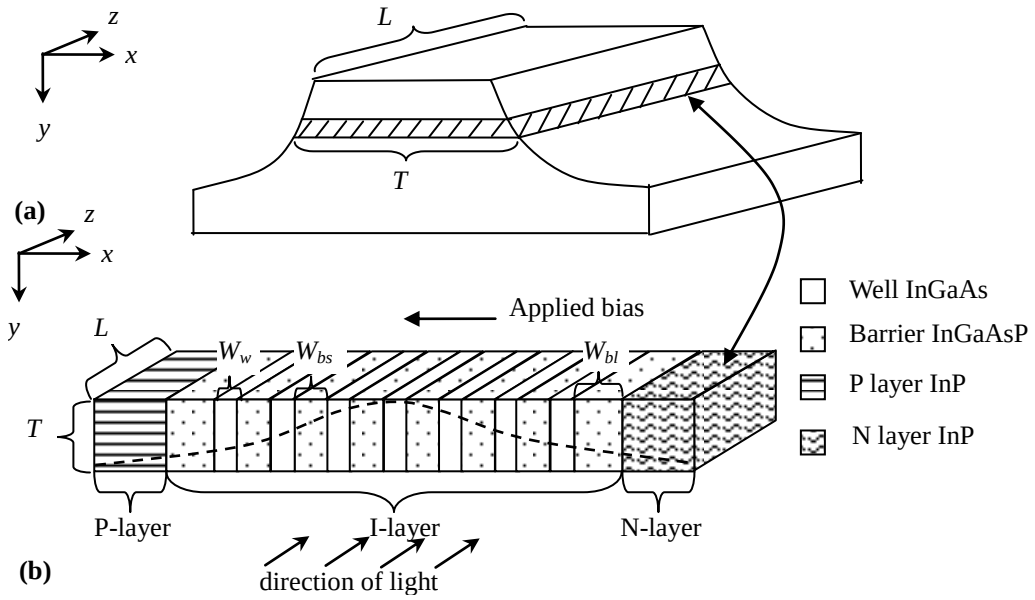


**Figure 8-2 (a)** MQW-EAM InGaAsP/InGaAs device structure and **(b)** the numerical modelled structure.

*L* and *T* represent the length and the thickness of the device. The device contains seven wells, and eight barriers. All the wells have the same width defined as $W_w$. The barriers have two different widths depending on their location, one is named as the long barrier and the other one is the short barrier. $W_{bs}$ is the length for the barriers in between wells, and is shorter than $W_{bl}$ the barriers separating the MQW from the P-layer or N-layer. The numerical modelled structure contained seven wells. That is because the extinction ratio loss and junction capacitance both reduced when the number of wells or the length depletion region is increased [143]. The depletion region can be also increased by having longer length barrier $W_{bl}$. As an edge-coupled device, the input light wave propagates along *z* axis and the generation term is defined as [144],

$$G(t) = \frac{\lambda P(t)\left[1 - e^{-\Gamma_i \alpha z}\right]}{hcW_w TL} \tag{8-1}$$

where $\alpha$ is the absorption coefficient and $\Gamma_i$ is the optical confinement factor for *i-th* well. The generation is assumed to occur only in the wells. According to Eq. (8-1), the generation term should exponentially decay along the *z* axis. Since the numerical model for is one dimensional along *x* axis, *z* is taken as being equal to *L* when evaluating carrier *g*(*t*). Thus, the carrier generation rate used is an average over the device volume and may not reflect conditions on a micron scale. The parameters for the calculation are listed in Table 8-1.

| | P-layer | I-layer | | | N-layer |
|---|---|---|---|---|---|
| | | $W_w$ | $W_{bl}$ | $W_{bs}$ | |
| Material | InP | $In_{0.53}Ga_{0.47}As$ | $In_{0.79}Ga_{0.21}As_{0.45}P_{0.55}$ | | InP |
| Bandgap (eV) | 1.35 [145] | 0.752 [59] | 1.0458 [146] | | 1.35 [145] |
| Width (nm) | 100 | 9.5 | 60 | 14 | 100 |
| Doping ($1/cm^3$) | $1\times10^{18}$ | $3\times10^{18}$ | $3\times10^{18}$ | | $1\times10^{18}$ |
| Refractive index | 3.2026 [147] | 3.7262 [148] | 3.3 [149] | | 3.2026 [147] |
| L (μm) | 80 | | | | |
| T (μm) | 3, 10 | | | | |

**Table 8-1** The simulation parameters for MQW-EAM

With the parameters listed in Table 8-1, the one dimensional numerical model for estimating confinement factors for each well were originally written by Qin Chen (Chinese Academy of Science), and they are listed in Table 8-2. What is more, the variation in the optical confinement factors for the wells devices from the power distribution of light guided in the fundamental mode of the slab waveguide is indicated schematically by the dashed line in Fig.8-2 (b).

| Well No. | Confinement factor |
|---|---|
| 1-*st* well | 0.02335987 |
| 2-*nd* well | 0.02679659 |
| 3-*rd* well | 0.02949664 |
| 4-*th* well | 0.03113257 |
| 5-*th* well | 0.03203950 |
| 6-*th* well | 0.03170746 |
| 7-*th* well | 0.03030964 |

**Table 8-2** The simulation parameters for MQW-EAM

The effective absorption coefficient for MQW-EAM is then estimated by,

$$\alpha_{eff} = \sum_i \alpha_{w\_i}\Gamma_i \tag{8-2}$$

where $\Gamma_i$ is the optical confinement factor and $\alpha_{w\_i}$ is the absorption coefficient of the *i-th* well. The output power of MQW-EAM is defined by,

$$P_{out} = P_{in} \exp\left(-\alpha_{eff} L\right) \tag{8-3}$$

where L is the device length. This neglects possible reflection at the output facet of the device.

For -1V/0V applied bias with 40ps/40ps on/off time step was shown in Fig. 8-1, the time dependent effective absorption coefficient for the device formed by using Eq.(8-2) under different input average power is shown in Fig.8-3 (a) and (b) for input optical power 10mW and 1mW respectively. Note these calculations fully are self-consistent taking into account the effect of changes in the positions of the quasi-Fermi levels.

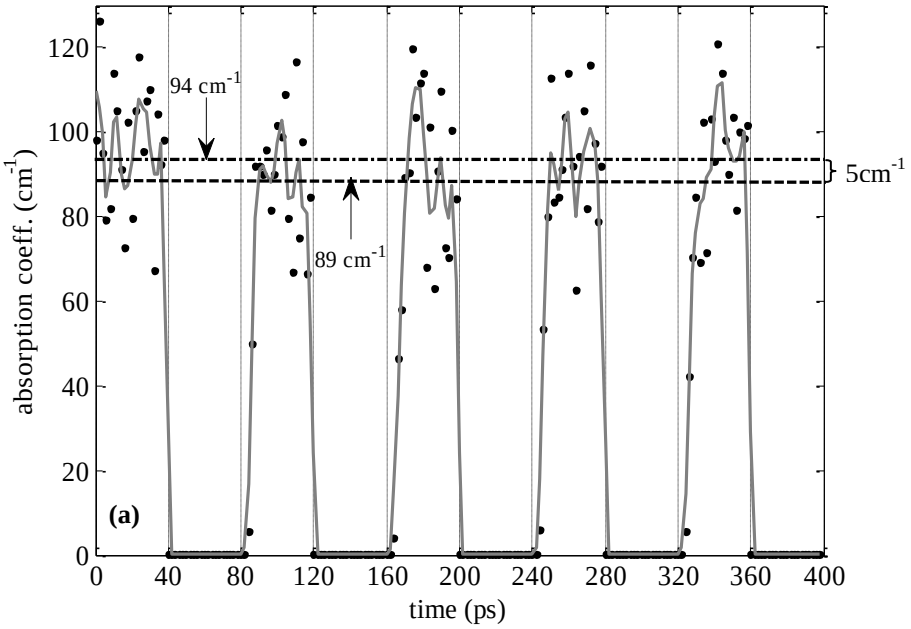

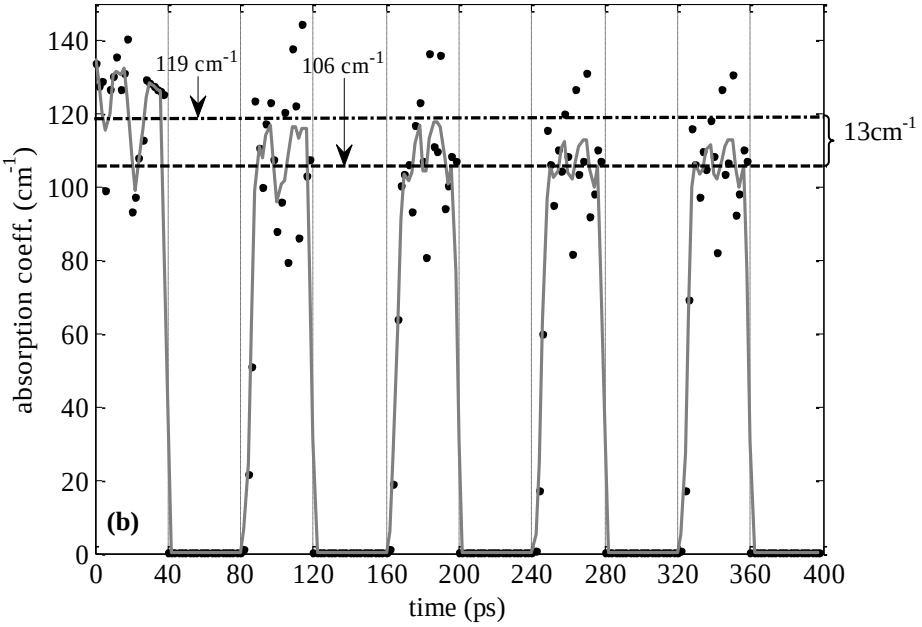


**Figure 8-3** Original data (black dot) and smoothed data (grey solid line) of effective absorption coefficient for InP/InGaAsP/InGaAs 7 wells MQW-EAM with thickness of 10μm under -1V/0V (40ps/40ps on/off time) applied bias and **(a)** 10mW or **(b)** 1mW input average power for the device. The two horizontal lines dashed dot line and dashed line indicate the changes in the average peak value (AVP) of first and second pulse.

As shown in Fig. 8-3(a) and (b), the original data (represented by black dots) contains significant variation that obscures important patterns in the data. The origin in the variation is unknown. Given that the solvers of the Poisson's equation and the current continuity equation are the same as those used in the PIN photodiode simulations, which did not show these variations, it is assumed the variability derives from the impact of the Schrödinger's equation solver on the self-consistent procedure. The instability in absorption coefficient calculation can be reduced by getting rid of the self-consistent calculation of Poisson's equation and Schrödinger equation. This is shown in Fig. 8-4. It is also possible that introducing a more stringent convergence criterion, for example requiring convergence to another significant figure would reduce the variations, however; the cost of a greater run time (three self-consistent loops for three equations) or the self-consistent loops might fall into an infinity calculation in order to achieve a smaller convergence value. Instead data smoothing was introduced to reduce the variability in the data to enable any trends to be observed more clearly.

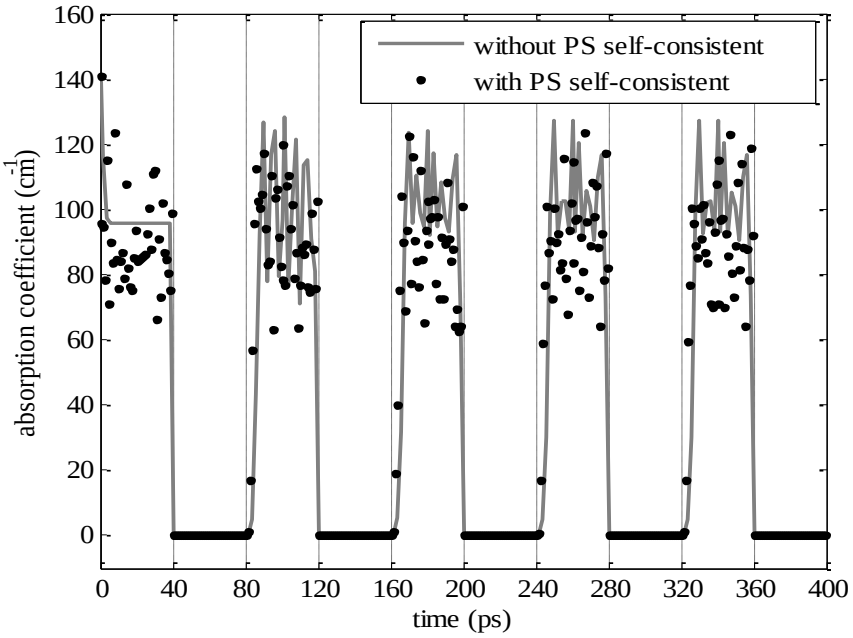


**Figure 8-4** The effective absorption coefficient for InP/InGaAsP/InGaAs 7 wells MQW-EAM with thickness of 10μm under -1V/0V (40ps/40ps on/off time) applied bias and 10mW input average power for the device, **(a)**with all self-consistent calculations (black dot) **(b)**without PS self-consistent calculation (grey solid line).

Data smoothed was introduced by creating approximation function to fit the original data by using the Matlab function package named "smooth()". The best fit to use original data obtained using this function is called "lowess" with 2% span and is shown by the grey solid lines in Fig. 8-3 (a) and (b). In Fig. 8-3 (a) and (b), the average peak values (APV) of the first pulse and second pulse have been indicated by dashed dot lines and dashed lines respectively for the two input optical powers considered. For 10mW input average power, the APV of the first pulse is around 94 $cm^{-1}$. It is smaller than the APV of the first pulse under 1mW input average power, which is 119 $cm^{-1}$. This is because greater absorption saturation occurs under larger input power intensity. The difference between APV of the first pulse and APV of the second pulse is 5$cm^{-1}$ under 10mW input power. The difference increases to 13$cm^{-1}$ when the input power is reduced to 1mW. Whilst the data in Fig. 8-3 is too scattered to show this, the trend of the data for both input power is indicated by the wide solid black line. It is possible that the drop in absorption occurs during the application of a single reverse bias pulse using the higher input optical power. If this interpretation is correct then the lack of a discernible change in the APV of subsequent pulses indicates that a steady state is achieved during a single 40ps on period at this power. This is not the case for an

input optical power level of 1mW where a pulse to pulse reduction in the APV of pulses 1-4 is just discernable.

For this lower input optical power, the APV shown by the smoothed curves in Fig. 8-3 (b) appears to decay over the train of fine on-pulse, reaching a saturation level > 13 $cm^{-1}$ below the APV of the first pulse, approximately a 10% reduction, however; this saturation APV is still higher than the APV of the first bias on-pulse for 10mW input optical power for which the maximum APV is ~ 95 $cm^{-1}$, dropping to ~90$cm^{-1}$ for subsequent on-pulses.

For smaller thickness of the device 3μm was also simulated because it is the common value for the thickness [54], as shown in Fig. 8-5.

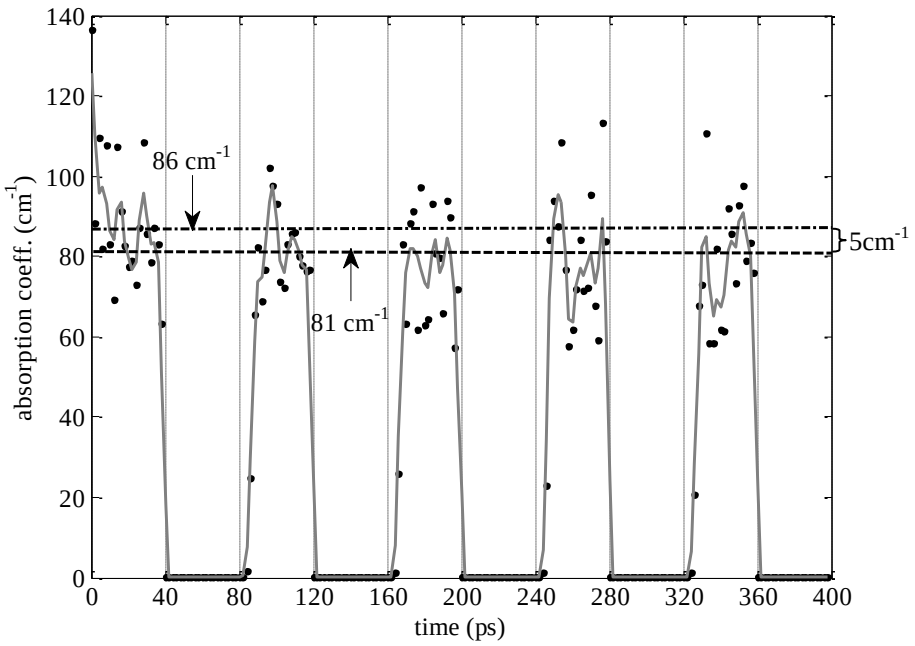


**Figure 8-5** Original data (black dot) and smoothed data (grey solid line) of effective absorption coefficient for InP/InGaAsP/InGaAs 7 wells MQW-EAM with thickness of 3μm under -1V/0V (40ps/40ps on/off time) applied bias and 10mW input average power for the device. Two horizontal lines dashed dot line and dashed line represented the average peak value (AVP) of first and second pulse.

The APVs of the absorption pulses in Fig. 8-5 are smaller compared with the APVs in Fig. 8-3(a). That is because for the waveguide device, smaller thickness means a smaller absorption area for the device, however; the difference between first and second absorption pulses is still around 5$cm^{-1}$, i.e. the same as the Fig. 8-3(a).

It is also easily noticed that apart from the first absorption coefficient pulse, the

onset of the following absorption pulses is time delayed for both power levels from both Fig.8-3 and Fig. 8-5. The cause of the delay is discussed a little later in this chapter. For a clearer view of the effect on the second pulse time delay under different input average power, the overlap of the three sets of smoothed data, and an enlarge view on second pulse, are shown in Fig. 8-6.

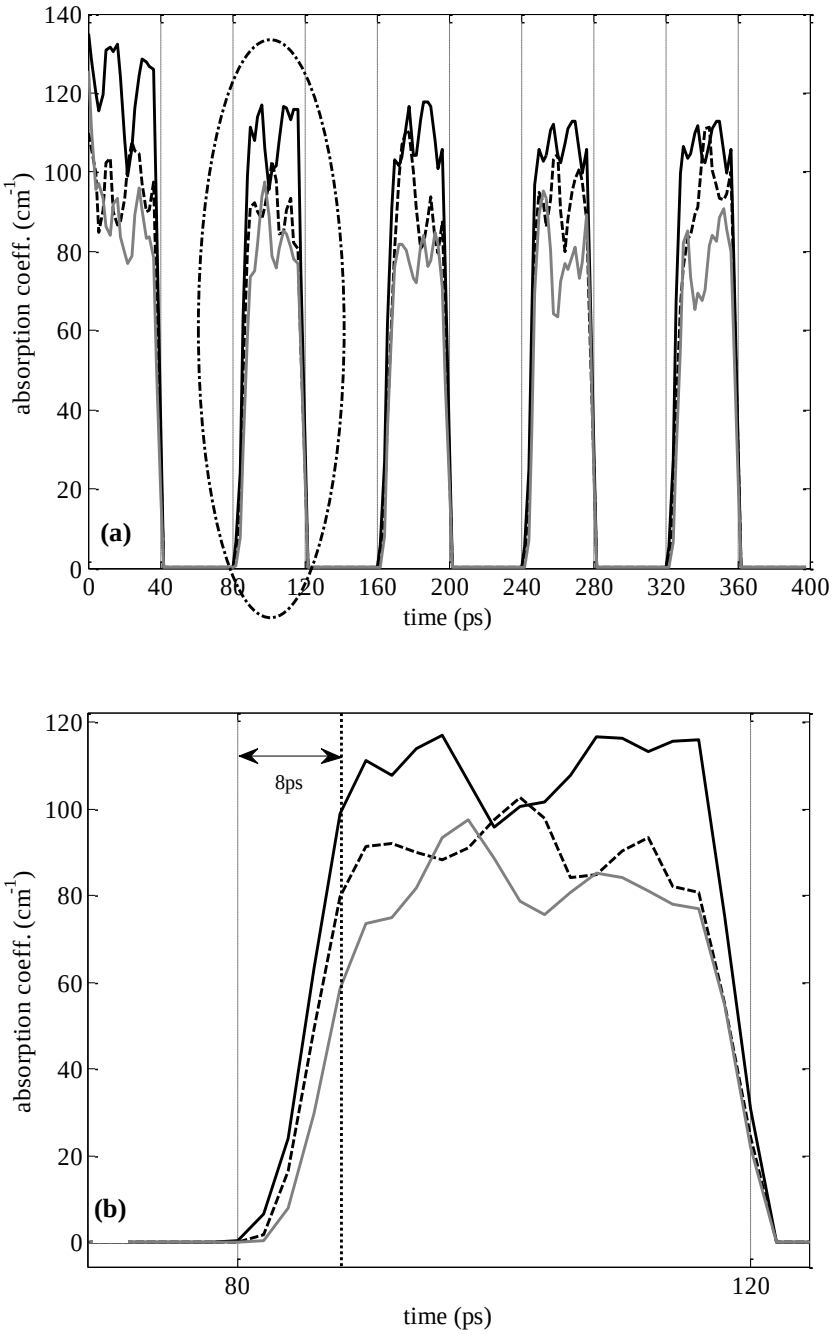


**Figure 8-6** Smoothed data of effective absorption coefficient for a InP/InGaAsP/InGaAs 7 wells MQW-EAM under -1V/0V (40ps/40ps on/off time) applied bias **(a)** five pulses **(b)** second pulse enlarged picture. Black solid line represents 1mW input light power and 10μm device thickness, black dashed line illustrates 10mW input light power and 10μm device thickness and grey solid line is 10mW input light power and 3μm device thickness.

The effective absorption coefficient data shown in Fig. 8-6 is the smoothed data.

The APVs of all pulses for 1mW input average power are largest amount of all three waves as shown in Fig.8-6 (a), however, Fig. 8-6 (b) shows that the delay and rise time of the second pulse is independent of power level and thickness of the device. Further, the unsmoothed data in Fig.8-3 and in Fig. 8-5 also demonstrate an absorption delay time. Therefore, this effect is not an artifact of the smoothing. Another point worth mentioning here is that the delay in achieving an absorbing condition will affect only the falling edge of the light pulses emitted from a MQW-EAM, broadening the light pulses by delaying the transition to the off-state.

To investigate the factors that influence the time delay in the absorption onset for pulses after first absorption coefficient pulse, the bias off time was varied whilst keeping the on time constant. If the on/off time 40ps/40ps, 40ps/30ps and 40ps/50ps are applied to the device respectively, under the same 10mW input average power, the absorption coefficient pulses are shown in Fig. 8-7(a), (b) and (c). Fig. 8-8 (a), (b) and (c) are the enlarged views of second absorption pulse in the chains of absorption pulses in Fig. 8-7 (a), (b) and (c) respectively.

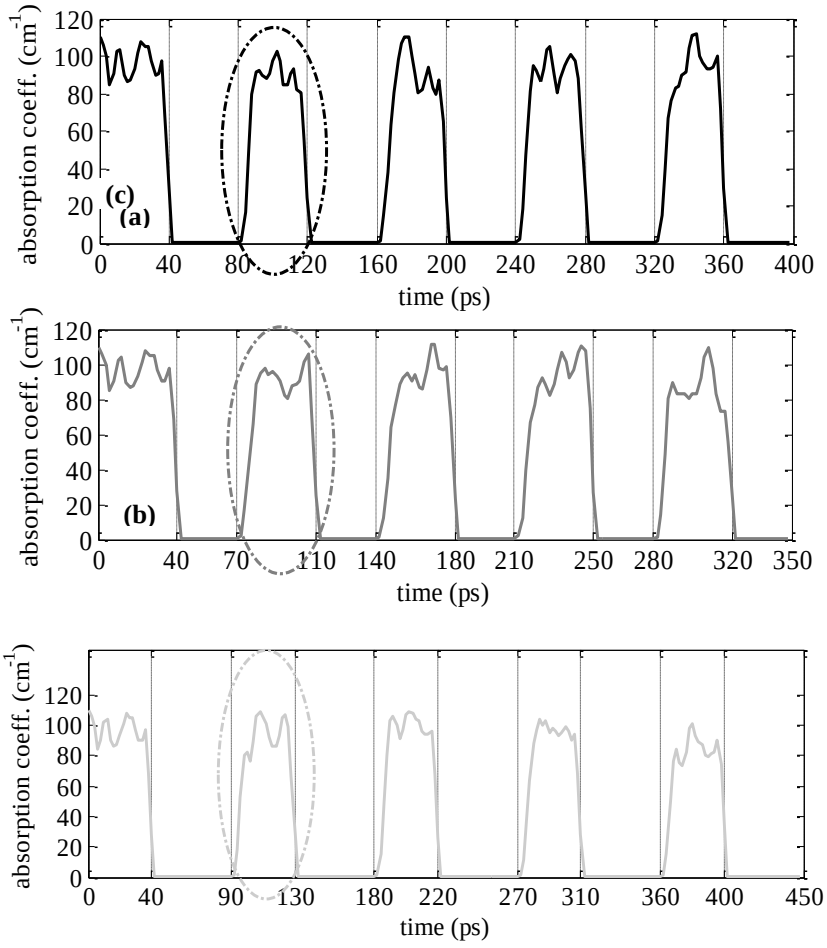

**Figure 8-7** Smoothed data of effective absorption coefficient for InP/InGaAsP/InGaAs 7 wells MQW-EAM with thickness of 10μm under -1V/0V applied bias **(a)** (40ps/40ps on/off time) **(b)** (40ps/30ps on/off time) **(c)** (40ps/50ps on/off time) and 10mW input average power.

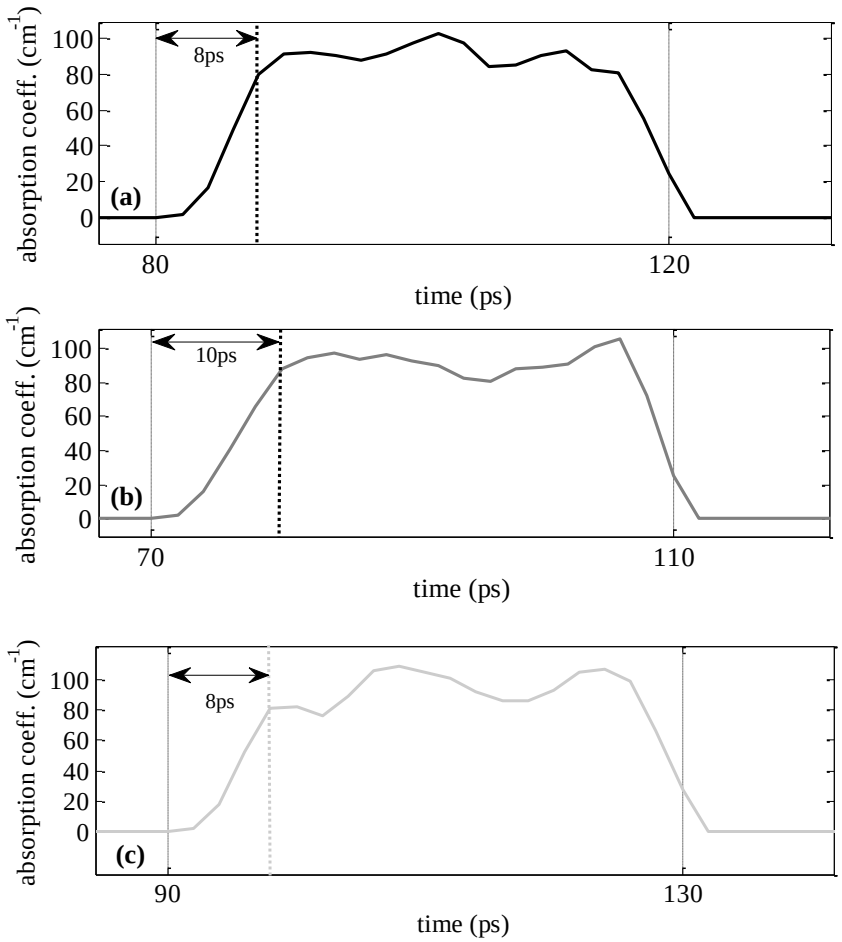


**Figure 8-8** Enlarged view of the second pulses for smoothed data of effective absorption coefficient for InP/InGaAsP/InGaAs 7 wells MQW-EAM with thickness of 10μm under -1V/0V applied bias **(a)** (40ps/40ps on/off time) **(b)** (40ps/30ps on/off time) **(c)** (40ps/50ps on/off time) and 10mW input average power.

The absorption pulse trains with 30ps off time have the longest time delay in the second absorption pulse. That means the shorter off time will cause longer time delay on the next absorption pulses, however, longer off time will not have any effect. The time delay from second to fifth pulses with different off-time in Fig. 8-7 is shown in Fig. 8-9. In Fig. 8-9, the time delay increases as the off-time of the applied bias pulses reduces from 40ps to 30ps whilst the on-time kept the same value (40ps). When then off-time increases from 40ps to 50ps, the time delay is very similar or same values.

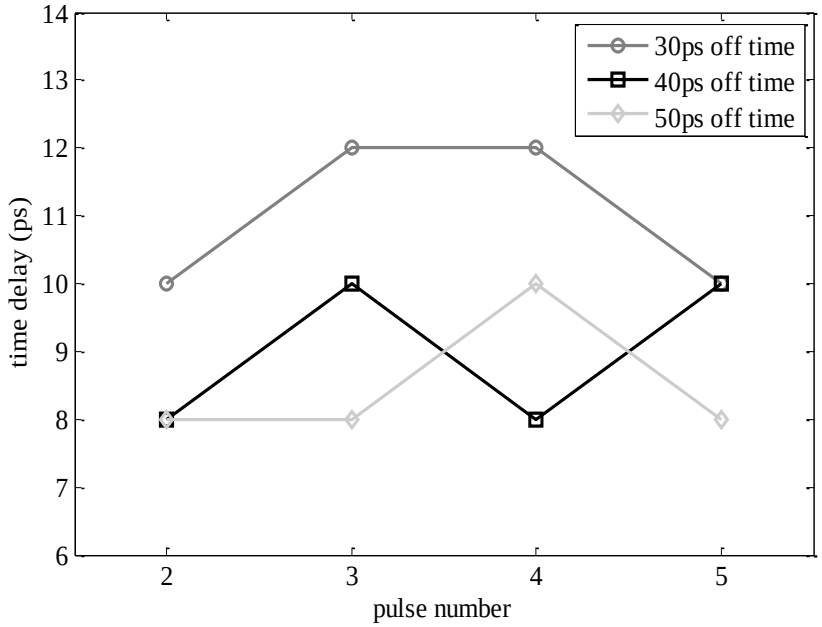


**Figure 8-9** Time delay for InP/InGaAsP/InGaAs 7 wells MQW-EAM with thickness of 10μm under -1V/0V applied bias (40ps/30ps, 40ps/40ps and 40ps/50ps).

Fig. 8-10 shows a comparison of the absorption coefficient pulses that were generated by 40ps/40ps on/off square applied bias pulses with the pulses that were generated by10ps/10ps on/off square applied bias pulses.

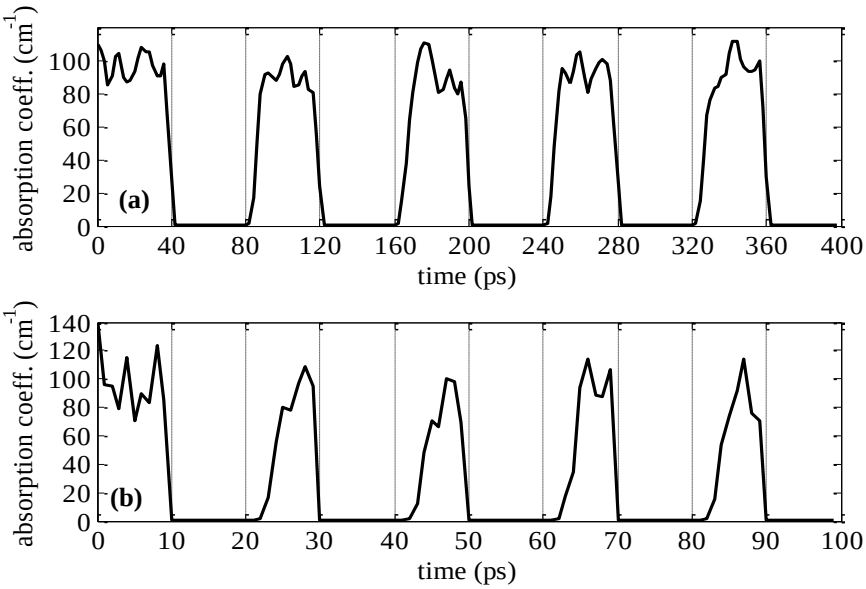


**Figure 8-10** Smoothed data of effective absorption coefficient for InP/InGaAsP/InGaAs 7 wells MQW-EAM with thickness of 10μm under -1V/0V applied bias **(a)** (40ps/40ps on/off time) **(b)** (10ps/10ps on/off time).

The absorption coefficient pulses obtained under 10ps/10ps on/off time applied bias pulse condition have less chance to obtain a square wave shape than the ones

are under 40ps/40ps on/off time applied bias pulses. The time delay from second to fifth pulses with 40ps/40ps on/off time and 10ps/10ps on/off time in Fig. 8-9 is shown in Fig. 8-11.

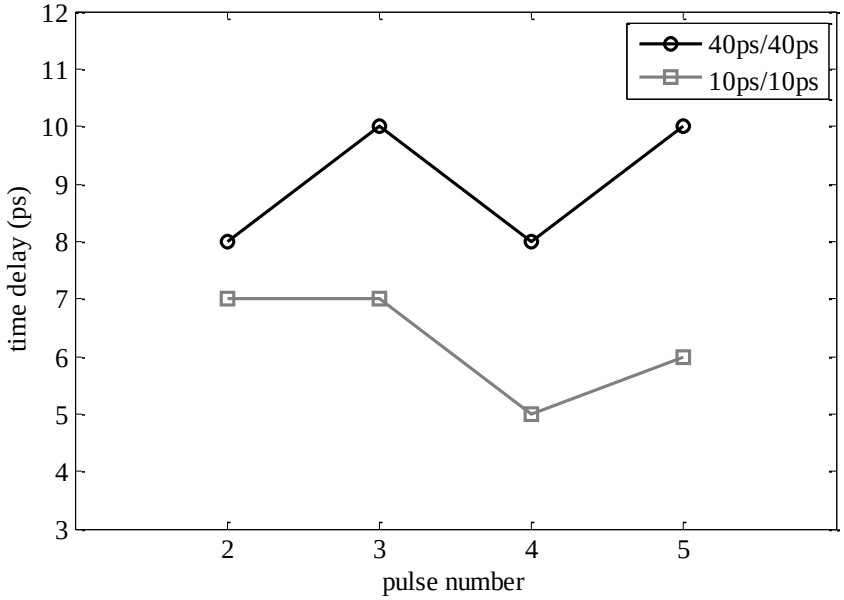


**Figure 8-11** Time delay for InP/InGaAsP/InGaAs 7 wells MQW-EAM with thickness of 10μm under -1V/0V applied bias (40ps/40ps and 10ps/10ps).

As shown in Fig. 8-11, the time delay in 10ps/10ps on/off time bias pulse train is shorter than the time delay for the 40ps/40ps on/off time bias pulses. Comparing the time delay with Fig. 8-9, the time delay in 10ps/10ps on/off output light pulses are actually the lowest for the different on/off light pulses simulated. A possible reason for the lack of increase in the delay despite the much shorter off-time could be because fewer carriers are generated by the shorter 10ps on-time with the result that the absorptions recovery is quicker, however, an argument against this is the fact that the APV is nearly unchanged; i.e. the absorption saturation is the same for 10ps on time as for a 40ps on-time. Therefore, the delay time is not due to the time taken for recovery in the wells but due to incomplete extraction of the photo generated charge from the I-layer. This space charge counteracts the applied bias, reducing the absorption coefficient. This is defined as the local charge screen effect that has been introduced in Chapter 3.

If the applied bias is modified to Gaussian wave with 200ps FWHM and 4.2×FWHM repetition time as shown in Fig. 8-12 (a), and the input optical power is a constant intensity light waveform, then the linear plot of absorption coefficient

pulses is shown in Fig. 8-12 (b). Note that a logarithm scale has been used in Fig.8-12 (c) in order to accurately capture the time dependence in the absorption. The finite rise and fall times of the bias transitions will now impact on the delay in the absorption changes due to carrier escape from the quantum wells and more importantly due to the bias recovery rate, which depends on the time taken to extract photo-generated carriers from the I-layer.

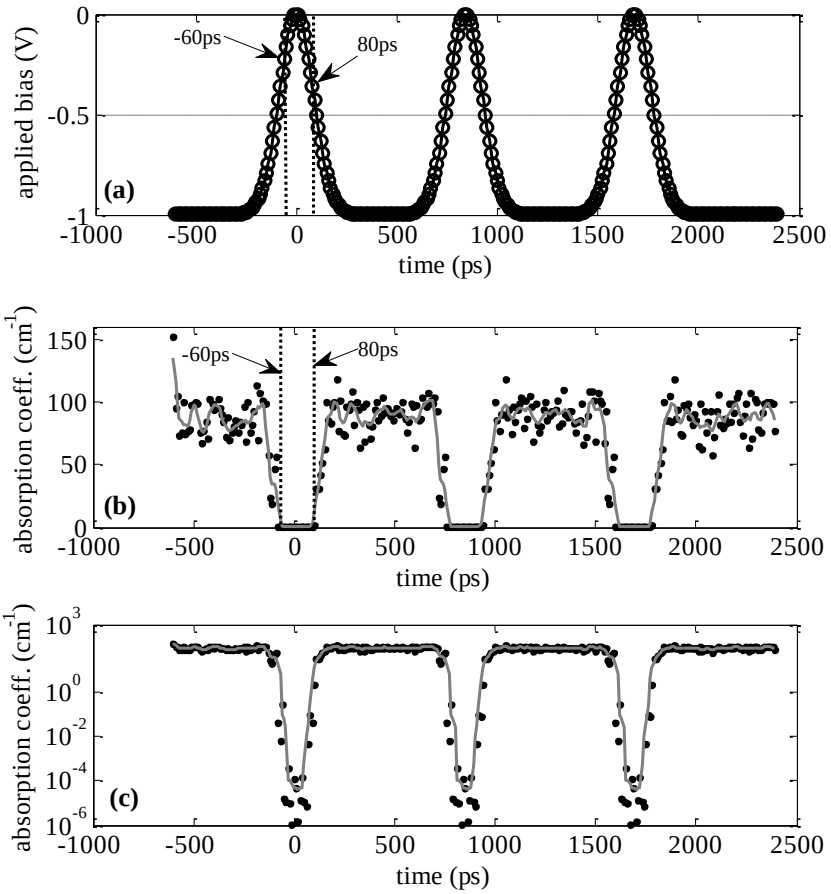


**Figure 8-12 (a)** Gaussian shaped applied bias with 200ps FWHM and **(b)** linear plot of absorption coefficient with original data (black dot) and smoothed data (grey solid line) for InP/InGaAsP/InGaAs 7 wells MQW-EAM with thickness of 10μm. **(c)** logarithms plot of absorption coefficient with original data (black dot) and smoothed data (grey solid line) for InP/InGaAsP/InGaAs 7 wells MQW-EAM with thickness of 10μm.

The applied bias pulses with 200ps FWHM and the consequent pulses in output power are both shown in Fig. 8-13.

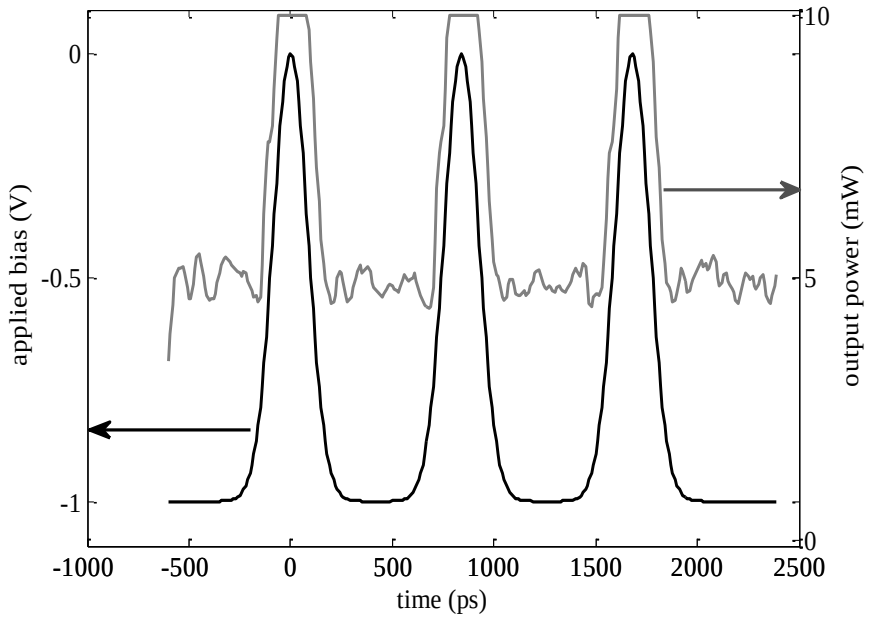


**Figure 8-13** Gaussian shaped applied bias with 200ps FWHM and estimated output power for InP/InGaAsP/InGaAs 7 wells MQW-EAM with thickness of 10μm.

The time dependence in the bias transition has been chosen to realize light pulses having the return-to-zero format found to be optimum for maximizing eye diagram ratio of the electric pulses achieved after photo detection. Based on the result of Chapter 7, the time resolution of ultra-fast photocurrent pulses, after photo detection, is improved if the off-time between Gaussian light pulses exceeds the FWHM of these light pulses. Generating such a pulse train by an MQW-EAM requires the latter to be in an absorbing state for a longer interval than a non-absorbing state during each bit period. As the bit period is reduced to increase the data rate, delay in the onset of the absorption pulses caused by not allowing enough time for the photo-generated carriers to exit the I-layer and rate of recovery in the absorption as the carriers are extracted from the quantum wells will now impact on the performance of the MQW-EAM. Referring to Fig. 8-13, FWHM of the output light pulse is slightly wider than the FWHM of the applied bias pulse. The valley point of the output power pulses cannot reach zero, due to the absorption not being large enough. This can be improved by increasing the length of the device. The peak point of the output power pulses does not appear to follow the Gaussian shape of the bias pulses because the output power will be virtually equal to 10mW when the absorption coefficient drops to a very small value by using Eq. (8-3). The model neglects propagation and reflection losses. Therefore, the output power can only be approximately Gaussian shape. Fig. 8-14 shows the behaviour when the

FWHM of applied bias reduced from 200ps to 10ps and then to 5ps whilst the repetition time is kept at 4.2×FWHM to create a fixed pulse on-off aspect ratio as the bit duration is decreased. Both the applied bias pulses and output light pulses are shown.

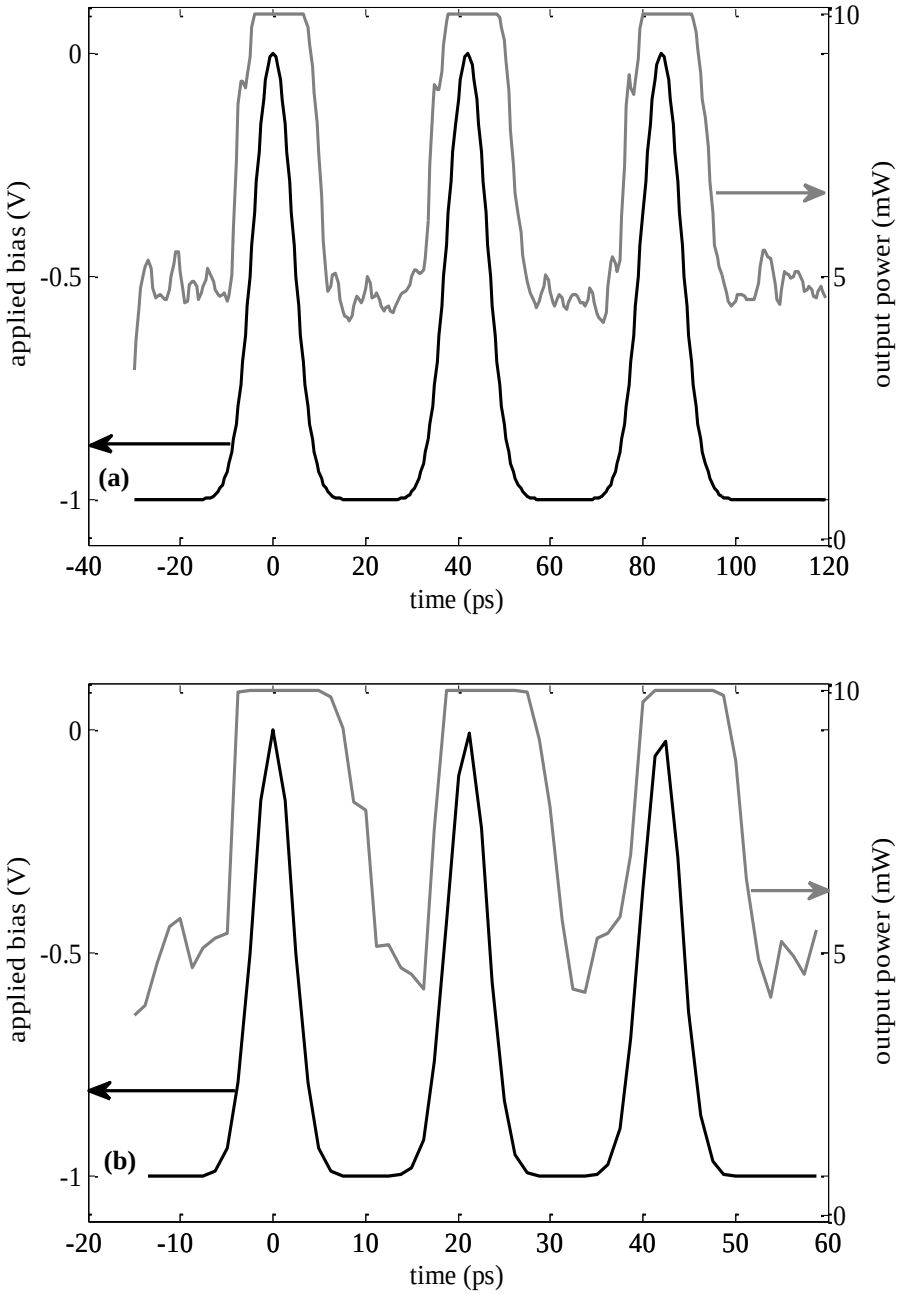


**Figure 8-14** Gaussian shaped applied bias pulses with FWHM of **(a)** 10ps and **(b)** 5ps and their estimated output light pulses for InP/InGaAsP/InGaAs 7 wells MQW-EAM with thickness of 10μm.

Comparing Fig. 8-13 with Fig.8-14 (a) and (b), the FWHM of output power pulses is a lot wider than the applied bias pulses comparing with output power pulse for 200ps FWHM for both 10ps FWHM and 5ps FWHM. What is more, the worst spreading case appears in the case of 5ps FWHM applied bias pulses. In other

words, the input applied bias pulse to output power pulse ratio decreases as the FWHM of input applied bias pulse is reduced. To analyse the spreading effect for different FWHM of Gaussian input applied bias, the spreading ratio $R_{spread}$ is defined as,

$$R_{spread} = \frac{FWHM_{bias}}{FWHM_{OutputPowerl}} \tag{8-4}$$

The spreading ratio against repetition rate is shown in Fig. 8-15. As shown in fig. 8-15, the spreading ratio decreases as the repetition rate increases. The 3dB point is about 11.9GHz.

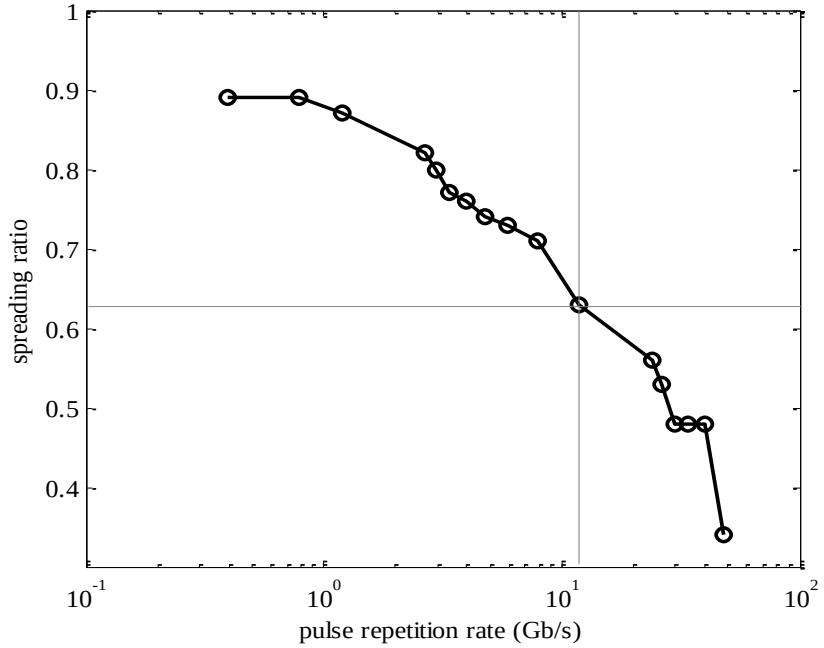


**Figure 8-15** The estimated spreading ratio against different pulse repetition rate for InP/InGaAsP/InGaAs 7 wells MQW-EAM with thickness of 10μm under -1V/0V applied bias and 10mW input average power.

The spreading ratio curve is not smooth in Fig.8-15, and this is because the noise introduced in the output power in the simulation. Using the eye diagram to analyse the output power with respect to repetition frequency, the eye diagram area ratio and the eye diagram height ratio are still defined by Eq. (2-4a) and Eq. (2-4b) in Chapter 2. The eye diagram of the original Gaussian shaped bias is formed shifting the waveform forward by half period with respect to the original Gaussian wave and is shown by the region in-filled with horizontal lines marked out in Fig.8-16. The waveforms shown with grey lines are the optical power output pulses that result from applying the Gaussian bias pulses to the MQW-EAM and its replica delayed by half a bit period to form an eye diagram.

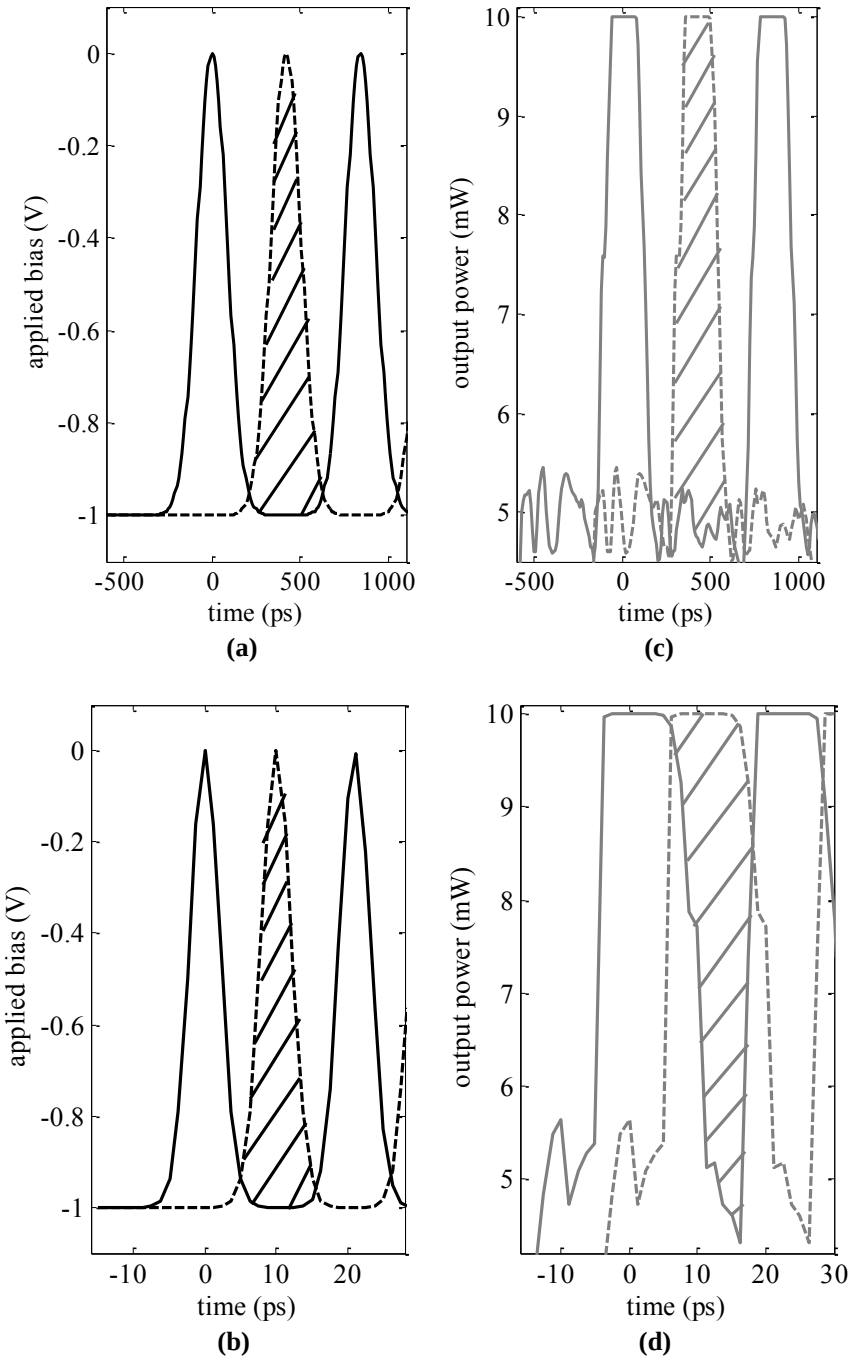


**Figure 8-16** Gaussian shaped applied bias (black solid line) and forward half period Gaussian shaped applied bias (black dashed line) with **(a)** 200ps FWHM, **(b)** 5ps FWHM and **(c), (d)** their estimated output power (grey solid line) and forward half period output power (grey dashed line) for InP/InGaAsP/InGaAs 7 wells MQW-EAM with thickness of 10μm. The eye diagram areas of applied bias for both FWHM are indicated by black horizontal lines and the eye diagram areas of output power for both FWHMs are indicated by grey diagonal lines.

As shown in Fig. 8-16, when the FWHM is decreased from 200ps to 5ps, the output power eye diagram height ratio and eye diagram area ratio does not decrease due to the spreading of the output power pulses. Therefore, the spreading ratio provides a better measure of the quality of the output light pulses. As shown in Fig. 8-16(d),

5ps bias-off pulses produce ~14.5ps wide light pulses which are only distinguishable because of the 21ps bias on time interval between the pulses. Whilst such a long time interval in the absorption on state will give rise to more photo generated carriers which must be extracted from first the quantum wells and then from the I-layer, this need not prevent optimising the bias on/off time interval in a bit period. In the 7 wells structure simulated carrier extraction from the I-layer is the cause of the optical pulse broadening by delaying the return to the absorption time on condition. This delay time can be accounted in optimising the bias on/off time intervals. The delay time means that the 4.2FWHM empirical rule for the PIN photodiode must be revised to a larger off time interval between the bias on time pulses. This is because the I-layer transit time is fixed by geometry and band offset.

## 8.3 Discussion

The simulation of one-dimensional 7 wells InP/InGaAsP/InGaAs MQW-EAM has been modelled for square shaped applied bias pulses and Gaussian shaped applied bias pulses. The absorption coefficient pulses are rather noisy for analysis. Therefore, smoothing has been applied to the original data. The “lowess” method with 2% span in the “smooth()” function by Matlab obtained better smoothed data than other methods. Therefore, this smooth data function applied to the original data throughout this chapter.

Under square shaped applied bias pulses, different parameters have been tested for device property, such as different device thickness, different input average power, different off time and different on/off time. If the thickness of the MQW-EAM device became smaller, the value of absorption coefficient reduced as well. That is simply because for the waveguide device, smaller thickness means smaller absorption area for the device. The decrement in input average power will lead to an increment in the absorption coefficient pulses. That is because absorption saturation occurs more rapidly for larger input light power intensity. The second absorption pulse is in fact reduced more under smaller input power. It is because a steady state is achieved during a single on period at larger input power. The second absorption pulse and the subsequent absorption pulses are all time-delayed under any conditions. It is shown that this delay is caused by the carriers generated from the previous on period pulse not having escaped from the I-layer before further

photo-generation took place. That is also the reason for the increment of the time delay when under the same on time (40ps) the off time decreased from 40ps to 30ps in applied bias. Under 40ps/40ps on/off time applied bias, the model is shown to predict individual square shaped absorption pulses. As the on/off time decreases to 10ps/10ps, the absorption pulses start losing the square shape, however, the time delay is smaller than applied bias pulses with 40ps/40ps on/off time, to confirm the delay time is not due to the time taken for recovery in the wells but due to extraction of the photo generated charge from the I-layer. This space charge counteracts the applied bias, reducing the absorption coefficient.

For the InP/InGaAs/InP PIN photodiode, the output current can still be distinct as the individual pulse for 1ps FWHM Gaussian wave with 4.2ps repetition time under different conditions, however, the FWHM of the output power for the 7 wells InP/InGaAsP/InGaAs MQW-EAM spreads more than twice comparing with the 5ps FWHM applied bias. That means the 7 wells InP/InGaAsP/InGaAs MQW-EAM cannot produce the shortest FWHM Gaussian output power pulses detectable by optimum InP/InGaAs/InP PIN photodiode.

## 8.4 Conclusion

The 7 wells InP/InGaAsP/InGaAs MQW-EAM was investigated by varied parameters. It is proved that the local charge screen effect actually plays an important role in the time delay for the following absorption pulses. The simulation of the one dimensional 7 wells InP/InGaAsP/InGaAs MQW-EAM has proven that the requirement of ultra-fast repetition time for output power is difficult to achieve, as the output power pulses start to merge together. Only the simple result has been presented in this thesis. For future work, more testing on the numerical model is needed and a two dimensional model that extends the length of the device will be useful for analysing the time dependent output power.

# Chapter 9

## Overall Conclusions and Future Work

## 9.1 Conclusions

The thesis presents the result of research based on numerical simulations of the InP/InGaAs/InP PIN photodiode and the InP/InGaAsP/InGaAs MQW-EAM at a wavelength of 1.55 μm. The photodiode device has been analysed in the time domain under mostly large signal conditions and at pulse repetition rates well beyond 3dB frequency point with device parameters varied. These studies have not been done before in the similar numerical model in PIN photodiode. The MQW-EAM numerical model also has been set up for applied bias under the fast repetition time.

The importance of having high speed device was reviewed in Chapter 1. The outline of methods and the content in different chapters were presented in this chapter. The numerical methods for both PIN photodiode and MQW-EAM were briefly introduced.

The reviews for the key physics of PIN photodiode were presented in Chapter 2, and this will help to understand the methods of simulation later. The effect of Franz-Keldysh effect is not included in the absorption calculation in the model. This chapter also includes the introduction of the eye diagram ratio as a method to analyse the results by defining the quality of the output current. It was found that the eye diagram methods developed provide a more intuitive means for analysing the simulated performance of PIN photodiodes and MQW-EAM, under large signal pulsed conditions. Further the eye diagram methods used clearly demonstrate the scope for extending the operational bandwidth of, in particular, edge-coupled PIN photodiodes to well beyond their 3dB bandwidth determined by small signal conditions.

The physical properties of the multiple quantum wells electro-absorption modulator (MQWs-EAM) were discussed in Chapter 3. The absorption coefficient is strongly affected by the quantum confined Stark effect (QCSE). The estimation of absorption coefficient does not include the excitonic effects because of the reported strong broadening of the absorption features in InGaAs(P) materials.

The method of estimating and determining the optical parameters for light

absorbing semiconductors, such as absorption coefficient, the guided wave confinement factor, input light wavelength selection and the generation term calculation were introduced in Chapter 4. The absorption coefficient is only influenced by the confinement factor in edge coupled mode. $InGa_{0.47}As_{0.53}$ is able to absorb the short-wavelength 1.55 μm. The simulations for both the PIN photodiode and the MQW-EAM were performed for this wavelength.

The details of modelling methods for PIN photodiode were presented in Chapter 5. In order to calculate the time dependent output electric current, the self-consistent solution of the Poisson's equation for calculating the electrostatic potential and electric field and continuity equations for the position and time dependent electron and hole carrier concentration are required to be solved. Under suitable boundary conditions for the electrostatic potential and electric field, the modified version of shooting method accompanied by a Runge-Kutta method were applied to solve the Poisson's equation. With reasonable boundary conditions for the carrier concentrations, the inverse matrix method and finite difference method were used to solve the current continuity equation. Our model also included both the diffusion and recombination terms in the intrinsic region and the thermionic emission effect across the hetero-junction.

A detailed definition and modelling theory for MQW-EAM were discussed in Chapter 6. The absorption coefficients and output power were calculated by solving the Poisson's equation, current continuity equation and Schrödinger's equation. For the quantum wells structure, the Poisson's equation included the carrier concentration in the quantum well and the current continuity equation had a different form for quantum wells region. The same numerical methods were used for solving Poisson's equation and current continuity equations. The transfer matrix method and effective mass equation were developed to solve the Schrödinger's equation. The model included both the diffusion and recombination terms in the intrinsic region, the current transport in between quantum well and bulk material, and the thermionic emission effect across the hetero-junction. A special technique of adding the carrier concentration in the wells to the Poisson's equation to make a better approximation was used in the model.

The simulation results and comparisons under different parameters for the InP/InGaAs/InP PIN photodiode were presented in Chapter 7. Different shaped input optical signals were tested in the model. The eye opening ratios of Gaussian wave were estimated and compared under different conditions, such as I-layer width, applied bias, input average power, doping density and input light method. The signals beyond 3dB frequency point had detail analysis under the above mentioned conditions. The Gaussian pulses with fast repetition rate can be detected for photodiode.

First of all, different shaped of input light pulses were tested on the PIN photodiode, such as square wave, constant intensity light wave, Sine wave and Gaussian pulses. All these input light wave and pulses showed a transit time delay in output current wave and pulses. What is more, the un-modulated constant intensity light wave was tested under different I-layer width as well. As expected the transit time reduced as the I-layer width decreased. Beside the transit time, the output current starts falling once it reach its peak value. This trend becomes more and more obvious when the I-layer width reduced. Especially when the I-layer reduced to 0.1μm, the predicted peak current is nearly reduced to zero after 5ps. This is because the saturation effect in the device. It becomes very obvious when the device was under the un-modulated constant intensity light wave. The other properties of the device were investigated more under Gaussian pulses. That is because Gaussian shaped pulses are widely used to simulate the response of active devices and optical fibres in digital communications systems.

The single Gaussian pulse under different FWHM was tested in the model at first. When the FWHM of Gaussian pulse reduced, the output current pulse was broadened compared to the input optical light pulse. What is more, the fall time of the current pulse relative to its rise-time was broadened. It is referred to as the “tail problem” throughout the thesis. The “tail problem” occurred due to the photo-generated carriers taking longer time relative to the duration of the optical stimulation to escape from I-layer when FWHM of Gaussian pulse is reduced. The “tail problem” had more influence when a sequence of Gaussian pulses is input to the device.

For a sequence of Gaussian pulses, different parameters were tested for the PIN photodiode. The different parameters included different I-layer width, applied bias, average input optical power, doping density and light input orientation. The eye opening ratio is determined only by the height of the eye diagram but not the area of the eye diagram. That is because the area of the eye diagram was influenced by the broadening effect as well. This effect was analysed separately by the spreading ratio. Therefore, the height of the eye diagram was considered as the eye opening ratio, however, the cut-off frequency of the PIN photodiode is also affected by the RC time constant. When the I-layer is too thin, the capacitance of the device is increased and the RC time constant starts to dominate the cut-off frequency. The I-layer width is the only parameter that can vary both peak value of eye opening ratio and the bandwidth of the PIN photodiode. The other parameters can only affect the peak value of eye opening ratio. The edge coupled mode input light method had very large output current because the absorption length is bigger than in the vertical light mode. The output current fell when the device length reduced. This also proved that the model that had been set up for edge-coupled device tends to over-estimate the photocurrent. The output current pulses beyond 3dB repetition frequency limit were also analysed in detail under different parameters, the 1ps FWHM with different repetition time is chosen for analysis.

For 1ps FWHM Gaussian pulses with 3.5ps repetition time, the output current pulse spreading was serious because of the "tail problem". Then output current pulse increasingly merges as the number of pulses in the train increases, however, if the repetition ratio, effectively the time interval between pulses, is increased to a suitable value (~≥4.2ps), there was still a chance to obtain well resolved output current pulses. When the number of input optical pulses increased to 8 pulses (1 byte data), the eye diagram slowly closed up with time. Despite this decay the eye diagram remains sufficiently opened for all eight current pulses to prove that the device can receive 1byte data at a very high data rate in this case nearly 240Gb/s, however, this is an optimistic prediction based on transit time consideration only, as the effect of noise and the RC time constant have so far been neglected; also the influence of carrier transport by diffusion along the light pulse (z-axis direction) is neglected in this model. Therefore the current will probably be too small to detect in the real time device at these ultra-high data rates. A method to have a better eye

diagram for 1ps FWHM or data rates beyond 3dB point Gaussian pulses is to increase the input optical power. This can avoid the case when the random noise level is close to the value of output current. This had been proved in section 7.3.3 in Chapter 7.

Finally, the simulation results for the InP/InGaAsP/InGaAs MQW-EAM were presented in Chapter 8. The effects of different device thickness, different input average power with different shaped pulses or different on/off time were tested on the device. It is proved that the local charge screen effect actually plays an important role in the time delay for re-establishing the absorption state of the MQW-EAM. It was demonstrated that extracting the photo-generated charge from the I-layer was the factor that limited the maximum data rate achievable by an MQW-EAM under bias and optical input power conditions assumed. In the model carrier extraction from the quantum wells was not a limiting factor for the 7 wells structure considered. In edge-coupled mode, the generation term should exponentially decay along the device length direction, however, due to the modelling being only one dimensional, it was assumed that the absorption was equally distributed along device length direction. Therefore, the model over-estimated the effect of carrier photo-generation on the electrostatic potential and current flow. This limitation applies to the PIN photodiode too.

The numerical model of InP/InGaAsP/InGaAs MQW-EAM device proved that the fast repetition time of optical power pulses detectable in the type of PIN photodiode simulated is hard to generate. Even for 10ps repetition time of square shaped applied bias, the output power started to lose its shape. It is proved that the local charge screen effect actually plays an important role in the time delay for the following absorption pulses. The simulation on the one dimensional 7 wells InP/InGaAsP/InGaAs MQW-EAM has proven that the requirement of fast repetition time for output power is difficult to achieve, as the output power pulses start to emerge together. The emerging of the pulses is because of the spreading of the output power pulse.

## 9.2 Further Work

The investigation on the photodiode and the analysis on its output data rate beyond

its 3dB frequency limit have met the primary objectives. Although the output current pulses with fast repetition time could be obtained on the InP/InGaAs/InP photodiode device, there is a need to compare and confirm the simulation results with measurement. Suitable measurement data is hard to find in the open literature and effects like parasitic capacitances make comparison difficult. Even so, a device manufacturer should be in a good position to test the results in this thesis against practice and if found valid, to use the simulators developed to assist product development for future broadband optical networks.

The simulation on photodiode for edge-coupled mode is only one dimensional. The absorption was assumed to be equally distributed along device length direction. Therefore, the model has over-estimated the effect of carrier photo-generation on the electrostatic potential and current flow. The only solution to improve the accuracy is to have two dimensional numerical model. Then the absorption coefficient can be estimated accurately across the device length. That is the main limitation for analysing the edge-coupled PIN photodiode. Further work to develop two or even three dimensional simulators will advance the design of devices for new-generation optical networks.

One dimensional simulation is a limitation factor for the MQW-EAM for the same reason. As a guided wave device, advancing MQW-EAM design would benefit from the development of a two/three dimensional model. What is more, the simulations of the MQW-EAM do not form a detailed investigation of the device due to time limitation. The existing simulator can be used to model the effects of varying the number of quantum wells and especially, the I-layer design. The model clearly demonstrated that carrier extraction from the I-layer is potentially a more severe problem than the build-up of photo generated carriers in the quantum wells. Thinner I-layer and smaller band-offsets to the P-type and N-type layers may reduce the problem of extracting carriers from the I-layer. Further simulations with the existing simulator would elucidate this, to enable optimisation of the active layer of the device.

Extending the model to deal with a Schottky contact device (replacing the P-layer) would advance the development of new concepts for high data rate MQW-EAMs.

This may require better convergence than the existing model achieves. A more stable Poisson's equation numerical solver is required than the existing basic shooting method. This is believed to be the cause of the "noise" in the results of the MQW-EAM simulations. Clearly effort directed towards eliminating the "noise" problem would be worthwhile.

## Appendix I Momentum Matrix Element

Momentum Matrix Element (Bulk Semiconductor)

$$\left|\hat{e}\cdot p_{cv}\right|^2 = M_b^2$$

where $M_b^2 = \left(\frac{m_0}{m_e^*} - 1\right)\frac{m_0 E_g\left(E_g + \Delta\right)}{6\left(E_g + \frac{2}{3}\Delta\right)}$, $\Delta$ is the split-off energy.

Momentum Matrix Element (Quantum Wells)

TE Polarization

$$\left|\hat{e}\cdot p_{cv}\right|^2 = \left\langle\left|\hat{e}\cdot M_{c-hh}\right|^2\right\rangle = \frac{3}{4}\left(1+\cos^2\theta\right)M_b^2$$

$$\left|\hat{e}\cdot p_{cv}\right|^2 = \left\langle\left|\hat{e}\cdot M_{c-lh}\right|^2\right\rangle = \left(\frac{5}{4} - \frac{3}{4}\cos^2\theta\right)M_b^2$$

TM Polarization

$$\left|\hat{e}\cdot p_{cv}\right|^2 = \left\langle\left|\hat{e}\cdot M_{c-hh}\right|^2\right\rangle = \frac{3}{2}\sin^2\theta M_b^2$$

$$\left|\hat{e}\cdot p_{cv}\right|^2 = \left\langle\left|\hat{e}\cdot M_{c-lh}\right|^2\right\rangle = \left(\frac{1}{2} + \frac{3}{2}\cos^2\theta\right)M_b^2$$

where $\cos^2\theta = \frac{E_{en} + \left|E_{hm}\right|}{E_{en} + \left|E_{hm}\right| + E_t}$,

$$k_t = \sqrt{\frac{2m_r}{\hbar^2}\left(\hbar\omega - E_{hm}^{en}\right)},$$

$$E_t = \frac{\hbar^2 k_t^2}{2m_r} = \hbar\omega - E_{hm}^{en}.$$

## Appendix II Transfer Matrix

Condition I,

$E < V_{EPi}, E < V_{EPi+1}$

$$M_i(1,1) = \frac{1}{2}\left(1 + \frac{\beta_{WFi} m_{i+1}^*}{\beta_{WFi+1} m_i^*}\right) \exp\left[(\beta_{WFi} - \beta_{WFi+1}) x_i\right]$$

$$M_i(1,2) = \frac{1}{2}\left(1 - \frac{\beta_{WFi} m_{i+1}^*}{\beta_{WFi+1} m_i^*}\right) \exp\left[(-\beta_{WFi} - \beta_{WFi+1}) x_i\right]$$

$$M_i(2,1) = \frac{1}{2}\left(1 - \frac{\beta_{WFi} m_{i+1}^*}{\beta_{WFi+1} m_i^*}\right) \exp\left[(\beta_{WFi} + \beta_{WFi+1}) x_i\right]$$

$$M_i(2,2) = \frac{1}{2}\left(1 + \frac{\beta_{WFi} m_{i+1}^*}{\beta_{WFi+1} m_i^*}\right) \exp\left[(-\beta_{WFi} + \beta_{WFi+1}) x_i\right]$$

Condition II,

$E < V_{EPi}, E > V_{EPi+1}$

$$M_i(1,1) = \left[\sin(\alpha_{WFi+1} x_i) + \frac{\beta_{WFi} m_{i+1}^*}{\alpha_{WFi+1} m_i^*} \cos(\alpha_{WFi+1} x_i)\right] \exp(\beta_{WFi} x_i)$$

$$M_i(1,2) = \left[\sin(\alpha_{WFi+1} x_i) - \frac{\beta_{WFi} m_{i+1}^*}{\alpha_{WFi+1} m_i^*} \cos(\alpha_{WFi+1} x_i)\right] \exp(-\beta_{WFi} x_i)$$

$$M_i(2,1) = \left[\cos(\alpha_{WFi+1} x_i) - \frac{\beta_{WFi} m_{i+1}^*}{\alpha_{WFi+1} m_i^*} \sin(\alpha_{WFi+1} x_i)\right] \exp(\beta_{WFi} x_i)$$

$$M_i(2,2) = \left[\cos(\alpha_{WFi+1} x_i) + \frac{\beta_{WFi} m_{i+1}^*}{\alpha_{WFi+1} m_i^*} \sin(\alpha_{WFi+1} x_i)\right] \exp(-\beta_{WFi} x_i)$$

Condition III,

$E > V_{EPi}, E < V_{EPi+1}$

$$M_i(1,1) = \frac{1}{2}\left[\sin(\alpha_{WFi}x_i) + \frac{\alpha_{WFi}m_{i+1}^*}{\beta_{WFi+1}m_i^*}\cos(\alpha_{WFi}x_i)\right]\exp(-\beta_{WFi+1}x_i)$$

$$M_i(1,2) = \frac{1}{2}\left[\cos(\alpha_{WFi}x_i) - \frac{\alpha_{WFi}m_{i+1}^*}{\beta_{WFi+1}m_i^*}\sin(\alpha_{WFi}x_i)\right]\exp(-\beta_{WFi+1}x_i)$$

$$M_i(2,1) = \frac{1}{2}\left[\sin(\alpha_{WFi}x_i) - \frac{\alpha_{WFi}m_{i+1}^*}{\beta_{WFi+1}m_i^*}\cos(\alpha_{WFi}x_i)\right]\exp(\beta_{WFi+1}x_i)$$

$$M_i(2,2) = \frac{1}{2}\left[\cos(\alpha_{WFi}x_i) + \frac{\alpha_{WFi}m_{i+1}^*}{\beta_{WFi+1}m_i^*}\sin(\alpha_{WFi}x_i)\right]\exp(\beta_{WFi+1}x_i)$$

Condition IV,

$E > V_{EPi}, E > V_{EPi+1}$

$$M_i(1,1) = \sin(\alpha_{WFi}x_i)\sin(\alpha_{WFi+1}x_i) + \frac{\alpha_{WFi}m_{i+1}^*}{\alpha_{WFi+1}m_i^*}\cos(\alpha_{WFi}x_i)\cos(\alpha_{WFi+1}x_i)$$

$$M_i(1,2) = \cos(\alpha_{WFi}x_i)\sin(\alpha_{WFi+1}x_i) - \frac{\alpha_{WFi}m_{i+1}^*}{\alpha_{WFi+1}m_i^*}\sin(\alpha_{WFi}x_i)\cos(\alpha_{WFi+1}x_i)$$

$$M_i(2,1) = \sin(\alpha_{WFi}x_i)\cos(\alpha_{WFi+1}x_i) - \frac{\alpha_{WFi}m_{i+1}^*}{\alpha_{WFi+1}m_i^*}\cos(\alpha_{WFi}x_i)\sin(\alpha_{WFi+1}x_i)$$

$$M_i(2,2) = \cos(\alpha_{WFi}x_i)\cos(\alpha_{WFi+1}x_i) + \frac{\alpha_{WFi}m_{i+1}^*}{\alpha_{WFi+1}m_i^*}\sin(\alpha_{WFi}x_i)\sin(\alpha_{WFi+1}x_i)$$

# References


1. Audren, J., Andersson, J., *et al.*, *Second Strategic Research Agenda in Photonics: Lighting the way ahead*. 2nd ed, ed. Flaig, K. and Wilkens, M. 2010: European Technology Platform Photonics21.
2. *Broadband Optical Access Networks and Fiber-to-the-Home: Systems Technologies and Deployment Strategies*, ed. Lin, C. 2006: John Wiley & Sons, Ltd. 334.
3. Shimizu, N., Muramoto, Y., *et al. High Speed InP/InGaAs Uni-Traveling-Carrier Photodiodes*. in *Indium Phosphide and Related Materials, 2000. Conference Proceedings. 2000 International Conference on*. 2000.
4. Dehlinger, G., Koester, S.J., *et al.*, *High-Speed Germanium-on-SOI Lateral PIN Photodiodes.* Photonics Technology Letters, IEEE, 2004. **16**(11): p. 2547-2549.
5. Lin, L.Y., Wu, M.C., *et al.*, *High-Power High-Speed Photodetectors-Design, Analysis, and Experimental Demonstration.* Microwave Theory and Techniques, IEEE Transactions on, 1997. **45**(8): p. 1320-1331.
6. Ishibashi, T., Kodama, S., *et al.*, *High-Speed Response of Uni-Traveling-Carrier Photodiodes.* Japanese Journal of Applied Physics, 1997. **36**: p. 6263-6268.
7. Knox, F.M., Forysiak, W., *et al.*, *10-Gbt/s Soliton Communication Systems over Standard Fiber at 1.55 um and the Use of Dispersion Compensation.* Lightwave Technology, Journal of, 1995. **13**(10): p. 1955-1962.
8. Mukasa, K., Akasaka, Y., *et al. Novel Network Fiber to Manage Dispersion at 1.55um with Combination of 1.3um Zero Dispersion Single Mode Fiber*. in *Integrated Optics and Optical Fibre Communications, 11th International Conference on, and 23rd European Conference on Optical Communications (Conf. Publ. No.: 448)*. 1997.
9. Williams, K.J., Esman, R.D., *et al.*, *Nonlinearities in p-i-n Microwave Photodetectors.* Journal of Lightwave Technology, 1996. **14**(1): p. 84-96.
10. Dentan, M. and de Cremoux, B., *Numerical Simulation of the Nonlinear Response of a p-i-n Photodiode under High Illumination.* Journal of Lightwave Technology, 1990. **8**(8): p. 1137-1144.
11. Sabella, R. and Merlie, S., *Analysis of InGaAs p-i-n Photodiode Frequency Response.* IEEE Journal of Quantum Electronics, 1993. **29**(3): p. 906-916.
12. Wu, T. and Vorst, A.V., *Nonlinearities in GaInAs/InP p-i-n Photodetectors.* Microwave and Optical Technology Letters, 1996. **13**(5): p. 297-300.
13. Snowden, C.M., *Introduction to Semiconductor Device Modelling*. 1986: World Scientific Publishing Co Pte Ltd.
14. Gautier, C., Orsal, B., *et al.*, *Evidence of Deep-Level Defects in an MQW Electroabsorption Modulator through Current-Voltage and Electrical Noise Characterization.* Quantum Electronics, IEEE Journal of, 1999. **35**(11): p. 1640-1648.
15. Horio, K. and Yanai, H., *Numerical Modeling of Heterojunctions Including the Thermionic Emission Mechanism at the Heterojunction Interface.* Electron Devices, IEEE Transactions on, 1990. **37**(4): p. 1093-1098.

16. Wang, J., Leburton, J.P., *et al.*, *Modeling of the Optical Properties of a Barrier, Reservoir, and Quantum-Well Electron Transfer Structure.* Quantum Electronics, IEEE Journal of, 1994. **30**(4): p. 989-996.
17. Wilson, S.P., Allsopp, D.W.E., *et al.*, *Application of an Efficient Algorithm for Solving the One-Band Effective Mass Equation Self-Consistently in the Modelling of Some Low-Dimensional Structure Devices.* International Journal of Numerical Modelling: Electronic Networks, Devices and Fields, 1992. **5**(1): p. 23-39.
18. Nag, B.R., *Physics of Quantum Well Devices*. Solid-State Science and Technology Library. 2000: Kluwer Academic Publishers.
19. Zhu, D.X., Dubovitsky, S., *et al.*, *Ambipolar Diffusion Coefficient and Carrier Lifetime in a Compressively Strained InGaAsP Multiple Quantum Well Device.* Applied Physics Letters, 1997. **71**(5): p. 647-649.
20. Keiser, G., *Optical Communications Essentials*. 2003: McGraw-Hill Professional.
21. Agrawal, G.P., *Lightwave Technology: Components and Devices*. 2004: Wiley-Interscience.
22. Adachi, S., *GaAs and Related Materials: Bulk Semiconducting and Superlattice Properties*. 1994: World Scientific Publishing Co. Pte. Ltd. .
23. Nomura, Y., Akiyama, K., *et al. Numerical Analysis of Effects of Incident Light Intensities on Extinction Ratio and Alpha Parameter of InGaAsP-InP Multi-Quantum-Well Modulator*. in *Numerical Simulation of Optoelectronic Devices, 2004. NUSOD '04. Proceedings of the 4th International Conference on*. 2004.
24. Ramey, S.M. and Khoie, R., *Modeling of Multiple-Quantum-Well Solar Cells Including Capture, Escape, and Recombination of Photoexcited Carriers in Quantum Wells.* Electron Devices, IEEE Transactions on, 2003. **50**(5): p. 1179-1188.
25. McQuarrie, D.A., *Quantum Chemistry*. 2nd ed. 2008: University Science Books.
26. Sackinger, E., *Broadband Circuits for Optical Fiber Communication*. 2005: Wiley InterScience.
27. Grote, N. and Venghaus, H., eds. *Fibre Optic Communication Devices*. Springer Series in Photonics, ed. Kamiya, T., Monemar, B., *et al.* 2001, Springer-Verlag Berlin Heidelberg.
28. Ghione, G. and Torino, P.d., *Semiconductor Devices for High-Speed Optoelectronics*. 2009: Cambridge University Press. 480.
29. Zheng, J., *Optical Frequency-Modulated Continuous-Wave (FMCW) Interferometry*. 2005: Springer Science+Business Media, Inc. .
30. Ściana, B., Radziewicz, D., *et al.*, *Technology and Properties of GaAs Doping Superlattices.* Materials Science-Poland, 2008. **26**(1): p. 71-78.
31. Wada, O., *Optoelectronic Integration: Physics, Technology, and Applications*. 1994: Kluwer Academic Publishers.
32. Miller, D.A.B., Chemla, D.S., *et al.*, *Band-Edge Electroabsorption in Quantum Well Structures: The Quantum-Confined Stark Effect.* Physical Review Letters, 1984. **53**(22): p. 2173-2176.
33. Miller, D.A.B., Chemla, D.S., *et al.*, *Electric Field Dependence of Optical Absorption near the Band Gap of Quantum-Well Structures.* Physical Review B, 1985. **32**(2): p. 1043-1060.
34. Daniela Dragoman, M.D., *Advanced Optoelectronic Devices*. 1998: Springer-Verlag Berlin and Heidelberg GmbH & Co. K.

35. Fukuda, M., *Optical Semiconductor Devices*. 1999: John Wiley & Sons, Inc.
36. Morrison, G.B., Raring, J.W., *et al.*, *Electroabsorption Modulator Performance Predicted from Band-Edge Absorption Spectra of Bulk, Quantum-Well, and Quantum-Well-Intermixed InGaAsP Structures.* Solid-State Electronics, 2007. **51**(1): p. 38-47.
37. Murphy, E.J., *Integrated Optical Circuits and Components: Design and Applications*. 1999: Marcel Dekker Ltd.
38. McMeekin, S.G., Taylor, M.R.S., *et al. Franz-Keldysh Effect in an Optical Waveguide Containing a Resonant Tunneling Diode*. in *Lasers and Electro-Optics Europe, 1994 Conference on*. 1994.
39. Figueiredo, J.M.L., Stanley, C.R., *et al.*, *Optical modulation in a resonant tunneling relaxation oscillator*. 2005.
40. Axt, V.M. and Kuhn, T., *Femtosecond Spectroscopy in Semiconductors: A Key to Coherences, Correlations and Quantum Kinetics.* Reports on Progress in Physics, 2004(4): p. 433.
41. Sanchez, T.G., Perez, J.E.V., *et al.*, *Electron Transport in InP under High Electric Field Conditions.* Semiconductor Science and Technology, 1992(1): p. 31.
42. Lopez-Hiquera, J.M., *Handbook of Optical Fibre Sensing Technology*. 2002: Wiley.
43. Lin, C.F., *Optical Components for Communications: Principles and Applications*. 2004: Kluwer Academic Publishers.
44. *WDM Technologies: Active Optical Components* Optics and Photonics Series ed. Fujiwara, M., Dutta, N.K., *et al.* 2002: Academic Press.
45. Singh, J., *Electronic and Optoelectronic Properties of Semiconductor Structure*. 2003: Cambridge University Press.
46. Alexander, S.B., *Optical Communication Receiver Design (Spie Tutorial Text in Optical Engineering)*. 2006: SPIE Society of Photo-Optical Instrumentation Engi. 340.
47. Tretter, S.A., *Communication System Design Using DSP Algorithms: with Laboratory Experiments for the TMS320C6701 and TMS320C6711*. 2003: Springer. 328.
48. Bullock, S.R., *Transceiver and System Design for Digital Communications*. 2nd ed. 2000: Noble Publishing Corporation. 280.
49. Sterling, D.J., Pardoe, T.D., *et al.*, *Technician's Guide to Fiber Optics*. 4th ed. 2003: Delmar Cengage Learning.
50. Decoster, D. and Harari, J., *Optoelectronic Sensors*. 2009: Wiley-Blackwell
51. Sze, S.M. and Ng, K.K., *Physics of Semiconductor Devices* 3rd ed. 1981: John Wiley & Sons, Inc. . 832.
52. Rogalski, A., *Foundamentals of Infrared Detector Technologies*. 2nd ed. 2010: CRC Press. 898.
53. Xiong, B., Sun, C., *et al.*, *Optimization of Multiple Quantum Well Electroabsorption Modulators Based on Transmission Performance Simulation.* Japanese Journal of Applied Physics, 2007. **46**: p. 3420-3423.
54. Hojfeldt, S. and Mork, J., *Modeling of Carrier Dynamics in Quantum-Well Electroabsorption Modulators.* Selected Topics in Quantum Electronics, IEEE Journal of, 2002. **8**(6): p. 1265-1276.
55. Bennett, B.R., Soref, R.A., *et al.*, *Carrier-Induced Change in Refractive Index of InP, GaAs and InGaAsP.* Quantum Electronics, IEEE Journal of, 1990. **26**(1): p. 113-122.

56. Hojfeldt, S. and Mork, J., *Modeling of Carrier Transport in Multi-Quantum-Well p-i-n Modulators.* Physica Scripta, 2002: p. 161.
57. Lapaul, S., de Lustrac, A., *et al.*, *Solving the Poisson's and Schrodinger's Equations to Calculate the Electron States in Quantum Nanostructures Using the Finite Element Method.* Magnetics, IEEE Transactions on, 1996. **32**(3): p. 1018-1021.
58. Davies, J.H., *The Physics of Low-Dimensional Semiconductors*. 1998: Cambridge University Press.
59. Martint, R.W., Wongt, S.L., *et al.*, *The Design of Quantum-Confined Stark Effect Modulators for Integration with 1.5um Lasers.* Semiconductor Science and Technology, 1993. **8**(6): p. 1173-1178.
60. Moseley, A.J., Robbins, D.J., *et al.*, *Quantum Confined Stark Effect in InGaAs/InP Single Quantum Wells Investigated by Photocurrent Spectroscopy.* Semiconductor Science and Technology, 1988. **4**(3): p. 184-190.
61. Prasad, P.N., *Nanophotonics*. 2004: John Wiley & Sons, Inc.
62. S.Schmitt-Rink, D.S.C.a.D.A.B.M., *Linear and Nonlinear Optical Properties of Semiconductor Quantum Wells.* Advances in Physics, 1989. **38**(2): p. 89-188.
63. Jamroz, W.R., Kruzelecky, R.V., *et al.*, *Applied Microphotonics*. 2006: Taylor & Francis Ltd.
64. *Properties of III-V Quantum Wells and Superlattices*. EMIS Datareviews, ed. Bhattacharya, P.K. 1996: Institution of Engineering and Technology.
65. Fukuda, M., *Optical Semiconductor Devices*. 1998: John Wiley & Sons, Inc.
66. Butcher, P.N. and Cotter, D., *The Elements of Nonlinear Optics* 1991: Cambridge University Press
67. Kost, E.G.a.A., ed. *Nonlinear Optics in Semiconductors I.* 1st ed. Semiconductors and Semimetals, ed. Weber, R.K.W.a.E.R. Vol. 58. 1998, Academic Press. 426.
68. Hanson, G.W., *Fundamentals of Nanoelectronics*. 2007: Pearson Prentice Hall.
69. *Semiconductor Quantum Optoelectronics: From Quantum Physics to Smart Devices - Proceedings of the Fiftieth Scottish Universities Summer School in Physics*, ed. Miller, A., Finlayson, D.M., *et al.* 1999: Edinburgh ; Bristol : Copublished by Scottish Universities Summer School in Physics.
70. Fox, A.M., *Optical Properties of Solids*. 2001: Oxford University Press.
71. Hunsperger, R.G., *Integrated Optics: Theory and Technology*. 2002: Springer-Verlag Berlin and Heidelberg GmbH & Co. K.
72. Miller, D.A.B., *Quantum Mechanics for Scientists and Engineers*. 2008, Cambridge University Press.
73. Ram-Mohan, R., *Finite Element and Boundary Element Applications in Quantum Mechanics*. Oxford Texts in Applied & Engineering Mathematics. 2002: Oxford University Press.
74. Akiyama, T., Georgiev, N., *et al. Nonlinearity and Response Time of 1.55um Intersubband Absorption in InGaAs/AlAs/AlAsSb Coupled Quantum Wells*. in *Lasers and Electro-Optics, 2001. CLEO '01. Technical Digest. Summaries of papers presented at the Conference on*. 2001.
75. Heber, J.D., Gmachl, C., *et al.*, *Comparative Study of Ultrafast Intersubband Electron Scattering Times at ~ 1.55um Wavelength in GaN/AlGaN Heterostructures.* Applied Physics Letters, 2002. **81**(7): p.

1237-1239.
76. *Confined Electrons and Photons: New Physics and Applications*, ed. Elias Burstein , C.W. 1995: Kluwer Academic / Plenum Publishers.
77. Lynch, S.A., Bates, R., *et al.*, *Intersubband Electroluminescence from Si/SiGe Cascade Emitters at Terahertz Frequencies.* Applied Physics Letters, 2002. **81**(9): p. 1543-1545.
78. Tomlinson, A.M., Chang, C.C., *et al.*, *Intersubband Transitions in GaAs Coupled-Quantum-Wells for Use as a Tunable Detector at THz Frequencies.* Applied Physics Letters, 2000. **76**(12): p. 1579-1581.
79. Xu, B., Hu, Q., *et al.*, *Electrically Pumped Tunable Terahertz Emitter Based on Intersubband Transition.* Applied Physics Letters, 1997. **71**(4): p. 440-442.
80. Yong, J.C.L., Rorison, J.M., *et al.*, *1.3um Quantum-Well InGaAsP, AlGaInAs, and InGaAsN Laser Material Gain: A Theoretical Study.* Quantum Electronics, IEEE Journal of, 2002. **38**(12): p. 1553-1564.
81. Wakita, K., *Semiconductor Optical Modulators*. 1998: Kluwer Academic Publishers.
82. Chuang, S.L., *Physics of Optoelectronic Devices*. Wiley Series in Pure and Applied Optics ed. Goodman, J.W. 1995: John Wiley & Sons, Inc.
83. Shin, D.S., *Reduction in Escape Times of Photogenerated Charge Carriers with Asymmetric Intrastep Quantum Wells and Subsequent Improvement in Saturation Optical Intensity.* Japanese Journal of Applied Physics, 2006. **45**: p. 9063-9065.
84. J.Wilson and J.F.B.Hawkes, *Optoelectronics: An introduction*. International Series in Optoelectronics, ed. P.J.Dean. 1983: Prentice-Hall International Inc.
85. Shin, D.S., *Effiect of a Step Barrier on the Quantum-Confined Stark Effect and Applications to Electroabsorption Modulators with High Saturation Optical Power.* Journal of the Korean Physical Society, 2005. **47**(2): p. 364-370.
86. Meglio, D., Lugli, P., *et al.*, *Analysis and Optimization of InGaAsP Electro-absorption Modulators.* IEEE Journal of Quantum Electronics, 1995. **31**(2): p. 261-268.
87. Yartiv, A., *Quantum Electronics*. 3rd. ed. 1989: John Wiley & Sons, Inc. p.240.
88. Garmire, E., Willardson, R.K., *et al.*, *Nonlinear Optics in Semiconductors I, Volume 58* 1999: Acdamic Press.
89. Glingener, C., Schulz, D., *et al.*, *Modeling of Optical Waveguide Modulators on III-V Semiconductors.* IEEE Journal of Quantum Electronics, 1995. **31**(1): p. 101-112.
90. Faist, J. and Reinhart, F.K., *Phase Modulation in GaAs/AlGaAs Double Heterostructures. I. Theory.* Journal of Applied Physics, 1990. **67**(11): p. 6998-7005.
91. Buus, J. and Botez, D., *Analytical Results for the Confinement Factor of Antiguides.* IEEE Photonics Technology Letters, 1996. **8**(1): p. 92-94.
92. Einarsson, G., *Principles of Light Wave Communications*. 1996: John Wiley&Sons.
93. *Guided-Wave Optoelectronics*. Springer Series in Electronics and Photonics, ed. Auston, D.H., Engl, W., *et al.* 1990: Springer-Verlag Berlin Heidelberg.
94. Dutta, A.K., Dutta, N.K., *et al.*, *WDM Technologies: Active Optical Components*. 2002: Elsevier Science.

95. Dagli, N., *High-Speed Photonic Devices*. Series in Optics and Optpelectronics. 2007: Taylor & Francis Group, LLC.
96. Singh, J., *Optical Properties of Condensed Matter and Applications*. 2006: WileyBlackwell
97. Huo, L., Yang, Y., *et al.*, *A Study on the Wavelength Conversion and All-Optical 3R Regeneration Using Cross-Absorption Modulation in a Bulk Electroabsorption Modulator.* J. Lightwave Technol., 2006. **24**(8): p. 3035.
98. Sze, S.M. and Ng, K.K., *Physics of Semiconductor Devices*. 3rd ed. 2007: John Wiley & Sons Inc.
99. Neudeck, G.W., *The PN Junction Diode*. Modular Series on Solid State Devices, ed. Neudeck, G.W. and Pierret, R.F. Vol. ii. 1989: Addison-Wesley Publishing Company.
100. Brennan, K.F., *The Physics of Semiconductors: With Applications to Optoelectronic Devices*. 1999: Cambridge University Press.
101. Pierret, R.F., *Advanced Semiconductor Fundamentals*. Modular Series on Solid State Devices, ed. Pierret, R.F. and Neudeck, G.W. Vol. VI. 1987: Addison-Wesley Publishing Company, Inc.
102. Kittel, C., *Introduction to Solid State Physics* 3rd ed. 1986: John Wiley&Sons.
103. Rajendran, V. and Marikani, A., *Materials Science*. Core Engineering Series. 2004: Tata McGraw-Hill Publishing Limited.
104. Yuan, J.S. and Liou, J.J., *Semiconductor Device Physics and Simulation*. Microdevices: Physics and Fabrication Technologies. 1998: Kluwer Academic / Plenum Publishers.
105. Blakemore, J.S., *Approximations for Fermi-Dirac Integrals, Especially the Function Used to Describe Electron Density in a Semiconductor.* Solid-State Electronics, 1982. **25**(11): p. 1067-1076.
106. Yacobi, B.G., *Semiconductor Materials: An Introduction to Basic Principles*. Mircrodevices:Physics and Fabrication Technologies. 2003: Kluwer Academic/Plenum Publishers, New York.
107. Morkoc, H., *Nitride Semiconductors and Devices*. Materials Sience. 1999: Springer-Verlag Berlin Heidelberg.
108. Press, W.H., Flannery, B.P., *et al.*, *Numerical Recipes in C-The Art of Scientific Computer*. 1988: Cambridge University Press.
109. Sambell, A.J. and Wood, J., *Unpinning the GaAs Fermi Level with Thin Heavily Doped Silicon Overlayers.* Electron Devices, IEEE Transactions on, 1990. **37**(1): p. 88-95.
110. Malagu, C., Guidi, V., *et al.*, *Model for Schottky Barrier and Surface States in Nanostructured n-type Semiconductors.* Journal of Applied Physics, 2002. **91**(2): p. 808-814.
111. Ancona, M.G., Yu, Z., *et al. Density-Gradient Simulations of Quantum Effects in Ultra-thin-oxide MOS Structures*. in *Simulation of Semiconductor Processes and Devices, 1997. SISPAD '97., 1997 International Conference on*. 1997.
112. Mishra, U.K. and Singh, J., *Semiconductor Device Physics and Design*. 2007: Kluwer Academic Publishers.
113. Pierret, R.F., *Semiconductor Fundamentals*. Modular Series on Solid State Devices, ed. Pierret, R.F. and Neudeck, G.W. Vol. I. 1988: Addison-Wesley Publishing company.
114. Betty Lise Anderson, R.L.A., *Fundamentals of Semiconductor Devices*. 2004: McGraw-Hill Higher Education.

115. Zeghbroeck, B.V., *Principles of Semiconductor Devices and Heterojunctions*. 2007: Prentice Hall.
116. Selberherr, S., *Analysis and Simulation of Semiconductor*. 1984: Springer-Verlag Wien.
117. Roy, D.K., *Physics of Semiconductor Devices*. 2004: Universities Press (India) Private Limited.
118. Fichtner, W., Rose, D.J., *et al.*, *Semiconductor Device Simulation.* IEEE Transactions on Electron Devices, 1983. **30**(9): p. 1018-1030.
119. Zeghbroeck, B.V., *Principles of Semiconductor Devices*. 2001: Colorado University
120. Grinberg, A.A. and Luryi, S., *On Electron Transport Across Interfaces Connecting Materials with Different Effective Masses.* Electron Devices, IEEE Transactions on, 1998. **45**(7): p. 1561-1568.
121. Wiedenhaus, M., Ahland, A., *et al.*, *Modelling and Simulation of Electroabsorption Modulators.* IEE Proceedings - Optoelectronics, 2002. **149**(4): p. 122-130.
122. Datta, S., *Quantum Phenomena*. Modular Series on Solid State Devices, ed. Pierret, R.F. and Neudeck, G.W. Vol. VII. 1989: Addison-Wesley Publishing Company.
123. Cole, E.A.B., Snowden, C.M., *et al.*, *Solution of the Coupled Poisson-Schrodinger Equations Using the Multigrid Method.* International Journal of Numerical Modelling-Electronic Networks Devices and Fields, 1997. **10**(2): p. 121-136.
124. Nelson, J., Paxman, M., *et al.*, *Steady-State Carrier Escape from Single Quantum-Wells.* IEEE Journal of Quantum Electronics, 1993. **29**(6): p. 1460-1468.
125. Nelson, J., Ballard, I., *et al.*, *Effect of Quantum Well Location on Single Quantum Well p-i-n Photodiode Dark Currents.* Journal of Applied Physics, 1999. **86**(10): p. 5898-5905.
126. Schiller, C., *Motion Mountain - The Adventure of Physics*. Quantum Theory: The Smallest Change. Vol. IV. 2009: www.motionmountain.net.
127. Jerome, J., *The Spacetime Model*. 2008: INPI.
128. Mitin, V.V., Kochelap, V.A., *et al.*, *Quantum Heterostructures: Microelectronics and Optoelectronics*. 1st ed. 1999: Cambridge University Press.
129. Lou, L.F., *Introduction to Phonons and Electrons*. 2003: World Scientific Publishing Co. Pet. Ltd. .
130. *Modeling and Diagnostics of Polymer Electrolyte Fuel Cells*. Modern Aspects of Electrochemistry, ed. Wang, C.Y. 2010: Springer Science+Business Media.
131. Enderlein, R. and Horing, N.J., *Fundamentals of Semiconductor Physics and Devices* 1997: World Scientific Publishing Co. Pte. Ltd.
132. Wong, K., *PhD Thesis: Modelling of Intersubband Absorption in Modulation Doped Deep Quantum Wells*, in *Department of Electronic and Electrical Engineering*. 2007, University of Bath: Bath.
133. Degani, M.H., *Electron Energy Levels in a Delta-Doped Layer in GaAs.* Physical Review B, 1991. **44**(11): p. 5580.
134. Singh, J., *Modern Physics for Engineers*. 1999: John Wiley & Sons, Inc.
135. Pedersen, F.B., *Simple Derivation of the Effective-Mass Equation Using a Multiple-Scale Technique* European Journal of Physics, 1997. **18**(1): p. 43-45.

136. Lundstrom, M., *Fundamentals of Carrier Transport*. 2 ed. 2000: Cambridge University Press.
137. Serway, R.A. and Jewett, J.W., *Physics for Scientists and Engineers with Modern Version 5, Chapters 39-46*. 7 ed. 12 July 2007: Thomson Higher Education
138. Harrison, P., *Quantum Wells, Wires and Dots*. 2nd ed. 2005: John Wiley & Sons Ltd.
139. Adachi, S., *Material Parameters of In1-xGaxAsyP1-y and Related Binaries* Journal of Applied Physics, 1982. **53**(12): p. 8775-8792.
140. Solgaard, O., *Photonic Microsystems*. Micro and Nanotechnology Applied to Optical Devices and Systems, ed. Senturia, S., Howe, R.T., *et al.* 2009: Springer Science+Business Media, LLC. .
141. Wake, D., *A 1550-nm Millimeter-Wave Photodetector with a Bandwidth-Efficiency Product of 2.4 THz.* Lightwave Technology, Journal of, 1992. **10**(7): p. 908-912.
142. Wake, D., Walling, R.H., *et al., Planar-junction, Top-Illuminated GaInAs/InP pin Photodiode with Bandwidth of 25 GHz.* Electronics Letters, 1989. **25**(15): p. 967-969.
143. *Optical Fiber Telecommunications IV-A: Components (Optics and Photonics)* 4th ed, ed. Kaminow, I.P. and Li, T. 2002: Academic Press.
144. Li, H., Yang, Y., *et al., A Study on the Wavelength Conversion and All-Optical 3R Regeneration Using Cross-Absorption Modulation in a Bulk Electroabsorption Modulator.* Lightwave Technology, Journal of, 2006. **24**(8): p. 3035-3044.
145. Chang, M.F., *Current Trends in Heterojunction Bipolar Transistors*. 1994: World Scientific Publishing Co Pte Ltd. 200.
146. Yamazoe, Y., Nishino, T., *et al., Bandgap Energy of InGaAsP Quaternary Alloy.* Japanese Journal of Applied Physics, 1980. **10**(8): p. 1473-1479.
147. Gini, E. and Melchior, H. *The Refractive Index of InP and its Temperature Dependence in the Wavelength Range from 1.2um to 1.6um*. in *Indium Phosphide and Related Materials, 1996. IPRM '96., Eighth International Conference on*. 1996.
148. Schmitt-Rink, S., Chemla, D.S., *et al., Linear and Nonlinear Optical Properties of Semiconductor Quantum Wells.* Advances in Physics, 1989. **38**(2): p. 89-188.
149. Olsen, G., Zamerowski, T., *et al., InGaAsP Quaternary Alloys: Composition, Refractive Index and Lattice Mismatch.* Journal of Electronic Materials, 1980. **9**(6): p. 977-987.